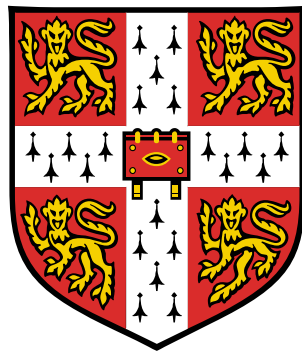


Grain Boundaries in Coated Conductors

Marcus Weigand
Jesus College
Cambridge



This dissertation is submitted
for the degree of Doctor of Philosophy
at the University of Cambridge

March 2010

Meinen Eltern

Declaration

This dissertation is the result of my own work and includes nothing which is the outcome of work done in collaboration except where specifically indicated in the text. No part of this dissertation has been submitted at Cambridge or any other University for a degree, diploma or other qualification.

Marcus Weigand
Cambridge
March 2010

Summary

The excitement which followed the discovery of *high-temperature superconductors* in 1986 was short-lived, as it became clear that their current carrying capacity (the critical current density J_c) was limited by grain boundaries (GBs). In order to reduce their detrimental effects *coated conductors* have been developed, in which a superconducting thin film is deposited on a polycrystalline, textured substrate.

Within certain temperature and magnetic field ranges, however, GBs still limit the overall J_c . This fact motivated the present thesis, for which the electrical properties of different types of coated conductors, and in particular their GBs, were investigated.

Several GBs and a single grain were isolated in a tape produced by metal-organic deposition (MOD), using a novel approach based on electron backscatter diffraction and a focused ion beam microscope. Measurements of their critical current densities for fields swept in the film plane showed the expected decrease with increasing misorientation angle at low fields. At higher fields an angle dependent crossover was found, from a GB to grain limited J_c .

In order to confirm this result and put it into broader perspective, the dependence of J_c on the width of polycrystalline tracks was studied, and then explained in terms of the behaviour of the single GBs. Investigations using low-temperature scanning laser microscopy rounded out the picture, which also showed GB dissipation at certain angles and grain limitation at others.

In measurements on samples produced by metal-organic chemical vapour deposition (MOCVD) characteristic differences compared to the MOD film were found. While both conductors exhibited high values of J_c , the variation with in-plane angle was significantly stronger for the MOCVD conductor, which can be explained by its sharper texture. In a track patterned perpendicular to the tape direction the phenomenon of vicinal channelling was observed, which previously was known only from films on single crystal substrates. Finally, an isolated boundary showed very high values of J_c , consistent with its low misorientation.

In order to better understand how the substrate influences the superconducting properties, measurements were carried out on otherwise identical samples grown on different substrates. A tape with grains elongated along its rolling direction showed particularly good properties at all examined field orientations. This extends the previously reported result that high aspect ratios are beneficial at fields applied perpendicular to the tape plane.

Acknowledgements

My first and greatest thanks, of course, go to my supervisor John Durrell. It is thanks to him that my PhD project became possible. He introduced me to thin film processing and to the measurement setup, and he certainly spotted many features in the obtained data which I would have overlooked. John was very supportive even though in the first part of my project I produced little to no useful results and showed an impressive lack of soldering skills. In addition to all that I got to appreciate his rather unique sense of humour!

Noel Rutter taught me how to perform XRD measurements and was strongly involved in the interpretation of both the J_c and the XRD data. In addition to that I am very grateful for the general knowledge on coated conductors he passed on to me.

A very important contribution to this project was made by Susannah Speller, who undertook the EBSD measurements. I am also very thankful for her answering general questions about this technique. Her colleague at Oxford, Gareth Hughes, performed most of the FIB work with great skill, which of course was an essential part of isolating grain boundaries. Chris Grovenor strongly contributed to both EBSD and FIB experiments and the interpretation of the J_c data with his broad knowledge of materials science.

I would like to recognise Mary Vicker's help with XRD measurements. She patiently discussed many aspects of this technique with me.

I am grateful to Jason Robinson and Atif Aziz for training me on the FIB and to Nadia Stelmashenko for showing me how to use the profilometer.

Suman-Lata Sahonta has done a great job in acquiring TEM images of my samples. I am also very grateful for her explanations of this complicated technique in general and her interpretation of the micrographs. This also extends to Sergio Lozano-Perez who acquired the cross-sectional TEM image presented in this thesis.

I should also like to thank my office mates Julia Linke, Alex Barcza, Kevin Musselman, Patrick Leung and James Witt for the nice atmosphere in our little home. In particular,

I owe a huge debt to Alex and Julia for taking care of me after a somewhat inelastic (and unplanned) scattering process involving my head and a metal bar during a hiking weekend in the Lake District.

The other colleagues working on applied superconductivity in our group have made my time here both very enjoyable and interesting, for which I am grateful. They are Judith Driscoll, Sophie Harrington, Rafael Dinner, Stuart Wimbush, Ahmed Kursumovic, Giorgio Ercolano and Zhang Han. This thanks, of course, also goes to all other members of the Device Materials Group not mentioned yet.

I am grateful to Ruben Hühne, Thomas Thersleff and Bernhard Holzapfel for two very pleasant visits at IFW Dresden. Tom has done some great FIB work on my samples. The group at IFW also supplied me with various tapes for my measurements.

Dmytro Abraimov performed the laser scanning measurements and explained a lot about this technique to me, for which I would like to thank him.

Marty Rupich from American Superconductor was kind enough to send me large pieces of their coated conductor and answered all questions I had about this product. The same thanks goes to SuperPower, from where I also obtained samples.

I would also like to thank Harald Weber and Michael Eisterer from the work group in Vienna, who supervised me during my diploma project. Without them I would not be in Cambridge.

The financial support by the Engineering and Physical Sciences Research Council (EPSRC) is greatly acknowledged. Funding from the Royal Academy of Engineering, the Institute of Physics, the Cambridge Philosophical Society and Jesus College Cambridge allowed me to attend several conferences. The stays at IFW Dresden were supported by the British Council and the Deutscher Akademischer Austausch Dienst.

Needless to say that very personal and special thanks go to my girlfriend Zarah, who certainly has more belief in me than I do. You mean a lot to me, Zarah.

Finally I would like to thank my parents for their support during my entire life.

Contents

Statement of Length	ix
Publications and Conference Presentations	x
Abbreviations	xv
1. Introduction	1
1.1. High-Temperature Superconductivity	1
1.2. Subject and Aims of this Thesis	2
1.3. Structure of this Thesis	3
I. Background	5
2. Superconductivity	6
2.1. Historical Background	6
2.2. Theories Describing Superconductivity	8
2.3. Type I and Type II Superconductors	11
2.4. Flux Lines	13
3. High-Temperature Superconductors and Their Grain Boundaries	27
3.1. Historical Background	28
3.2. Crystal Structure of YBCO	28
3.3. Superconducting Properties of Cuprates	29
3.4. Grain Boundaries	32
3.5. Applications	53

4. Coated Conductors	56
4.1. HTS Wires	56
4.2. Basic Architecture of Coated Conductors	58
4.3. Achieving Texture in Coated Conductors	59
4.4. Thin Film Deposition Techniques	62
4.5. Architectures of Samples in this Thesis	66
4.6. Current Percolation	69
II. Experimental	72
5. Sample Preparation	73
5.1. Processing Steps for the Different Experiments	73
5.2. Deposition of Contacts	74
5.3. Thin Film Patterning	75
5.4. Electron Backscatter Diffraction	77
5.5. Isolation of Grains and Grain Boundaries with a Focused Ion Beam	78
6. Characterisation Techniques	82
6.1. Electrical Characterisation – the Measurement Setup	82
6.2. Electron Backscatter Diffraction	86
6.3. X-Ray Diffraction	90
6.4. Low-Temperature Scanning Laser Microscopy	92
III. Results	94
7. Isolated Grain and Grain Boundaries in MOD CCs	95
7.1. Previous Studies	95
7.2. TEM and HR-EBSD	100
7.3. Critical Current Densities	102
7.4. Summary and Conclusions	116
8. Polycrystalline Tracks in MOD CCs	117
8.1. Previous Studies	118
8.2. XRD – Texture Analysis	119

Contents

8.3. Critical Current Densities of a Track of Different Widths	121
8.4. Comparison Between Single Grain/GBs and Polycrystalline Tracks	128
8.5. Summary and Conclusions	132
9. Low-Temperature Scanning Laser Microscopy of MOD CCs	134
9.1. Previous Studies	134
9.2. LTSLM	136
9.3. Critical Current Densities	139
9.4. Summary and Conclusions	141
10. MOCVD CCs	142
10.1. Previous Studies	143
10.2. TEM and FIB	152
10.3. XRD – Texture Analysis	154
10.4. Critical Current Densities	157
10.5. Comparison between MOCVD and MOD Coated Conductors	180
10.6. Summary and Conclusions	181
11. CCs Based on Different RABiTS Tapes	183
11.1. Previous Studies and Substrate Fabrication	183
11.2. Critical Current Densities	184
11.3. Summary and Conclusions	190
12. Conclusions and Further Work	192
12.1. Conclusions	192
12.2. Further Work	193
Bibliography	196

Statement of Length

The length of this thesis does not exceed the limit of 60,000 words set by the Degree Committee of Physics and Chemistry. Its total length in words is: 56,223.

Of which:

- Text: 45,838
- Headers: 541
- Figure and table captions and footnotes: 4,757
- Bibliography: 5,087

Publications and Conference Presentations

This thesis led to the following publications:

- **M. Weigand**, S. C. Speller, G. M. Hughes, N. A. Rutter, S. Lozano-Perez, C. R. M. Grovenor and J. H. Durrell: “Individual grain boundary properties and overall performance of metal-organic deposition coated conductors”, *Phys. Rev. B* **81**, 174537 (2010)
- R. Hühne, J. Eickemeyer, V. S. Sarma, A. Güth, T. Thersleff, J. Freudenberger, O. de Haas, **M. Weigand**, J. H. Durrell, L. Schultz and B. Holzapfel: “Application of textured highly alloyed Ni–W tapes for preparing coated conductor architectures”, *Supercond. Sci. Technol.* **23**, 034015 (2010)
- **M. Weigand**, S. Speller, N. A. Rutter, G. M. Hughes, C. Grovenor and J. H. Durrell: “Critical Current Densities of Isolated Grain Boundaries in Coated Conductors”, *IEEE Trans. Appl. Supercond.* **19**, 3569 (2009)

The following conference and seminar presentations were given by the author:

- M. Weigand, S. Speller, G. M. Hughes, N. A. Rutter, S. Lozano-Perez, C. Grovenor and J. H. Durrell: “The Interplay between Individual Grain Boundary Properties and Overall Coated Conductor Performance”, poster presented at the IOP Superconductivity Group Seminar: Development and Applications of HTS Conductors, London (15 January 2010)
- M. Weigand, S. Speller, G. M. Hughes, S. Lozano-Perez, N. A. Rutter, C. Grovenor and J. H. Durrell: “The Influence of Grain Boundaries and Vicinality on Coated Conductor Performance”, invited talk given in the Seminar of the Low Temperature

Physics and Superconductivity Group, Institute of Atomic and Subatomic Physics, Vienna University of Technology (16 November 2009)

- M. Weigand, S. Speller, G. M. Hughes, S. Lozano-Perez, N. A. Rutter, C. Grovenor and J. H. Durrell: “The Interplay between Individual Grain Boundary Properties and Overall Coated Conductor Performance”, talk given at the European Conference on Applied Superconductivity, Dresden (13–17 September 2009)
- M. Weigand, S. Speller, N. A. Rutter, G. M. Hughes, C. Grovenor and J. H. Durrell: “Critical Current Densities of Isolated Grains and Grain Boundaries in Coated Conductors”, poster presented at the Meeting of the Institute of Physics Superconductivity Group, London (30 January 2009)
- M. Weigand, S. Speller, N. A. Rutter, G. M. Hughes, C. Grovenor and J. H. Durrell: “Critical Current Densities of Isolated Grains and Grain Boundaries in Coated Conductors”, talk and invited poster at Coated Conductors for Applications, Houston (4–6 December 2008)
- M. Weigand, S. Speller, N. A. Rutter, G. M. Hughes, C. Grovenor and J. H. Durrell: “Critical Current Densities of Isolated Grain Boundaries in Coated Conductors”, poster presented at Applied Superconductivity Conference, Chicago (17–22 August 2008)
- M. Weigand, J. H. Durrell, N. A. Rutter and S. Speller: “Angular Field-Dependence of the Critical Current Density of Coated Conductors for Different Track Widths”, poster presented at Condensed Matter and Materials Physics Conference, Royal Holloway London (26–28 March 2008)
- M. Weigand, J. H. Durrell, N. A. Rutter and S. Speller: “Angular Critical Current Measurements on Coated Conductors”, talk given in the Seminar of the Device Materials Group, Dept. of Materials Science, University of Cambridge (11 December 2007)
- M. Weigand, J. H. Durrell, N. A. Rutter and S. Speller: “Angular Field-Dependence of the Critical Current Density of Coated Conductors for Different Track Widths” poster presented at the Meeting of the Institute of Physics Superconductivity Group, London (30 November 2007)

- M. Weigand, J. H. Durrell, N. A. Rutter and S. Speller: “Critical Current Densities of Isolated Grain Boundaries in Coated Conductors”, poster presented at the European Conference on Applied Superconductivity, Brussels (16–20 September 2007)
- M. Weigand, J. H. Durrell, N. A. Rutter and S. Speller: “Angular Critical Current Measurements on Coated Conductors”, talk given in the Postgraduate Seminar, Dept. of Materials Science, University of Cambridge (25, 26 June 2007)
- M. Weigand, J. H. Durrell, N. A. Rutter, J. L. MacManus-Driscoll and S. Speller: “Critical Current Densities of Coated Conductors for Different Track Widths and an Isolated Grain Boundary”, poster presented at the Condensed Matter and Materials Physics Conference, Leicester (12, 13 April 2007)
- M. Weigand, J. H. Durrell, N. A. Rutter and J. L. MacManus-Driscoll: “Dependence of the critical current density of coated conductors on the track width”, poster presented at the Meeting of the Institute of Physics Superconductivity Group, London (29 November 2006)

The work in this thesis contributed to these presentations:

- S.-L. Sahonta, **M. Weigand**, J. H. Durrell and J. L. MacManus-Driscoll: “Strain Accommodation Mechanisms for Oxide Inclusions in REBa₂Cu₃O_{7- δ} Coated Conductors”, poster presented at the MRS Spring Meeting (5–9 April 2010)
- S.-L. Sahonta, **M. Weigand**, J. L. MacManus-Driscoll and J. H. Durrell: “Grain Rotations in REBCO Coated Conductors”, poster presented at the IOP Superconductivity Group Seminar: Development and Applications of HTS Conductors, London (15 January 2010)
- R. Hühne, J. Eickemeyer, U. Gaitzsch, T. Thersleff, J. Freudenberger, L. Schultz, B. Holzapfel, O. de Haas, V. S. Sarma, **M. Weigand**, J. H. Durrell: “Application of textured highly alloyed Ni-W tapes for coated conductors”, invited talk given at Coated Conductors for Applications, Barcelona (22–24 November 2009)
- A. Kießling, J. Hänisch, E. Reich, T. Thersleff, B. Holzapfel, L. Schultz, **M. Weigand**, J. Durrell: “Influence of the deposition temperature on the superconducting

properties of YBCO/BZO quasimultilayers”, invited talk given at Coated Conductors for Applications, Barcelona (22–24 November 2009)

- R. Hühne, J. Eickemeyer, V. S. Sarma, A. Güth, T. Thersleff, J. Freudenberger, O. de Haas, **M. Weigand**, J. H. Durrell, L. Schultz and B. Holzapfel: “Application of textured highly alloyed Ni-W tapes for coated conductor architectures”, talk given at the European Conference on Applied Superconductivity, Dresden (13–17 September 2009)
- A. Kießling, J. Hänisch, E. Reich, T. Thersleff, **M. Weigand**, J. H. Durrell, B. Holzapfel and L. Schultz: “Deposition temperature dependence on the superconducting properties of YBCO/BZO quasimultilayers”, talk given at the European Conference on Applied Superconductivity, Dresden (13–17 September 2009)
- R. Hühne, J. Eickemeyer, T. Thersleff, B. Holzapfel, V. S. Sarma, **M. Weigand**, J. H. Durrell, O. de Haas, L. Schultz: “Application of textured highly alloyed Ni-W tapes for coated conductor architectures”, talk given at the Cryogenic Engineering Conference and International Cryogenic Materials Conference, Tucson, Arizona (28 June – 2 July 2009)
- D. Abraimov, P. Li, D. Larbalestier, X. Li, M. Rupich, **M. Weigand**, J. Durrell, N. Rutter: "Visualization of dissipation at different magnetic field orientations in RABiTS coated conductors", talk given at MRS Spring Meeting, San Francisco (13–17 April 2009)
- R. Hühne, J. Eickemeyer, V. S. Sarma, T. Thersleff, O. de Haas, **M. Weigand**, J. H. Durrell, L. Schultz and B. Holzapfel: “Application of textured highly alloyed Ni-W tapes for coated conductor architectures”, talk given at Coated Conductors for Applications, Houston (4–6 December 2008)
- **M. Weigand**, N. A. Rutter, J. H. Durrell, S. Speller, G. M. Hughes and C. Grovenor: “Elimination of the grain boundary suppression of J_c in YBCO”, invited talk given at Nanostructured Superconductors: From fundamentals to applications, Freudenstadt-Lauterbad, Germany (13–17 September 2008)
- S. C. Speller, **M. Weigand**, J. H. Durrell and N. A. Rutter: “Critical Current Densities of Isolated Grain Boundaries in Coated Conductors”, talk given at the

International Conference on Superconductivity and Magnetism, Side-Antalya, Turkey (25–29 August 2008)

- J. H. Durrell, **M. Weigand**, N. A. Rutter, S. Engel, R. Hühne and B. Holzapfel: “Meandered grain boundaries and the elimination of the ‘grain boundary’ dominated regime in RABiTS conductors”, talk given at Applied Superconductivity Conference, Chicago (17–22 August 2008)
- R. Hühne, J. Eickemeyer, T. Thersleff, L. Schultz, B. Holzapfel, V. Subramanya Sarma, **M. Weigand** and J. H. Durrell: “Preparation of coated conductor architectures on textured highly alloyed Ni-W tapes”, poster presented at Applied Superconductivity Conference, Chicago (17–22 August 2008)

Abbreviations

The abbreviations used in this thesis are defined and the pages are given where they are explained / discussed in more detail.

Abbreviation	Description	Page(s)
APB	anti-phase boundary	38, 160
BSCCO	$\text{Bi}_2\text{Sr}_2\text{Ca}_{n-1}\text{Cu}_n\text{O}_{2n+4+\delta}$	28
CC	coated conductor	56
EBS	electron backscatter diffraction	77, 86
FIB	focused ion beam	78
FLL	flux line lattice	15
FWHM	full width at half maximum	
GB	grain boundary	32
HAGB	high-angle grain boundary	37
HR	high-resolution (TEM or EBSD)	
HTS	high-temperature superconductor	27
IBAD	ion beam assisted deposition	61
IG	intragranular	
LAGB	low-angle grain boundary	35
LTS	low-temperature superconductor	6
LTSLM	low-temperature scanning laser microscopy	92
MOCVD	metal-organic chemical vapour deposition	64
MOD	metal-organic deposition	64
ND	normal direction (of a tape)	
PLD	pulsed laser deposition	63
RABiTS	rolling assisted bi-axially textured substrates	59
RD	rolling direction (of a tape)	
REBCO	$\text{REBa}_2\text{Cu}_3\text{O}_{7-\delta}$ (RE = rare earth)	28
SEM	scanning electron microscopy	77, 86
TD	transverse direction (of a tape)	
TEM	transmission electron microscopy	100, 152
XRD	x-ray diffraction	90
YBCO	$\text{YBa}_2\text{Cu}_3\text{O}_{7-\delta}$	28

1 Introduction

1.1. High-Temperature Superconductivity

So far most applications of superconductivity have been realised with conventional *low-temperature superconductors (LTS)*. The high cooling costs involved mean that they are limited to rather specialised tasks (e.g. magnets for scientific research), which cannot be fulfilled by normal conducting wires. Except for magnetic resonance imaging in health care, all of these applications represent niche markets.

As their name implies *high-temperature superconductors (HTS)* remain superconducting up to (comparably) elevated temperatures. Some of the materials in this class can be used at liquid nitrogen temperature, thus removing the need for more expensive cryogenics like liquid helium.

It is clear that the possibility of using an affordable coolant is a prerequisite to a broader application of superconductors, for example in superconducting wires for power transmission¹ and coils in motors and generators. It is important to bear in mind, however, that (with very few exceptions) these tasks can also be fulfilled by conventional conductors. The only reason for utilities and other potential customers to switch to HTS would be reduced total lifetime costs.

This implies that superconducting wires need to be optimised to a very high extent. It was found soon after their discovery that the critical current density J_c of HTS (i.e. their current carrying capacity) is seriously limited by grain boundaries (GBs). A mis-

¹Superconducting cables would be mainly employed in densely populated areas, where their lower cross-section offers an additional advantage over conventional cables.

alignment of only a few degrees between neighbouring grains can reduce J_c by an order of magnitude. Consequently, methods were sought to align grains and achieve wires with low-angle grain boundaries only.

This led to the development of *coated conductors* or second generation HTS wires. A superconducting thin film is deposited on a substrate which provides a template of aligned grains, thus significantly higher values of J_c can be achieved than in wires with randomly oriented grains. The material of choice for these conductors is usually $\text{YBa}_2\text{Cu}_3\text{O}_{7-\delta}$ (YBCO), which offers the highest critical current density and irreversibility field.²

1.2. Subject and Aims of this Thesis

Even in coated conductors, however, over large ranges of temperature and applied magnetic field the grain boundaries, rather than the intrinsic bulk properties of the material itself, limit J_c . As a consequence, enhancing the performance of the grains would not lead to a noticeable improvement of the conductor.

It is clear from these considerations that further optimisations are only possible through a deep understanding of the physics governing the behaviour of CCs. Consequently, not only research and development into the fabrication of CCs deserve large efforts, but also their characterisation. It is the latter area to which this thesis contributes.

While there are many different techniques for investigating the current carrying capacity of a superconductor, the most direct and reliable of these are transport measurements, where current is applied to a sample while the voltage across it is measured. It is, however, far from trivial to separate contributions from grains and GBs in these measurements. The best way to achieve this is to isolate single grains and GBs in a real coated conductor and investigate their properties. This was done for this thesis on several samples, leading to new insights into their electrical properties.

The transport measurements were carried out using a probe which allows the sample to be rotated about two axes with respect to the applied magnetic field. As is shown in this thesis, measurements where the field is swept in the plane of a film allow one to study how microscopic currents flow in the sample.

²At a magnetic field equal to the irreversibility field the critical current density becomes zero while the sample is still superconducting.

Another approach to investigate GBs is the measurement of wider, polycrystalline tracks. By comparing J_c of tracks of different widths, conclusions can be drawn as to how the current is limited; this is the second route that has been pursued.

The third “pillar” of the present work is low-temperature scanning laser microscopy, which allows one to probe dissipation in a superconductor with spatial resolution.

It needs to be pointed out that all of these experiments were performed on coated conductor samples supplied by industry market leaders and other research institutions. While a lot has been learnt in the past (and probably will be in the future) from model grain boundaries, in particular those grown on bicrystal substrates, it is invaluable to investigate the properties of “real-world products” as well.

1.3. Structure of this Thesis

This thesis is divided into three parts. In *Part I – Background* a review is given of the different topics relevant to this work. In Chap. 2 superconductivity itself is discussed, as only a good understanding of the fundamental physics governing current transport in coated conductors allows one to interpret the measured data correctly. This is followed by Chap. 3, which covers HTS and their grain boundaries in detail. By discussing the knowledge on GBs already available this chapter both motivates the experiments carried out for this thesis and puts them in a broader perspective. Chapter 4 at the end of the first part treats coated conductors, in particular their fabrication.

A variety of advanced sample preparation and characterisation methods were employed for this thesis, which are described in *Part II – Experimental*. The techniques used to prepare the samples (Chap. 5) include conventional photolithography, electron backscatter diffraction and focused ion beam patterning. The samples were investigated by transport measurements, electron backscatter diffraction, x-ray diffraction and scanning laser microscopy, as discussed in Chap. 6.

This leads to *Part III*, where the *results* obtained are presented. In Chap. 7 the J_c data from a grain and several GBs isolated in a tape produced by Metal-Organic Deposition (MOD) are discussed, in particular the angle dependent crossover from GB to grain limited behaviour. The results fit well to the findings on the dependence of J_c on the width of polycrystalline tracks (Chap. 8). The variation of J_c when a magnetic field is rotated in the film plane becomes weaker when the track is narrowed down,

consistent with the angular behaviour of isolated GBs. This is in agreement with low-temperature scanning laser microscopy maps obtained from the same tape (Chap. 9). As this technique allows one to determine where on a sample dissipation occurs it proved a powerful tool to support the conclusions drawn in the previous two chapters. Moving on to different samples, a thorough investigation of a conductor produced by Metal-Organic Chemical Vapour Deposition (MOCVD) is presented in Chap. 10. A large number of different angular measurements were performed on this tape, which, due to its vicinality and the presence of various pinning centres, allowed several interesting phenomena to be observed, for example vicinal channelling. A grain boundary was isolated in this conductor as well. Chapter 11 at the end of this thesis is dedicated to an investigation of the influence of the substrate on the superconducting properties. To this end angular critical current density measurements were performed on samples produced from different substrates.

Part I.
Background

2 Superconductivity

Superconductivity was discovered about 100 years ago. In this chapter the physical foundations of superconductivity are discussed. A separate chapter is dedicated to high-temperature superconductors (Chap. 3); where appropriate, however, they will be mentioned in the present chapter.

At the start of this chapter a summary is given of the most important discoveries relating to superconductivity and the conditions under which this phenomenon can be observed. In Sec. 2.2 different theories are delineated which have been developed in order to explain superconductivity. The differences between the two classes of superconductors—type I and type II—are then discussed in Sec. 2.3. The largest part of this chapter (Sec. 2.4) is dedicated to the flux lines which occur in type II superconductors, the properties of which are highly relevant to the investigations presented in this thesis.

2.1. Historical Background

In the year 1908 Heike Kamerlingh Onnes successfully liquefied helium for the first time. This allowed him to perform resistivity measurements on mercury at very low temperatures.

It was expected that the resistivity would drop steadily with temperature to reach zero (or some finite value due to impurity scattering) at 0 K. In 1911 Onnes found, however, that it dropped abruptly to zero over the range of a few hundredths of a Kelvin at 4.2 K [1], a phenomenon which he later termed *superconductivity*. The fact that currents in a

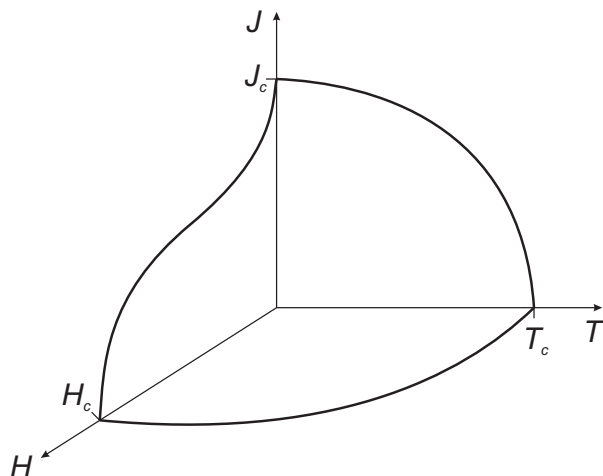


Figure 2.1: Superconductivity occurs only below a certain temperature, field and current, i.e. below the surface shown in this schematic phase diagram (after [2]).

superconducting loop do not decay over time proves that it is a real disappearance of resistivity and not just a drop below the sensitivity of a voltmeter.

Subsequently, it was discovered that most metals and some nonmetals under high pressure as well as certain alloys become superconducting below their respective *critical temperature* T_c . These temperatures, also termed *transition temperatures*, are below 10 K for elements, whereas alloys reach critical temperatures of up to 23 K. Due to their rather low values of T_c , these materials are classed as conventional or *low-temperature superconductors (LTS)*. It was not until the discovery of the *high-temperature superconductors (HTS)* in 1986, discussed in detail in Chap. 3, that the achievable transition temperatures rose significantly.

Superconductivity disappears below T_c if the sample is exposed to a magnetic field higher than the *critical field* H_c or if a current larger than the *critical current* I_c is passed through it. According to *Silsbee's rule* this is based on the same effect: in the simple case of a superconducting wire H_c is equivalent to the field at its surface which would be generated by a current I_c passing through it.¹ The schematic phase diagram in Fig. 2.1 shows how the emergence of the superconducting state depends on temperature, field and current.

A superconductor at a temperature below T_c expels an applied magnetic field $H < H_c(T)$ (except for a certain penetration depth), similar to an ideal conductor. If a field is applied above T_c and the superconductor is then cooled through its transition, the flux is expelled as well, rather than being trapped as would be expected for an ideal

¹This, however, is true only for type I superconductors. Type II superconductors remain superconducting up to $H_{c2} > H_c$, see Sec. 2.3.

conductor [3]. This phenomenon is called the *Meissner effect*, which necessitates the flow of screening currents in the superconductor and makes it a perfect diamagnet.

The loss in free energy when a material changes from its normal into its superconducting state is called *condensation energy*. If the energy necessary to expel an applied magnetic field becomes larger than the condensation energy it is favourable for the system to become normal conducting again. The field at which this happens is the critical field H_c mentioned above.

2.2. Theories Describing Superconductivity

There are three main theories which describe the superconducting state. The *London* and the *Ginzburg-Landau theory* deal with it by a phenomenological approach, whereas the *BCS theory* is a microscopic treatment of the phenomenon.

2.2.1. London Theory

This electromagnetic theory, which was developed by F. and H. London [4] in 1935, extends the Maxwell equations by the two *London equations*

$$\mathbf{E} = \frac{\partial}{\partial t}(\Lambda \mathbf{j}_s) \quad (2.1)$$

and

$$\mathbf{b} = -\text{curl}(\Lambda \mathbf{j}_s), \quad (2.2)$$

where

$$\Lambda = \mu_0 \lambda_L^2 = \frac{m_e}{n_s e^2}. \quad (2.3)$$

\mathbf{E} and \mathbf{b} are the microscopic electric field and magnetic flux density, \mathbf{j}_s the microscopic current density,² Λ the (phenomenological) *London parameter*, m_e the electronic mass, n_s the number density of superconducting electrons and e the elementary charge.

If Eq. (2.1) is rewritten as $\partial \mathbf{j}_s / \partial t = (n_s e^2 / m_e) \mathbf{E}$ one can see that it describes the free acceleration of superelectrons in an applied electric field and that the current does not decay if the field is subsequently turned off.

²In this thesis small letters are used to refer to microscopic quantities. Consequently, $\mathbf{b} = \mu_0 \mathbf{h}$ is the microscopic flux density in free space, whereas \mathbf{B} denotes a macroscopic average. \mathbf{E} is always used for the electric field, however, in order to avoid confusion with the elementary charge e .

The second London equation (2.2) together with Ampère's law $\text{curl } \mathbf{b} = \mu_0 \mathbf{j}$ gives the screening equation

$$\nabla^2 \mathbf{b} = \frac{\mathbf{b}}{\lambda_L^2}, \quad (2.4)$$

hence the magnetic induction and the supercurrent density in a sample decay exponentially with the *London penetration depth* λ_L .

Even though London theory is a rather simple description of the phenomenon of superconductivity it describes HTS well due to their high Ginzburg-Landau parameter (see Secs. 2.2.2 and 2.4).

2.2.2. Ginzburg-Landau Theory

This theory, which was established by V. L. Ginzburg and L. D. Landau in 1950, for the first time delivered quantitative results for the case that parts of the sample are superconducting while others are in the normal state, as is the case for type I superconductors in the intermediate state and for type II superconductors in the mixed state (see Sec. 2.3). It describes the ceramic oxide superconductors well, but as mentioned previously it is a phenomenological theory, hence it does not explain how superconductivity works on a microscopic scale. It is based on a general theory of phase transitions of second order by Landau [5] in which the free energy is developed with respect to a (complex) order parameter Ψ close to T_c . In Ginzburg-Landau theory this order parameter is treated as space dependent and interpreted as an effective wave function of the superconducting charge carriers [6]. It can be normalised as

$$\int_{-\infty}^{+\infty} \Psi \Psi^* dV = n_p \quad (2.5)$$

in order to relate it to the effective pair density $n_p = \frac{1}{2}n_s$ (the superconducting charge carriers are electron pairs, as discussed in Sec. 2.2.3).

When a magnetic field is introduced the free energy of the superconducting state F_s can be written as

$$F_s = F_n + \int_V \left[\alpha \Psi^* \Psi + \frac{1}{2} \beta (\Psi^* \Psi)^2 + \epsilon \left| \nabla \Psi - \frac{2e}{i\hbar} \mathbf{A} \Psi \right|^2 \right] dV + \int \frac{1}{2\mu_0} (\mathbf{B} - \mathbf{B}_E)^2 dV, \quad (2.6)$$

2. Superconductivity

where F_n is the free energy of the normal state and $\alpha = \alpha(T)$ and $\beta = \text{const.}$ are parameters taken from the general theory by Landau. ϵ is a parameter which may be treated as constant near T_c , \mathbf{A} the vector potential of the magnetic field and \mathbf{B}_E the externally applied field. It can be shown that the normalisation by Eq. (2.5) implies that $\epsilon = \hbar^2/4m_e = \hbar^2/2m$ with the pair mass m twice the electron mass, and thus all superconducting properties depend on the two parameters α and β only.

One can now determine the equilibrium state by minimising the free energy with respect to small changes in Ψ and to the magnetic field and obtain the two *Ginzburg-Landau equations*

$$\frac{1}{2m}(-i\hbar\nabla + 2e\mathbf{A})^2\Psi + (\alpha + \beta \Psi^*\Psi)\Psi = 0 \quad (2.7)$$

and

$$\mathbf{J}_s = \frac{ie\hbar}{m}(\Psi^*\nabla\Psi - \Psi\nabla\Psi^*) - \frac{4e^2}{m}\mathbf{A}\Psi^*\Psi. \quad (2.8)$$

While Eq. (2.7) is an energy eigenvalue equation, Eq. (2.8) describes the current density in terms of a quantum mechanical probability density flow.

In Ginzburg-Landau theory there are two characteristic lengths. Similar to London theory (discussed in Sec. 2.2.1) the *Ginzburg-Landau penetration depth*

$$\lambda = \sqrt{\frac{m\beta}{4\mu_0 e^2 |\alpha|}} \quad (2.9)$$

describes the decay of a magnetic field in the superconductor. The distance over which spatial changes in Ψ occur is given by the *Ginzburg-Landau coherence length*

$$\xi = \sqrt{\frac{\hbar^2}{2m|\alpha|}}. \quad (2.10)$$

As T approaches T_c both λ and ξ diverge. The ratio of these two lengths,

$$\kappa = \frac{\lambda}{\xi}, \quad (2.11)$$

which is approximately independent of temperature, is called the *Ginzburg-Landau parameter* and determines if a material is a type I or a type II superconductor (see Sec. 2.3).

2.2.3. BCS Theory

In 1957 J. Bardeen, L. N. Cooper and J. R. Schrieffer postulated a theory which became known as the *BCS theory* [7]. It explains superconductivity by the exchange of phonons between electrons via the ionic lattice (electron-phonon coupling). This causes an attractive potential between electrons leading to the formation of *Cooper pairs*, i.e. a small proportion of electrons near the Fermi energy are coupled in pairs. The BCS coherence length ξ_0 describes the radius of the orbital state of these pairs, which is about $1\ \mu\text{m}$ in a conventional superconductor at $T = 0\ \text{K}$. The electrons of a pair have opposite momentum and spin, hence the total spin of a pair is zero. Consequently, they behave like bosons and can be in the same quantum mechanical state.

When two electrons form a pair the condensation energy $\mu_0 H_c^2/2$ is gained, and the same amount of energy is needed to break up a pair. As a consequence, an *energy gap* is observed: there are no allowed states in an energy range of 2Δ around the Fermi level. Above the gap are the states of the free electrons, below those of the Cooper pairs. The BCS relation

$$2\Delta(0) = 3.53 k_B T_c \quad (2.12)$$

relates the energy gap at $T = 0\ \text{K}$ to the critical temperature.

It was shown by L. P. Gor'kov that the Ginzburg-Landau theory discussed in Sec. 2.2.2 can be deduced from the BCS theory [8]. It needs to be mentioned, however, that the BCS theory only describes low T_c superconductors and fails to explain the behaviour of HTS. The BCS theory is discussed in more detail in several reference works [9, 10, 11].

2.3. Type I and Type II Superconductors

The surface energy σ_{ns} , i.e. the energy necessary to introduce a boundary between a superconducting and a normal region, consists of two parts: on the one hand there is the positive energy needed in order to expel the field and make a region of the sample superconducting. On the other hand there is the negative energy which is gained when electrons condense to Cooper pairs.

If σ_{ns} is positive phase boundaries are unfavourable and, if the sample is a thin slab parallel to the applied field, it will remain in the Meissner state as a whole up to the critical field H_c (see Sec. 2.1). This is the case for a Ginzburg-Landau parameter $\kappa < 1/\sqrt{2}$; this class of materials is called *type I superconductors*.

2. Superconductivity

If the sample is of a different geometry, however, the actual field it is exposed to will be higher, due to the *demagnetisation effect*, which leads to a feedback by the sample's magnetisation on the applied field. In the simple case of a spheroid it can be described by the demagnetisation factor D and the effective field in the sample is then given by

$$H_{\text{eff}} = \frac{H}{1 - D}, \quad (2.13)$$

where H is the applied field. As $0 \leq D \leq 1$ the demagnetisation effect always leads to a field enhancement.

Normal conducting lamellae parallel to the field will, therefore, form in the sample at an applied field $H < H_c$ and it will enter what is called the *intermediate state*. The volume of the normal regions increases with field until the whole sample turns normal at $H = H_c$.

If $\kappa > 1/\sqrt{2}$ the surface energy becomes negative, the consequences of which were not anticipated until A. A. Abrikosov predicted correctly in 1957 that in this case small normal conducting areas would develop, termed *flux lines* or *vortices* [12]. The lowest energy state of these *type II superconductors* would be the one with the longest normal–superconducting boundaries and hence the normal regions would be subdivided until a quantum limit was reached. Each flux line then carries a flux quantum $\Phi_0 = h/2e = 2.07 \times 10^{-15}$ Wb.

Type II superconductors behave like type I superconductors up to the *lower critical field* H_{c1} where the first flux lines penetrate. In the *mixed state* which then follows, superconductivity persists until the *upper critical field* H_{c2} is reached where the cores of neighbouring vortices begin to overlap and the whole sample turns normal. Because of the partial flux penetration the energy needed to expel the field from the rest of the sample is much smaller and thus H_{c2} can reach values much larger than H_c . This is the reason why superconductors used in applications can sustain strong magnetic fields without turning normal over their whole volume.

All elementary superconductors except for niobium, vanadium and technetium are type I superconductors while all alloys (and the HTS) are type II superconductors.

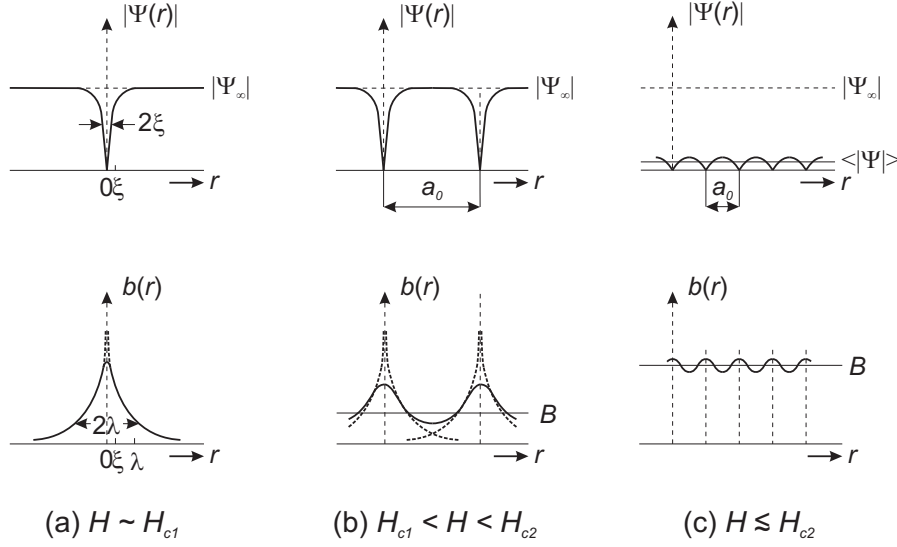


Figure 2.2.: Spatial variation of the order parameter and magnetic field. (a) An isolated flux line. (b) At intermediate flux densities the fields superimpose. (c) Close to the upper critical field there are no more distinct vortices (after [13]).

2.4. Flux Lines

Shielding currents flow around each vortex, which is why the field decays in the superconducting regions over the characteristic length λ . This is illustrated for an isolated flux line in Fig. 2.2(a). The order parameter Ψ on the other hand is constant far away from the vortex, but vanishes at its centre, which can be quantified by the coherence length ξ . As the density of flux lines increases [Fig. 2.2(b)] the fields of neighbouring vortices begin to overlap, but the order parameter still reaches its maximum value between them. This is not the case any more in Fig. 2.2(c) where the field is close to the upper critical field and there are no more distinct vortex lines.

Making an appropriate ansatz and substituting it in the Ginzburg-Landau equations (2.7) and (2.8) it can be shown that for an isolated flux line $\Psi(r)$ is approximately proportional to $\tanh \frac{\nu r}{\xi}$ where ν is a constant ~ 1 .

For general κ the Ginzburg-Landau equations can only be solved numerically in order to obtain the behaviour of b . In the limit $\lambda \gg \xi$ (i.e. $\kappa \gg 1$, termed extreme type II superconductors), however, Ψ has a constant value Ψ_∞ almost everywhere except for a small core region of radius $\sim \xi$. The sample can then be treated as an ordinary London superconductor by a London equation [see Eq. (2.2)] which has been extended by a term

2. Superconductivity

to include the flux line:

$$\Lambda \operatorname{curl} \mathbf{j}_s + \mathbf{b} = \hat{\mathbf{n}} \Phi_0 \delta_2(\mathbf{r}), \quad (2.14)$$

where $\hat{\mathbf{n}}$ is the unit vector in the direction of the vortex. Using Ampère's law a solution for $b(r)$ can be found with a spatial dependence of $r^{-1/2}e^{-r/\lambda}$ for $r \rightarrow \infty$ and $\ln \frac{\lambda}{r}$ for $\xi \ll r \ll \lambda$.

In the following an expression for the lower critical field shall be deduced. At $H = H_{c1}$ the Gibbs free energy has to be the same with and without a vortex in the superconductor. This leads to

$$H_{c1} = \frac{\epsilon_l}{\Phi_0}, \quad (2.15)$$

where ϵ_l is the free energy per unit length of the flux line. Neglecting the core one can calculate ϵ_l from the contributions from the field energy and the kinetic energy of the currents. With the result for $b(r)$ obtained above one finds

$$\epsilon_l = \frac{\Phi_0 H_c}{\sqrt{2}\kappa} \ln \kappa \quad (2.16)$$

and using Eq. (2.15)

$$H_{c1} = \frac{H_c}{\sqrt{2}\kappa} \ln \kappa. \quad (2.17)$$

The upper critical field is the field where superconductivity is nucleated. As Ψ is small in that case, the problem can be treated by the *linearised Ginzburg-Landau equation*³ which has the same form as the Schrödinger equation for a free particle of mass m and charge $2e$ in a uniform applied magnetic field. The largest field at which a solution for this equation exists is the upper critical field

$$H_{c2} = \frac{\Phi_0}{2\pi\mu_0\xi^2} = \sqrt{2}\kappa H_c. \quad (2.18)$$

This shows that for type I superconductors (where $\kappa < 1/\sqrt{2}$) $H_{c2} < H_c$, which means that they “supercool”, i.e. they remain normal below H_c down to H_{c2} . In practice, however, nucleation can take place at sample defects at $H > H_{c2}$, hence the upper critical field represents only a theoretical limit.

³One obtains the linearised Ginzburg-Landau equation by dropping the term in β in Eq. (2.7). This is feasible for small Ψ .

2.4.1. Flux Line Lattice

The total flux density of two vortices can be written as the linear superposition of the contributions of each flux line. A similar derivation as above for the line energy of one vortex shows that the interaction is repulsive. Flux lines, thus, form an array, the *flux line lattice (FLL)*, where the force per unit length on a vortex can be written as

$$\mathbf{f} = \mathbf{J}_s \times \hat{\mathbf{n}}\Phi_0. \quad (2.19)$$

\mathbf{J}_s is the total supercurrent density due to all other vortices and a potential transport current.

Abrikosov proposed a square lattice, but it can be shown that a hexagonal lattice has a lower free energy. The number density of vortices is $n_v = B/\Phi_0$ and geometrical considerations lead to a vortex spacing

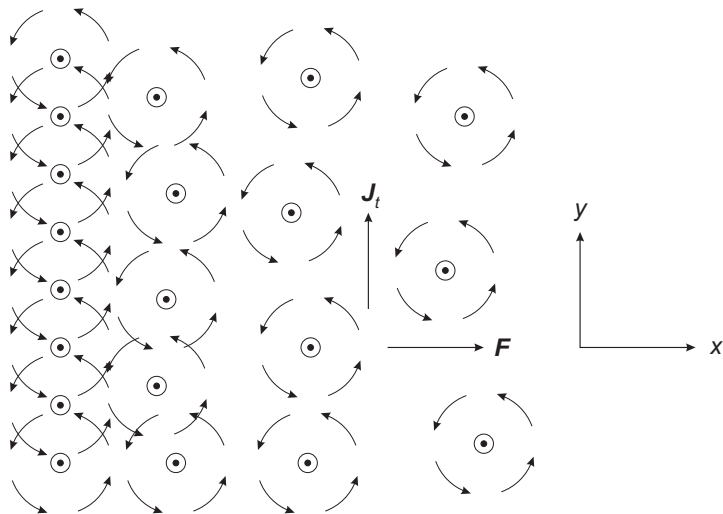
$$a_0 = \left(\frac{2\Phi_0}{\sqrt{3}B} \right)^{1/2}. \quad (2.20)$$

A square lattice would have a slightly smaller a_0 which makes it less favourable, given the mutual repulsion of flux lines. The hexagonal lattice, therefore, is stable whereas the square lattice is not, which has been confirmed by electron micrographs of vortices made visible by decorating the sample with a magnetic powder [14]. The influence of the crystal structure of the sample, however, can lead to a square or rectangular array of flux lines.

2.4.2. Flux Motion and Loss of Zero Resistance

While there are various materials with an upper critical field high enough for almost every application, the real limitation lies in the current a superconductor can transport without turning normal. The reason for this is that according to Eq. (2.19) any transport current of density \mathbf{J}_t exerts a Lorentz force density

$$\mathbf{F} = \mathbf{J}_t \times \mathbf{B} \quad (2.21)$$


Figure 2.3:

The density gradient in the x direction of the flux lines (pointing in the z direction, out of the paper) leads to a net current in the y direction where the circulating supercurrents of the different vortices overlap. The resulting driving force on the vortices in the x direction has to be compensated for by a pinning force, otherwise the flux lines will start to move and cause electric resistance (after [15]).

on the vortex lattice.⁴ If there is no other force balancing this the flux lines will move with a velocity \mathbf{v} transverse to the current (as illustrated in Fig. 2.3) which leads to a finite $\partial\mathbf{B}/\partial t$. With Faraday's law this gives an electric field

$$\mathbf{E} = \mathbf{v} \times \mathbf{B} \quad (2.22)$$

in which normal electrons can be accelerated and subsequently transfer energy to the crystal lattice by scattering, thus leading to energy dissipation and electric resistance.

In conclusion, this means that in a type II superconductor in the mixed state dissipation-free current transport is only possible if the vortices are held in place, i.e. *pinned* by some force balancing the Lorentz force. The current density where the Lorentz force equals this pinning force is called the *critical current density* J_c .

2.4.3. Pinning

Pinning occurs when there is a spatial variation of ξ , λ or H_c on a local scale ($\sim 10^{-8}$ to 10^{-7} m), for example due to crystal defects or inclusions of a second phase. In this case it is energetically favourable for a flux line to pass through this pinning centre as it leads to a reduction of ϵ_l , its free energy per unit length.

If the vortices are separated far enough from each other so as that individual cores exist a variation on the length scale of ξ can lead to *core pinning*. The loss of condensation

⁴ J_t describes the total current reduced by equilibrium magnetisation currents. The latter have no impact on the FLL as the forces related to them are compensated by other equilibrium forces.

energy which usually occurs when Cooper pairs are broken apart in order to form a flux line can be avoided if the flux line rests on a void or a normal conducting inclusion.

For pinning centres of the size of λ on the other hand the whole line energy ϵ_l can be saved. In this case it is mainly the interaction of the circulating supercurrents with the pinning centre which holds the vortex in place.

Because of the large values of λ in the HTS the magnetic field is relatively constant and thus core pinning is the predominant mechanism in these materials.

Types of Pinning Centres

There are various kinds of inhomogeneities which can lead to pinning. In the following a short summary of the most important pinning centres is given, in particular those which are most relevant in HTS [10]:

Point defects Because of the small coherence length of the cuprates even inhomogeneities on an atomic scale can be effective for pinning. The most prominent example is oxygen deficiency, i.e. some oxygen sites in the CuO_2 planes are not occupied.

Twin planes In orthorhombic crystal structures (like YBCO, see Sec. 3.2) twinning occurs, which means that in some regions the unit cell is rotated by $\sim 90^\circ$ about the c axis with respect to other areas. Point defects and impurities along the planes separating these domains lead to the suppression of superconductivity and thus pin vortices. This is particularly effective if the vortices lie parallel to the twin boundaries.

Other structural defects Stacking faults (intergrowth of other phases) and screw dislocations can also pin flux lines.

Artificial defects There have been various efforts to introduce pinning sites into materials. This can be either achieved during the sample production (e.g. by heat treatment or doping with certain elements) or by irradiation. For the latter approach protons, neutrons or heavy ions as well as fission fragments can be used. These can create defects situated on a straight line, which are very effective in pinning flux lines in the same direction.

Intrinsic pinning Due to the layered structure of the cuprates superconductivity is suppressed between the CuO_2 planes. As a consequence a vortex can be pinned if it

lies between these layers (see Sec. 2.4.9).

Pinning in high-quality single crystals was found to be rather weak, compared to thin films. This is because point defects are the only pinning centres in these samples. They are randomly positioned and pinning in this case can be described by the collective pinning model (see below). Thin films, on the other hand, have a large number of dislocations resulting from the growth process which act as linear and thus strong pinning centres leading to much higher values of J_c [16, 17].

Critical State Model

In the case of strong pinning magnetisation curves $M(H)$ are highly hysteretic. This can be understood by the *critical state model*. If a type II superconductor is exposed to an applied magnetic field a density gradient of flux lines develops which leads to a decay of B in the sample. If the force due to the gradient equals the pinning force this is called the critical state. As the field is increased the flux gradient moves further towards the centre of the sample until the whole superconductor is penetrated by a non-zero B at an applied field $H = H^*$. If the field is then reduced, an inverse gradient at the edges is observed, whereas the original gradient is still present further inside. At zero applied field there is trapped flux left in the sample, which explains the hysteretic behaviour of $M(H)$.

The slope of B is given by J_c , which itself depends on B . In the most simple approach however, the *Bean model*, J_c is assumed to be constant and so is the gradient [18]. This is illustrated in Fig. 2.4.

Magnetisation measurements can be used to obtain the critical current density of a sample with the help of this model.

The hysteresis described above leads to dissipation as the field is changed which limits ac applications of type II superconductors [19, 20, 21].

Collective Pinning and Elasticity of the Flux Line Lattice

In order to obtain the pinning force per volume, in general one cannot simply add up the maximum pinning force of each pinning centre. Firstly, they might not be saturated at low fields, i.e. there might not be a vortex at every pinning centre. Secondly, the rigidity of the FLL has to be taken into account: randomly positioned defects could exert no net force on a completely rigid lattice since forces pulling it in one direction would

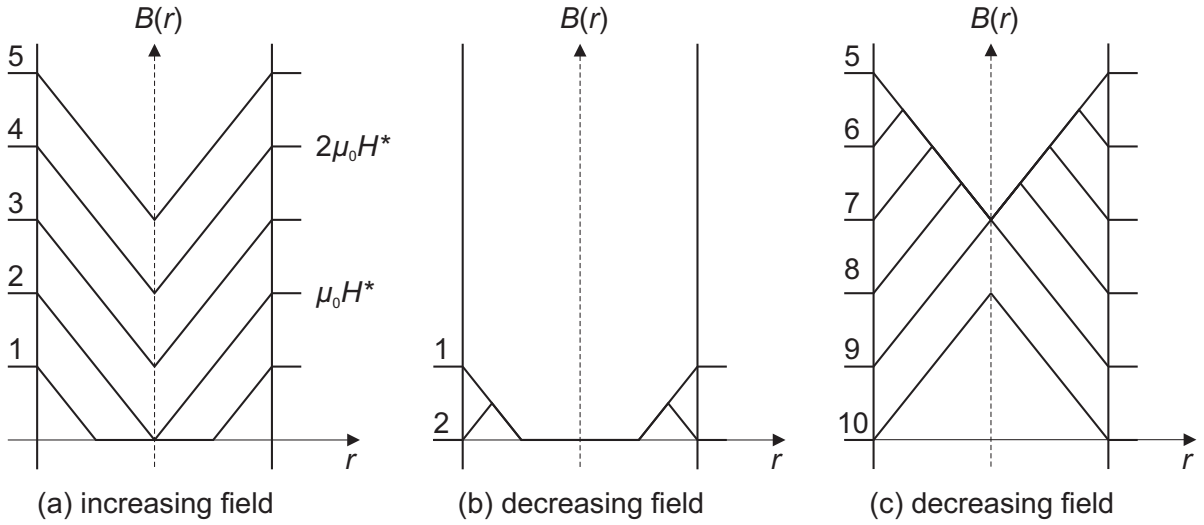


Figure 2.4.: The Bean Model. (a) As the field is increased from step 1 to 5 the gradient of B moves further into the sample, which is fully penetrated at $H = H^*$. (b) Reducing the field to zero leaves trapped flux in the superconductor which reaches a maximum value if the sample has been exposed to a field $H \geq 2H^*$ before, as is shown in (c).

be counterbalanced by forces in the opposite direction. In that case the vortex lattice could be moved through the sample reversibly. In order to achieve a net pinning force a certain degree of elasticity has to be permitted. According to the *Larkin-Ovchinnikov theory of collective pinning* the flux lines would then reduce the free energy by passing through pinning centres, whereas the elastic energy would increase as vortices bend. The resulting configuration would be the one where the sum of these energies is a minimum [22].

Equating the pinning force per unit volume obtained like this to the Lorentz force gives

$$J_c B = \frac{n^2 f^4}{2C_{44} C_{66}^2 \xi^3} \quad (2.23)$$

where n is the defect density and f the force of an individual pinning centre on the FLL. The elasticity of the lattice is described by the elastic moduli C_{44} and C_{66} . This shows that a softer lattice (characterised by smaller elastic moduli) would have a larger J_c .

In YBCO thin films, however, pinning centres are strong, which means that in contrast to the collective pinning model each vortex interacts with the pinning potential of only one pinning site. In that case the collective pinning theory does not apply and the

individual pinning forces can be added directly to obtain the pinning force per volume.

2.4.4. Flux Flow

The situation of moving flux lines with no pinning present shall be treated in the following. Their motion is retarded by *viscous damping* resulting from normal current losses within the moving core. The resulting force per unit length on a vortex can be written as $-\eta v$ (with the viscous drag coefficient η) and equating this to the Lorentz force given by Eq. (2.19) leads to

$$v = \frac{J\Phi_0}{\eta}. \quad (2.24)$$

Together with Eq. (2.22) this gives

$$E = \frac{\Phi_0 B}{\eta} J = \rho_f J, \quad (2.25)$$

where ρ_f is the flow resistivity. This leads to an energy dissipation $W = -Fv = \eta v^2$. ρ_f increases with field until it reaches the normal resistivity ρ_n at $H = H_{c2}$, as will be shown in the following.

The *Bardeen-Stephen model* assumes that the core is fully normal within a radius $\sim \xi$ [23]. One can then use the first London equation to derive the microscopic electric field outside of the core and (assuming continuity) one obtains a constant field inside, which immediately gives the dissipation per unit length of the vortex. Equating this to the dissipation obtained above, an expression for η can be derived, which [after substituting into Eq. (2.25)] gives

$$\frac{\rho_f}{\rho_n} = \frac{B}{B_{c2}}. \quad (2.26)$$

If a material with a finite critical current density J_c is considered, a term due to the frictional forces of the pinning sites has to be included in order to obtain the total dissipation. Equation (2.25) has to be modified to

$$J = J_c + \frac{B_{c2}}{B\rho_n} E, \quad (2.27)$$

which is illustrated in Fig. 2.5(a).

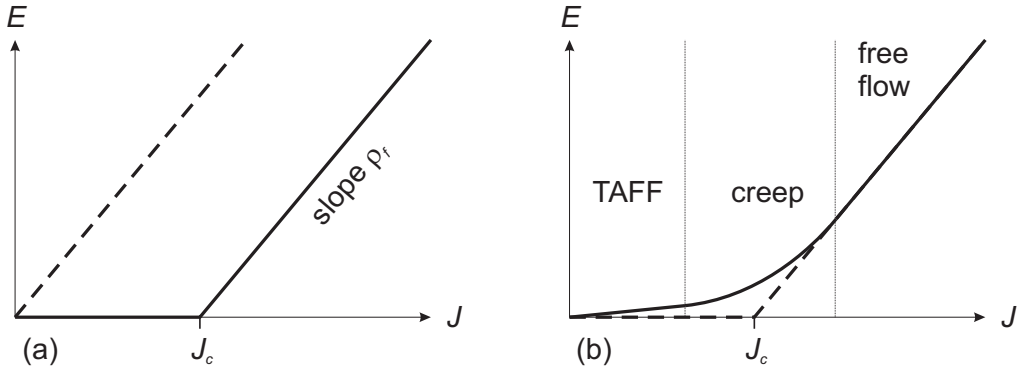


Figure 2.5.: Dependence of the electric field E on the current density J . (a) No thermally activated flux motion: pinning leads to a non-zero critical current density, hence the point where flux flow starts is shifted to $J = J_c$. (b) Due to thermally activated flux flow and flux creep E is finite even below J_c (after [24]).

2.4.5. Thermally Activated Flux Motion

At finite temperatures flux lines can jump from one pinning centre to another because of thermal excitations which leads to a rounding of the $E(J)$ curves discussed in the last section [see Fig. 2.5(b)]. This phenomenon has two consequences: firstly, trapped fields (e.g. in a solenoid) will decay slowly. As this reduces the flux-density gradient the driving force for flux motion decreases as well and one observes a logarithmic decay with time of this effect. Secondly, a superconductor carrying a transport current will show resistance similar to flux flow, but even at currents below J_c .

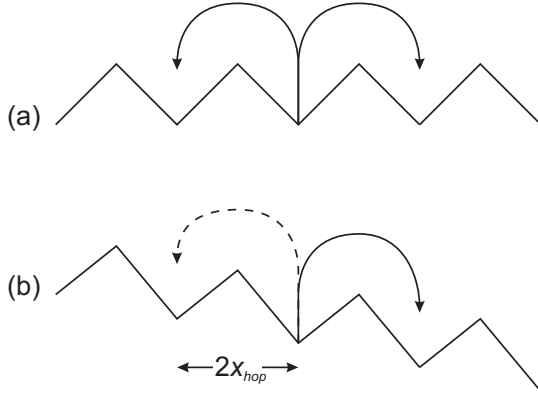
Whereas thermally activated flux motion is negligible in conventional superconductors it can be quite prominent in HTS.

The phenomenon can be described by the *Anderson-Kim flux creep theory* [25, 26]. If there is no flux-density gradient jumps occur in both directions with the same probability as shown in Fig. 2.6(a). If, however, the spatial energy dependence is tilted by a transport current as depicted in Fig. 2.6(b) it is easier for flux lines to overcome the pinning potential in one direction than in the other and a net creep velocity is observed.

The rate of jumping to the right can be written as

$$\nu_{\text{net}} = \nu \exp\left(-\frac{U - fx_{\text{hop}}}{kT}\right) - \nu \exp\left(-\frac{U + fx_{\text{hop}}}{kT}\right) \quad (2.28)$$

with the attempt frequency ν and the height of the pinning barrier U (which is increased or decreased by the applied force f multiplied by the distance x_{hop} between the minimum


Figure 2.6:

Idealised sawtooth pinning potential. (a) Without a flux-density gradient jumps are as likely to occur in one direction as in the other. (b) With a gradient jumps to the right are favoured (after [24]).

and the maximum of the potential barrier). This gives the mean flux line velocity and the electric field resulting from this motion

$$E = 4x_{hop}\nu B e^{-\epsilon} \sinh\left(\frac{\epsilon J}{J_c}\right) \quad (2.29)$$

where $\epsilon = U/kT$.

For small currents E is proportional to J , as illustrated in Fig. 2.5(b), which is equivalent to a (small) resistance. This regime is labelled *thermally activated flux flow (TAFF)* [27]. What follows for higher currents is *flux creep* with a dramatic increase in electric field until linear behaviour returns with free flux flow.

2.4.6. Irreversibility Line

Magnetisation measurements for cuprates show a reversible behaviour above a certain applied field which depends on the temperature. This means that the superconductor is not in a critical state in this regime and that J_c equals zero. In addition to that the resistive transition $\rho(T)$ not only shifts to lower temperatures with increasing fields (as is also the case for LTS), but broadens significantly. In this temperature range flux flow occurs very easily compared to lower temperatures where pinning is strong and the resistance is zero (or extremely small). In conclusion, this means that for $H < H_{c2}$ there is a region where current transport is resistive, even if the order parameter Ψ is non-zero. The field above which this is the case is termed the *irreversibility field* H_{irr} which determines the *irreversibility line (IL)* in an H - T phase diagram. Unlike H_{c1} , H_{c2} and H_c its dependence on temperature is concave, as depicted for various cuprates in Fig. 2.7.

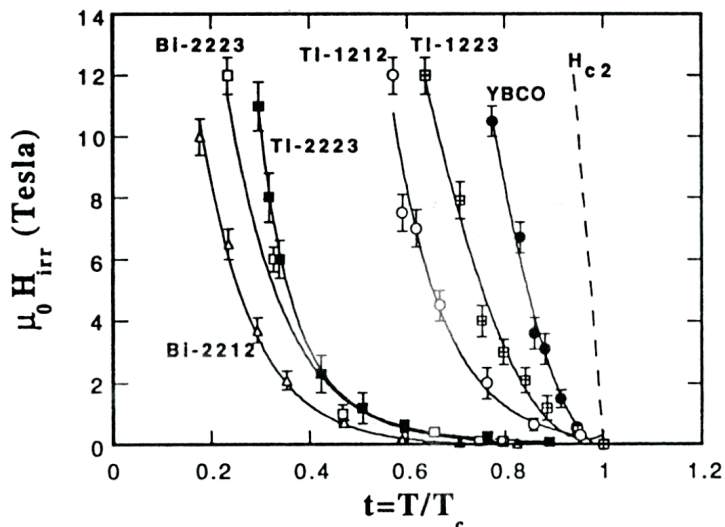


Figure 2.7: The irreversibility line for different cuprates, all of which have a similar behaviour of H_{c2} [28].

There have been different attempts to explain this phenomenon. One is the *melting* of the flux line lattice above H_{irr} , which means that thermal vibrations destroy the ideal Abrikosov lattice. In this model the empirical Lindemann parameter c_L determines the vibration amplitude at which the FLL is thought to have undergone a solid-liquid transition. The melting field $B_m(T)$, where this happens, is then associated with the irreversibility line.

Another explanation is based on the fact that the irreversibility line is lowest for those cuprates where the coupling of electron pairs between neighbouring CuO_2 planes is weak (see Sec. 3.2). Flux lines in the c direction would then break up into *pancake vortices* within the planes which are only weakly coupled by Josephson vortices [29] (see Sec. 2.4.9). The pancakes, thus, could move independently within the CuO_2 planes under the influence of a Lorentz force and “miss” pinning sites not lying in the planes. This would explain why pinning is so ineffective and J_c is suppressed above H_{irr} .

2.4.7. Anisotropic and Layered Superconductors

High-temperature superconductors are anisotropic and have a layered structure. This means that the values of H_{c1} , H_{c2} , ξ and λ vary with the orientation of the magnetic field relative to the unit cell of the crystal. In addition to that, the order parameter can change from layer to layer, which leads to the formation of pancake vortices mentioned earlier. In some materials this variation is so strong that the area between the CuO_2

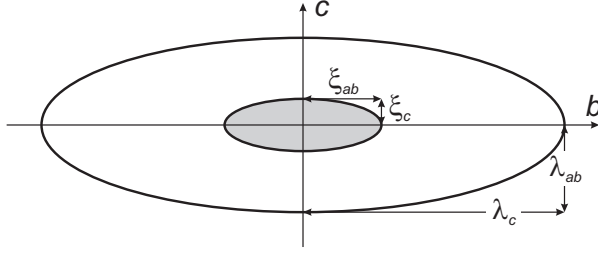


Figure 2.8: A flux line in the crystallographic a direction in an anisotropic superconductor. The core is shaded (after [32]).

layers, where superconductivity is suppressed, acts as a Josephson junction⁵ [30].

2.4.8. Anisotropic Ginzburg-Landau Theory

If the layered nature of HTS is left aside, one can extend the Ginzburg-Landau theory discussed in Sec. 2.2.2 in order to describe anisotropic superconductors. A charge carrier mass tensor is introduced, therefore, which has the values m_{ab} in the a and b directions and m_c in the c direction⁶ [31]. Adapting Eq. (2.6) one obtains anisotropic versions of the Ginzburg-Landau equations with the parameters λ_{ab} (corresponding to shielding currents in the ab plane, for fields $H||c$) and λ_c (currents in c direction, $H||ab$) as well as ξ_{ab} and ξ_c (for changes of Ψ in the respective directions).

The anisotropy can then be described by the anisotropy parameter

$$\epsilon = \frac{1}{\gamma} = \frac{\lambda_{ab}}{\lambda_c} = \frac{\xi_c}{\xi_{ab}} = \sqrt{\frac{m_{ab}}{m_c}} \quad (2.30)$$

with the reciprocal anisotropy parameter γ introduced for convenience.

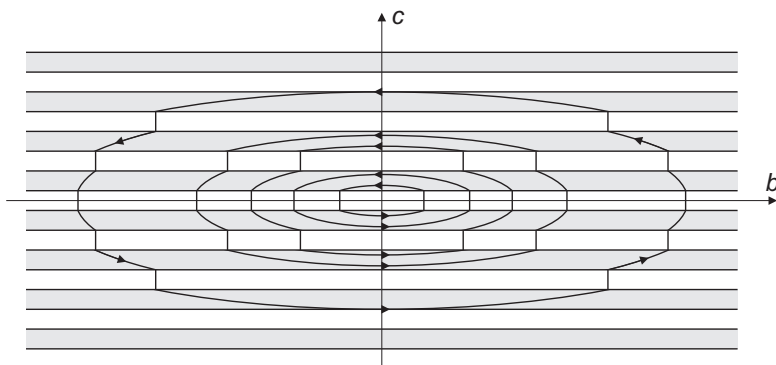
As a consequence, vortices not lying in the c direction have an elliptic cross section, as shown in Fig. 2.8 for a flux line along the a axis.

2.4.9. Lawrence-Doniach Model

If the coherence length in the c direction ξ_c is of the order of or smaller than the distance s between adjacent CuO_2 layers (which is the case in YBCO below $T \approx 75$ K) the material cannot be treated as a continuum as in the anisotropic Ginzburg-Landau theory. W. E. Lawrence and S. Doniach proposed a model for this case even before the discovery of HTS which applies well to the layered cuprates [33].

⁵A general discussion of the Josephson effect can be found in various reference works [10, 11, 9].

⁶Due to the weakly orthorhombic or tetragonal crystal structure of the cuprates the anisotropy in the ab plane can be neglected and m_{ab} is the same in the a and b directions.


Figure 2.9:

A Josephson vortex in the crystallographic a axis and its corresponding supercurrent distribution. The superconducting layers are shaded (after [36]).

If the field is parallel to the c axis ($H||c$) vortices consist of *flux pancakes* which are formed by shielding currents circulating in the CuO_2 planes, where Ginzburg-Landau theory still applies [29, 34, 35]. They are aligned in stacks because the potential due to the magnetic fields surrounding them is attractive.

In the case of $H||ab$ so-called *Josephson vortices* form. Their core is positioned in one of the non-superconducting layers and the screening currents are governed by the Josephson effect as they pass through these layers [36, 34]. In these Josephson junctions the current density has only a component in the c direction, whereas in the CuO_2 layers the elliptical current flow as discussed in Sec. 2.4.8 is found. Figure 2.9 shows a cross section of a Josephson vortex. In contrast to a conventional Abrikosov vortex no condensation energy is lost because the core lies in a normal conducting region. Hence the flux line is held in position by what is called *intrinsic pinning* (see Sec. 2.4.3).

If the field is tilted at an angle to the CuO_2 planes, different flux line structures are observed, depending on temperature and tilt angle. If the angle between ab -planes and field is described by θ then for $\theta < \theta_2$ the flux lines consist of a chain of pancakes which are coupled by Josephson vortices, as depicted in Fig. 2.10. For $\theta_2 < \theta < \theta_1$ they are only distorted towards this kinked state, and at even higher angles rectilinear (i.e. not kinked) Abrikosov vortices are present. This is only the case below a critical temperature T_{cr} , however; at higher T straight Abrikosov vortices are formed at all field orientations. For YBCO T_{cr} is approximately 80 K [37].

2.4.10. Angular J_c Measurements

Measurements of the critical current density while the magnetic field is rotated with respect to the sample are a powerful tool to investigate the structure of the FLL. Any

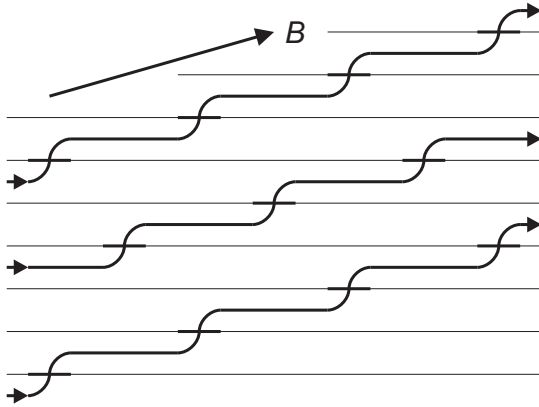


Figure 2.10:

In the case of a field inclined at an angle to the planes pancake vortices form which are connected by Josephson vortices.

theory describing the vortex structure will have to fit angular data over at least a certain range.

Angular measurements allow one to distinguish between different pinning mechanisms. In the case of layered superconductors, like the HTS, a maximum for fields applied parallel to the layers is found [38], due to intrinsic pinning, discussed in Sec. 2.4.3. For $H||c$ in many cases a peak is found as well, caused by pinning by dislocations at the edge of growth grains. This effect is even more pronounced if the sample contains artificially introduced pinning centres, aligned with the c -axis.

These features are due to intrinsic sample properties, i.e. they can be observed in measurements where the field is rotated such that the Lorentz force remains constant. If, on the other hand, the field is rotated in a plane that contains the current direction (usually $||ab$ in the case of HTS), the flux line lattice does not change its structure, but the Lorentz force is varied and minima and maxima in J_c are found due to maximum and minimum F_L , respectively. The amount of this variation in J_c allows one to draw conclusions as to the extent to which microscopic currents flow parallel to the macroscopic current direction.

3 High-Temperature Superconductors and Their Grain Boundaries

In 1986 Bednorz and Müller discovered the high-temperature superconductors, for which they were awarded the Nobel Prize. An entirely new field of research was founded, with a large number of (real and potential) applications.

As their name implies these new materials exhibited a (relatively) high transition temperature. Their physical properties, however, turned out to be very difficult to understand and control. From a theoretical point of view they offered various riddles to be solved. From an application point of view in particular their grain boundaries, suppressing the overall critical current density, posed large problems.

Following the history of their discovery, in Sec. 3.2 of this chapter the crystallographic structure of the high-temperature superconductors is discussed. In the next section their superconducting properties are addressed, followed by a detailed discussion of their grain boundaries (Sec. 3.4). This should prepare the ground for the presentation of the results on grain boundaries in coated conductors obtained for this thesis in Chaps. 7 to 11. The current chapter ends with a brief overview of applications of superconductivity.

3.1. Historical Background

Until 1986 the superconductor with the highest known transition temperature was Nb_3Ge with a T_c of 23 K [39]. It was in this year that Bednorz and Müller [40] reported superconductivity in a La-Ba-Cu-O system at a temperature of ~ 30 K. This discovery was remarkable, not only because of the high T_c , but also because it opened the door to a new class of materials, the *high-temperature superconductors (HTS)*. A more specific name for those compounds is *cuprates*, which indicates that they have CuO_2 planes in common.

In the following years the substitution of elements allowed even higher transition temperatures to be achieved. In 1987 $\text{YBa}_2\text{Cu}_3\text{O}_{7-\delta}$ (YBCO) was discovered with $T_c \approx 93$ K [41, 42, 43]. This high critical temperature made cooling with liquid nitrogen possible (rather than with the more expensive helium), and thanks to the highest J_c of all known cuprates, YBCO is the most promising material for applications. Other compounds with even higher transition temperatures were found soon afterwards. These are, in particular, the BSCCO family (oxides of Bi, Sr, Ca and Cu) [44] and TBCCO family (oxides of Tl, Ba, Ca and Cu) [45, 46]. Today over 100 superconducting cuprates are known [47].

A material located in a region between LTS and HTS is MgB_2 with a T_c of 39 K, which—despite being known for over 50 years—was found to be superconducting only in 2001 [48].

The *iron pnictides*, which form a second class of HTS after the cuprates, were discovered in 2008. After superconductivity was reported in $\text{LaFeAsO}_{1-x}\text{F}_x$ [49], many other pnictides followed, with $\text{SmFeAsO}_{1-x}\text{F}_x$ showing the currently highest T_c of ~ 55 K [50]. Table 3.1 gives a summary of the most important HTS and their critical temperatures.

3.2. Crystal Structure of YBCO

As all samples measured for this thesis were $\text{REBa}_2\text{Cu}_3\text{O}_{7-\delta}$ films (abbreviated as REBCO, where RE is a rare earth; the most common example is $\text{YBa}_2\text{Cu}_3\text{O}_{7-\delta}$ or YBCO), the following sections focus on this material. Similarities and differences to other cuprates are mentioned, however.

The YBCO unit cell is either tetragonal (space group $P4/\text{mmm}$) or orthorhombic

Table 3.1.: Transition temperatures of several high-temperature superconductors (both cuprates and pnictides) as well as of MgB₂.

Compound	T_c (K)	Ref.
La _{2-x} Sr _x CuO ₄	38	[51]
YBa ₂ Cu ₃ O _{7-δ}	93	[41, 42, 43]
Bi ₂ Sr ₂ CaCu ₂ O _{8+δ}	85	[52]
Bi ₂ Sr ₂ Ca ₂ Cu ₃ O _{10+δ}	110	[44]
Tl ₂ Ba ₂ Ca ₂ Cu ₃ O _{10+δ}	125	[46]
HgBa ₂ Ca ₂ Cu ₃ O _{8+δ}	133	[53]
MgB ₂	39	[48]
LaFeAsO _{1-x} F _x	26	[49]
SmFeAsO _{1-x} F _x	55	[50]

(Pmmm), depending on oxygen content and temperature. It is made up of three perovskite cells stacked on top of each other, as is depicted in Fig. 3.1. In its centre an Y atom and two CuO₂ planes above and below are found. These layers are present in all cuprates and are mainly responsible for superconductivity. Adjacent to them there are layers of BaO. CuO_x chains in the basal plane complete the unit cell. They are unique to YBCO; in all other cuprates the Cu atoms are found in CuO₂ planes only. It is these chains, running in the crystallographic *b* direction, which are responsible for the difference in the *a* and *b* lattice parameters in the orthorhombic phase of YBCO.

The oxygen content of YBa₂Cu₃O_{7-δ}, described by the value of δ , determines the crystal system. As can be seen in Fig. 3.2(a) the unit cell is orthorhombic for higher oxygen content, but becomes tetragonal at $\delta \approx 0.6$. The specific amount of oxygen doping is determined by the number of oxygen atoms in the CuO_x chains.

At high temperatures (at which samples are usually grown) the oxygen positions are randomly occupied in the plane where the CuO_x-chains would be found at lower T [see Fig. 3.1(b)]. This increases the symmetry and the material becomes tetragonal even for $\delta < 0.6$. When orthorhombicity develops upon cooling down, domains form where the *a* and *b* axes change role, i.e. YBCO becomes heavily *twinned* (see also Sec. 10.2.1).

3.3. Superconducting Properties of Cuprates

High-temperature superconductors have three properties separating them from conventional low-temperature superconductors:

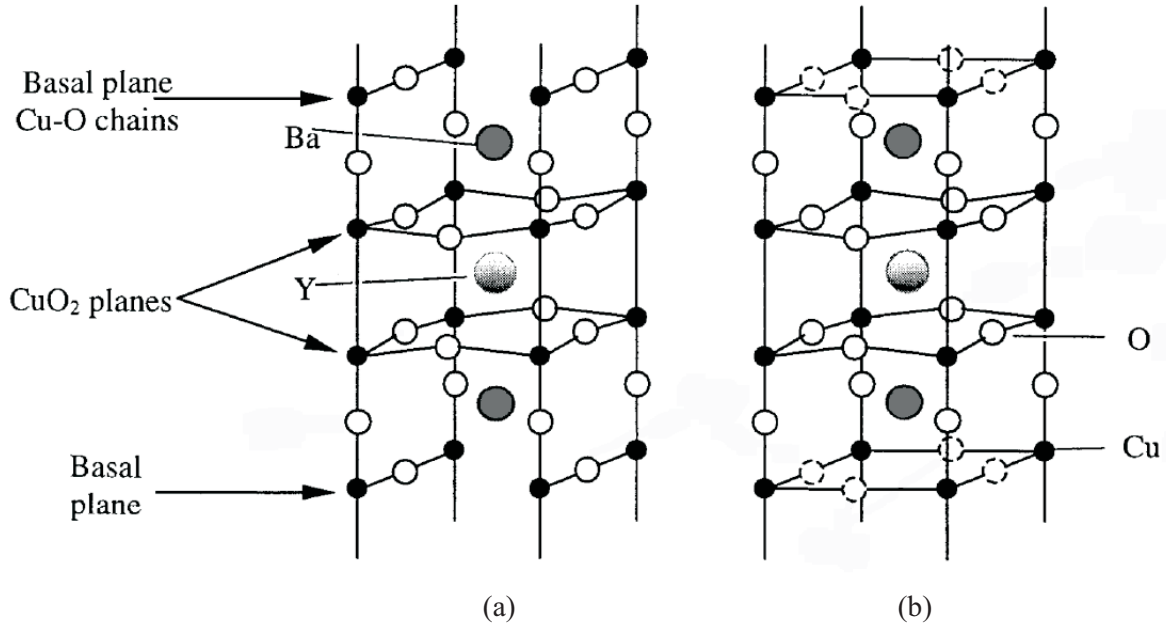


Figure 3.1.: Unit cell of (a) $\text{YBa}_2\text{Cu}_3\text{O}_7$ and (b) $\text{YBa}_2\text{Cu}_3\text{O}_{7-\delta}$. Oxygen sites which are only partially filled are depicted as dashed circles [54].

High transition temperature As shown in Table 3.1 the highest T_c obtained so far is around 135 K.

High Ginzburg-Landau parameter Whereas the coherence length is small the penetration depth is relatively large, which leads to a high value of the Ginzburg-Landau parameter ($\kappa \gg 1/\sqrt{2}$). The cuprates are, therefore, considered as “extreme type II superconductors”.

Anisotropy The crystallographic lattice parameters vary strongly for the ab and c direction (see Sec. 3.2) and so do the superconducting parameters ξ and λ as well as H_{c1} and H_{c2} .

If phase diagrams for LTS and HTS are compared, it is found that for the cuprates H_{c1} is rather low, whereas H_{c2} reaches very large values. In addition to that, an irreversibility line as discussed earlier is observed (see Section 2.4.6). The reversible parameters of YBCO are summarised in Table. 3.2.

The short coherence length entails that the superconducting properties, in particular the critical current density, are very sensitive to local disruptions of the crystal structure caused by, for example, impurities or grain boundaries [57]. Whereas in LTS the high

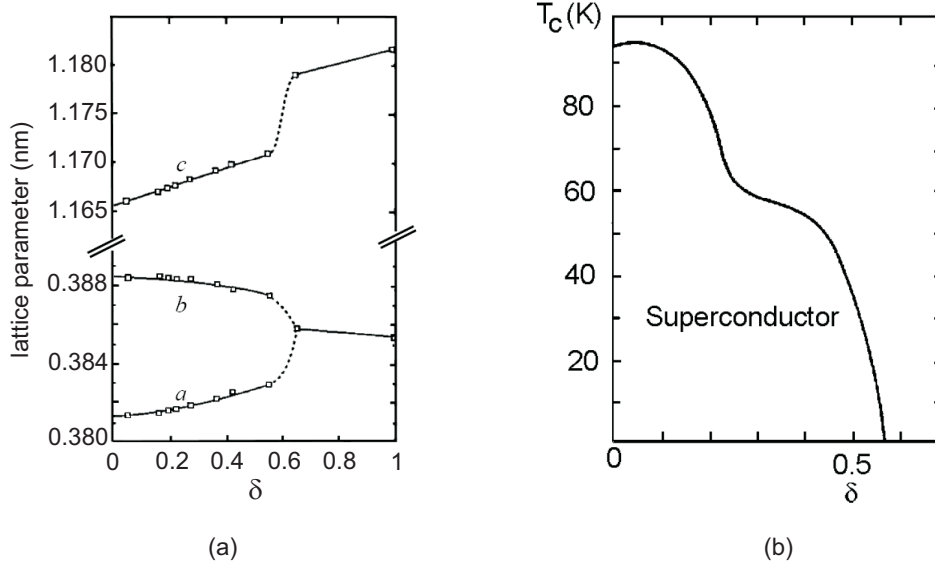


Figure 3.2.: (a) The lattice parameters and the tetragonal to orthorhombic transition (adapted from [55]). (b) The critical temperature of YBCO varies strongly with the oxygen content (adapted from [54]).

ξ would lead to their effects being averaged over a larger area, therefore only weakly suppressing the order parameter, they have a more significant impact on the properties of HTS. While defects with dimensions of the order of ξ can act as pinning centres, enhancing J_c , in general impurities and grain boundaries are deleterious when it comes to the current carrying capacity of a HTS.

The superconducting properties of cuprates are very dependent on their oxygen content. As is illustrated in Fig. 3.2(b) the transition temperature of $\text{YBa}_2\text{Cu}_3\text{O}_{7-\delta}$ varies strongly with the value of δ , reaching a maximum $T_c = 93$ K at $\delta = 0.08$, which then drops dramatically with decreasing oxygen level until superconductivity is lost at $\delta = 0.56$. This sensitivity to oxygen doping is probably the main reason why the HTS were only discovered so late.

Table 3.2.: Reversible parameters of YBCO at $T = 0$ K, derived from magnetic measurements [56].

$\mu_0 H_c$ (T)	$\mu_0 H_{c1}^c$ (T)	$\mu_0 H_{c2}^c$ (T)	λ_{ab} (nm)	ξ_{ab} (nm)	λ_c (nm)	ξ_c (nm)
1.1	0.050	130	135	1.6	890	0.24

3.3.1. YBCO Thin Films on Single Crystal Substrates

The large potential of HTS became clear soon after their discovery, when Chaudhari *et al.* [58] demonstrated that very high critical current densities could be achieved by depositing a layer of YBCO on a SrTiO₃ single crystal substrate [59]. With the substrate acting as a template for epitaxial growth, thin films with the crystallographic *c*-axis perpendicular to the sample plane could be produced, which showed a critical current density in excess of 10⁹ A/m² at $T = 77$ K, as obtained by transport and magnetic measurements [58]. As predicted by the authors of this study, this value of J_c turned out to be only a lower limit. Improvements in the homogeneity¹ of the films increased J_c by an order of magnitude.

The high critical current density of single crystalline thin films is due to two factors. Firstly, no grain boundaries are present (with the exception of twin boundaries and boundaries between separate growth grains, neither of which suppress J_c significantly). As discussed in Sec. 3.4, GBs in polycrystalline samples can significantly impede the current flow. Secondly, the slight mismatch between the lattice parameters of the substrate and the superconductor leads to the formation of dislocations during the growth process. These defects were found to act as effective pinning centres [16], greatly enhancing J_c compared to that obtained on a “perfect” single crystal.

The critical current density of a thin film can be further increased by the introduction of artificial pinning centres [60]. This can be achieved by nanoinclusions (e.g. BaZrO₃ [61]) or by rare earth doping (in order to introduce a certain amount of disorder [62, 63]). Another, novel approach is based on the introduction of magnetic pinning centres [64].

3.4. Grain Boundaries

The initial excitement in the scientific community at the discovery of the high-temperature superconductors gradually faded when it turned out that the critical current densities which could be achieved in the first wires fabricated from the new materials were rather small. They were only of the order of 10⁶ A/m² at $T = 77$ K in the case of YBCO [65]. In fact J_c of the then available polycrystalline samples showed the characteristics of Josephson junctions [66]. This was in strong contrast to the high critical current

¹The samples discussed in Ref. [58] suffered from regions where the *c*-axis lay in the film plane and from a certain amount of secondary phases.

densities obtained already in the very early single crystals [67]. Chaudhari *et al.* [68] confirmed the earlier suspicion [69, 70] that the weak links responsible for this behaviour were the grain boundaries. As the bicrystalline technique was only about to be developed (see Sec. 3.4.1), they deposited a YBCO layer on a polycrystalline SrTiO₃ substrate and used an excimer laser to pattern tracks within single grains and across boundaries. In all cases the GBs had a significantly suppressed critical current density compared to the two abutting grains [68]. The values of J_c not only of the boundaries, but also of the different grains, showed significant scatter. In the case of the first this can be attributed to different grain misorientations (see Sec. 3.4.3), in the case of the second to poor reproducibility of the deposition process.²

The reason why—unlike in LTS—grain boundaries have such a detrimental effect in the cuprates is their low coherence length, as discussed in Sec. 3.3. As a consequence, the order parameter can be significantly suppressed over short length scales, like the dimensions of a GB. This intrinsic property of the material appeared to preclude all applications requiring high critical current densities over long lengths, in particular wires for power generation and transport [71].

In the ~ 20 years following the discovery of the cuprates significant insights have been gained into the properties of grain boundaries. The progress made has been well documented by several review papers. These are, in particular Ref. [72] by Hilgenkamp and Mannhart; Ref. [73] by Ayache; Ref. [74] by Feldmann *et al.*; Ref. [75] by Durrell and Rutter (the latter two focus on low-angle grain boundaries occurring in coated conductors).

Grain boundaries were investigated in both bulk material and thin films. In general their effect on J_c was found not to depend on the specific type of sample or production route [76] (even though in later studies subtle differences between different types of GBs were discovered, see page 44). The physics of GBs in cuprates, however, proved to be a very diverse field, requiring a huge research effort. Consequently, a review of grain boundaries in HTS and their properties is given in the following sections. It is focused on the results most important for the topic of this thesis, coated conductors; hence other scenarios where GBs affect applications are only mentioned briefly. Most of the results discussed in the next sections were obtained on films grown on bicrystal substrates, i.e. model grain boundaries. Studies on isolated, “real” coated conductor GBs will be

²Note that the first successful epitaxial growth of YBCO on single crystal substrates had been reported only a year before [58].

reviewed at the beginning of Chap. 7, followed by the results on single CC boundaries obtained for this thesis.

3.4.1. Preparation of Artificial Grain Boundaries

Methods were sought to prepare well-defined artificial grain boundaries in order to investigate their structural and electromagnetic properties and to make use of them in devices for applications (see Sec. 3.5). To this end several different techniques have been developed, which are briefly discussed in the following.

Bicrystals

For the bicrystalline technique, developed by Dimos *et al.* [77], two separate single crystals are used as a substrate. Commonly SrTiO₃, YSZ (yttria-stabilised zirconia), MgO or sapphire are employed. The two crystals are cut appropriately, polished and sintered together with the desired misorientation between their lattices (see Sec. 3.4.2). The crystal orientations are then transferred into a superconducting film grown epitaxially on top of them. Consequently, a grain boundary is achieved in the superconducting layer with (almost) exactly the same misorientation as that in the substrate. Since the misorientation angle can be defined as needed this is a very versatile technique. Also, tracks can be patterned across the GB and onto a grain on the same sample, which allows one to directly compare the critical current density of the boundary and the grain. The bicrystal technique has been employed in a large number of studies which have provided valuable insights into the physics of grain boundaries (for example [78, 79, 80, 81, 82, 83, 84], for an overview see [76]). It is this approach which has proven to be most valuable in preparing model GBs similar to those found in coated conductors.

Biepitaxial technique

This approach relies on the fact that YBCO unit cells (or those of cuprates, in general) are rotated by 45° about their *c*-axis when an additional buffer layer (e.g. MgO) is inserted on top of the substrate. If part of the substrate is covered by this buffer then the superconducting film grown on top of it will form a 45° [001]-tilt boundary with the section of the film grown directly on the substrate [85]. These boundaries can be used, for example, as Josephson junctions in SQUIDS (see Sec. 3.5.1). There are only

few reports of other, smaller misorientation angles achieved by the biepitaxial technique, hence it is not relevant for coated conductors, in which only low-angle grain boundaries occur (see Sec. 3.4.2).

Step-edge junctions

When a superconducting film is grown on top of a substrate into which a step has been patterned by photolithography and ion milling, two GBs are formed in series at the edges of the step [86]. Unlike in the biepitaxial technique the tilt is out-of-plane, rather than in-plane. The boundary location on the substrate can be chosen freely, making this another technique useful for device fabrication. The GB angle can be defined by how the substrate is patterned, but usually high-angle grain boundaries are formed, hence the technique is of limited use for the investigation of GBs occurring in coated conductors.

3.4.2. Crystallographic Structure of Grain Boundaries

Grain boundaries can be described by their type and the misorientation angle θ_{mis} between the two adjacent grains [72]. This is illustrated in Fig. 3.3. If the two grains are rotated with respect to each other about an axis parallel to the GB plane, this results in a *tilt* boundary. To further specify the type of the boundary the direction of the axis of rotation is given as a lattice vector, i.e. [001] or [010] as shown in Fig. 3.3(a–c). If, on the other hand, the grains are rotated about an axis perpendicular to the GB interface, a *twist* boundary is observed [Fig. 3.3(d)]. In polycrystalline samples (e.g. in coated conductors) there are often combinations of different rotations, and the GBs are then termed mixed boundaries.

If the misorientations of the two grains with respect to the GB plane are identical, the boundary is called symmetric, otherwise asymmetric.

Shown in Fig. 3.4 is a high resolution TEM image of a 31° [001]-tilt boundary in a flux-grown YBCO bicrystal [87]. The two grains are clearly visible. Their crystallographic structure remains intact right up to the boundary; no voids or impurities are seen. This is frequently observed in cuprate GBs. It implies that the reduced critical current density of GBs is related to the properties of the boundaries themselves, rather than to defects in their vicinity.

For low misorientation angles $\theta_{\text{mis}} \lesssim 10^\circ$ *low-angle grain boundaries (LAGBs)* are formed, which are made up of arrays of separate dislocations. In the case of pure tilt

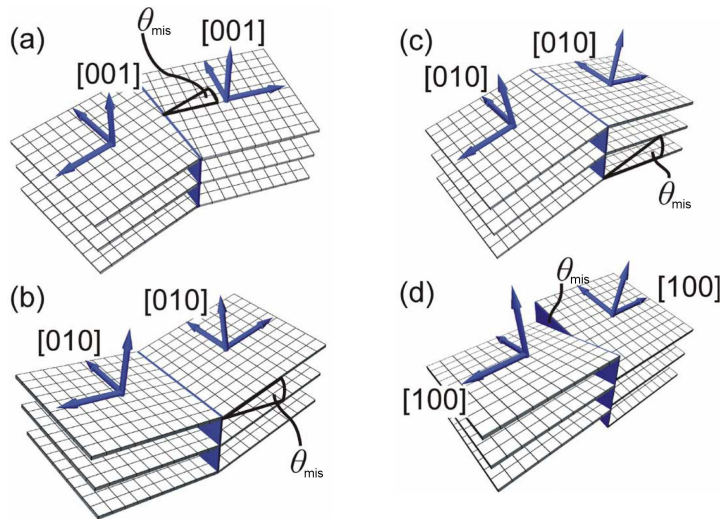


Figure 3.3:

Schematics of different GBs obtained by grain rotations: (a) [001]-tilt, (b) [010]-tilt valley-type, (c) [010]-tilt roof-type and (d) [100]-twist grain boundaries (adapted from [84]).

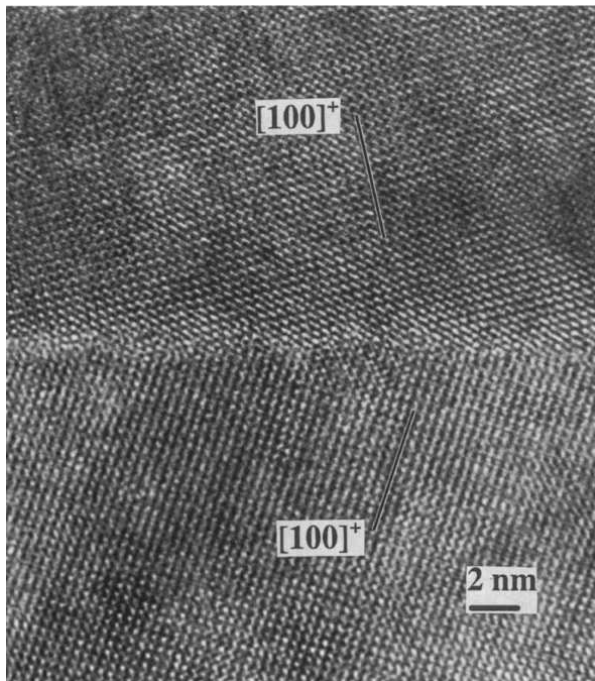


Figure 3.4:

High resolution TEM image of a 31° [001]-tilt boundary in a YBCO bicrystal. The direction of the [100] lattice axes of the two grains are indicated [87].

boundaries these are edge dislocations, while in pure twist boundaries screw dislocations are found. This can be seen clearly in the TEM image in Fig. 3.5(a), obtained from a 5° [100]-tilt grain boundary in bulk-processed YBCO [88]. In between the dislocations the matrix remains unaltered [89, 90]. From simple geometric considerations the distance D between the dislocations can be calculated as [72]

$$D = |\mathbf{b}| / \sin \theta_{\text{mis}} \quad (3.1)$$

where \mathbf{b} is the Burgers vector [91]. In the case of the GB in Fig. 3.5(a) a value of $|\mathbf{b}| = 1.17$ nm was determined, which equals the c -axis lattice parameter of YBCO [see Fig. 3.2(a)]. The value of $D = 13$ nm derived from Eq. (3.1) agrees reasonably well with $D \approx 15$ nm, as determined from the TEM image.

Figure 3.5(b) is a graphical representation of how the misorientation between the lattices of the two abutting crystals is accommodated for by the introduction of dislocations.

As the misorientation angle θ_{mis} increases the dislocations move closer together until at $\theta_{\text{mis}} \approx 10^\circ$ they merge and a *high-angle grain boundary (HAGB)* is formed. The GB then constitutes a continuous layer where the crystallographic structure of the grains is lost.

HAGBs can be described by the *coincidence site lattice (CSL)*, formed by superimposing the lattices of the two adjacent grains [93]. The CSL allows one to calculate the boundary energy, which exhibits minima for certain values of θ_{mis} , where the two lattices match closely. Experiments on grains in MgO and CdO smoke [94] and on melt-grown YBCO [95] showed that low-energy GBs, as calculated from the CSL, occur more frequently, confirming its applicability. This result, however, is only of limited importance for coated conductors, where the YBCO grain misorientations are determined by the underlying buffer grains (see Chap. 4). Also, the main purpose of a strong grain texture, as achieved by the coated conductor technology, is to avoid HAGBs, which is why they are not covered in more detail here.

As discussed in Sec. 3.2, YBCO is usually heavily twinned. Twin boundaries are basically 89.1° [001]-tilt boundaries running along the (110) planes [72]. As they occur within each grain, however, they should not be considered as grain boundaries, but rather as boundaries between twinned domains. They do not consist of dislocations and neither do they constitute a significant barrier to current flow; in fact they can even

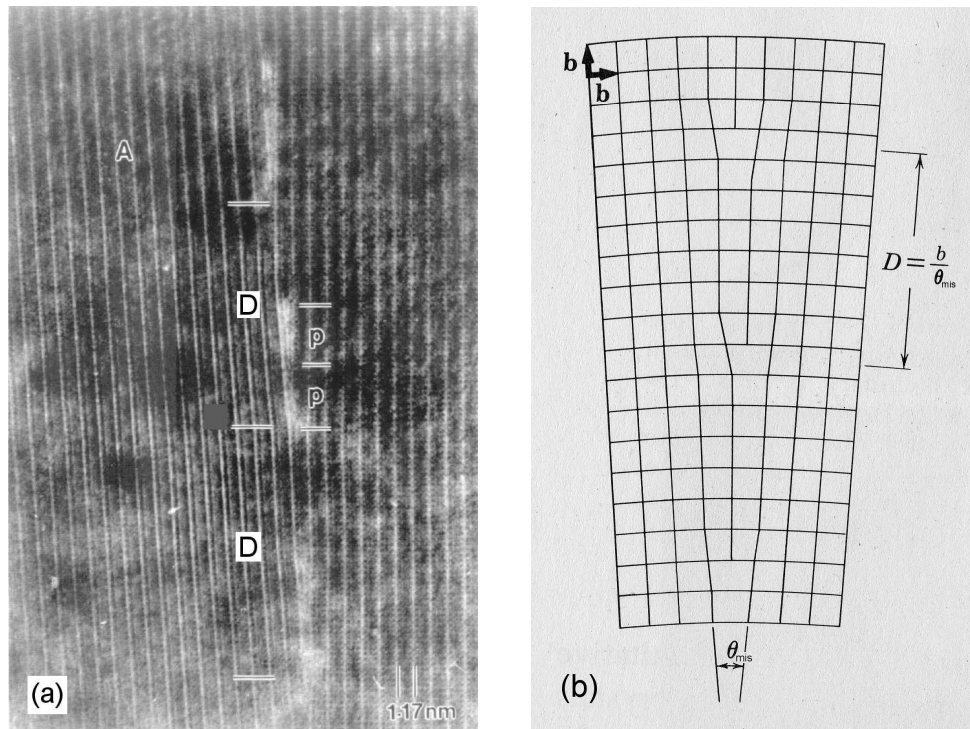


Figure 3.5.: (a) Dislocations making up a 5° [100]-tilt GB in YBCO as imaged by HR-TEM. The distance between consecutive dislocations is given by D (adapted from [88]). (b) Schematic diagram illustrating how edge dislocations make up a tilt grain boundary (adapted from [92]).

act as pinning centres (see Sec. 2.4.3). Due to the small size of twinned domains many twin boundaries can be expected to coincide with a “real” grain boundary. This implies that the grain boundary incurs a slight change of its misorientation angle every time it encounters a twin boundary [96]. Consequently, in orthorhombic materials, there are no grain boundaries with a constant misorientation angle along their entire length; instead, a certain variation of θ_{mis} can always be expected.

In addition to tilt and twist boundaries, grain boundaries arise if the lattice of one grain is shifted in one direction with respect to the other. A translation over $1/3$ or $2/3$ of the [001] lattice vector in a c -axis oriented YBCO thin film is a typical example, which is called *anti-phase* or *out-of-phase* boundary [97, 98] (see Fig. 10.15).

3.4.3. Dependence of the Critical Current Density on GB Angle

After it had been established that the total J_c in polycrystalline samples is usually limited by grain boundaries [68], the electric properties of GBs were investigated in more detail in several studies. In particular the dependence of j_c of grain boundaries³ on their type and misorientation angle θ_{mis} was under scrutiny. Most of these measurements have been carried out on thin films grown on bicrystal substrates.

Different suggested dependencies and models

The first study on the dependence of j_c on θ_{mis} is that by Dimos *et al.* [77], who measured the critical current density of several (nominal) [001]-tilt boundaries in YBCO films. Due to large variations of j_c measured within different grains (intragrain, j_c^{IG}) they did not plot j_c of the boundaries (j_c^{GB}) vs. θ_{mis} . Instead, they presented $j_c^{GB}/j_c^{IG}(\theta_{\text{mis}})$, in order to compensate for the differences in absolute critical current density from sample to sample, and for small angles they found a decay proportional to $1/\theta_{\text{mis}}$. In a more elaborate study [79] it was ascertained that the different types of grain boundaries depicted in Fig. 3.3 show the same behaviour of j_c^{GB}/j_c^{IG} when plotted against the total misorientation angle,⁴ as can be seen in Fig. 3.6(a).

Since according to Eq. (3.1) the distance D between dislocations is also approximately proportional to $1/\theta_{\text{mis}}$, Dimos *et al.* [77] proposed a simple model. Structural disorder and strain fields around dislocation cores would suppress superconductivity, hence superconducting channels would develop, separated by non-superconducting regions at the dislocations. As a consequence, the effective cross-section of the grain boundary would decrease with increasing θ_{mis} , leading to a decay in j_c^{GB} proportional to $1/\theta_{\text{mis}}$. For high misorientation angles they observed a plateau in j_c^{GB}/j_c^{IG} , which could be explained by the dislocation cores overlapping above a certain critical angle, hence there would be no more channels of undistorted material in between them and j_c^{GB} saturates. If the radius of dislocation cores is assumed to be equal to the Burgers vector (for a [001]-tilt boundary $|\mathbf{b}| \simeq 0.39$ nm, the a -axis lattice parameter) [77] this occurs at $\theta_{\text{mis}} \approx 30^\circ$, which would agree with the high-angle plateau observed by Dimos *et al.* [77].

³Again small letters denote microscopic quantities, i.e. j_c stands for the critical current density across a grain boundary or within a grain whereas J_c represents the value over a large area, e.g. a tape.

⁴Most of the GBs in Ref. [79] were mixed boundaries, i.e. while one boundary type dominated other tilt / twist components were also present. The total misorientation angle was calculated from the complete rotation matrix.

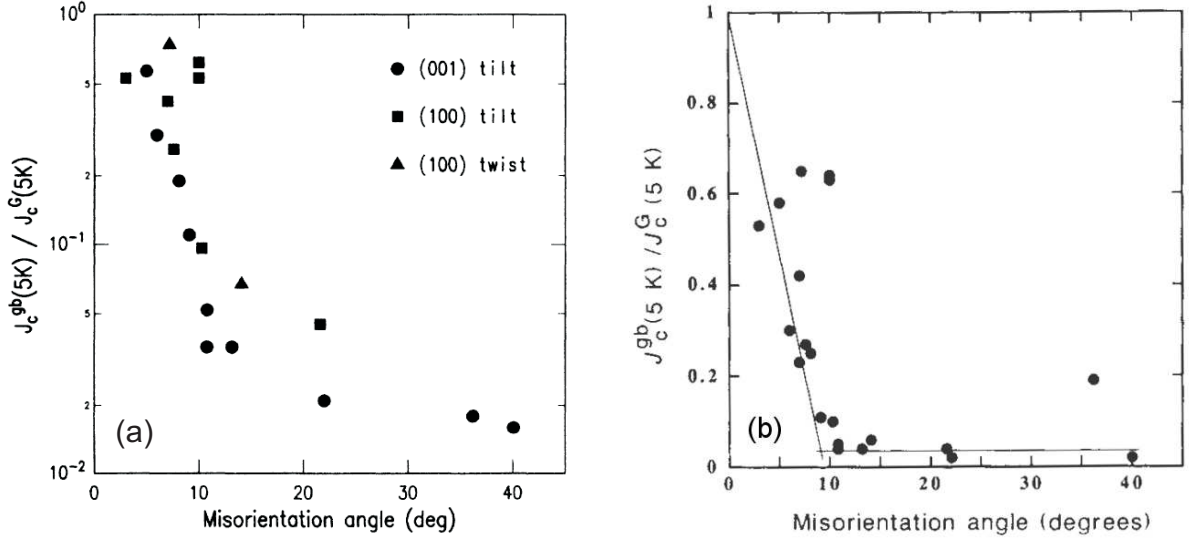
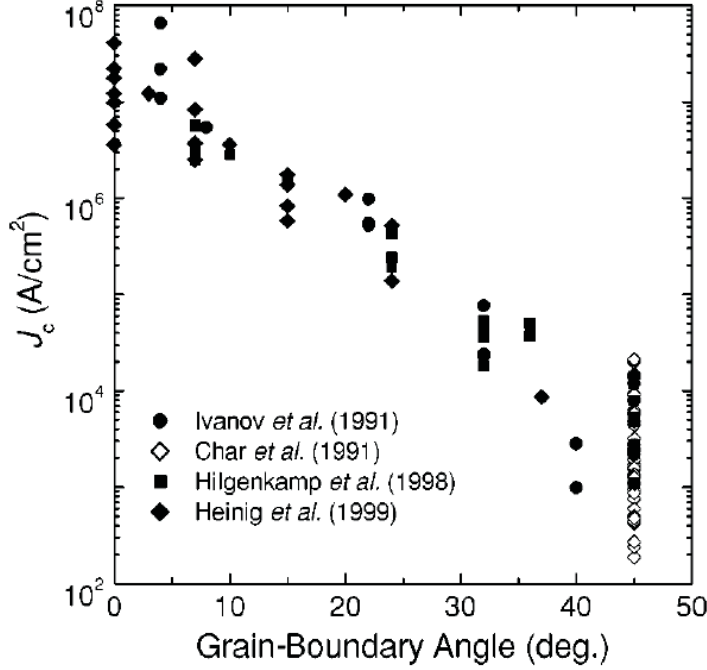


Figure 3.6.: (a) Dependence of the ratio between the critical current density of boundary and grain on the total misorientation angle for different kinds of GBs in YBCO bicrystals [79]. Note the similar behaviour irrespective of GB type. (b) A linear fit to data from the same source for $\theta_{\text{mis}} \leq 10^\circ$ [89].

Chisholm and Pennycook [89] explored and applied this model further. If r is the radius of a dislocation core then the ratio between j_c of the boundary and within the grain should be $(D - 2r)/D$, which, with Eq. (3.1), leads to

$$\frac{j_c^{GB}}{j_c^{IG}} = 1 - \frac{2r}{|\mathbf{b}|} \theta_{\text{mis}}. \quad (3.2)$$

This expression predicts a linear dependence on θ_{mis} (rather than $1/\theta_{\text{mis}}$), and a fit to the low-angle data of Dimos *et al.* [79] is reasonably good, as is shown in Fig. 3.6(b). It leads to a core radius of $r \simeq 2.9|\mathbf{b}|$, however, which is significantly larger than the expected $r \simeq |\mathbf{b}|$ [77]. While the higher value agrees well with $r \simeq 1$ nm, as determined by TEM investigations [99], it would imply that dislocation cores merge already at $\theta_{\text{mis}} \approx 10^\circ$, inconsistent with the plateau found above $\theta_{\text{mis}} \approx 30^\circ$ in several measurements [77, 79]. Consequently, the dislocation model can *either* describe the strong decrease of $j_c^{GB}/j_c^{IG}(\theta_{\text{mis}})$ at low θ_{mis} *or* the high-angle plateau, but not both. Chisholm and Pennycook [89] explained the larger effective core radius by a strain field surrounding the dislocations, which would suppress the order parameter. Merging of the strained zones due to dislocation cores at $\theta_{\text{mis}} \approx 10^\circ$ could, however, be responsible for the transition


Figure 3.7:

This compilation [72] of critical current densities of [001]-tilt grain boundaries in YBCO films obtained by different groups shows an exponential dependence of j_c^{GB} on the grain boundary angle. All data were obtained at (or rescaled to) $T = 4.2$ K. They were taken from the following references: Ivanov *et al.* [80], Char *et al.* [85, 101], Hilgenkamp *et al.* [102], Heinig *et al.* [100].

from strong to weak coupling, which occurs at about the same angle, as discussed below. The situation is complicated further if one takes into account that the channel between dislocations should close already when its width decreases below the coherence length, as noted by Heinig *et al.* [100]. Consequently, the critical angle would be even lower than 10° [81].

As an alternative explanation for their results, Dimos *et al.* [77] suggested that GBs could be a region of reduced vortex pinning, thus providing a channel for easy flux flow. Vortices in the GB plane would be elongated along its length and be pinned less strongly than their counterparts lying entirely in the grain. Flux lines would get more distorted the higher the misorientation angle of the boundary was, which would account for the behaviour of $j_c^{GB}(\theta_{\text{mis}})$.

Measurements subsequent to those of Dimos *et al.*, performed by Ivanov *et al.* [80] and other groups [85, 101, 102, 100] on grain boundaries where the misorientation was more precisely defined, allowed the absolute value of j_c^{GB} to be plotted vs. θ_{mis} , which gave an *exponential decay*. These results are presented in Fig. 3.7.

It is now generally accepted that $j_c^{GB}(\theta_{\text{mis}})$ is best described by an exponential law, not by a $1/\theta_{\text{mis}}$ or $-\theta_{\text{mis}}$ dependency. The discrepancy with respect to the earlier measurements [77, 79] can be explained by the fact that Dimos *et al.* normalised j_c^{GB} to j_c^{IG}

in order to compensate for variations in sample quality. This led to a wrong angular dependency as a reduced value of j_c^{IG} in a certain sample does not necessarily imply that j_c^{GB} is decreased by the same factor [81]. Also, their grain boundaries consisted of more than one misorientation component, i.e. they were not, for example, pure [001]-tilt boundaries. Ignoring the other misorientation components, as in Ref. [77] leads to a further distortion of the angular dependence.

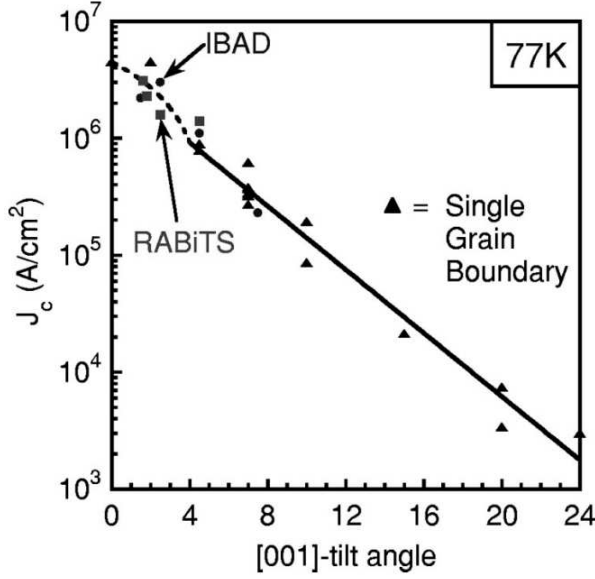
Low- and high-angle plateaus

Heinig *et al.* [90, 100] found a low-angle plateau in their measurements on [001]-tilt bicrystal films. They claimed that up to $\theta_{\text{mis}} = 7^\circ$ the critical current densities measured across a GB and within a grain were the same. It needs to be pointed out, however, that only one out of their four measured 7° GBs did show a j_c equal to that of the grain, whereas for the weakest boundary j_c^{GB}/j_c^{IG} reached only a value of 0.3 at $T = 77$ K. Heinig *et al.* explained this by a varying amount of Sr and Ti diffusion from the substrate into the YBCO film, thus increasing the dislocations core sizes in the GBs by different amounts and causing the high scatter in j_c^{GB}/j_c^{IG} . They concluded that the boundary with the highest j_c represented a “pure” YBCO GB best, hence their claim of a 7° plateau [100].

This finding disagrees with other studies in which a dependence of j_c^{GB} on θ_{mis} down to 2° [103] or $3\text{--}4^\circ$ [81] has been observed. In the latter publication a 2° boundary exhibited the same j_c as a grain, while a 4.5° boundary had a significantly suppressed critical current density. This is depicted in Fig. 3.8, which combines bicrystal data with results obtained on IBAD and RABiTS coated conductors. The plot also shows nicely the exponential decrease of $j_c^{GB}(\theta_{\text{mis}})$ over a large angular range.

A low-angle plateau can of course be caused by grains adjacent to the boundary with a somewhat suppressed j_c^{IG} . Consequently, the measured $j_c^{GB}(\theta_{\text{mis}})$ would saturate once it reaches j_c^{IG} and the overall J_c of the link would become limited by the grains. In this scenario an increasing j_c^{GB} with decreasing θ_{mis} down to $\theta_{\text{mis}} = 0^\circ$ is conceivable, despite an apparent plateau in data from transport measurements. A reduced j_c^{IG} can either be related to film growth and sample processing, or to twinning. Verebelyi *et al.* [96] explained the fact that 2° GBs in their study showed no j_c suppression with respect to grains by a current limitation due to twinning of the the latter.

As dislocations can act as pinning centres, it is imaginable that in certain cases pinning


Figure 3.8:

The critical current densities of different bicrystal boundaries and two coated conductors vs. the GB misorientation angle [81]. In the case of the CCs an equivalent angle θ_{eq} has been used, determined from EBSD maps such that 70% of the tape cross-section is connected by GBs with $\theta_{mis} \leq \theta_{eq}$.

in GBs is stronger than that in grains, leading to a superior value of j_c in the boundary. It needs to be mentioned, however, that while pinning by GB dislocations was confirmed by angular J_c measurements [104], the absolute critical current density of the grain was still higher than that of the boundary.

In the first measurements on the dependence of j_c^{GB} on θ_{mis} [77, 79] indications for a plateau at high angles were found, which would be consistent with the dislocation model and the closure of strongly coupled channels above a certain critical angle (see above). This result, however, was not reproduced in later studies [80, 100], which reported an exponential decay up to the highest angles investigated (see Fig. 3.7). The plateau can probably be attributed to the fact that Dimos *et al.* [77, 79] scaled j_c^{GB} to j_c^{IG} , which led to a wrong angular dependence at high θ_{mis} .

Classification of grain boundaries

As mentioned earlier grain boundaries can be divided into low-angle and high-angle boundaries (LAGBs and HAGBs, respectively). In the first the cuprate matrix remains intact between the dislocations [89] and the critical current density is governed by flux flow [105]. In the second the boundary layer is structurally distorted along its entire length and it shows the characteristics of a Josephson junction. Different values for the exact misorientation angle of the transition between the two regimes have been published, but in general boundaries are considered to be strongly coupled below $\theta_{mis} \approx 10^\circ$ and

weakly above [106, 100]. Coated conductors were developed with the objective to achieve a kilometre-long, highly-textured superconducting layer without HAGBs, in order to maximise the overall I_c .

An interesting question—also for coated conductors—is, whether in- or out-of-plane misalignment is more detrimental to the current carrying capacity of a boundary. Dimos *et al.* [79] investigated all three major GB types sketched in Fig. 3.3 and found that their (normalised) critical current densities exhibited the same angular dependence. Götz *et al.* confirmed that within experimental scatter $j_c^{GB}(\theta_{\text{mis}})$ was the same for [001]-tilt and [100]-tilt boundaries, as reported in Ref. [72], but found a suppressed critical current density for [100]-twist GBs. While at elevated misorientation angles⁵ the latter finding was also observed in a recent study by Held *et al.* [84], they reported an improved behaviour of [010]-tilt boundaries over [001]-tilt boundaries, both at zero-field and up to high H . The smaller j_c -degradation due to out-of-plane tilts was explained by TEM images which show that in the [010]-tilt boundaries the lattice accommodated for the misorientation by bending, thus reducing the density of dislocations detrimental to current flow. Held *et al.* concluded that for coated conductors in-plane alignment was more crucial than that out-of-plane.

3.4.4. Grain Boundaries in Applied Magnetic Fields

As discussed earlier, high-angle GBs behave like Josephson junctions. In applied fields, therefore, their $j_c(H)$ shows a Fraunhofer-like pattern [107]. The LAGBs relevant for coated conductors (and this thesis), on the other hand, exhibit a smooth field dependence. The rest of this section shall focus on them.

Relation between inter- and intragranular critical current density

The zero-field j_c of GBs is usually suppressed with respect to that of grains, but the field dependence of j_c^{GB} is weaker than that of j_c^{IG} [100]. As a consequence, a crossover field B_{cr} is observed above which the grains, rather than the grain boundaries, limit the overall critical current density. From measurements on YBCO films grown on SrTiO₃ bicrystals [81] B_{cr} was found to be ~ 3 T for a 4.5° boundary and ~ 5 T for a 7° boundary at $H||c$ and $T = 77$ K, as depicted in Fig. 3.9(a). Consistent with this crossover is the

⁵ [100]-twist GBs showed a low-angle plateau in Ref. [84], hence their j_c was not reduced with respect to the other GB types at low θ_{mis} .

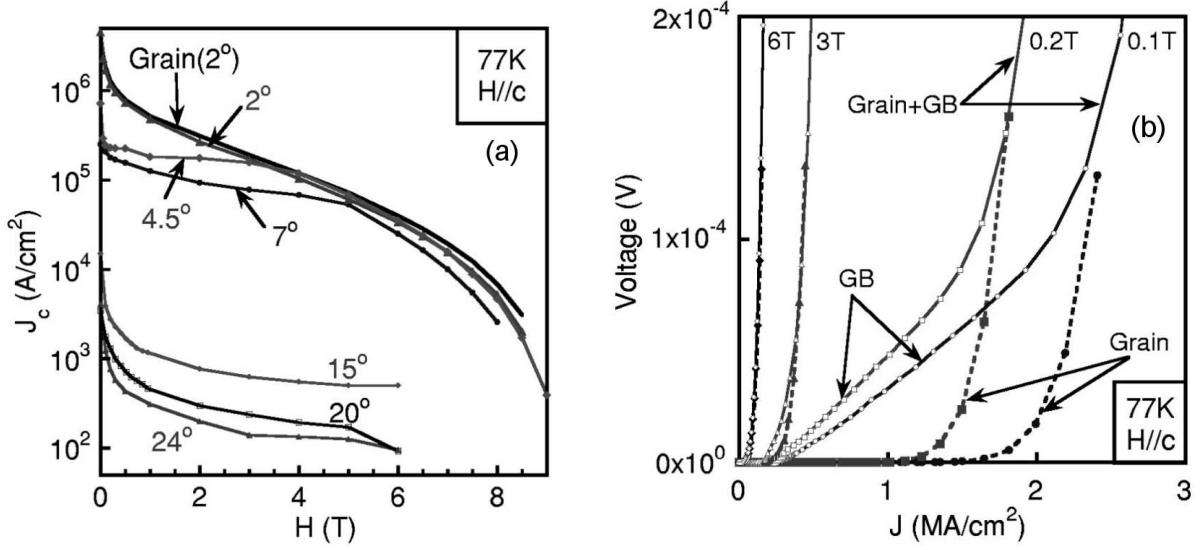


Figure 3.9.: (a) Magnetic field dependence of the critical current densities of different single GBs and a grain showing the crossover between grain boundary and grain dominated j_c [81]. (b) $V(J)$ characteristics of a 4.5° GB and a grain exhibit different shapes at low fields only [81].

shape of the corresponding $V(J)$ -curves, plotted in Fig. 3.9(b). Up to $\mu_0 H \approx 4$ T the 4.5° GB shows non-ohmic, linear differential (NOLD) behaviour, whereas the single grain's $V(J)$ -curve can be described by a power-law. At higher fields, where j_c is governed by pinning in the grains, the $V(J)$ -curves of the tracks across the boundary and within the grain are identical.

The crossover from GB to grain limitation was confirmed by Holzapfel *et al.* [108]. At $T = 77$ K their bicrystals showed the transition at $\mu_0 H = 1$ T (4° GB), 4 T (8° GB) and 6 T (12° GB). The change in shape of the $V(J)$ -curves (NOLD to power-law) occurred at the same respective fields. The slight differences compared to the results [81] presented in Fig. 3.9(a) are most likely due to a varying degree of pinning in the grains, related to different growth parameters.

As one would expect, the critical current density of coated conductors was also found to be limited by GBs at low fields and by grains at high fields [109] (see Sec. 8.1).

Vortices in the plane of a grain boundary

Linear current-voltage characteristics measured on GBs have been reported previously by Díaz *et al.* [105]. They explained the shape of the $V(I)$ -curves by the boundaries

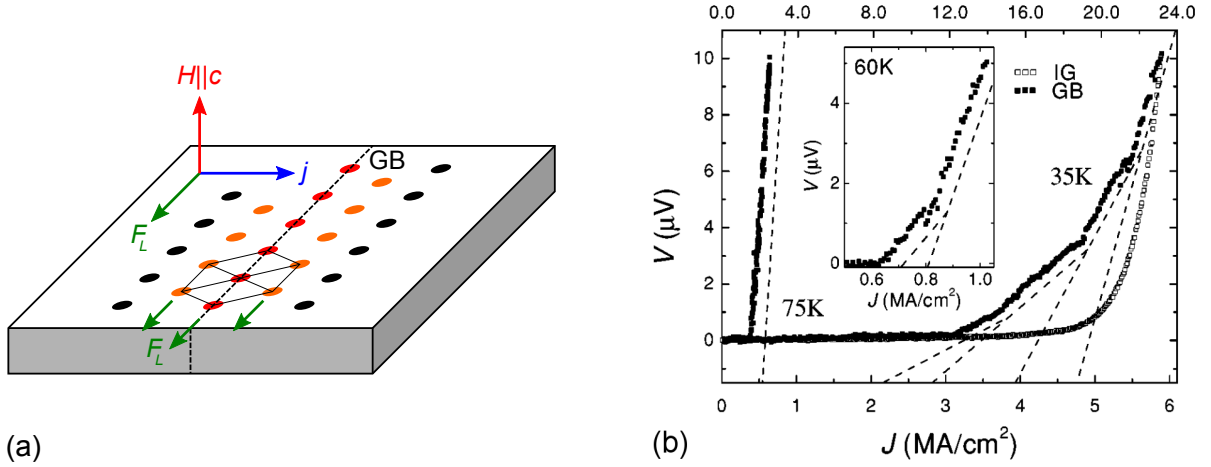


Figure 3.10.: (a) Due to the small width of a GB and the resulting high electric field across it only one vortex row (in red) moves along the boundary once its j_c is exceeded (after [105]). As j increases further, more vortex rows (in orange) can become depinned. This leads to linear, kinked $V(J)$ -curves, as depicted for a 4° GB in (b). Note the nonlinear behaviour of the grain's $V(J)$, free of kinks (main panel: $\mu_0 H = 1$ T, inset: $\mu_0 H = 1.9$ T) [110].

being limited by viscous flux flow, compared to flux creep present within the grains [78]. In the latter dissipation occurs over the whole length of the track once J_c is exceeded. Due to the narrow dimensions of a GB the voltage drops over a significantly shorter length in a track straddling a boundary, hence the electric field is higher by a factor of the order of 10^4 . The enhanced value of E causes a single row of vortices to move along the grain boundary, thus its j_c is limited by flux flow, rather than flux creep, and a linear current-voltage characteristic is observed. This is illustrated in Fig. 3.10(a).

Flux flow along GBs was investigated further by Hogg *et al.* [110], who measured kinked current-voltage curves on bicrystal samples, i.e. $V(J)$ showed a linear behaviour with the slope increasing in distinct steps [see Fig. 3.10(b)]. They concluded that the peculiar shape was due to different vortex rows parallel to the boundary depinning one after the other, thus increasing dV/dJ stepwise. As the temperature is reduced the slope of $V(J)$ decreases, due to a smaller flux flow resistivity at low T [110].

Theoretical aspects of current flow across GBs, leading to the crossover at B_{cr} , have been studied in detail by Gurevich *et al.* [111]. While the exact treatment is rather complex, the basic phenomenon can be explained by Fig. 3.10(a). If one assumes a high flux density $B > B_{cr}$ the intervortex spacing will be rather small, leading to a strong

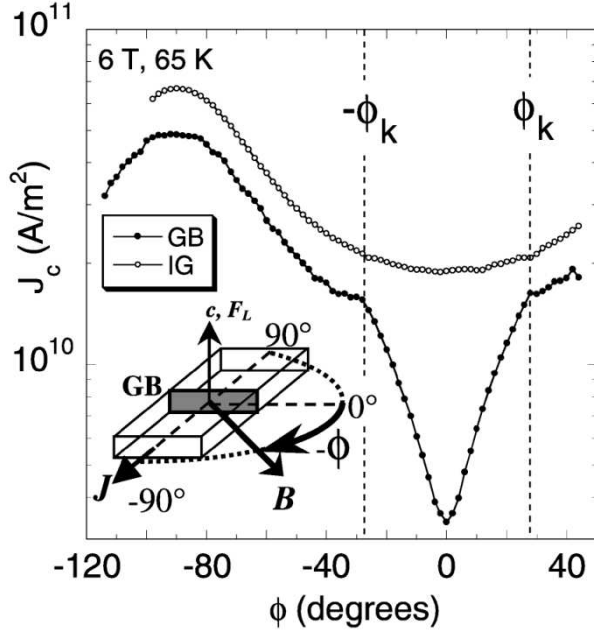
vortex–vortex repulsion. Since the vortices drawn in orange and black are strongly pinned in the grains, the forces between vortices will prevent the red flux lines in the GB from moving along the boundary, hence the GB becomes “invisible” for a transport current.

Angular measurements on single grain boundaries

In general grain boundaries are considered zones of reduced vortex pinning. Under certain conditions, however, the dislocations making up LAGBs can act as pinning centres, thus enhancing j_c . This was shown in angular measurements on a 4° [001]-tilt boundary where the magnetic field was rotated in the GB plane (i.e. with $H \perp J$) [104]. In addition to the intrinsic J_c maximum at $H||ab$, at small and intermediate fields another peak was found approximately parallel to the c -axis (and thus the orientation of dislocations). This second maximum was absent in IG measurements, confirming that it is related to pinning by dislocations in the grain boundary. It needs to be noted, however, that despite the improved j_c^{GB} for $H||c$ the absolute value of j_c^{IG} was found to be still higher. Pinning by dislocations was also suspected to be the reason for an increase in the irreversibility field of GBs with grain boundary misorientation up to $\theta_{\text{mis}} \approx 10^\circ$, as derived from the analysis of $V(I)$ characteristics [100].

Hogg *et al.* [112] performed similar angular measurements as Díaz *et al.* on a YBCO bicrystal boundary (again H was swept in the plane of the GB). They reported hysteresis in $J_c(\theta)$, where θ is the angle between the magnetic field and the crystallographic c -axis; the ab -peaks, due to intrinsic pinning, were shifted depending on the direction in which the scans were performed. This was explained by flux trapped in the grains [113], leading to a change in flux density within the boundary as the field orientation is changed and thus the component of the applied field parallel to the c -axis is altered (reduced). Hogg *et al.* confirmed this by $J_c(H||c)$ measurements (i.e. at fixed $\theta = 0^\circ$) for increasing and decreasing fields, which also showed hysteresis; the maximum in $J_c(H)$ of the branch with decreasing fields was found at $\mu_0 H > 0$ T.

In measurements where a magnetic field was swept in the plane of a film with a single boundary Durrell *et al.* [82] showed that j_c^{GB} is only suppressed significantly with respect to j_c^{IG} for fields approximately parallel to the grain boundary plane (see Fig. 3.11). For other orientations the overall critical current is limited by the grains, not the grain boundary. Consequently, there is an angle dependent crossover from GB to IG limited


Figure 3.11:

In in-plane measurements a 4.9° [001]-tilt bicrystal boundary showed a suppressed j_c (compared to that of a grain) only for fields approximately parallel to the GB plane [82].

j_c . This behaviour was explained by vortices channelling along the boundary for applied fields in an angular range $-\phi_k < \phi < +\phi_k$. At other angles the flux lines crossing the boundary are strongly pinned in the grains on either side, hence no j_c depression is observed.

3.4.5. Other Techniques to Investigate GBs

Transport measurements have contributed much to our knowledge of the properties of grain boundaries in HTS, however several other techniques have also been employed successfully. While they have not been used in this thesis (with the exception of low-temperature scanning laser microscopy) their general importance warrants a brief overview of them, which will be given in this section.

Magnetisation measurements (e.g. by SQUID or VSM) have the advantage that there are no current limitations (due to the power supply, contact heating etc.), but they suffer from the fact that both inter- and intragranular currents contribute to the detected magnetic moment m . Consequently, it is hard to separate j_c^{GB} from j_c^{IG} . This shortcoming was overcome by patterning circular tracks (rings) on bicrystal samples, both within a single grain and across the boundary. In the latter case the magnetisation current is forced to cross the boundary twice during one cycle. The critical current density can then be deduced from the measured moment by the Bean model. Using this approach

Verebelyi *et al.* [96] showed that a 2° [001]-tilt GB does not suppress the critical current density. In a similar study [114] the moment of rings across 5.1° and 7° boundaries was compared to “open circuit” rings within a single grain, into which a line had been etched across the entire track width. When the moment was measured for increasing and decreasing fields, the GB rings showed a maximum at $H > 0$ for decreasing fields, while $m(H)$ of the open rings was symmetric. This behaviour was explained by flux trapped in the grains, which compensates for the applied field in the GBs [113], enhancing their j_c . In the case of the open rings, on the other hand, a field compensation in the region of the etched line of course had no impact on the sample’s moment.

A technique that proved very useful for the investigation of both bicrystal and coated conductor GBs is *magneto-optical (MO) imaging*, in which an indicator film is placed on top of a thin film in order to map the local flux density in the sample. The current flow in the superconductor can then be reconstructed with the help of the Bean model [18] and the Biot-Savart law. Using this technique Polyanskii *et al.* [115] were able to show that flux first penetrates along the boundary of a YBCO film grown on a bicrystal substrate. As would be expected, the critical current densities of their LAGBs, derived from MO images, decreased with increasing θ_{mis} , and the values of j_c^{GB} and j_c^{IG} were consistent with those obtained from transport measurements [90] on similar samples. While the MO technique is limited to fields of a few hundred Millitesla [75] it has the advantage that j_c^{GB} can be obtained independently from j_c^{IG} , unlike in transport measurements where a boundary is always measured in series with two grains. Also, in transport measurements the GB is in the flux flow state, due to the high electric field across it [105]. As discussed by Jooss *et al.* [116] MO imaging allows one to investigate much smaller E ranges where j_c^{GB} is governed by flux creep. In their study they showed that while the area of high electric fields is very localised at the boundary, it still covers a channel significantly wider than one single row of flux lines. Building on Ref. [115] Born *et al.* [117] examined inconsistencies between MO measurements and Bean model calculations. They concluded that the self-field, generated by magnetisation currents parallel to the bicrystal GB, was responsible for the observed deviations. In another study [118] a combination of magnetisation measurements and MO imaging of a ring patterned across a single GB was employed to determine the temperature dependence of the ratio between j_c^{GB} and j_c^{IG} .

Scanning Hall probe microscopy allows one to map the flux distribution in a sample at fields up to several Tesla by moving a Hall probe across the specimen. Similar to

magneto-optic imaging the current density and electric field can then be reconstructed [119]. Hall scanning measurements confirmed that magnetic flux preferentially penetrates along GBs. Dinner *et al.* [120] investigated tracks patterned across a single GB at different angles and compared their current carrying capacity obtained by Hall scanning to that measured by transport. While the latter technique gave a stronger j_c -enhancement for a highly tilted track than what would be expected from geometrical effects, Hall probe microscopy indicated that the higher j_c can be explained solely by the increased GB cross-sectional area. This result is of particular interest for the development of coated conductors, where meandering grain boundaries exhibit enhanced values of j_c^{GB} , which is at least to a certain extent due to their larger cross-section (see Sec. 7.1). Scanning Hall probe microscopy also allows the tracing of vortices when they hop from one pinning centre to the next in order to determine current-voltage characteristics on a femtovolt scale [121].

Another spatially resolved method to measure j_c is *low-temperature scanning laser microscopy (LTSLM)*. This technique has been used to examine one of the samples in this thesis and it is described in Sec. 6.4.

3.4.6. Theories Explaining the Effect of Grain Boundaries on J_c

A model by Dimos *et al.* [77] (extended by Chisholm and Pennycook [89]), based on dislocations making up grain boundaries, has already been discussed in Sec. 3.4.3. While it can explain some of the more fundamental features observed in measurements, it fails to describe current transport across grain boundaries in sufficient detail. It did not, for example, predict the exponential decay of j_c^{GB} with misorientation angle, nor the field-dependent crossover from GB to grain limited j_c or vortex channelling. Another limitation is that it only covers edge dislocations, ignoring screw dislocations as found in twist boundaries, which might cause very different strain fields.

Other theories have, thus, been proposed. This includes the work by Gurevich *et al.* [122], who also considered dislocations in LAGBs in their model. They treated them by Ginzburg-Landau theory as insulating cores, surrounded by a conducting (but non-superconducting) shell. Using a term for the potential in the GL equation which describes both the modulated, suppressed order parameter along the length of the GB and the reduction in superconducting cross-section, they derived an expression for $j_c^{GB}(\theta_{\text{mis}})$, which is plotted in Fig. 3.12(a) together with experimental data. As can be seen the

result is close to an exponential decay.

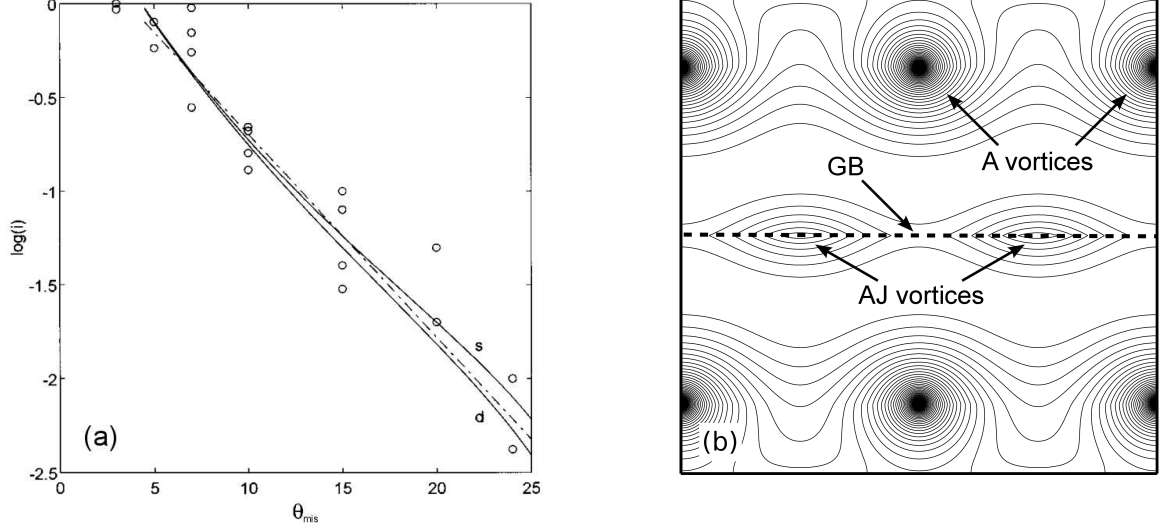


Figure 3.12.: (a) The normalised critical current density across GBs vs. their misorientation angle for s- and d-wave pairing, as derived from a model by Gurevich *et al.* (adapted from [122]). For comparison the dashed line shows an exponential decrease. The curves were fitted to experimental data from Ref. [90] (circles), obtained on [001]-tilt YBCO bicrystal boundaries. (b) Calculated current streamlines making up Abrikosov (A) vortices in the grains and Abrikosov-Josephson (AJ) vortices on the boundary (adapted from [111]).

Gurevich *et al.* [111] also studied GBs in applied fields, and in particular how vortices interact with a boundary. For low misorientation angles conventional Abrikosov (A) vortices are found, pinned by GB dislocations. As θ_{mis} increases j_c^{GB} declines, which also affects the currents making up the flux lines positioned on the boundary. Consequently, they become elongated along the GB plane and their normal core turns into a Josephson core; Abrikosov-Josephson (AJ) vortices are observed, as illustrated in Fig. 3.12(b). At very high θ_{mis} pure Josephson (J) vortices evolve. Due to their larger core size, less energy is gained by placing an AJ vortex on a dislocation, and consequently they are pinned more weakly, which directly explains vortex channelling. The model can further describe the crossover from GB to grain limited J_c (see Sec. 3.4.4) and the transition from LAGBs to HAGBs (as a conversion of AJ into J vortices).

A significant number of other models and mechanisms have been proposed to explain current transport across grain boundaries. They are discussed in more detail in Ref. [72] and shall only be mentioned briefly here. One mechanism that could be responsible for

a reduced critical current density is the suspected charging of GBs, which could, for example, be caused by point defects in the boundary's stress field. It would increase charge carrier scattering in the boundary region, thus reducing j_c^{GB} . Another explanation related to structural properties are broken Cu-O bonds in the GB region [123], changing the density of states of Cu d electrons. Variations in stoichiometry, on the other hand, are less likely to be the reason for a depressed critical current density of GBs, since also samples with undistorted lattices up to the interface (as shown by TEM), exhibit a reduced j_c^{GB} . Local deviations from the ideal oxygen doping, however, could well have an impact on the current carrying capacity of GBs. The effect of the pairing symmetry ($d_{x^2-y^2}$ -wave symmetry is expected for the cuprates) on j_c^{GB} has also been considered in detail [124]. It can explain a depressed order parameter in the GB region, where the spatial coherence of Ψ is interrupted. Also, bending of the electronic band structure in the GB [124] was investigated, analogous to band bending in interfaces in semiconductors. This would again lead to a suppression of the order parameter and under certain circumstances even a transition into the antiferromagnetic insulating state, as discussed in a model [122] mentioned above.

While the different models and theories might be more or less relevant in different scenarios, it is clear that in most cases a combination of several mechanisms will contribute to the observed behaviour of $j_c^{GB}(\theta_{\text{mis}}, T, H)$.

3.4.7. Grain Boundaries in Other HTS

The other cuprates show a very similar dependence of misorientation angle on the critical current density as YBCO [72]. Plotted in Fig. 3.13 is a comparison between j_c^{GB}/j_c^{IG} of $\text{Bi}_2\text{Sr}_2\text{CaCu}_2\text{O}_{8+\delta}$ and $\text{YBa}_2\text{Cu}_3\text{O}_{7-\delta}$. It needs to be mentioned, however, that when absolute values of inter- and intragranular critical current density are considered, YBCO in general surpasses other materials.

Similar to the cuprates grain boundaries in the recently discovered pnictide superconductors exhibit weak link characteristics [126] and a decrease of j_c^{GB} with increasing θ_{mis} , which possibly also follows an exponential law [127]. More data are still required to confirm the exact dependence on misorientation angle.

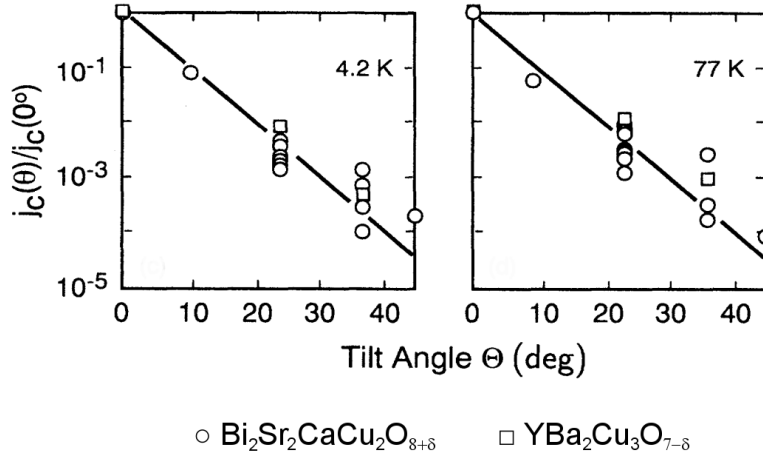


Figure 3.13: Both $\text{Bi}_2\text{Sr}_2\text{CaCu}_2\text{O}_{8+\delta}$ and $\text{YBa}_2\text{Cu}_3\text{O}_{7-\delta}$ show an exponential dependence of j_c^{GB} on θ_{mis} , as was determined from measurements on thin film bicrystals (adapted from [125]).

3.5. Applications

The fact that superconducting materials offer dissipation-free current transport at high current densities makes them very attractive for applications. While some of them have been in use for many years, others are still in a conceptual stage.

In general applications of superconductors can be grouped into two classes, namely those where high current densities are required (and consequently grain boundaries, at least in the case of HTS, are detrimental) and those which exploit the properties of weak links in order to fabricate devices (making use of the Josephson effect, for example in HTS GBs). The first group comprises:

Magnets Superconducting coils can be used to create strong magnetic fields. The most prominent application is their use in magnetic resonance imaging (MRI), primarily for medical diagnostics, but they are also used in scientific laboratories and to create the magnetic fields necessary for particle accelerators [e.g. the Large Hadron Collider (LHC) at CERN] and for fusion reactors [e.g. the International Thermonuclear Experimental Reactor (ITER)]. In addition to that they are an alternative for conventional magnets for high speed levitating trains.

Power generation and motors Superconducting materials can replace conventional ones in generators and motors. The main benefit is a reduction in size and weight accompanied by higher efficiency.

Power storage The field in large superconducting coils or the rotational energy in flywheels (where a superconducting stator spins almost friction-less) could be used

to store energy.

Power transmission Superconducting cables offer the possibility to transport energy free of losses. In addition to that they can support a higher current density than conventional conductors, which is advantageous in densely populated areas. Losses could also be reduced if superconducting materials were used in transformers. Another promising application for utilities are fault current limiters, which break the circuit in the event of an excess current.

The second class of applications includes:

SQUIDs Superconducting Quantum Interference Devices use the Josephson effect in order to measure magnetic fields with high precision.

Electronics Highly integrated circuits of Josephson junctions could be used to replace conventional semiconductor electronics. Their advantages would be high speed and extremely low power dissipation.

3.5.1. HTS

So far in most cases LTS (mainly NbTi and Nb₃Sn) are used due to limitations of HTS (grain boundaries, mechanical strength, cost etc.). Nevertheless the latter offer a range of new perspectives because of higher values of H_{c2} , J_c and T_c compared to conventional superconductors. In particular cooling costs could be significantly reduced if liquid nitrogen, rather than helium, was employed. An overview of the current status of HTS applications is given in Ref. [47].

When it comes to wires, first generation cables [made from (BiPb)₂Sr₂Ca₂Cu₃O_{10+δ} or Bi-2223] can be distinguished from second generation cables (“coated conductors”, comprising a YBa₂Cu₃O_{7-δ} layer, which are the topic of this thesis; see Sec. 4 for an introduction). In several projects the feasibility of HTS cables is currently studied by replacing a certain length (of the order of 100 m) of copper wires in live power grids by superconducting wires.

HTS wires offer a significantly lower heat leak compared to copper wires when they are used to supply LTS magnets. The current leads for the magnets of the LHC at CERN and those of ITER have been or will be made from Bi-2223 wires.

3. *High-Temperature Superconductors and Their Grain Boundaries*

Blocks of melt-textured YBCO (“bulks”) can be used to construct superconducting, frictionless bearings and magnets (e.g. for future magnetic levitation trains).

The first successful “consumer application” of HTS already in use are front-end filters in base-station receivers in mobile phone networks.

Significant progress has also been made in the field of HTS SQUIDS [128]. They make use of the fact that HAGBs behave like Josephson junctions. A device structure, patterned into an HTS film deposited on a bicrystal substrate can, therefore, be used as a SQUID.

4 Coated Conductors

This chapter covers coated conductors (CCs), the HTS tapes investigated for this thesis.

After a brief review of the different HTS wires currently available the basic architecture of CCs is introduced in Sec. 4.2. In the next sections methods to achieve grain alignment in CCs and thin film deposition techniques are described. This is followed by a listing of the different architectures of the samples in this thesis (Sec. 4.5). The chapter ends with a discussion of the phenomenon of current percolation.

4.1. HTS Wires

The size and orientation of grains with respect to each other is termed *texture*. The amount to which the *c*-axes of different grains are aligned with respect to each other is described by the *out-of-plane* texture (e.g. grains separated by a [100]-tilt boundary). Different rotations about the *c*-axes of grains, which might or might not lie with their *ab*-layers in the same plane, (e.g. [001]-tilt) are quantified by the *in-plane* texture.

As discussed in detail in Sec. 3.4 grain boundaries are, in general, detrimental to the flow of a supercurrent. Methods were, therefore, sought to reduce their negative effects by aligning grains with respect to each other. There are two different approaches to achieve good texture and consequently high critical current densities, implemented in the “first generation” (1G) and “second generation” (2G) wires.

In the case of 1G wires [129, 130] filaments of $\text{Bi}_2\text{Sr}_2\text{CaCu}_2\text{O}_{8+\delta}$ (Bi-2212) or

$\text{Bi}_2\text{Sr}_2\text{Ca}_2\text{Cu}_3\text{O}_{10+\delta}$ (Bi-2223) are embedded in a matrix of, typically, silver or a silver alloy. In order to fabricate such a wire a technique called “powder-in-tube” (PIT) is employed, similar to that used for Nb_3Sn , NbTi [131] and MgB_2 [132] wires. In short, the reacted or unreacted superconducting powder is filled into a metal tube, which is then drawn to a wire. Several of those strands are subsequently bundled and drawn again to obtain a multifilamentary wire. The metallic matrix gives both mechanical stability and an electrical contact to the superconductor.

In the case of BSCCO wires *uniaxial* alignment is achieved by a rolling process, thus the obtained micaceous grains are oriented along their *c*-axis, but there is no in-plane alignment. As a consequence, the critical current density of the GBs is not particularly high, but their cross-sectional area is rather large due to the high aspect ratio of the grains, allowing current to percolate in a way described by a “brick-wall” model [133].

A very different approach is pursued in the case of 2G wires or “coated conductors” (CCs) which aims at achieving *biaxial* texture, i.e. grain-to-grain alignment both in- and out-of-plane. To this end the superconductor (usually $\text{REBa}_2\text{Cu}_3\text{O}_{7-\delta}$, where RE is a rare earth element) is deposited as a thin film on a textured substrate. Due to the heteroepitaxial growth process the grain alignment is transferred from the substrate into the superconductor, ideally leading to low-angle grain boundaries (LAGBs) only. In this way a single crystal-like REBCO layer is obtained in kilometre-long tapes with superconducting properties comparable to those of thin films deposited on single crystal substrates (e.g. SrTiO_3). It is this technology which after many years of research and development has made possible “the emancipation from the tyranny of the grain boundary” [75].

Thanks to the unprecedented sharp texture and the superior superconducting properties of REBCO over BSCCO, significantly higher critical current densities are achieved in coated conductors than in 1G wires. The topic of this thesis are CCs and their grain boundaries, which—despite good grain alignment—in certain scenarios are still the factor limiting the overall J_c . This is why the present chapter is dedicated to the different coated conductor production routes and the structural properties of these wires.

4.2. Basic Architecture of Coated Conductors

While the exact structure and manufacturing route can be quite different between the various types of CCs, they have a basic architecture in common [134]:

1. Substrate In most cases Ni-based alloys are employed as a substrate. It provides the mechanical strength and flexibility expected from an industrial conductor, thus it has to be deformable but stable. This is crucial since after the wire fabrication it will have to withstand, for example, being wound into a multifilamentary cable or a coil. During operation of the latter the substrate will also have to counteract significant electromagnetic forces. With this in mind it should be as thin as possible in order to achieve a high engineering critical current density.¹ Another important issue is thermal expansion. If upon cooling down from deposition temperature the substrate contracts more or less than the buffer and superconducting layers, the latter two will experience compressive or tensile stress, respectively, both of which will degrade the superconducting properties. Tensile stress can lead to cracks, consequently the substrate should have a similar or slightly higher thermal expansion coefficient than the layers above. Furthermore, an ideal substrate should not react chemically with the HTS material² and exhibit as little ferromagnetism as possible in order to reduce ac losses.

2. One or several buffer layers These form a chemical barrier to protect the superconductor from diffusion from the substrate, which would occur during processing steps at high temperatures. Inter-diffusion needs to be avoided because most metals react chemically with REBCO, degrading its superconducting properties. Even small amounts of metal atoms in the HTS matrix can significantly reduce T_c [135]. The buffer should also prevent diffusion in the other direction, namely of oxygen from the superconducting layer into the substrate, as oxygenation of the metal would have a negative influence on the mechanical stability of the tape. Additionally, the mismatch of the lattice parameters of the (top) buffer layer with respect to the superconductor should be as small as possible in order to provide a good template for epitaxial growth. Also, the buffer needs to be well textured

¹The engineering critical current density J_e is defined as the critical current divided by the total cross-sectional area of the conductor (i.e. including substrate, buffer and any other layers).

²This is not highly critical though, as in most cases a buffer layer separates substrate and superconductor.

so as to achieve low-angle grain boundaries. This can be achieved either through a deformation-textured substrate, like RABiTS, or through growth texturing, like IBAD (see Sec. 4.3). Usually oxides are used as buffer layers.

3. Superconducting layer This is of course the most important layer. It should be well textured and free of cracks and voids to allow a high critical current. The cuprate layer is usually between a few hundred nanometres and several micrometres thick.

4. Passivation/insulation layer It protects the HTS layer from the ambient and also prevents current from leaking between conductor filaments if the CC is used as a multilayer.

The schematics in Fig. 4.1 show the typical architectures of a RABiTS and an IBAD coated conductor.

4.3. Achieving Texture in Coated Conductors

The different techniques to achieve biaxial texture can be grouped into two classes: deformation-textured substrates and growth texturing.

In the first case the metallic substrate itself is treated such that its grains adopt in- and out-of-plane alignment. The most prominent example is RABiTS. Growth texturing, on the other hand, employs an unoriented substrate and achieves texture by depositing an aligned seed layer on top of it. IBAD is the most commonly used exponent of this technique.

In the following the key points of the two approaches are discussed. A more detailed review can be found in Ref. [2].

4.3.1. RABiTS

It was demonstrated in 1996 by Norton, Goyal *et al.* [136, 137] that a sharp cube texture can be imparted to a metal (e.g. Ni, Cu)³ by thermomechanical processing. The technique labelled *Rolling Assisted Bi-axially Textured Substrates (RABiTS)* exploits the fact that when a metal ingot is rolled to a sheet at room temperature (*cold rolling*) not only is its thickness reduced, but also do the crystallites adopt a certain amount of

³In general Ni is preferred as it oxidises less than Cu [138].

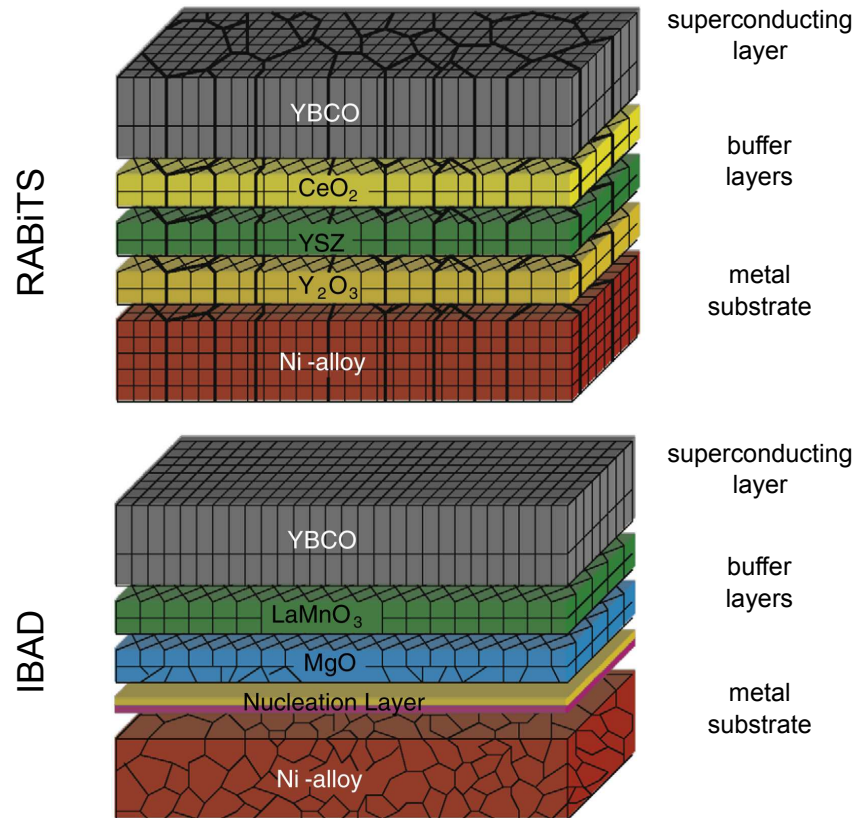


Figure 4.1.: The structure of typical RABiTS and IBAD coated conductors (without the passivation/insulation layer). Note the outlines of the unit cells, indicating that in RABiTS the grain alignment arises from a textured Ni-alloy whereas in IBAD it is due to the oriented MgO layer (adapted from [75]).

alignment. In the case of Ni and Cu $\{112\}\langle 111\rangle$ -texture develops. This nomenclature describes a crystallite orientation where the $\{112\}$ planes are parallel to the sheet plane and the $\langle 111\rangle$ direction coincides with the tape's rolling direction.

If the cold worked material, which is under a certain strain, is now heated to about 0.4–0.5 times its melting temperature a new unstrained grain structure develops in a process labelled *primary recrystallisation*. Tiny grains nucleate, which finally substitute the original grains. For Ni and Cu the $\{100\}\langle 001\rangle$ cube texture is obtained with highly oriented grains with respect to the rolling, transverse and normal directions (RD, TD and ND). Their diameter ranges from several micrometres to several hundreds of micrometres.

The architecture of a typical RABiTS coated conductor is shown in Fig. 4.1.

4.3.2. IBAD

While under certain conditions c -axis oriented YBCO films can be deposited on polycrystalline substrates the in-plane misorientation remains, considerably suppressing J_c .

It was shown in 1985 by Yu *et al.* [139] on Nb thin films that in-plane texture can be achieved by bombarding an amorphous substrate with an Ar ion beam directed at a certain angle with respect to the substrate normal while the film is deposited. This technique is now known as *Ion Beam Assisted Deposition (IBAD)*. In 1992 Iijima *et al.* [140] were the first to successfully employ it for the growth of HTS thin films. Using IBAD they produced textured YSZ (yttria-stabilised zirconia) buffer layers on a polycrystalline substrate, which itself had no texture, and deposited YBCO on top. Even though their in-plane orientation was still poor it led to a dramatic increase in J_c . Typical examples of IBAD layers are YSZ, MgO and GdZrO [141].

There are different theories why ion bombardment is favourable for grain orientation. It might be that misoriented grains are sputtered away because the sputtering yield is higher for them [142]. Another proposed explanation is that grains in certain orientations can grow more easily because the ion beam channels along planes with larger interplanar spacings parallel to them and thus does less damage [143]. Alternatively, the ion beam might lead to an orientation of the nuclei as they are formed, leading to the growth of aligned grains. In either case in order to grow an in-plane oriented film it was found that the ion beam needs to be directed along a major crystallographic direction, e.g. parallel to $\langle 111 \rangle$, which corresponds to an angle of 54.7° with respect to the substrate normal if cubic material is deposited.

The grains produced by IBAD have a diameter between 100 nm and $2 \mu\text{m}$, hence they are significantly smaller than those due to RABiTS. The grain size strongly influences how currents percolate through the film, as discussed in Sec. 4.6, and how J_c depends on track width (see Chap. 8). In general the IBAD process leads to a slight vicinality, i.e. the ab -planes are tilted with respect to the film plane. Due to the resulting anti-phase boundaries in the superconducting layer this can be beneficial for flux pinning and enhance J_c for current flow parallel to the vicinal steps [144].

An example of a coated conductor with an IBAD architecture is sketched in Fig. 4.1.

4.3.3. Other Techniques

In addition to RABiTS and IBAD several other approaches have been pursued to achieve biaxial texture.

Inclined Substrate Deposition (ISD) exploits the fact that in-plane orientation can be achieved if the buffer layer is deposited on an untextured substrate at an angle with respect to the substrate normal [145, 146].

In a technique termed *Rolling Assisted Tilted Substrates (RATS)* a rolled Ni tape is annealed in a similar way as in the case of RABiTS, however up to higher temperatures [147]. Under these conditions grain boundaries are energetically unfavourable, which, in a process known as *secondary recrystallisation*, leads to very large, well aligned grains, which are tilted significantly with respect to the substrate plane. The downside is that substrates produced by RATS suffer from rather poor mechanical properties.

In a completely different approach a YBCO layer was deposited by metal-organic chemical vapour deposition (MOCVD) on a polycrystalline Ag substrate in a high magnetic field. This was reported to lead to grain alignment and enhanced values of J_c [148].

4.4. Thin Film Deposition Techniques

There are various techniques to produce thin films. In general they can be divided in three groups:

Physical Vapour Deposition (PVD) The material is evolved by physical means before it is deposited on a substrate. This technique includes sputtering, Pulsed Laser Deposition (PLD) and electron-beam evaporation.

Chemical Vapour Deposition (CVD) The precursor is introduced into the reaction chamber in its vapour phase and then reacts on the surface of the substrate to form the film. An example for this processing route is Metal-Organic Chemical Vapour Deposition (MOCVD).

Chemical Solution Deposition (CSD) Here the starting material is deposited on the substrate in its liquid phase as for example in Trifluoroacetate Metal-Organic Deposition (TFA-MOD) as well as in Liquid Phase Epitaxy (LPE).

In this section a short introduction is given to the techniques used to produce and prepare the samples measured for this report.

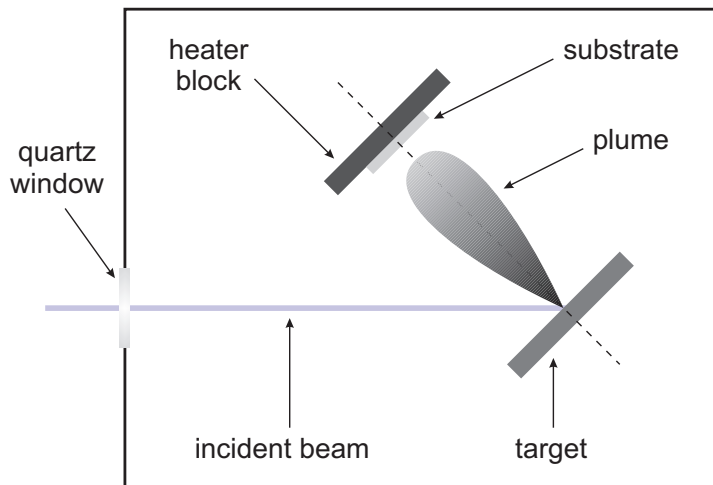


Figure 4.2:
Schematic of a PLD system.

4.4.1. PLD

In a Pulsed Laser Deposition (PLD) system the beam of a powerful laser (usually a pulsed UV laser) is directed at the target. Material is ablated and deposited onto a substrate, as shown in Fig. 4.2.

In most cases oxygen is used as a sputter gas. It reduces the mean free path, thus a plume develops in front of the target and material moves primarily towards the substrate instead of dispersing throughout the chamber. In addition to that it can provide the oxygen necessary for the growth of the thin film as is the case with YBCO.

The process of the ablation is complex. Not only are atoms from the target sputtered off, but the material below the surface region which is hit by the beam starts to boil. Usually the target rotates in order to remove material not only from one spot. The substrate is heated so as to increase mobility after adhesion and facilitate the growth process.

PLD has the advantage that it can be used for almost every material including ceramics and polymers. Furthermore, the film thickness can be controlled relatively well, since every pulse deposits a certain amount of material. Its downsides are the need for a high vacuum and that it is hard to scale up, limiting the use of PLD for industrial applications. This makes it mainly a research deposition technique.

In general films are underdoped, whether grown by PLD or another method. In order to reach the optimum oxygen content, crucial for the superconducting properties of HTS (see Sec. 3.2), the film has to be annealed in oxygen at 500 to 600 °C.

4.4.2. MOCVD

A technique originally developed for the semiconductor industry [149], Metal-Organic Chemical Vapour Deposition (MOCVD) has also been employed successfully for the growth of HTS films [62]. A solid or, preferably, liquid [150] precursor is used which consists of organic compounds of the elements to be deposited. It is vaporised and transported to the reaction chamber (the MOCVD reactor) by a carrier gas (e.g. Ar). There it is deposited on a heated substrate, directly forming the HTS layer while the organic reaction by-products leave the chamber. This makes MOCVD an *in situ* technique.

One advantage of MOCVD is that it can be scaled up easily, as the reactor with the showerhead, responsible for the vapour deposition, is essentially unlimited in size. Additionally, no high vacuum is required, removing the need for sophisticated vacuum equipment. Since the composition of the liquid precursor can be modified easily it is straight-forward to change the concentration of a certain dopant unlike in PVD, where different targets would have to be fabricated. For example Zr doping, forming BaZrO₃ nanocolumns, was found as a feasible method to introduce pinning centres into MOCVD films, enhancing the in-field critical current density [151]. Furthermore, multizone showerheads allow the production of multilayer films.

The columnar microstructure of REBCO films produced by MOCVD is very similar to that in films grown by PLD, and so are the superconducting properties [152]. This is in contrast to the laminar microstructure of films grown by MOD (see below) [153]. The similarities between PLD and MOCVD have the beneficial side effect that in many cases results obtained from (research-scale) PLD samples also apply to (industry-scale) MOCVD films.

4.4.3. TFA-MOD

In Trifluoroacetate Metal-Organic Deposition (TFA-MOD) in order to obtain the precursor material the acetates of the elements to be deposited (for YBCO these are Y, Ba and Cu in a 1:2:3 cation ratio) are dissolved in deionised water and trifluoroacetic acid⁴ [154, 155]. After drying and dissolving in methyl alcohol the precursor is deposited by spin coating or dip coating (the latter being advantageous for the growth of thicker films [156]) on the substrate which has been thoroughly cleaned.

⁴While the oxides of Y and Cu are formed easily, Ba tends to convert to BaCO₃ instead. The use of TFA acid avoids this.

Following that, the sample is fired in two stages in order to obtain the crystalline HTS phase. First an oxyfluoride film is formed by decomposition of the metal trifluoroacetates during calcination at relatively low temperatures (pyrolysis, at $\sim 400^\circ\text{C}$) in a humid oxygen atmosphere. Subsequent annealing in humid nitrogen/oxygen gas at higher temperatures ($> 700^\circ\text{C}$) gives the HTS film. Since the final superconducting phase is only formed after deposition, MOD is considered an *ex situ* technique.

Like MOCVD but in contrast to physical techniques like PLD this processing route does not need sophisticated (and thus expensive) vacuum and laser systems. In addition to that high deposition rates can be achieved while the film composition remains uniform [153].

Similar to MOCVD by changing the precursor composition MOD allows for the inclusion of nanoparticles (e.g. Y_2O_3 or BaZrO_3), which act as pinning centres [157].

4.4.4. Sputtering

In *dc sputtering* a glow discharge is created between an anode (at ground potential) and a cathode (at 1000 to 2000 V) in a chamber with Ar gas at a pressure of a few Pascal [158]. Ar ions are then accelerated to the cathode, which is made of the material to be deposited (the target) and sputter atoms off. Because of the momentum transferred to them they move to the anode where they are deposited on a substrate or a film. The creation of secondary electrons when Ar ions hit the target helps sustain the plasma. In dc sputtering the target material needs to be electrically conducting.

Most secondary electrons, however, do not cause ionisation but travel directly to the anode. In order to increase the density of electrons close to the target a magnet (usually a racetrack magnet) can be placed on its other side. Because of the component of its field parallel to the surface of the cathode the trajectories of the created secondary electrons are bent and they are directed back, ionising more Ar atoms close to the target. This leads to a higher sputtering yield, which increases the deposition rate. The technique is known as *magnetron sputtering*.

In order to deposit insulating materials *rf (radio frequency) sputtering* can be employed. Rather than exposing the Ar gas to a constant electric field like in dc sputtering, an alternating field is applied. The electrons begin an oscillating motion, hence ionising a high number of Ar atoms. The pressure can, therefore, be lower than for dc sputtering. The ions are accelerated to the target by an offset voltage between cathode and anode,

sputtering off target material which then gets deposited.

Reactive sputtering also allows the deposition of insulating material. In this technique the Ar gas is mixed with, for example, O₂ or N₂, which then react with the sputtered material (e.g. deposition of Al₂O₃ from an Al target).

Different sputtering techniques can be combined, e.g. reactive magnetron sputtering.

4.4.5. Electron-Beam Evaporation

In this process an electron beam generated by a tungsten filament and a high acceleration voltage is focused by a magnetic field onto the material to be deposited which is in a copper crucible cooled by recirculating water [159]. The material is evaporated and deposited onto the substrate which is positioned above the crucible.

The advantages of this technique are a high deposition rate and an efficient utilisation of the material. In addition to that the stoichiometry of the precursor material is preserved which is why no complicated composition control is necessary.

In general e-beam evaporation is not a continuous process as the crucible needs re-filling. There are modifications, however, where the ingot is fed to the electron beam on a turntable which allows uninterrupted deposition [160].

4.5. Architectures of Samples in this Thesis

For this thesis three different types of coated conductors have been measured. These are a RABiTS-MOD tape by American Superconductor (AmSc) [161, 153, 157], an IBAD-MOCVD tape by SuperPower (SP) [141, 162] and three RABiTS-PLD tapes by IFW Dresden [163, 164, 165]. Table 4.1 gives an overview of their architecture. The structure of the American Superconductor and SuperPower tapes is sketched in Fig. 4.3.

In the following sections the different architectures are delineated.

American Superconductor

The Ni substrate used by AmSc is alloyed with W. It was found that even minor alloying additions to Ni increase the yield strength and reduce its Curie temperature [168], which is beneficial because a magnetic substrate increases ac losses [169, 170, 171] in the superconductor. As mentioned earlier one of the functions of the buffer is to avoid

Table 4.1.: Architectures of the samples measured in this thesis. The nominal thickness t of each layer is given together with the employed deposition technique [Abbreviations: rf sputt. = rf sputtering, e-beam = electron-beam evaporation, r. mf mag. sputt. = reactive mf (medium frequency) magnetron sputtering].

	American Superconductor RABiTS-MOD [157, 166]			SuperPower IBAD-MOCVD [162]			IFW Dresden RABiTS-PLD [163, 164, 165, 167]		
	material	t (nm)	dep. tech.	material	t (nm)	dep. tech.	material	t (nm)	dep. tech.
HTS	YBCO	800	TFA-MOD	REBCO ^a	1000	MOCVD	YBCO ^b	300	PLD
buffer	CeO ₂	75	rf sputt.	LaMnO ₃	30	rf sputt.	CeO ₂	50	PLD
	YSZ	75	rf sputt.	MgO ^c	20	r. mf mag. sputt.	YSZ	200	PLD
	Y ₂ O ₃	75	e-beam	MgO	10	IBAD / sputt.	Y ₂ O ₃	100	PLD
				Y ₂ O ₃	7				
			Al ₂ O ₃	80					
substrate	Ni-5at%W	75 μm		Hastelloy	50 μm		Ni- x at%W ^d or Ni-Ag-Y	80 μm 80 μm	

^aThe HTS layer was capped by Ag, which was removed by Ar ion milling before sample preparation.

^bThe HTS layer was capped by Au, which was removed by a potassium iodide etch before sample preparation.

^cThis second MgO layer is deposited homoepitaxially, rather than by IBAD.

^dSamples from IFW with tungsten alloying amounts of 5 and 7.5% were analysed.

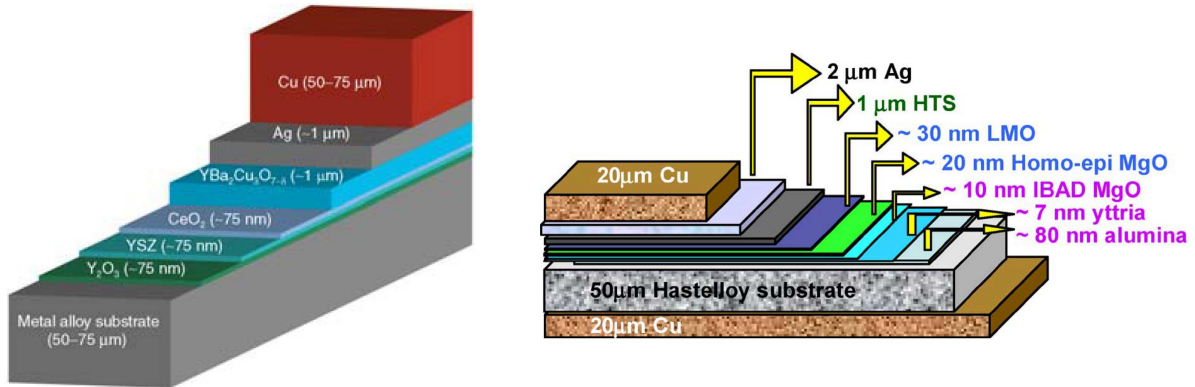
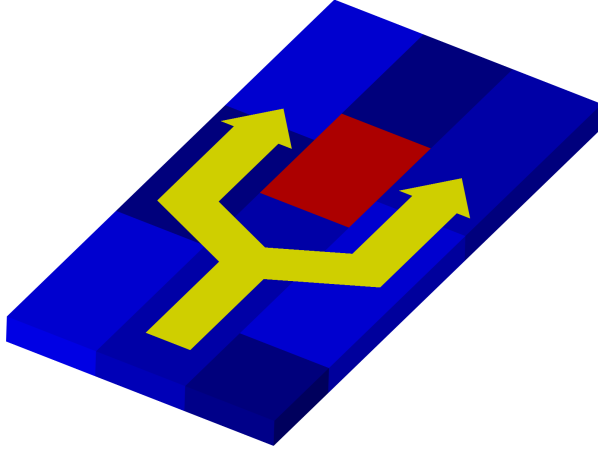


Figure 4.3.: Architectures of the American Superconductor (left) and SuperPower (right) tapes measured for this thesis. Unlike in the schematics the AmSc samples had no Ag cap layer and Cu stabiliser and the SP samples had no Cu stabiliser [153, 162].

diffusion of oxygen and metal atoms. The thickness of the buffer layers in the AmSc tape guarantees that this is prevented [157], while not being unnecessarily high, which would increase production costs. CeO_2 was chosen as the top buffer layer because of its smaller lattice mismatch with respect to YBCO, compared to YSZ.

SuperPower

The nanocrystalline or amorphous Al_2O_3 layer deposited directly on top of the Hastelloy substrate acts as a diffusion barrier. It was found that this task is better performed by a nanocrystalline or amorphous film, compared to material with larger grain sizes. The next deposition step consists of an Y_2O_3 seed layer, which supports the subsequent IBAD MgO growth. The latter is of course the most important layer in the buffer stack as it introduces the required grain alignment. The advantage of MgO is that texture evolves in an exceptionally thin layer already, reducing the deposition time significantly compared to, for example, YSZ. The ion assist beam is directed parallel to the MgO $\{101\}$ layers, i.e. at an angle of 45° away from the surface normal. The IBAD process, however, leads to a certain damage in the MgO layer, slightly altering the MgO lattice parameter, which necessitates the growth of a homoepitaxial MgO layer on top of the IBAD layer in order to prevent strain-related misorientations in the next layer. Finally LaMnO_3 reduces the lattice mismatch with respect to REBCO, which is grown by MOCVD. The IBAD architecture employed by SuperPower is described in more detail in Refs. [141, 162].

**Figure 4.4:**

Schematic showing a very simple grain boundary network. Currents percolate around a grain (in red) with GBs with low values of j_c^{GB} .

IFW Dresden

Due to the similar architectures the basic characteristics of the AmSc architecture also apply to the samples supplied by IFW Dresden. They were, however, grown on different substrates: (i) a conventional Ni-5at%W tape [163], (ii) a Ni substrate with a higher W content of 7.5% for increased mechanical strength and reduced ferromagnetism [164] and (iii) a Ni tape micro-alloyed with Ag and Y, consisting of grains elongated along the rolling direction [165].

4.6. Current Percolation

In a network of grains separated by grain boundaries of different misorientation angles θ_{mis} , as is the case in a coated conductor, *percolative current flow* takes place. This means that grain boundaries with a higher j_c^{GB} carry a higher current density compared to those with a lower j_c^{GB} , and consequently the current percolates through the sample, as illustrated in Fig. 4.4.

In order to examine the phenomenon and develop models for it *percolation maps* can be studied. These images are derived from misorientation maps obtained by EBSD (see Sec. 6.2) which show the grains with their respective orientations. In a percolation map only grain boundaries above a certain misorientation angle are drawn and thus it can be determined whether or not a sample is percolatively connected, i.e. if there is a current path from one end to the other which only has to cross grain boundaries below the criterion angle. The probability for this is the percolation probability which

is one of three *percolation parameters*. The other two are the area which is percolatively connected and the limiting cross section which describes the smallest cross section the current has to pass.

4.6.1. Modelling

In order to model current percolation grains can be represented either as squares or as hexagons, the latter being more realistic because a number of six neighbours per grain approximates real CC grains better than four. The critical current densities of the boundaries are related to the misorientations of the grains by an exponential law (see Sec. 3.4.3). Simple models predict the total J_c using an average grain boundary angle or a critical angle determined from the percolation parameters together with a certain criterion. In a more sophisticated model each boundary is represented as an arc with a certain j_c^{GB} connecting two nodes (the grains). One can then make imaginary cuts along GBs across the entire width of the sample. The cut where the overall J_c of all the arcs taken away is the smallest limits the critical current density of the whole sample and thus determines its J_c . If more current is passed through it flux will start to flow in the channel given by this cut and dissipation will occur.

It is, however, a rather coarse approximation to model coated conductor grains as squares or hexagons. Models have, thus, been developed which describe grains by groups of pixels, hence allowing more arbitrary and realistic grain geometries [172]. This approach was taken even one step further by simulating the current flow in a real sample [173], using a misorientation map obtained by EBSD and the exponential dependence of j_c^{GB} on θ_{mis} mentioned above.

One result from modelling is that J_c increases with the number of grains across the width of the sample. On the other hand it becomes lower the more grains the sample contains along its length, because this makes it more likely that one “hits” a grain boundary with a low j_c^{GB} [174].

These models are computationally very intensive which limits them to a certain number of grains. In order to obtain results for realistic tape lengths statistical means have to be employed like the *Weibull analysis* which describes the probability that a short section of a conductor has a J_c above a certain value by an exponential law. Consequently, the probability for n elements in series is the n th power of the value for one element. One result of this analysis is that the dependence of J_c on the number of grains in the

length N_l and in the width N_w can be written as

$$J_c \propto \left(\frac{1}{N_l} \right)^{\frac{1}{N_w}}. \quad (4.1)$$

The models can be further extended to treat subgrains within grains due to the growth process and the fact that in certain cases J_c is limited by the grains and not the boundaries. This can be used in order to see whether in a specific case more effort should be made to improve the texture (i.e. reduce the misalignment) or to increase the intragranular j_c [172].

Part II.
Experimental

5 Sample Preparation

Well prepared samples are a prerequisite to successful measurements. In this chapter the necessary steps, for both grain / grain boundary isolation and wider, polycrystalline tracks are described.

In the first section the two different types of experiments performed for this thesis are delineated. In the following part it is explained how contacts were deposited (Sec. 5.2) and how wider tracks were patterned (Sec. 5.3). The last two sections deal with Electron Backscatter Diffraction and Focused Ion Beam microfabrication, which were used to obtain single grains / GBs.

5.1. Processing Steps for the Different Experiments

In order to measure the critical current density of a thin film superconductor, like a coated conductor, by a transport measurement (see Sec. 6.1) a certain sample preparation process is required. This usually involves the deposition of Ag/Au contacts and the patterning of one or several tracks onto the sample. The latter is necessary in order to limit the critical current (for obvious reasons I_c can only be measured if it is below the maximum current of the power supply used) or if only a certain area of a sample is to be investigated.

Two different types of experiments were carried out for this thesis in order to characterise the superconducting properties of the coated conductor samples (see Part III):

Polycrystalline tracks The critical current densities were obtained of tracks covering a few up to several thousands of grains. These tracks were between 6 and 250 μm

wide and $100\ \mu\text{m}$ to $1\ \text{mm}$ long.

Single grains and grain boundaries Specific grains and grain boundaries were isolated in order to measure their J_c .

Both classes of experiments required tracks to be patterned by a conventional lithographic process as described in Sec. 5.3. In order to isolate grains / GBs this was followed by Electron Backscatter Diffraction (EBSD, see Sec. 5.4) to locate specific grains on the sample. Grains or GBs could then be isolated by patterning microbridges onto the previously prepared tracks using a Focused Ion Beam microscope (see Sec. 5.5).

5.2. Deposition of Contacts

In a first step a sample, typically $\sim 10 \times 5\ \text{mm}^2$ in size, was cut from the CC tape. This was done using a guillotine paper cutter, which allowed precise cuts with sharp edges. The tape was protected by sheets of paper during this process.

In order to apply contacts, at first the sample was coated by a layer of photoresist, which was subsequently removed in the areas where the contact pads should go, using a lithographic process described in more detail in Sec. 5.3. The metals were then deposited by magnetron sputtering (see Sec. 4.4.4) on the entire sample surface. The lower chamber pressure, compared to conventional sputtering, means that Ag and Au atoms hit the sample with a higher momentum, thus being implanted into the thin film, which leads to high-quality contacts with a low contact resistance. Silver was deposited directly on top of the superconductor, because it does not react chemically with the latter. The following Au layer provided a good contact to indium pads and the pins of the measurement system (see Sec. 6.1). After the metals had been deposited the photoresist (with Ag and Au on top) was removed by acetone in a “lift-off” process, leaving Ag/Au only in the area of the contact pads.

Some of the samples analysed in this thesis had been supplied with a Ag or Au coating. In this case lithography and ion milling or a potassium iodide etch were employed to remove the metallic layer everywhere except for the areas of the contact pads.

5.3. Thin Film Patterning

After the deposition of contacts, the samples were spin-coated with a $\sim 2\ \mu\text{m}$ thick layer of AZ 4533 photoresist and baked for 60 s at 115°C . The desired pattern was then transferred from a mask into the resist using either a projection or a contact photolithography system.¹

Lithography masks typically consist of a soda lime glass plate coated with a Cr layer which defines the features. Masks with different patterns had been designed by the author for the different experiments. They were fabricated by *Compugraphics* with a pixel size of $0.5\ \mu\text{m}$, allowing a minimum feature size of $2\ \mu\text{m}$. Shown in Fig. 5.1 are two $10 \times 5\ \text{mm}^2$ cells on such masks, used for the preparation of polycrystalline tracks and the initial, wider tracks for grain / GB isolation, respectively. In the first case only one track is patterned onto a sample, which allows five contacts on either side of the track to be used for current injection, reducing sample heating, while the voltage is measured on the sixth pad.

The pattern used for GB isolation deserves further description. As can be seen in Fig. 5.1(b), it consists of five tracks per sample, which—in principle—allow the isolation of five boundaries or grains on one single sample. Due to their limited I_c compared to wider tracks one contact pad for current injection on either side of a track is sufficient. The small recesses in the track edges ($5\ \mu\text{m}$ deep) are an essential feature as they are visible on the EBSD maps and thus serve as alignment marks together with the numbers on either side of the track, allowing one to correlate EBSD maps to FIB images.²

After exposure in visible or UV light, the resist was developed in an AZ 351 developing solution, which removed it from the areas which had not been covered by the pattern on the mask. Optimum exposure and development times are crucial; the entire resist thickness needs to be removed while over-exposure or over-development have to be avoided as they lead to less sharply defined edges.

In the next step the pattern was transferred from the resist into the superconducting layer by broad beam Ar ion milling. For this purpose Ar ions are accelerated towards

¹While both mask aligners offered sufficient resolution for the required feature size, contact lithography has the advantage that the coated conductor tape was flattened during exposure, hence the whole sample was in focus. In some cases slightly bent tapes posed difficulties with focusing when (contact-free) projection lithography was employed.

²In general the grains are not visible on FIB micrographs, hence the FIB cuts had to be made “blindly” with the help of the EBSD maps.

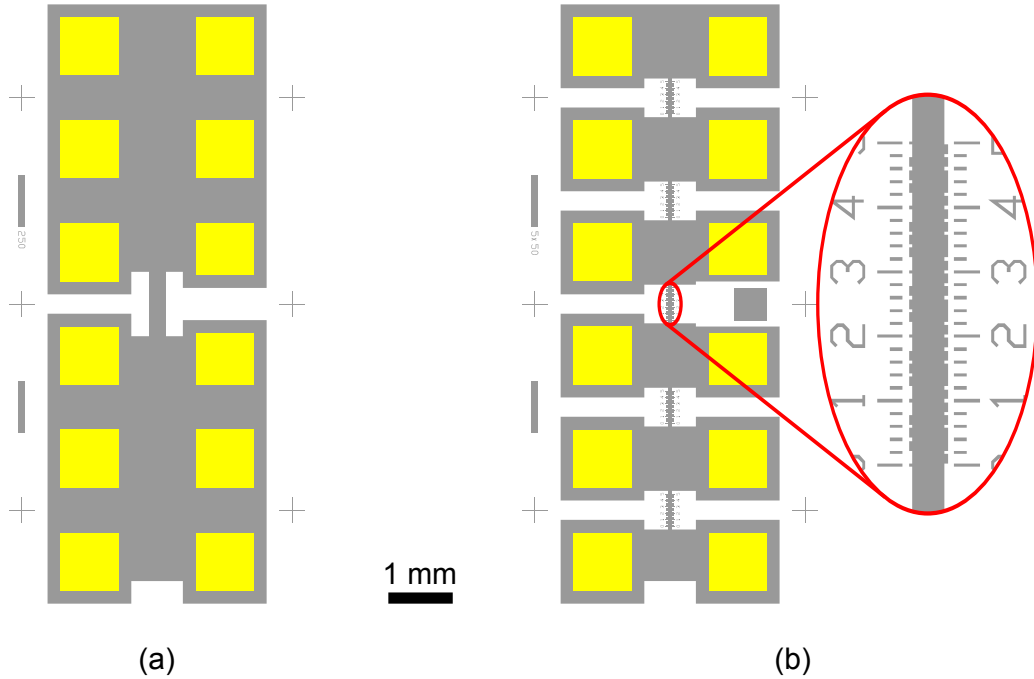


Figure 5.1.: Two cells on a lithography mask. (a) A polycrystalline track (in the centre). (b) A pattern used for GB isolation. In the blowup marks in the edge of the track can be seen, which allowed the spatial correlation of EBSD maps and FIB images. The contact pads are indicated in yellow.

the sample, where they sputter off material. This process is not selective, hence resist is removed as well, which necessitates a sufficient resist thickness. Milling was ideally stopped as soon as the (insulating) buffer was reached, as exposing the Ni substrate can lead to shorts. As long as the short is only in parallel to the superconducting layer with no direct connection between contact pads and metallic substrate, one can still expect all current to pass through the superconducting track, rather than the substrate. It was found, however, that a Ni shunt increases the observed noise level.

The residual photoresist was removed by acetone after the milling, which concluded the sample preparation for polycrystalline tracks. If grains or grain boundaries were to be isolated, the next steps were the acquisition of EBSD maps and the actual isolation by FIB.

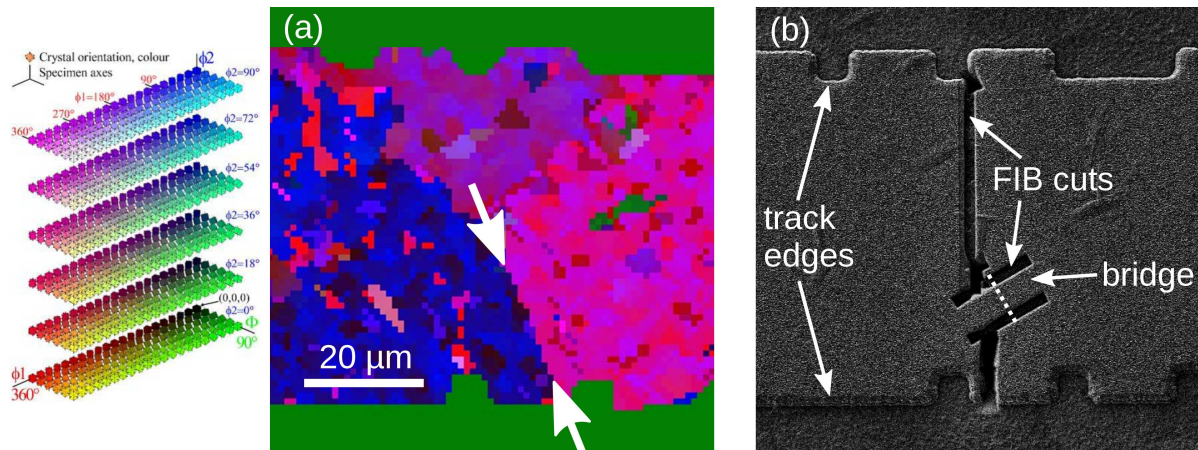


Figure 5.2.: (a) An EBSD map in Euler angle representation, showing a grain boundary (marked by arrows). The key on the left defines which colour represents which set of Euler angles, which give the local grain orientation. (b) FIB cuts were made to create a bridge in order to force the current across the GB in (a). The boundary position is indicated by white dots. Note the recesses in the track edges visible in both micrographs, used to correlate EBSD and FIB images. Both images have the same scale.

5.4. Electron Backscatter Diffraction

Electron Backscatter Diffraction (EBSD), an extension to an SEM, allows the localisation of grains in polycrystalline samples. Furthermore, the orientation of grains, and thus the grain boundary misorientation angles, can be determined. As it is a characterisation rather than a preparation technique, however, EBSD is discussed in more detail in Sec. 6.2. In the current chapter only its application to the isolation of GBs is described.

After patterning tracks typically 50 μm wide, using the pattern depicted in Fig. 5.1(b), the samples were cleaned thoroughly in an ultrasound bath using chloroform, acetone and isopropanol. Any residues of photoresist had to be removed in order to facilitate the EBSD pattern acquisition, which by its own is a challenging task on the rough surface of a coated conductor manufactured by a chemical process.

All EBSD maps presented in this thesis have been acquired by Susannah Speller, using a JEOL JSM6480LV microscope and HKL software.

An example of such a map is reproduced in Fig. 5.2(a), showing three grains and the corresponding boundaries, one of which was isolated subsequently.

5.5. Isolation of Grains and Grain Boundaries with a Focused Ion Beam

In this section first the general operating procedure of a *Focused Ion Beam microscope (FIB)* is discussed. This is followed by a description of how a FIB was used to isolate coated conductor grains and grain boundaries for this thesis.

5.5.1. Principle and Capabilities

FIB microscopes were originally developed for the semiconductor industry, like several other techniques which nowadays are also employed in thin film superconductor research and development, e.g. MOCVD (Sec. 4.4.2) and thin film processing (Sec. 5.3).

The basic concept of a FIB is derived from that of an SEM, but as the name suggests a FIB uses ions instead of electrons. Similar to an SEM it can be employed for imaging, but in addition to that a FIB is also capable of milling and deposition, making it a very powerful microfabrication tool. Among its benefits are the high resolution and the fact that almost every material can be visualised (without pretreatment like coating) and milled. In addition to that, a FIB offers a wide range of magnifications and has the advantage that it is a local process leaving the surrounding areas unaffected. A review of FIB microfabrication can be found in Ref. [175].

5.5.2. Basic System Setup

The main components are the ion column, the work chamber, the vacuum system, the gas system and the user interface.

In the ion column (shown schematically in Fig. 5.3) a liquid-metal ion source produces Ga^+ ions by field emission. Similar to an SEM the beam is then refined and condensed by an aperture and an electrostatic lens, below which the upper octopole is found (for stigmatism adjustment). A variable aperture allows the current to be set to different values in the range of picoamperes to nanoamperes. Another octopole rasters the beam over the sample surface, onto which it is focused by the second electrostatic lens.

The sample is mounted on a stage, which can be rotated. This allows one to mill and image in directions other than perpendicular to the sample surface. Both the ion column and the work chamber are under high vacuum. Different gases can be introduced

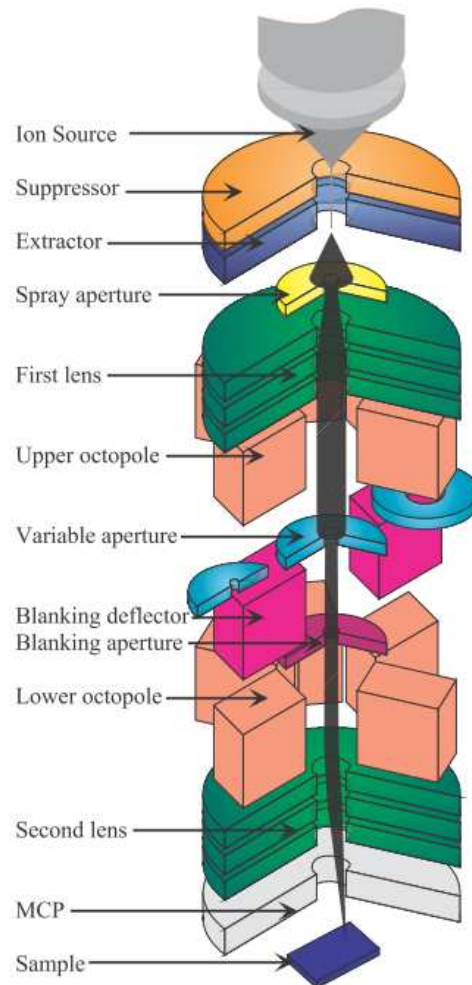


Figure 5.3.: Sketch of a FIB column [175].

in order to achieve more selective and faster etching or to deposit material.

Usually all operations except for sample mounting are controlled via a computer.

5.5.3. Imaging

When the ion beam hits the sample particles (neutral and charged atoms and secondary electrons) are sputtered off. The latter two species can be detected by a microchannel plate (MCP) via their charge in order to acquire images of the sample from the measured intensity as the beam is rastered over it. This is possible because different materials have different sputtering yields, and thus the number of sputtered particles changes as the beam moves over different parts of the sample. The best resolution which can be obtained

is below 10 nm.

A certain amount of Ga⁺ ions tends to be implanted, however, causing (potential) damage to the sample. This is aggravated at higher ion currents. There is, hence, a trade-off between image quality and sample degradation.

Newer systems often combine a FIB with an SEM. The imaging can be performed by the SEM, allowing more frequent (or even constant) imaging with negligible sample damage.

5.5.4. Milling

A FIB can be used to pattern samples by the removal of material in certain areas by rastering a high current beam across them. Significantly higher resolution than by conventional photolithography and broad beam ion milling can be achieved. Also, arbitrary patterns can be introduced into the sample, unlike conventional lithographic processes, which rely on pre-made masks. A FIB etch is very time consuming, however, if large volumes are to be taken away.

In order to know when a layer has been completely removed an “end point detection” method is employed. The secondary electron intensity vs. time is plotted in a graph in real-time; increases or decreases when the beam hits a different material give an indication as to when a certain layer has been milled through.

5.5.5. Isolation of Grains and Grain Boundaries

Cuts were made using a Zeiss Nvision 40 FIB/SEM system in order to obtain 4.5 to 5.0 μm wide bridges within a single grain or spanning a GB, as shown in Fig. 5.2(b). These bridges force the current across the single grain or boundary. They were positioned with high precision, which was possible because of the alignment marks in the track edges and inclusions in the film, which were visible on both EBSD and FIB images.

Only a few FIB images were taken of each bridge (with a low beam current ≤ 10 pA) in order to accurately align the ion beam. The milling process itself was controlled by SEM imaging only, avoiding sample degradation by Ga⁺ implantation.

Coated conductor grains and GBs have been isolated previously by Feldmann *et al.* [176, 83]. While their approach was also based on EBSD, they employed conventional lithography and broad beam ion milling for the entire sample preparation, including the

GB / grain isolation. The advantage of the approach in this thesis is that a FIB offers a significantly higher resolution when it comes to the positioning of the bridges. Consequently, it allows one to target specific grains and GBs more precisely. Additionally, an IBAD boundary has been isolated for this thesis, which would not be possible by a conventional technique, due to the small IBAD grain size.

Most of the FIB work (in particular the GB / grain isolation) was carried out by Gareth Hughes, who has access to an advanced FIB system. The author performed certain preparation work (e.g. surface treatment for the acquisition of the EBSD background signal and cuts used as alignment marks³) as well as sample cross-sectioning, using a FEI FIB200.

³Due to the small grain size of the IBAD-MOCVD coated conductor analysed, the alignment marks in the track edges were too large. Smaller marks by FIB had to be prepared, therefore.

6 Characterisation Techniques

In this chapter the different measurement and characterisation techniques employed for this thesis are introduced.

The most important of these is the setup used for critical current density measurements (Sec. 6.1). Its discussion is followed by sections on electron backscatter diffraction and x-ray diffraction. At the end of this chapter low-temperature scanning laser microscopy is discussed (Sec. 6.4).

6.1. Electrical Characterisation – the Measurement Setup

The transition temperatures T_c and critical current densities J_c of the samples in this thesis were obtained by four-terminal measurements, in which a current is applied across a track patterned onto the sample (see Chap. 5) while the voltage is measured.

These experiments were performed using a probe which is inserted into the VTI (variable temperature insert) of a cryostat with an 8 T magnet. The probe is (rather) unique, insofar as it consists of a *two-axis goniometer* which allows one to rotate the sample not only about one, but about two axes [177, 178]. Any desired orientation between magnetic field and sample can, therefore, be achieved.

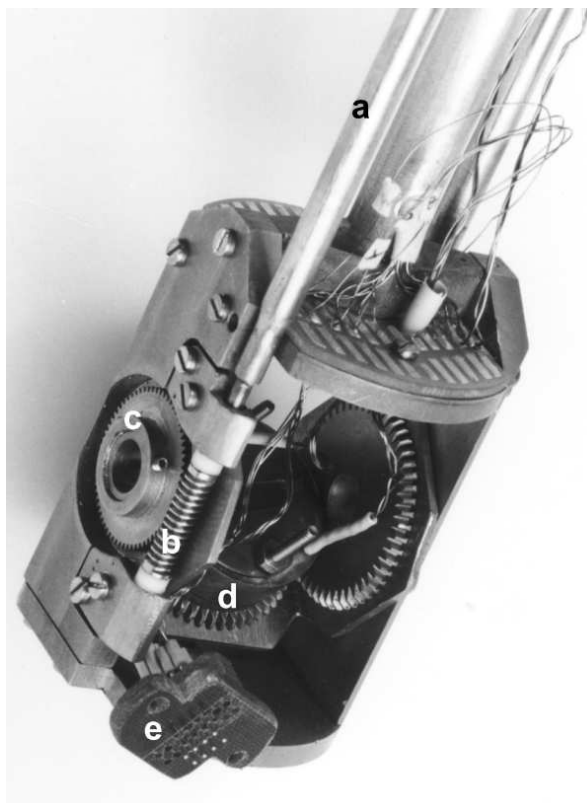


Figure 6.1:

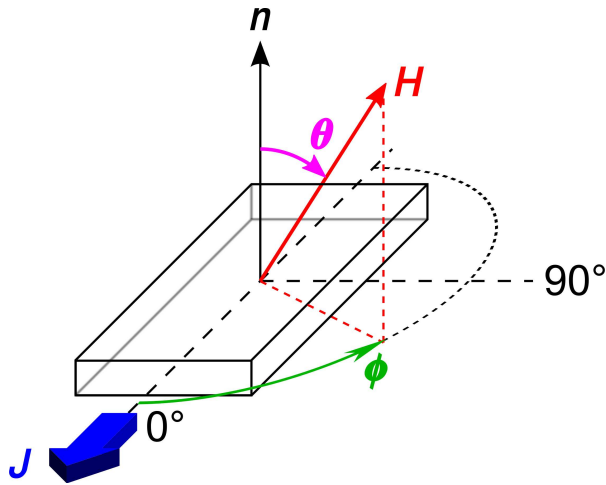
The two-axis goniometer. Indicated are the drive shafts (a), the worm gears (b), the drive gear (c), the copper block containing temperature sensor and heater element (d) and the tufnol block, in which the Pogo pins are mounted (e). (Image courtesy of John Durrell.)

6.1.1. Two-Axis Goniometer Probe

The probe consists of two units: an upper part with two stepper motors and the connectors for signal wires, temperature sensor and heater. The lower part is the rotator, where the sample is mounted. The two units are connected by a stainless steel tube, which also contains the wiring, and two drive shafts.

A photograph of the bottom unit of the probe is shown in Fig. 6.1. It consists of a yoke, which can be tilted about the first goniometer axis from a horizontal into a vertical position, described by the angle θ . A cylindrical copper block, acting as the sample stage, is mounted on the yoke. It can be rotated about its axis, given by the second angle ϕ . The copper block consists of two parts glued together with Stycast resin, with a constantan heater wire in between. The top part of the copper block has a hole in it which accommodates a Cernox temperature sensor providing reliable readings in the range from 3 to 300 K. The torque provided by the stepper motors is transferred to the yoke and the stage by the two drive shafts and two sets of worm gears and wheels.

The sample is placed on top of the copper stage, where it is held in place by twelve

**Figure 6.2:**

Definition of the out-of-plane angle θ and the in-plane angle ϕ between sample and applied magnetic field. The current direction J is indicated for the typical case where the track is parallel to the long edge of the sample.

Pogo pins, fixed in a tufnol block, which also provide the contacts for the current / voltage wires. Small pieces of indium between the pins and the sample's gold pads ensure good contact even if thermal expansion causes small movements of sample or pins.

All parts of the goniometer are made of brass to ensure even thermal contraction, except for the sample stage, the PTFE bearings and the worm wheels, which were manufactured from stainless steel.

The definition of the angles θ and ϕ is illustrated in Fig. 6.2.

6.1.2. Cryostat

The measurements were performed in an Oxford Instruments NMR cryostat with an 8 T magnet, which can operate in persistent mode. Liquid He is sucked into the VTI from a He bath by a vacuum, which is created by an external diaphragm pump and controlled by a needle valve. It then boils and reaches the sample space. The flow can be controlled by a second needle valve and the temperature of the VTI is regulated by a heater. During normal operation the VTI temperature is set to 5 K. A toroidal liquid nitrogen container around the He bath acts as a radiation shield.

6.1.3. Electronics

All electronic components of the measurement setup are controlled by a standard PC, running a LabVIEW program.

Current can be applied to the sample by one of two current sources: a Keithley 6221 (up to 100 mA) and a Keithley 2440 (up to 5 A). The voltage across the track is measured by a Keithley 2182A Nanovoltmeter. Current source and voltmeter can be connected to any combination of contact pins of the probe either manually through a matrix board or using a Keithley 3706 Switch, controlled by the measurement software.

The two control loops of a LakeShore 331 are used to regulate the temperature of both VTI and sample stage.

The two stepper motors are driven by a custom-built controller. As there is no feedback, position indicators on top of the probe directly connected to the drive shafts give the actual orientation of the yoke and the copper block, which can be compared to the values used by the LabVIEW program. This allows one to detect if the motors have “lost” steps, which can occur when wires get entangled and jam the goniometer.

Both current sources, the nanovoltmeter, the temperature controller and the magnet power supply are connected to the measurement computer via IEEE-488. The stepper motor controller is addressed via the RS-232 port of the PC using a proprietary protocol.

6.1.4. Measurements

All operations other than sample mounting and He flow control can be performed from a computer.

T_c Measurements

The critical temperature can be obtained by measuring the resistance vs. temperature. An ac current is applied (in order to eliminate dc offsets) while the voltage is measured. T_c can be deduced from the resulting $R(T)$ curve, an example of which is shown in Fig. 6.3(a), usually as the onset of zero resistance.

J_c Measurements

In order to obtain the critical current density from a *transport measurement* the current applied to a track is increased in steps, while the voltage is recorded. I_c is determined from the observed voltage rise in the region of the transition as the current at a certain criterion voltage. A typical $V(I)$ -curve is shown in Fig. 6.3(b). The measurement setup

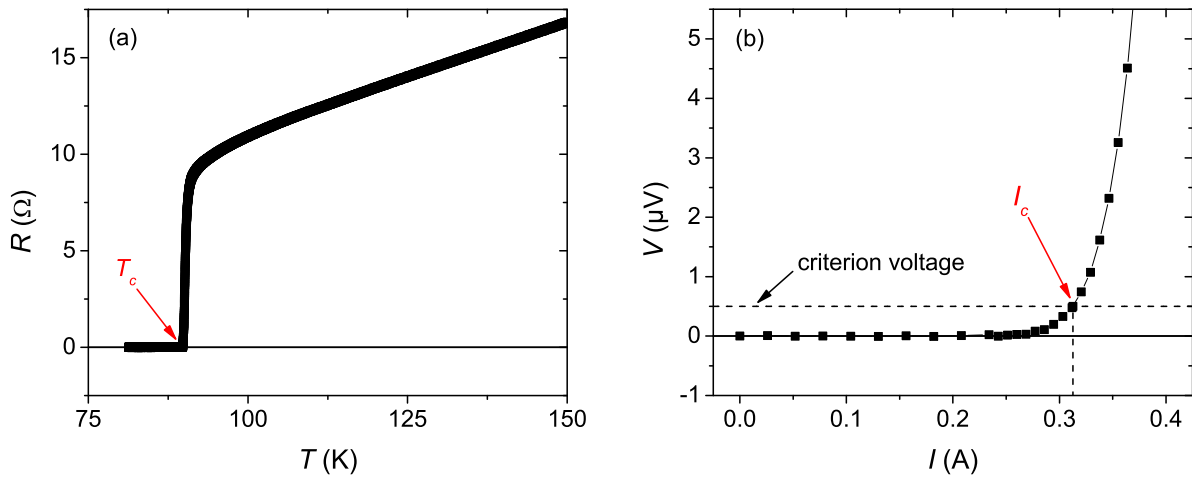


Figure 6.3.: Measurements of (a) resistance vs. temperature to determine T_c , (b) voltage vs. current to obtain I_c .

employed for this thesis can apply current in pulses in order to reduce sample heating due to ohmic losses in the contacts and wires.

Sequences can be written in a LabVIEW program, which are then carried out without user intervention. In this way it is possible to collect large amounts of data by measuring successive $V(I)$ -curves while one or more parameters are changed stepwise (T , H , ϕ or θ). Typical measurements include angular scans, in particular $J_c(\theta)$ at a fixed ϕ or $J_c(\phi)$ at a fixed θ , at a given field and temperature. J_c can also be measured vs. magnitude of field or temperature.

6.1.5. Accuracy and Errors

The angular positioning of the sample stage is achieved with an accuracy of about 0.02° . The sample temperature is stable within ~ 20 mK.

The noise of the measured voltage depends on various factors (e.g. the quality of the contacts, thermal stability and magnitude of field). In optimum conditions the noise level is ~ 20 nV.

6.2. Electron Backscatter Diffraction

A Scanning Electron Microscope (SEM) can be equipped with an *Electron Backscatter Diffraction (EBSD)* detector. EBSD is a powerful technique for phase identification and

crystallographic orientation analysis. For this thesis the latter capability was employed to obtain maps showing the grains and their misorientations (see Sec. 5.4). In the present section a brief introduction to EBSD itself is given. A more detailed discussion can be found in Refs. [179, 180].

6.2.1. Basic System Setup

The sample is mounted on a stage tilted by $\sim 70^\circ$ from the horizontal. This tilt is a key feature: electrons hit the sample at a relatively low glancing angle, which leads to a high yield of backscattered electrons with a sharp energy spectrum. These electrons form a diffraction pattern on a phosphor screen, which is then digitised by a CCD camera.

6.2.2. Formation of Diffraction Patterns

While the exact image formation is a very complicated process, its basic principle can be explained in simple terms. When the incident electron beam hits the sample, electrons scatter inelastically. The interaction volume, the size of which is determined by the beam spot size, can be thought of as a divergent source of electrons close to the sample surface. As shown in Fig. 6.4 electrons can then be reflected by the crystal planes, with maximum intensities at angles satisfying the Bragg equation

$$n\lambda = 2d \sin \theta, \quad (6.1)$$

where n is an integer, λ the electron wavelength, d the lattice plane spacing and θ the angle between incident electrons and atomic planes. Since diffraction occurs at both the front and the back of the planes two cones are formed. Due to the low wavelength of electrons it follows from Eq. (6.1) that these cones are very flat, with values of θ typically only 1° to 2° . Consequently, two almost straight parallel lines are observed on the phosphor screen (the *Kikuchi band*). A typical pattern formed by an ensemble of such bands can be seen in Fig. 6.5.

The centre of each Kikuchi band corresponds to the intersection between the crystallographic plane which was responsible for its formation and the screen. Consequently, the location of the bands is directly related to the orientation of the unit cells, which can be exploited to determine crystal orientations. To this end the angles between different planes are deduced from the position of the observed Kikuchi bands. Comparing these

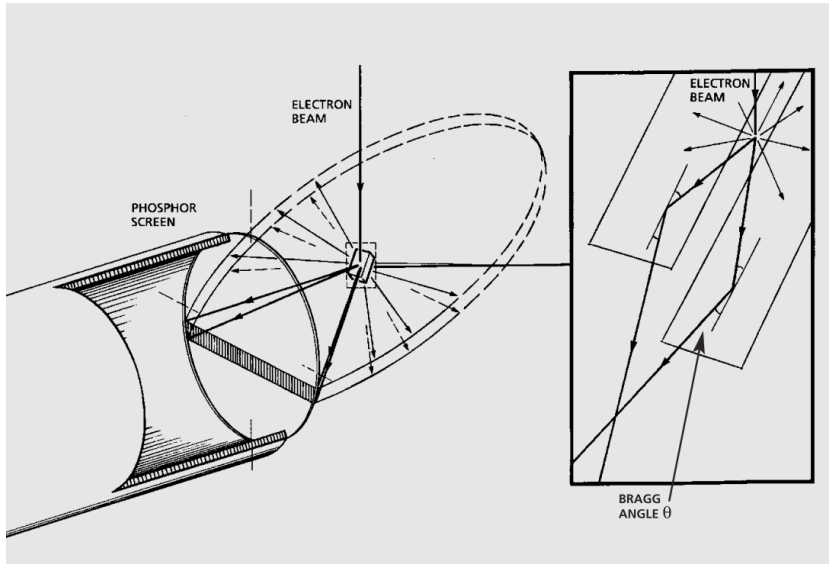


Figure 6.4: The diffraction process leading to Kikuchi bands on a phosphor screen [180].

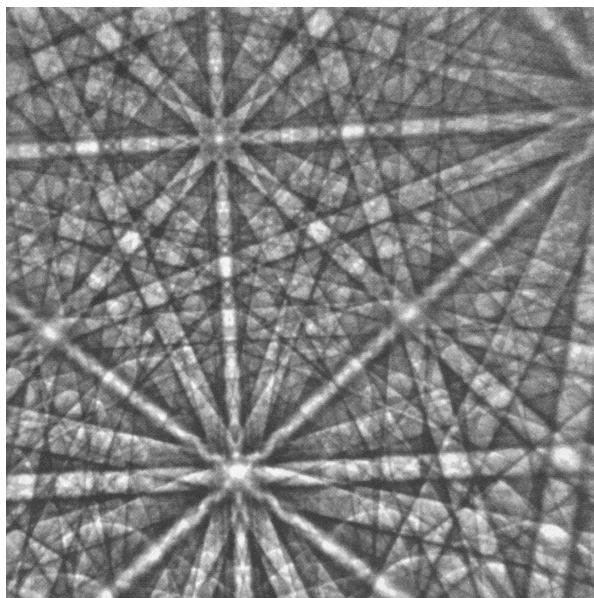


Figure 6.5: Kikuchi pattern created by backscattered electrons [181].

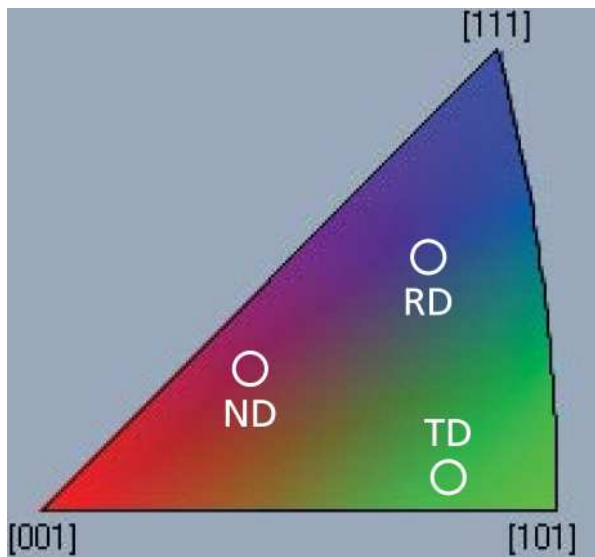


Figure 6.6:

An inverse pole figure. The orientations between the unit cell and the ND, RD and TD are indicated for one specific point in an exemplar EBSD map. The corresponding colours would then be used at this coordinate in the ND, RD and TD map, respectively [180].

angles with the known values of the crystal structure of the sample allows Miller indices to be assigned to each Kikuchi band and the orientation of the crystal to be calculated.

6.2.3. Crystal Orientation Mapping

Consecutive diffraction patterns can be recorded while the electron beam is scanned across the sample surface. If the crystal orientation is then deduced for each point, a (mis)orientation map can be drawn. To this end the crystallographic directions with respect to the unit cell are determined which are parallel to the sample's normal (ND), rolling (RD) and transverse (TD) directions. Using an inverse pole figure, like the one depicted in Fig. 6.6, these directions can be translated into colours, allowing one to compose ND, RD and TD maps. Alternatively, a map can be drawn where the colours represent the three Euler angles.¹ Figure 5.2(a) is an example of such a map.

In EBSD maps areas with the same orientation are displayed in the same colour, thus showing the shape of the grains and allowing one to deduce the angle of the corresponding grain boundaries.

¹The Euler angles ϕ_1 , Φ and ϕ_2 are a different way to describe crystal orientations.

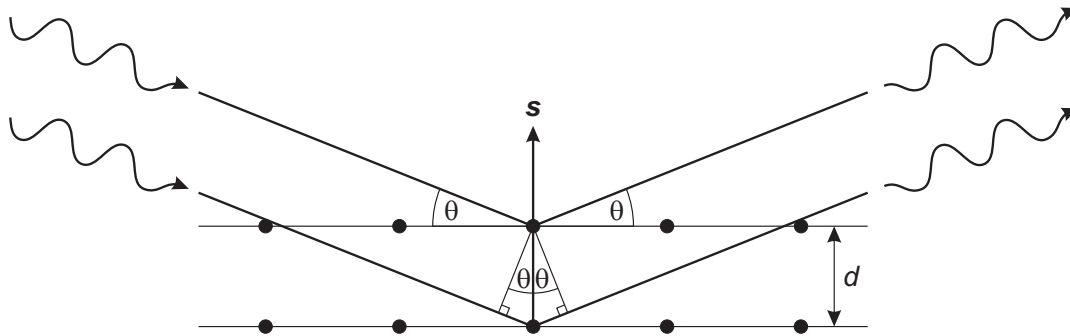


Figure 6.7.: X-Rays are reflected by lattice planes. Constructive interference occurs at the Bragg angle θ . $s = 1/d$ is the scattering vector (after [182]).

6.3. X-Ray Diffraction

X-ray Diffraction (XRD) can be used to identify phases and to determine lattice parameters, crystal orientations and strain in a sample. It is even possible to obtain the coordinates of atoms in the unit cell (by Rietveld refinement). For this thesis XRD was used to determine the sample texture, i.e. the level of grain alignment. Due to the large beam size, the information obtained is a statistical average of an area covering many grains, unlike EBSD, which measures the *local* orientation.

6.3.1. Diffraction of X-Rays

If x-rays are scattered on crystal planes, constructive interference occurs at angles satisfying the Bragg equation (6.1), as shown in Fig. 6.7.

6.3.2. Basic System Setup

X-rays are generated in an x-ray tube by accelerating electrons towards a target typically made of Cu. This causes inner atomic shells to be ionised; electrons from a higher shell subsequently occupying these positions leads to the emission of x-rays of a characteristic frequency.

The sample is mounted on a stage and the x-ray intensity is measured by a detector. Depending on the type of diffractometer used either sample and detector or source and detector can be rotated in order to achieve geometries where the Bragg condition is fulfilled.

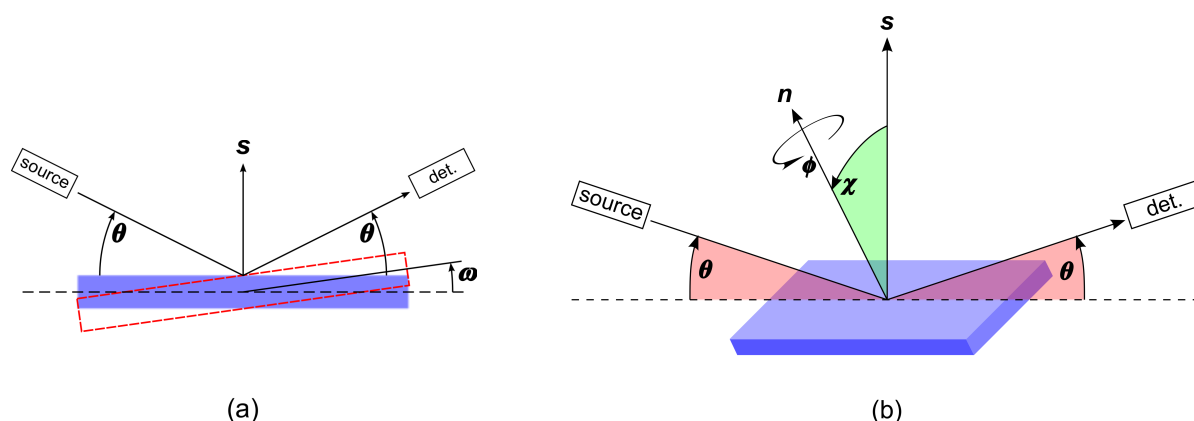


Figure 6.8.: Geometries of (a) rocking curve and (b) pole figure measurements. Note that in (b) s is in a plane with incident / scattered beam, while the sample normal n is tilted away from that plane by the angle χ .

6.3.3. Texture Measurements

Both the out-of-plane and the in-plane grain alignment can be quantified by XRD.

Out-of-Plane Texture

In order to obtain a *rocking curve* source, sample and detector are oriented such that the Bragg condition for a certain reflection is fulfilled. The sample is then rotated (“rocked”) in ω while the intensity of the scattered beam is measured with source and detector remaining at a fixed angle relative to each other [see Fig. 6.8(a)]. The width of the recorded curve is related to the out-of-plane texture. It is broad if grains are highly misoriented, whereas perfectly aligned samples give a very sharp peak.

In-Plane Texture

From a *pole figure* the in-plane alignment can be determined. A texture goniometer is employed, which allows one to rotate the sample stage about two axes (described by ϕ and χ), as sketched in Fig. 6.8(b). The diffractometer is set up such that θ satisfies the Bragg condition for a set of atomic planes which are *not* parallel to the sample surface. Measurements are then performed while the stage is rotated in ϕ (“ ϕ -scans”, usually from 0° to 360°). After each scan χ is increased.

The dependence of the intensity on ϕ and χ can be plotted as a pole figure. The reflection due to a lattice plane with a four-fold symmetry in a sample with perfectly

aligned crystals gives four sharp peaks (or *poles*) at symmetric positions in the pole figure. The higher the misorientation is, the broader are these maxima.

6.4. Low-Temperature Scanning Laser Microscopy

A spatially resolved technique to investigate properties of HTS is *Low-Temperature Scanning Laser Microscopy (LTSLM)*, in which a laser beam is rastered over the sample [183]. Unlike magneto-optical imaging, which measures the local magnetic flux density (see Sec. 3.4.5), LTSLM probes the local electric field; hence the two techniques can be considered as being complementary.

6.4.1. Basic System Setup

The components of a typical scanning laser microscope are shown in the schematic in Fig. 6.9. The beam generated by a laser diode first reaches the optomechanical module, where two scanning mirrors allow its direction to be adjusted in two dimensions. A system of lenses and collimators focuses the laser light onto a small spot on the sample. The latter is placed on a cold stage in a cryostat with a glass window through which the beam can enter.

6.4.2. Image Formation

Where the laser beam hits the sample heating leads to a local nonequilibrium in the material's electronic system, which also affects its superconducting properties. In dc voltage contrast mode the track to be measured is biased by a constant current $I_b \gtrsim I_c$, while the voltage across it is measured (at $T < T_c$). The local reduction of J_c caused by the laser beam leads to a voltage response δV , the amount of which depends on the properties of the material underneath the beam.² By recording δV while the beam is rastered over the sample a two-dimensional map can be obtained, in which higher intensities are related to inferior superconducting properties (e.g. due to grain boundaries). The interpretation of these maps is not trivial, however; in several experiments it was found that δV was highest in the close vicinity of a defect, rather than on it. This is

²Note that this is different from a transport measurement (Sec. 6.1), where J_c is obtained from $V(I)$ -curves. It is possible, however, to deduce J_c from the LTSLM voltage response [184].

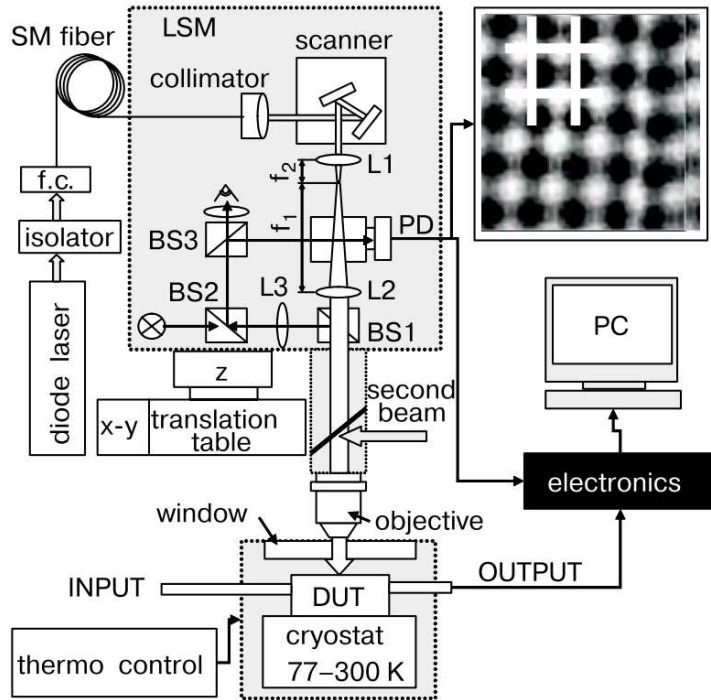


Figure 6.9: Setup of a scanning laser microscope [183].

due to the fact that currents percolate around regions of reduced J_c and therefore areas bordering the defect, which carry an increased current, are particularly sensitive to the laser beam (see Sec. 9.1). The achievable resolution is given by the spot size and thermal diffusion in the sample; usually it is between 1 and 4 μm .

Other scanning modes include measuring the light reflected by the sample or the thermoelectric voltage (“thermo-power”) due to heating by the beam (at $T > T_c$). The latter is related to the out-of-plane grain orientation, which allows grains to be identified.

Part III.

Results

7 Isolated Grain and Grain Boundaries in MOD CCs

One of the main objectives of this thesis was the isolation of grain boundaries in coated conductors. In this chapter results are presented which were obtained on single GBs and a single grain in samples produced by American Superconductor's Metal-Organic Deposition process.

The first section is dedicated to a brief review of previous studies on grain boundaries in CCs. In Sec. 7.2 TEM and HR-EBSD images are presented. Following this is the main part of the present chapter, consisting of critical current density measurements for magnetic fields applied perpendicular to the film plane and swept in the plane (Sec. 7.3).

7.1. Previous Studies

While grain boundaries in HTS in general are discussed in Sec. 3.4, here the focus is on GBs found in coated conductors, in particular in Metal-Organic Deposition films.

7.1.1. Texture and Grain Boundary Morphology in MOD Tapes

The most comprehensive study on the texture of MOD films and the microstructure of their GBs is that by Feldmann *et al.* [185]. They investigated samples grown by MOD and PLD on the same RABiTS tape with the same buffer architecture. Using EBSD

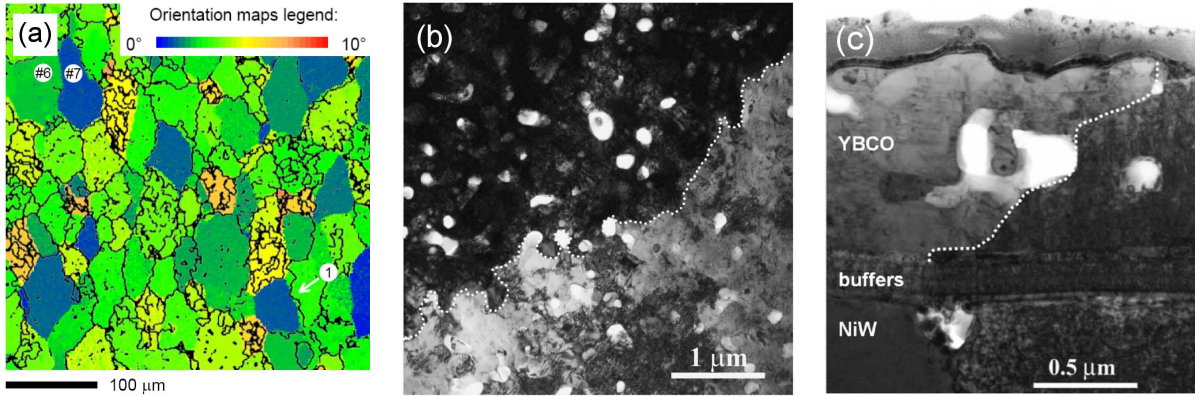


Figure 7.1.: (a) Out-of-plane orientation EBSD map of an YSZ buffer layer with MOD-YBCO grain boundaries indicated by lines. Note the YBCO GB meandering and their local shift with respect to the YSZ boundaries (adapted from [185]). (b) Plan-view and (c) cross-sectional TEM images, showing the GB meandering (adapted from [83]).

and ion milling they were able to establish a depth profile of grains and GBs from the superconducting layer through the buffer stack into the Ni-W substrate.

As regards the texture, an improvement of the out-of-plane alignment was found from the Ni-W to the YSZ buffer layer. The YBCO layer deposited by MOD exhibited a further enhancement in the out-of-plane texture, unlike the PLD film which replicated the YSZ alignment. Only minor improvements of the in-plane grain orientation were found for the buffer and MOD-YBCO layers with no improvement for the PLD-YBCO layer. Furthermore, the MOD film showed a sub-grain structure (i.e. smaller grains within YBCO grains defined by the template grains), which was more pronounced for grains with a large out-of-plane tilt.

While PLD grain boundaries were found to be well aligned with the buffer GBs and planar through the entire thickness of the YBCO layer, MOD boundaries showed a different morphology. In films above a certain thickness they *meandered* both along their length and through the film thickness, as can be seen in the EBSD map and the TEM images in Fig. 7.1. In some cases the position of the YBCO GB $0.2\ \mu\text{m}$ above the buffer layer–YBCO interface was displaced laterally by over $10\ \mu\text{m}$ compared to the position of the corresponding buffer GB. This is due to the meandering and possibly also due to a certain amount of overgrowth of buffer GBs by the YBCO grains, which is related to the lamellar growth mode of MOD films.

It is because of this meandering that a GB with an out-of-plane component changes its

type along its length, i.e. twist becomes tilt and vice versa. Consequently, a meandering GB will never be a pure tilt- or twist-boundary (unless both grains are perfectly c -axis aligned and a [001]-tilt boundary is observed).

It shall be noted that films grown from BaF₂-based YBCO precursors, similar to those employed in the study above [185], but deposited by physical vapour deposition (PVD), rather than MOD, were also found to have meandering GBs [186, 187]. This appears to be a common feature of CCs produced by *ex situ* methods involving lateral grain growth.

7.1.2. Transport Measurements on Isolated Grain Boundaries

Coated conductor grain boundaries have been isolated previously by Feldmann *et al.*, who employed EBSD and conventional photolithography / ion milling. They found that J_c of GBs in 300–400 nm thick films grown by the BaF₂ technique and MOD on RABiTS showed the exponential decrease with the misorientation angle θ_{mis} known from bicrystal boundaries [176]. Samples of this thickness exhibit no significant GB meandering even if they are produced by *ex situ* techniques [187]. Feldmann *et al.* concluded that the considerably lower critical current density observed in full-width samples, with respect to isolated grains, was caused by a current limitation by the boundaries.

In a more recent study [83] Feldmann *et al.* investigated the properties of grain boundaries isolated in thicker films (600–800 nm) grown by both PLD and MOD on the same RABiTS tape and buffer stack. Whereas $J_c(\theta_{\text{mis}})$ of the PLD GBs again followed an exponential law, the MOD GBs showed significantly enhanced critical current densities and no clear dependence of J_c on θ_{mis} , as reproduced in Fig. 7.2(a). Unlike planar PLD boundaries, those in MOD films of such a thickness are known to meander. Feldmann *et al.*, therefore, attributed the better performance of MOD boundaries to two factors related to the morphology of meandering GBs:

Larger cross-sectional area: Due to the meandering the total GB area is enhanced, leading to a higher I_c of the interface even if its (microscopic) j_c is comparable to that of a PLD boundary.

Suppression of vortex channelling: In the case of a meandering boundary vortices cannot lie in the GB plane over significant lengths, which for planar boundaries was found to lead to a J_c suppression due to vortex channelling [82]. Due to

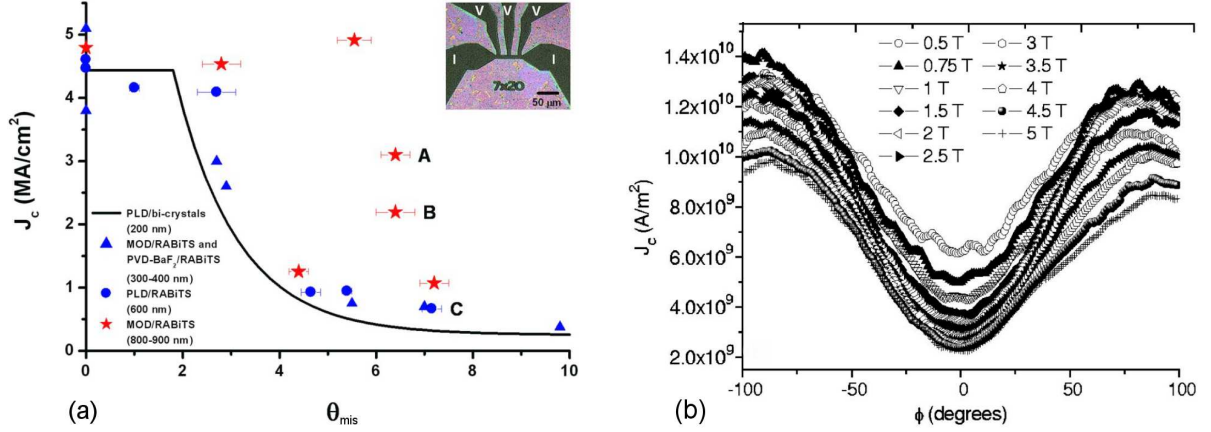


Figure 7.2.: (a) Isolated GBs in thick MOD films (stars) showed superior values of J_c (self-field) compared to boundaries which do not meander (adapted from [83]). (b) In-plane scans on an MOD GB [188] [see Fig. 7.8 for a definition of ϕ , note that there is a 90° offset; measurements in both (a) and (b) were performed at $T = 77$ K].

the boundary geometry in (thick) MOD films weakly pinned Abrikosov Josephson vortices in the GB region extend over short lengths only, while the rest of the Abrikosov flux line is pinned strongly in the grains on either side of the boundary.

This result is very important for the optimisation of CCs, as it implies that GB properties can be significantly enhanced by tuning the growth mode to achieve strong meandering, rather than employing complicated doping of the boundaries (e.g. by Ca [189]).

In measurements where the magnetic field was swept in the film plane Durrell *et al.* [188] showed that J_c of an isolated MOD boundary behaves in a very similar way as that of a single grain [see Fig. 7.2(b)]. Its strong field dependence is in contrast to that of a PLD boundary, which showed only a weak suppression of J_c with increasing H . These results can also be explained by the beneficial properties of meandering GBs and the suppression of vortex channelling.

7.1.3. Hysteretic Behaviour of $J_c(H)$

It was first shown by Evetts and Glowacki [113] that YBCO wires exhibit an irreversible dependence of J_c on applied field. If H is increased beyond a certain field and then reduced to 0 again, the branch for decreasing field differs from that for increasing field, as depicted in Fig. 7.3(a). This hysteretic behaviour was explained by flux trapped in

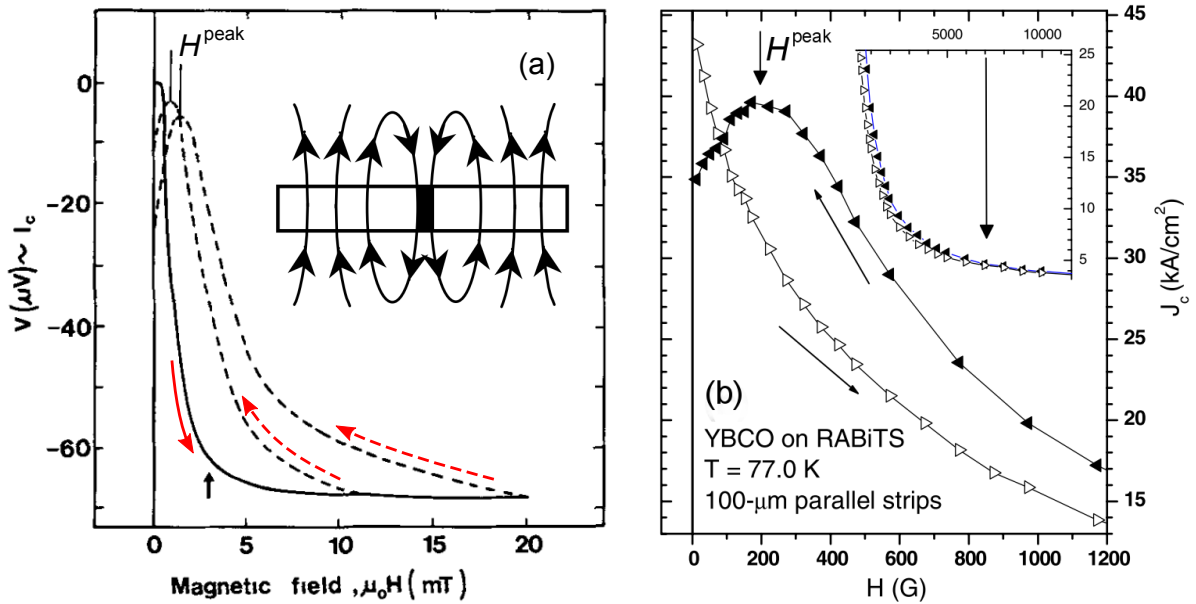


Figure 7.3.: (a) In YBCO wires hysteresis in $J_c(H)$ was found for increasing and decreasing fields (adapted from [113]). This can be explained by flux trapped in grains (in white) which cancels the flux in a grain boundary (in black) [112]. (b) Coated conductors show a similar behaviour (adapted from [190]).

the grains, which, when it is not supported by an applied field anymore, leads to an inverse flux in grain boundaries, locally cancelling the (residual) applied field. As a consequence, maximum J_c is found at an applied field $H^{\text{peak}} > 0$.

The same effect was also observed in angular transport measurements on thin film bicrystal boundaries¹ [112] as well as in magnetic measurements on rings patterned across bicrystal GBs² [114] and on coated conductors [191]. Recently Gapud *et al.* [190] reported hysteresis in transport measurements on coated conductors [see Fig. 7.3(b)]. They patterned $\sim 100 \mu\text{m}$ wide tracks onto IBAD and RABiTS samples, thus reducing the number of percolative current paths and enhancing the impact of grain boundaries on the overall J_c . In contrast to measurements performed on full-width / unpatterned samples, hysteresis evolved in the narrower tracks. It was more pronounced in the case of the RABiTS conductor, which is expected to be more strongly GB dominated than the IBAD tape.

¹See also page 47.

²See also page 49.

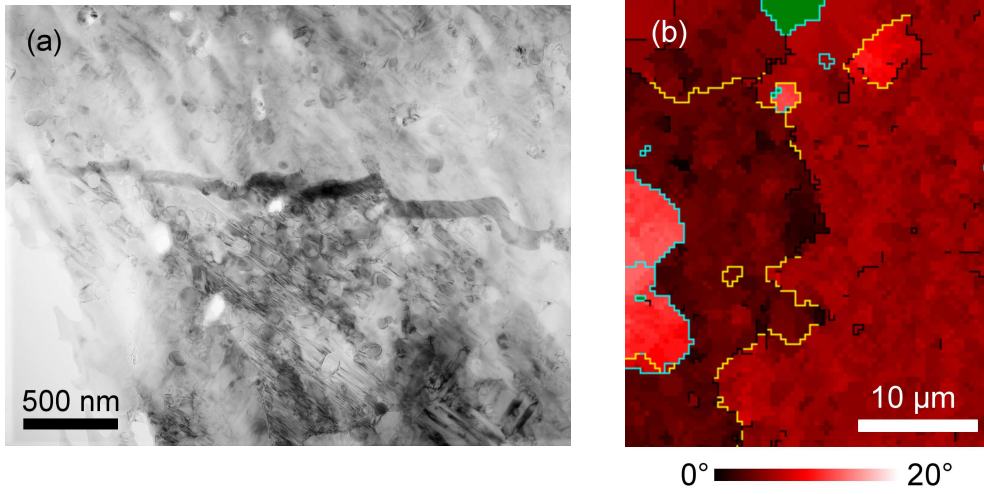


Figure 7.4.: Plan-view (a) TEM and (b) HR-EBSD images of grain boundaries.

7.2. TEM and HR-EBSD

Transmission electron microscope (TEM) and high-resolution electron backscatter diffraction (HR-EBSD) images of MOD samples were obtained in order to investigate the microstructure of their grain boundaries. The samples were taken from the same batch as those used for transport measurements.

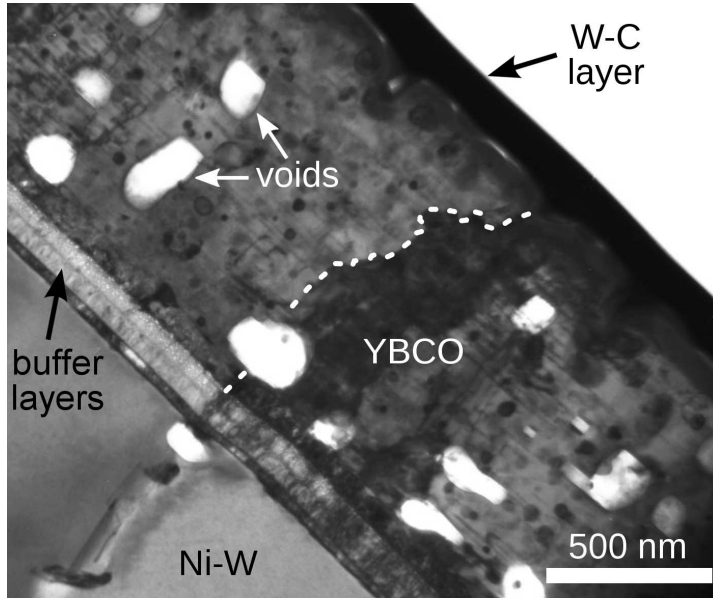
The TEM images presented in this section were acquired by Suman-Lata Sahonta (plan-view) and Sergio Lozano-Perez (cross-section). The FIB preparation of the cross-section had been carried out by Gareth Hughes. The HR-EBSD map was obtained by Susannah Speller.

The architecture of the samples investigated in this chapter can be found in Sec. 4.5.

7.2.1. Plan-View

A TEM image of a grain boundary, viewed along the [001] zone axis, is presented in Fig. 7.4(a). The GB is visible as a dark band approximately 100 nm wide. Its apparent width is due to the boundary being inclined with respect to the c -axis; its location at the bottom of the film differs from that at the top. The GB shows the expected meandering along its length.

The meandering was confirmed—on a different length scale, however—by a high-resolution electron backscatter diffraction image, which is shown in Fig. 7.4(b).

**Figure 7.5:**

A cross-sectional TEM image of one of the boundaries which has also been examined by transport measurements (GB4, see Table 7.1). The GB is indicated by a dashed line. The W-C layer was deposited during sample preparation.

7.2.2. Cross-Section

A cross-sectional TEM image was acquired of one of the boundaries previously measured by a transport current technique (labelled GB4, see Table 7.1). The TEM sample had been prepared using a FIB after the transport measurements.

The through-thickness meandering of boundaries in MOD films as reported previously [185, 83] was confirmed in GB4, as can be seen in the image in Fig. 7.5. The two neighbouring grains are clearly visible thanks to the diffraction contrast achieved by aligning a zone axis of one of the grains with the electron beam. Whereas the YBCO GB lines up with the substrate GB more closely than the boundary presented in Ref. [83] [see Fig. 7.1(c)], its morphology is nevertheless very different from the planar boundaries characteristic of PLD films. The boundary meanders through the thickness of the film with amplitudes of less than 50 nm. On the film surface the GB is displaced by about 300 nm from its location directly above the grain boundary in the buffer layer.

Stacking faults parallel to the ab -planes are present in the YBCO layer, separated from each other by 20 to 50 nm along the c -axis. Several voids, between 50 and 300 nm in diameter, are visible. Pores similar to these voids have been reported previously in TFA-MOD samples [192, 193, 194]. The surface of the film is relatively rough, which leads to a variation in thickness at different positions of almost 100 nm. The buffer layer–YBCO interface on the other hand is very smooth. The asymmetry of in-plane J_c measurements at low fields can be explained by this difference in roughness between the

Table 7.1.: Summary of the properties of the isolated grain and GBs: crystallographic misorientation angles θ_{mis} , self-field J_c and in-plane crossover field B_{cr} at maximum Lorentz force (both at $T = 77.35$ K). The scatter in θ_{mis} is due to grain mosaicity, rather than measurement error.

Sample	θ_{mis} (deg)	$J_c(\text{sf})$ (A m^{-2})	B_{cr} (T)
IG	(grain)	6.08×10^{10}	–
GB1	4.9 ± 0.4	4.98×10^{10}	< 0.25
GB2	5.7 ± 0.9	4.36×10^{10}	0.75
GB3	6.5 ± 1.3	2.17×10^{10}	3
GB4	5.1 ± 1.3	2.76×10^{10}	1

two opposed YBCO surfaces (see page 111).

7.3. Critical Current Densities

Four individual grain boundaries (labelled GB1 – GB4) and one single grain (IG, for *intragranular*) were isolated for this investigation as described in Sec. 5.5 and their key parameters are listed in Table 7.1. EBSD maps also showed a certain amount of mosaicity within each grain, as in the upper grain in Fig. 5.2(a) for instance. The misorientation angles θ_{mis} are, therefore, averages of values obtained at several points along the length of each GB.

The transition temperatures of GB1 – 3 and the single grain lay between 90.8 and 91.8 K, determined as the onset of zero resistance. These values are only slightly lower than T_c of a polycrystalline sample which had not been prepared by FIB (see Sec. 8.3), hence it can be assumed that the FIB patterning did not cause any significant damage. GB4 showed a lower transition temperature (between 88.3 and 89.5 K in separate measurements), which might be related to its different behaviour in angular measurements (see Sec. 7.3.2).

A $0.5 \mu\text{V}$ voltage criterion was employed to determine I_c from $V(I)$ -curves, which appeared a reasonable value given the observed level of noise. A nominal thickness of the superconducting layer of 800 nm was used to calculate J_c from I_c , however a certain local variation in thickness was seen in the cross-sectional TEM image (see Fig. 7.5). Unless stated otherwise the J_c measurements were performed at $T = 77.35$ K.

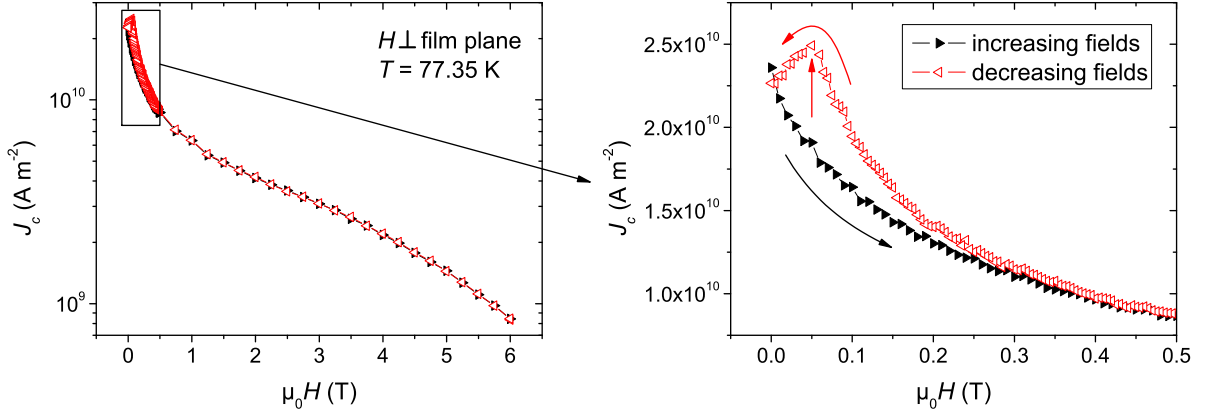


Figure 7.6.: The critical current density of GB3 vs. fields applied perpendicular to the film plane. Hysteretic behaviour is seen. The field H^{peak} is indicated by a vertical arrow.

7.3.1. Fields Perpendicular to the Film Surface

Measurements of the critical current density were performed for fields applied perpendicular to the film plane. As an example the results obtained from GB3 are plotted in Fig. 7.6. At low H hysteretic behaviour was found for increasing and decreasing fields³ with a maximum in J_c for decreasing fields at $H = H^{\text{peak}} > 0$, similar to what has been reported by Gapud *et al.* [190] (see Sec. 7.1).

Hysteresis was observed in all four grain boundaries and the isolated grain. In the case of the latter this is surprising, as the explanation for hysteresis is flux trapped in the grains, reducing the magnetic flux in the *boundaries*; one would, therefore, expect $J_c(H)$ of a *grain* to be reversible. The observed behaviour of the single grain could be related to growth grain boundaries or twin boundaries within the isolated grain.

While the single grain did show a certain hysteresis, its extent is smaller than that of the GBs. This can be seen in Fig. 7.7, where the relative increase due to the hysteresis $[J_c(H^-) - J_c(H^+)]/J_c(H^+)$ is plotted vs. field. $J_c(H^+)$ and $J_c(H^-)$ are the critical current densities for increasing and decreasing fields, respectively. The relative increase has a maximum⁴ at $H = H^{\text{max}} > 0$. The value of H^{max} shows no correlation with the GB misorientation angle θ_{mis} . The relative J_c enhancement, however, clearly increases

³The sample had been warmed up to $T > T_c$ and was then zero-field cooled to 77.35 K before this experiment was performed in order to expel any flux trapped in the grains from previous measurements.

⁴In general it was found that $H^{\text{max}} > H^{\text{peak}}$, in agreement with Ref. [190].

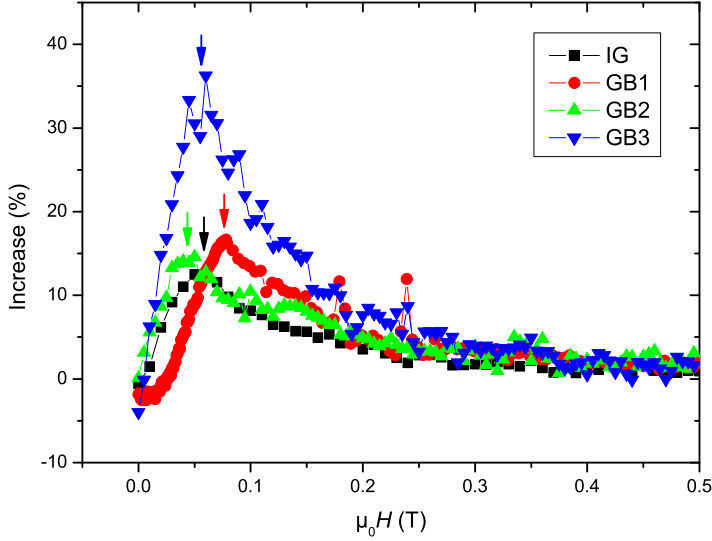


Figure 7.7: The relative increase in J_c due to the hysteresis for increasing and decreasing fields. The different fields H^{\max} are indicated by arrows.

with the misalignment. It is smallest for the grain and most pronounced for the boundary with the strongest misorientation (GB3). This is consistent with the fact that in Ref. [190] a RABiTS tape, which can be expected to be more GB limited, showed a significantly larger relative enhancement than an IBAAD tape, which is mainly governed by IG properties.

If one presumes that for the decreasing field branch at $H = H^{\text{peak}}$ the trapped flux in the grains cancels the applied field in the GB completely, the difference between $J_c(H^+)$ and $J_c(H^-)$ at this field is a measure for the decrease of the grain boundary's critical current density with increasing field. As a higher grain misorientation leads to a weaker field dependence, however, this is not consistent with the above observation, which indicates a stronger field dependence for GBs with a higher misalignment.

GB1 and GB3 were also analysed at $T = 65$ K and 85 K. These measurements confirmed the previously reported increase of H^{peak} with decreasing temperature [190], explained by enhanced flux pinning in the grains at lower T .

7.3.2. Fields In-Plane

The critical current densities of the isolated grain boundaries and the single grain were measured for magnetic fields swept in the plane of the films. As can be seen in the sketch in Fig. 7.8, this corresponds to a rotation in ϕ with $\theta = 90^\circ$ held constant. At $\phi = 0^\circ$ the (macroscopic) current direction and the applied field are parallel to each other, leading to a minimum in Lorentz force, hence this field orientation is termed “force free (FF)

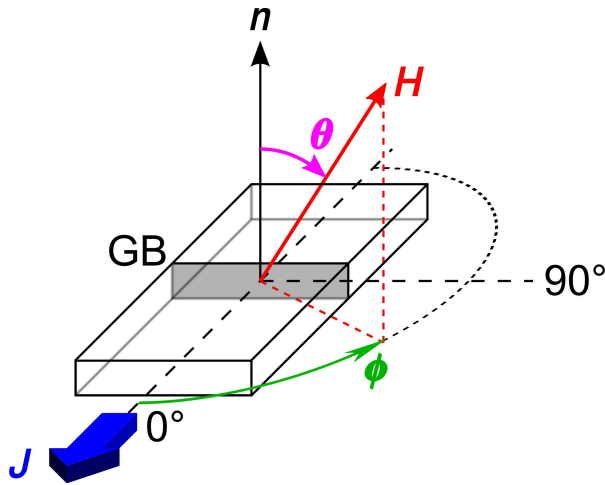


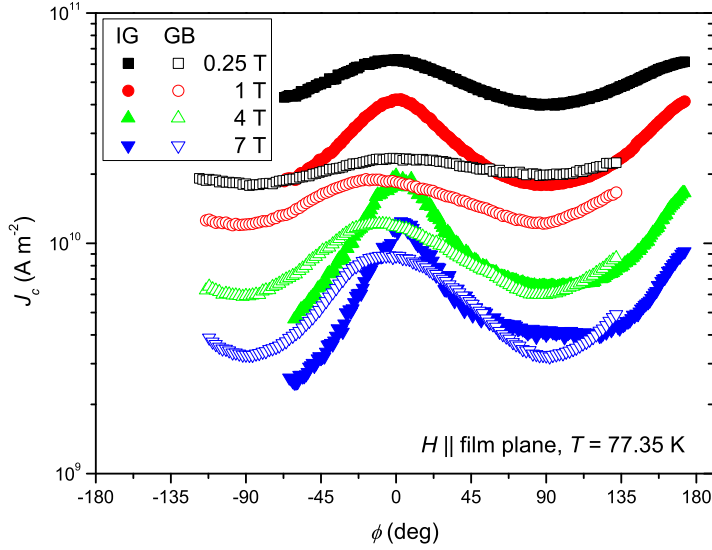
Figure 7.8: Definition of the angles ϕ and θ for a measurement on an isolated grain boundary. The outlined track represents the bridge patterned by FIB.

configuration". At $\phi = \pm 90^\circ$, on the other hand, F_L reaches a maximum. It needs to be borne in mind that the structure of the flux line lattice does not change, as the field is always oriented in the same way with respect to the ab -planes, regardless of the value of ϕ [195].

In-plane measurements are of use for two reasons. Firstly, in coils the strongest component of the magnetic field is parallel to the the tape plane, hence knowing the behaviour of J_c for this geometry is invaluable for applications. Secondly, as will be shown in this and the following chapters, the variation of J_c when the magnetic field is swept in the film plane allows one to draw conclusions on the flow of microscopic currents in the sample.

Figure 7.9 shows $J_c(\phi)$ (also termed " ϕ -scans") of the isolated grain and one grain boundary (GB3) at $T = 77.35$ K. The most striking feature is that at low fields J_c of the GB is suppressed significantly with respect to the grain, whereas at high fields they roughly overlap. This behaviour is consistent with the crossover from GB to grain limited critical current density for $H \perp$ film plane reported previously in several studies [109, 196, 197, 83].

Upon closer inspection, however, it can be seen that at angles around the force free orientation ($\phi \approx 0^\circ$) even at $\mu_0 H = 7$ T the grain still has a somewhat higher J_c than the GB. Around maximum Lorentz force orientations, on the other hand, they overlap above a crossover field B_{cr} . This is the opposite behaviour of what was found by Durrell *et al.* [82] for grain boundaries in films grown by PLD on bicrystal substrates. As reproduced in Fig. 3.11 they showed that J_c of the boundary was only reduced compared to a single

**Figure 7.9:**

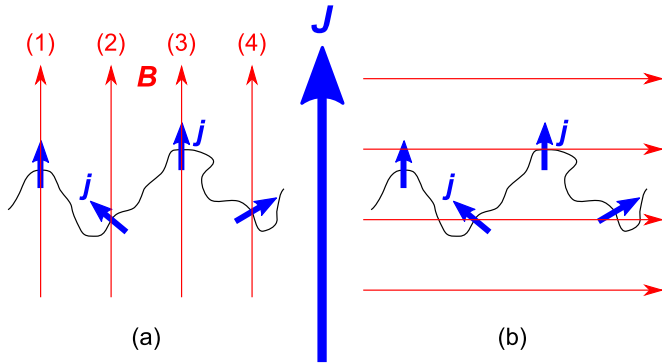
In-plane scans for the isolated grain and one of the grain boundaries (GB3).

grain when the field was within a certain angle ϕ_k of the GB plane (which corresponds to $\phi \approx 90^\circ$ in the measurement geometry employed in this thesis).

The results presented in Fig. 7.9 can be explained by grain boundary meandering, discussed in Sec. 7.1.1. In a field and temperature regime where J_c is limited by the GB, microscopic currents cross it perpendicular to the specific boundary segments [120]. They flow in many different directions, as is illustrated in Fig. 7.10, hence the majority of microscopic currents j is not parallel to the macroscopic current J .⁵ Consequently, at $\phi = 0^\circ$ a significant number of the vortices do not experience zero Lorentz force as is illustrated in Fig. 7.10(a), where vortices (2) and (4) are exposed to a Lorentz force > 0 . This is a fundamentally different situation than in a single grain or a planar PLD grain boundary, where all currents flow parallel to the macroscopic current direction or in one direction perpendicular to the GB, respectively. This implies that the same Lorentz force acts on all vortices. Because of the different way in which currents cross an MOD GB one would expect it always to have a reduced J_c at the macroscopic force free orientation.

At $\phi = \pm 90^\circ$ meandering improves the performance of a grain boundary. Although all vortices in the grain are subject to maximum Lorentz force, a large proportion of the flux lines in the GB experience a smaller force since microscopic currents flow at angles

⁵Note that a slightly different convention is employed here compared to the one used in Chap. 3. J now represents the current density across the entire isolated GB segment (rather than that of a track several grains wide), while j is the current density across an even smaller boundary segment which, in a first approximation, is planar.

**Figure 7.10:**

Current flow across a meandering grain boundary for (a) the macroscopic force free orientation ($\phi = 0^\circ$) and (b) maximum Lorentz force ($\phi = 90^\circ$).

$< 90^\circ$ relative to them [see Fig. 7.10(b)]. One, therefore, finds J_c of the grain and the GB to overlap above a certain field, which means that in the case of the bridge across the boundary it is in fact the grains on either side, rather than the GB, which limit J_c .

Figure 7.11 presents in-plane scans of the grain and the GB discussed above together with data obtained from two other boundaries (GB1 and GB2). It can be seen in the 0.25 T scans that as expected at low fields J_c decreases monotonically with increasing misorientation angle (see also Table 7.1).

Grain boundary GB1 has the lowest crystallographic misorientation of the three GBs analysed. This is why even at a field as small as 0.25 T its J_c equals that of the grain at ϕ around 90° . This region broadens as the field is increased (see Fig. 7.11) until at 8 T only at angles close to the force free orientation does the grain still show a slightly higher critical current density.

At $\mu_0 H < B_{cr}$ the critical current density of GB2 lies between the curves obtained on GB1 and GB3 at all angles, consistent with its intermediate misorientation angle. The crossover at maximum Lorentz force occurs at a field of 0.75 T confirming that B_{cr} increases monotonically with θ_{mis} (see Table 7.1).

The data from the fourth boundary (GB4) showed a completely different behaviour. As can be seen in Fig. 7.12 at low fields its critical current density was virtually independent of ϕ . Only from $\mu_0 H = 1$ T upwards was a dip found in $J_c(\phi)$ at about 90° . Around this angle J_c of the GB overlapped almost exactly with that of the single grain. This can again be explained by a current limitation caused by the grains adjacent to the boundary.

At present it is not clear why the shape of $J_c(\phi)$ of GB4 is qualitatively different from the curves obtained from the other three boundaries. A likely explanation would be a limitation of the critical current density in a direction perpendicular to the plane

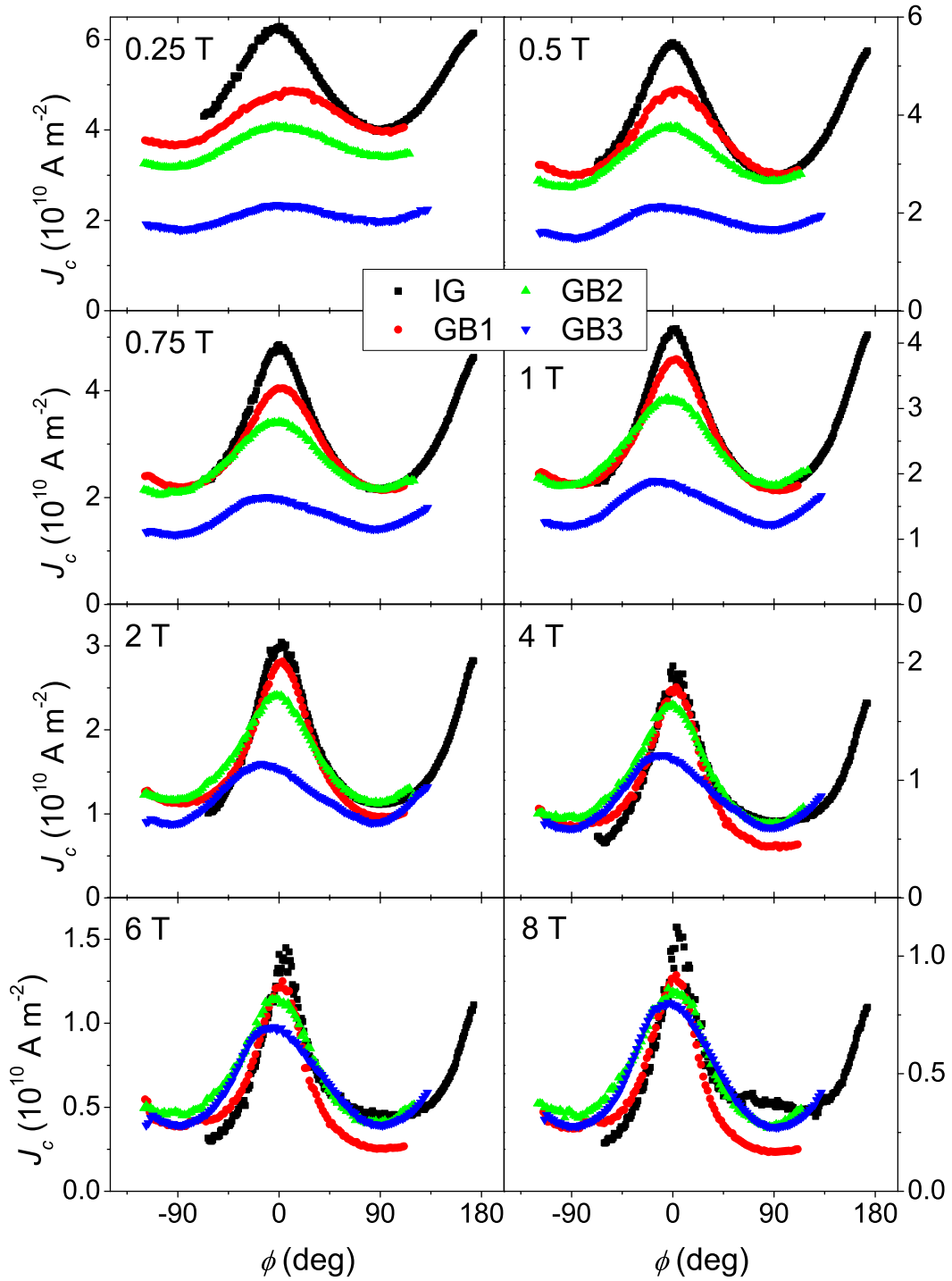
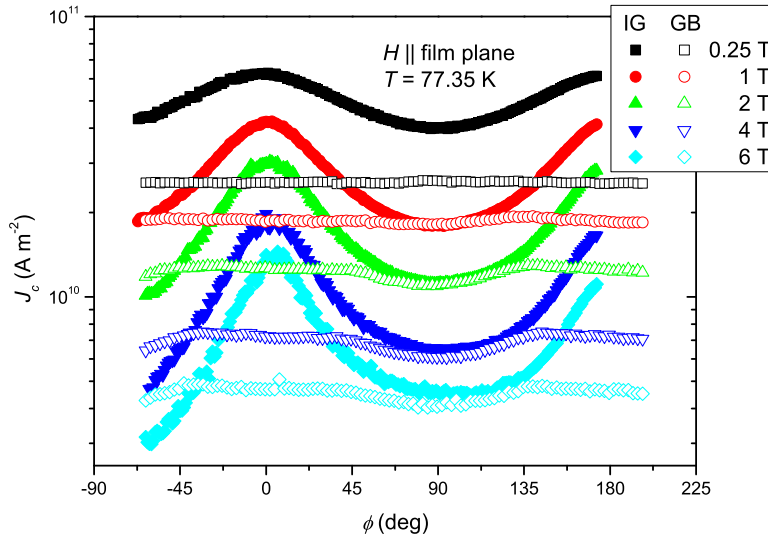


Figure 7.11.: The critical current densities of GB1 – 3 and the single grain at 77.35 K for magnetic fields of 0.25, 0.5, 0.75, 1, 2, 4, 6 and 8 T swept in the plane of the films. The crossover from GB to grain limitation is clearly visible.

**Figure 7.12:**

In-plane scans of the fourth boundary (GB4) together with the single grain.

of the sample, that was not detected by EBSD imaging on the surface. This would be conceivable if the boundary meandered strongly through the film thickness, running approximately parallel to the film plane over a certain length. Consequently, currents would flow parallel to the tape normal as they cross the boundary, which of course is also the axis of rotation in ϕ , hence no dependence of J_c on ϕ would be seen. The cross-sectional TEM image of GB4 (presented in Fig. 7.5) does not support this explanation, however.

As mentioned earlier, T_c of GB4 was lower than that of GB1 – 3 and the single grain, which could well be related to its behaviour. One might reason that the whole sample had suffered some damage during preparation or measurements. It is intriguing, however, that the angle dependent crossover from GB to IG limited J_c is observed also for GB4, confirming that the grains on either side of the boundary are intact. This would imply that *only* the interface between the grains had degraded, which is a possible but rather unlikely scenario. A J_c limitation in a different region of the sample (i.e. not in the FIB bridge) cannot be excluded either. Given the significantly larger cross-section of the track patterned by lithography / ion milling compared to the FIB bridge, however, one would expect the latter to always limit the critical current I_c of the sample, even if other regions had a somewhat degraded J_c .

A different morphology of GB4 compared to GB1 – 3, therefore, is the most likely explanation for the dissimilar angular J_c measurements. That this was not confirmed by TEM could be due to the fact that the image of the cross-section only shows the

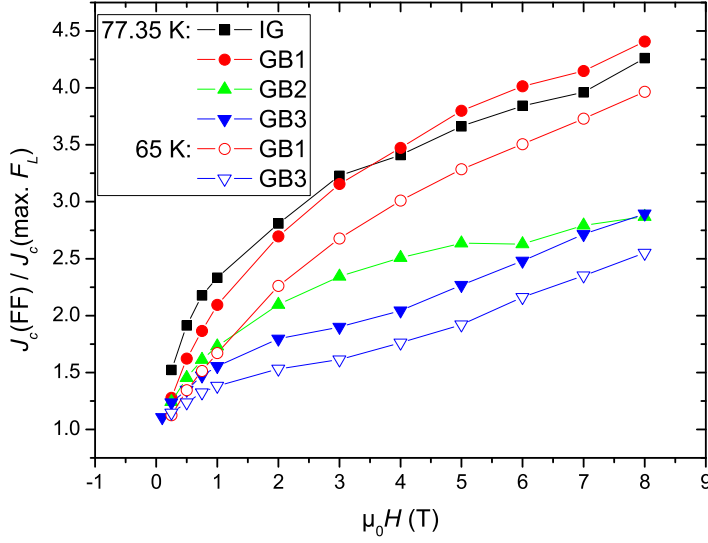


Figure 7.13: The in-plane anisotropy decreased with increasing misorientation angle and with decreasing temperature.

boundary in one plane along the length of the original FIB bridge, which might not be representative for the whole GB.

The difference in J_c at FF and maximum Lorentz force orientations can be described by the in-plane anisotropy $\zeta = J_c(\text{FF})/J_c(\text{max. } F_L)$, which is plotted vs. field in Fig. 7.13 for GB1 – 3 and the single grain (IG). As expected at low fields ζ is highest for the single grain. Unlike in the bridges containing a GB, microscopic currents flow parallel to the macroscopic current direction, leading to a strong FF maximum and a high ζ value. Above 2 T, where J_c of the single grain and GB1 overlap over almost the entire angular range, their in-plane anisotropies are also very similar. The lower values of the critical current densities of GB2 and GB3 at FF on the other hand are reflected in a lower value of ζ .

$J_c(\phi)$ of the single grain and GB1 were asymmetric at fields $\mu_0 H > 1$ T, i.e. the minima at $\phi = +90^\circ$ and -90° were found at different values (see Fig. 7.11). This can be explained by a certain amount of out-of-plane tilt of the limiting grain(s). In order to align the sample parallel to the applied magnetic field it was rotated about the second goniometer axis θ (see Fig. 7.8). θ -scans had been performed at $\phi = +90^\circ$ (single grain) and $\phi = -90^\circ$ (GB1), the maximum of which gave the value of θ where $B \parallel ab$. If the sample is now rotated in ϕ by 180° , however, the ab -planes are not parallel to the field any more, due to the misalignment between film surface and grain(s). As a consequence, the second minimum is suppressed with respect to the first one. A similar situation arises in vicinal films, as discussed in Sec. 10.4.3.

At low fields up to about 0.5 T $J_c(\phi)$ of GB1 – 3 showed asymmetric behaviour of a different kind.⁶ As can be seen in Fig. 7.14(a), the asymmetry is reversed upon change of sign of the applied magnetic field. It can, therefore, be concluded that it is caused by a different surface barrier [198] for flux entry through the film surface and the substrate–YBCO interface. Positive ϕ and positive fields correspond to flux entry through the substrate, which gives a higher J_c than when the vortices enter from the top of the samples. The surface of the films is rough compared to the substrate–YBCO interface, as was shown by TEM (see Sec. 7.2.2). It is reasonable to assume that this roughness causes increased localised fields due to the demagnetisation effect (see Sec. 2.3), making it easier for flux lines to penetrate the sample in this direction and hence suppress J_c [199]. The sketch in Fig. 7.15 illustrates how a field reversal changes the direction of Lorentz force F_L and thus the direction in which vortices move. This explanation is supported by the fact that the asymmetry is also reversed when the current direction is changed—Fig. 7.14(b) shows that positive applied fields and positive currents give the same results as negative H and I . This also applies to the inverse configurations, i.e. $(+H, -I)$ give the same results as $(-H, +I)$ [Fig. 7.14(c)].

In order to quantify the asymmetry the cross correlation

$$r = \frac{\sum_i [(x_i - \bar{x})(y_i - \bar{y})]}{\sqrt{\sum_i (x_i - \bar{x})^2} \sqrt{\sum_i (y_i - \bar{y})^2}} \quad (7.1)$$

was determined for each set of ϕ -scans at a given positive and negative applied field (x_i is the value of J_c at a specific ϕ_i for a certain positive H , y_i for the same ϕ_i and negative H , and \bar{x} and \bar{y} are the averages of the entire ϕ -scans). Figure 7.16 shows that the field where r becomes 1, corresponding to a perfect overlap of the curves for positive and negative field and thus the disappearance of asymmetry, shifts to higher fields as the grain boundary misorientation angle becomes higher (see Table 7.1 for the values of θ_{mis}). It can, thus, be concluded that a stronger GB limitation enhances asymmetry. This is consistent with the fact that asymmetry persists up to higher fields at $T = 65$ K (where more influence of GBs is expected, see below) than at 77.35 K.

As can be seen in Fig. 7.14, J_c at the FF orientation was almost the same at $\mu_0 H = 0.1$ and 0.25 T. Weak field dependence is in general associated with critical current density governed by GBs [82, 188]. It can, therefore, be concluded that J_c is strongly GB limited

⁶ $J_c(\phi)$ of the isolated grain is most probably asymmetric as well, however only one minimum was measured, hence this cannot be confirmed.

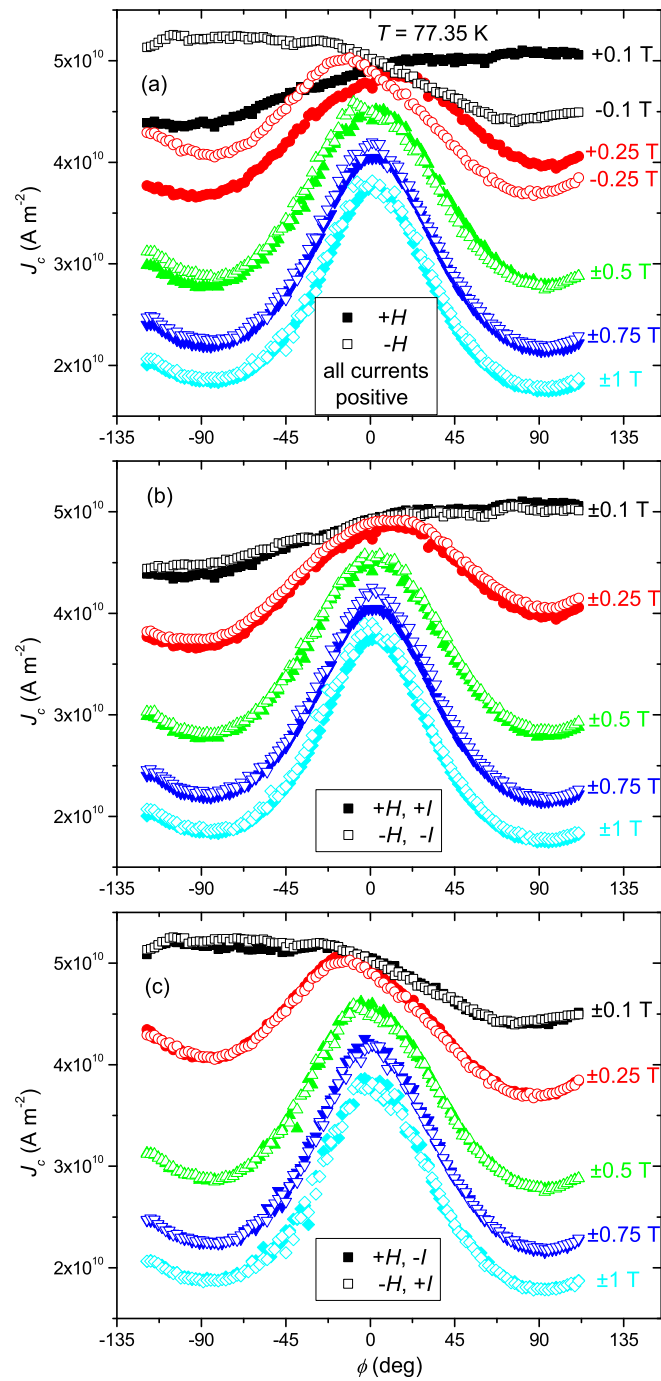


Figure 7.14.: At low fields the in-plane scans became asymmetric, as is shown here for boundary GB1. Changing the sign of the applied field or the current direction reverses the asymmetry.

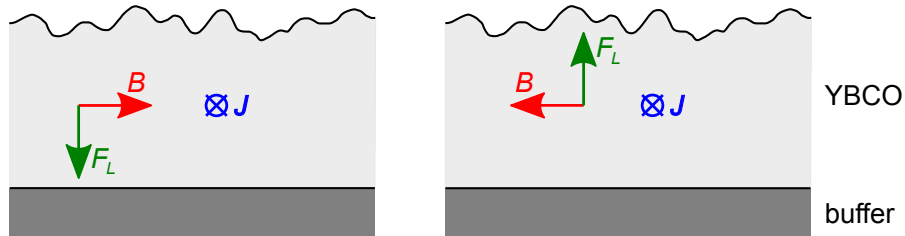


Figure 7.15.: Depending on the direction of applied field vortices move either from the film surface to the buffer–YBCO interface or in the opposite direction.

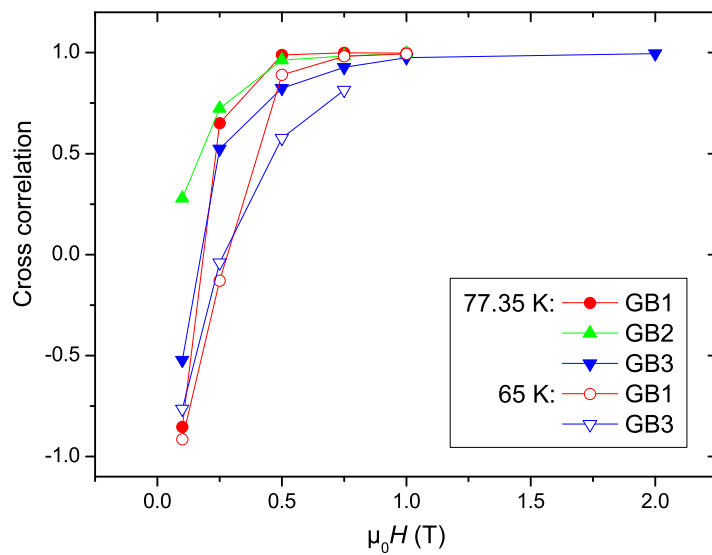


Figure 7.16:

The cross correlation for positive and negative fields shows that asymmetry persists to higher fields the higher the GB misorientation and the lower the temperature.

in this field and angular range, which is consistent with the observation that the crossover to grain limited behaviour occurs first at maximum Lorentz force.

The fact that at very low fields J_c of the bridges with a grain boundary is completely limited by the GB could also explain the peculiar behaviour at $\mu_0 H = 0.1$ T [see Fig. 7.14(a)]. At this field the critical current density exhibits a broad maximum at $\phi \approx +90^\circ$ and a minimum at -90° . At the macroscopic force free configuration an intermediate value is measured. One can reason that due to the strong meandering at low fields the direction of microscopic currents covers at least the angular range of $\pm 90^\circ$ relative to the macroscopic current direction. If all directions occur with the same frequency one would expect no angular dependence of J_c of the bridge at all. At $\phi = -90^\circ$, however, all (or at least the vast majority of) vortices experience a Lorentz force pointing from the sample surface to the substrate, i.e. along the direction with a lower surface barrier. At $+90^\circ$ the opposite is the case. At 0° half the vortices are pushed in one direction and the other half in the other, which explains why $J_c(-90^\circ) < J_c(0^\circ) < J_c(+90^\circ)$.

The boundaries GB1 and GB3 were also measured at $T = 65$ K (not shown), and qualitatively similar behaviour was found as at 77.35 K. Again the ϕ -scans were asymmetric for both GBs at low fields and for GB1 also at high fields. As expected at low fields J_c of the 6.5° boundary (GB3) was suppressed with respect to the 4.9° boundary (GB1) at all angles. At maximum Lorentz force both boundaries could support the same current from ~ 4 T upwards, whereas no overlap was found for the force free orientation, where even at $\mu_0 H = 8$ T J_c of GB1 surpassed that of GB3 by a factor of 1.7. An increased crossover field at a lower temperature is consistent with results for $H \perp$ film plane [109]. As was shown above, strong GB limitation at FF causes a flattening of ϕ -scans, and in fact the in-plane anisotropy was reduced at the lower temperature, as can be seen in Fig. 7.13. This behaviour can also be understood in terms of increased current percolation, which is expected when a CC becomes more GB dominated and which leads to flatter ϕ -scans [200]. It fits well into this picture that at $T = 65$ K $J_c(\phi = 0^\circ)$ is almost completely independent of field up to $\mu_0 H = 0.5$ T, which is higher than the corresponding field found at 77.35 K.

7.3.3. Pole Figure

A pole figure allows one to display the complete angular dependence of J_c of a sample in one graph. To this end ϕ -scans are performed from $\phi = -180^\circ$ to $+180^\circ$ at different

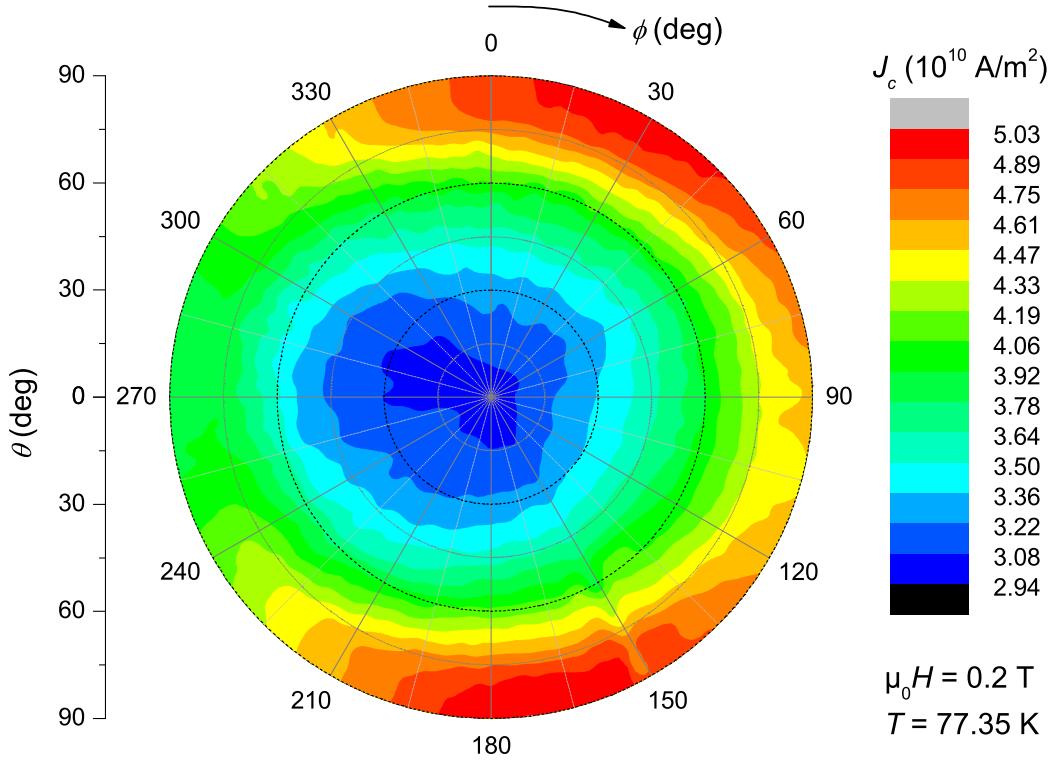


Figure 7.17.: A pole figure obtained from GB1.

values of θ ranging from $\theta = 0^\circ$ to 90° . Shown in Fig. 7.17 is the result of such a measurement performed on GB1 at $\mu_0 H = 0.2 \text{ T}$. A circular cut through the pole figure corresponds to a ϕ -scan at a given θ , a radial cut to a θ -scan at a given ϕ .

As expected, the lowest values of J_c (in blue) are found around $\theta = 0^\circ$, where H is perpendicular to the film plane. The critical current density increases radially from there as θ moves towards 90° and intrinsic pinning sets in. The ϕ -scan at $\theta = 90^\circ$ has maxima (in red) at $\phi \approx 0^\circ$ and 180° and minima (in yellow / green) at $\phi \approx 90^\circ$ and 270° , which are due to minimum and maximum Lorentz force, respectively.

The pole figure reveals a certain asymmetry: the red areas are somewhat shifted from $\phi = 0^\circ$ and 180° towards 90° and the minimum at $\phi \approx 270^\circ$ is more pronounced than that at 90° . This is the same effect as the asymmetry at low fields discussed in Sec. 7.3.2 (in particular Fig. 7.14).

7.4. Summary and Conclusions

In this chapter results on isolated MOD grain boundaries and a single grain were presented.

In measurements of $J_c(H)$ with fields perpendicular to the film plane hysteresis was found, similar to what has been reported in previous studies. The surprising result is that this was also the case for the isolated grain, where reversible behaviour would have been expected.

For fields swept in the film plane two regimes, depending on both in-plane angle and magnitude of field, can be distinguished: (1) low H regardless of angle, as well as high H around the force free (FF) orientation and (2) elevated fields around the maximum Lorentz force configuration. In regime (1) the isolated GBs show a suppressed J_c with respect to the grain; in (2) J_c of all GBs and the single grain become the same. This means that boundaries do not limit the current flow any more in the latter case. The angle dependent crossover from GB to grain limited behaviour can be explained by the fact that MOD boundaries are not planar but meander. Microscopic currents do not, in general, flow parallel to the macroscopic current direction. As a consequence, GBs behave comparably better at macroscopic maximum Lorentz force than at the force free orientation. It is remarkable that, despite the meandering, grain boundary limitation at FF persists up to 8 T, the highest field analysed.

8 Polycrystalline Tracks in MOD CCs

Measurements on wider (i.e. polycrystalline) tracks can give very valuable insights into the influence of grain boundaries on the performance of coated conductors. Such experiments were, therefore, carried out on samples from the American Superconductor tape in order to complement the results on the isolated grain and grain boundaries in Chap. 7. In particular the dependence of J_c on the track width was investigated. It was found that the data obtained from polycrystalline tracks can be explained by the results on the single grain and GBs.

A number of important previous studies on polycrystalline CC tracks are discussed in Sec. 8.1. In the next section results of X-ray diffraction measurements are presented, which had been carried out to quantify the degree of texture of the American Superconductor tape. Very similar critical current density measurements as those performed on the isolated grain and GBs were done for polycrystalline tracks, which are discussed in Sec. 8.3. The present chapter ends with a comparison between the behaviour of J_c of single GBs and polycrystalline tracks.

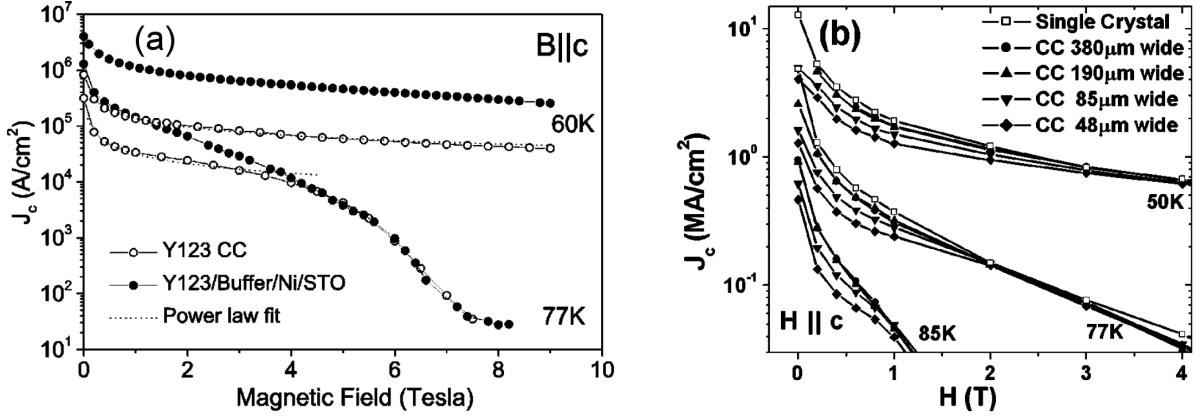


Figure 8.1.: (a) At the crossover field $J_c(H)$ of a single crystal and a CC merge [109]. (b) At low fields J_c decreases as tracks are narrowed down [196].

8.1. Previous Studies

Fernández *et al.* [109] compared $J_c(H)$ of coated conductors and films grown on buffered single crystals by PLD for fields parallel to the film normal. While at low fields the single crystal showed superior properties the curves merged at a crossover field B_{cr} , as shown in Fig. 8.1(a). Below B_{cr} $J_c(H)$ of the CC could be described by a power-law [108]

$$J_c(H) = J_c(0)[H_0/H]^n, \quad (8.1)$$

which had been shown to apply to bicrystal boundaries. $J_c(0)$, H_0 and n are fit parameters. Above the crossover field the CC data could be fitted to an exponential decay (which is typical for a single crystal and, thus, grain-limited J_c).

Fernández *et al.* were able to relate the behaviour of $J_c(H)$ to the shape of the current-voltage curves: $V(I)$ changed from a NOLD characteristic at low fields (non-Ohmic linear differential, representing flux flow along the grain boundaries) to a power-law dependence at high fields (flux creep as dissipation occurs in the grains; see Sec. 3.4.4). The transition between the two regimes occurred at exactly the crossover field deduced from the $J_c(H)$ curves.

Building on the work by Fernández *et al.*, Kim *et al.* [196] confirmed the crossover between $J_c(H)$ of a single crystal and a RABiTS coated conductor, both of which had been deposited by MOD. Due to a higher degree of texture they found a crossover field

at $T = 77\text{ K}$ of only $\sim 2\text{ T}$ (rather than $\sim 4\text{ T}$ as in Ref. [109]).

In an alternative approach to deduce the value of B_{cr} Kim *et al.* [196] successively narrowed down a CC track and measured its $J_c(H)$ dependence. At high fields J_c was the same for all widths, whereas at low H it decreased as the track got narrower [see Fig. 8.1(b)]. They concluded that this reduction was due to J_c being limited by GBs at low fields. This was supported by the fact that the current-voltage curves obtained from their two narrowest tracks showed clear characteristics of GB dissipation. Narrowing down a track reduces the number of percolation paths. A boundary segment with a low critical current density has a stronger effect on a narrow track, compared to a wider one where currents can percolate around the weak segment. A reduction in width can thus be expected to lead to a suppression in overall J_c , as long as track length \gg grain diameter, and therefore it is very likely that there is a weak GB in every track. A width reduction has less or no impact at high H , where the coated conductor behaves single crystal-like and current flow is not percolative, and thus the critical current density becomes independent of track width. The field at which Kim *et al.* observed the transition between the two regimes in the width-dependent measurements agreed well with B_{cr} determined from the comparison of single crystal and coated conductor.

In a similar study Hänisch *et al.* [197] hindered percolative current flow not by reducing the width, but by cutting a track into filaments using a Focused Ion Beam microscope (FIB). This gave curves akin to those depicted in Fig. 8.1(b).

Knowledge about the width dependence of J_c not only deepens the understanding of current transport across GBs, but it is invaluable if striation is considered as a means of reducing ac losses [201, 202].

The crossover from boundary to grain limited J_c was also observed in neutron irradiation experiments on CCs by Eisterer *et al.* [203]. Irradiation reduced J_c at low H only, corroborating the fact that in this field regime the current is limited by GBs, which incur more damage by neutrons than grains.

8.2. XRD – Texture Analysis

The degree to which the grains are aligned was determined by X-ray diffraction measurements.

The samples studied in this chapter were taken from the same American Supercon-

ductor tape used for the isolation of grain boundaries in Chap. 7. Their architecture is given in Sec. 4.5.

8.2.1. Out-of-Plane

The out-of-plane alignment was deduced from XRD rocking curves, as described in Sec. 6.3. The results for the (003)-, (005)- and (006)-reflections¹ can be seen in Fig. 8.2. All scans were performed for the rolling (RD) and the transverse (TD) direction of the tape.²

For all three orders of diffraction the grain alignment, which can be quantified by the full width at half maximum (FWHM) of the rocking curves, was slightly better in the rolling than in the transverse direction. Values of 3.2°–3.4° (RD) and 4.4°–4.5° (TD) were obtained, confirming the high quality of the samples. Intriguingly, a better alignment in RD disagrees with what is normally observed in RABiTS tapes, namely a better alignment in TD [168, 167].

8.2.2. In-Plane

In order to quantify how well the grains are aligned in-plane, ϕ -scans and a pole figure were obtained, both on the {103}-reflection. The peak widths in ϕ (FWHM) were found to be 5.7°–6.6°.

The pole figure can be seen in Fig. 8.3, which confirms the good in-plane alignment. It is visible in the 2D representation that the poles at $\phi=0^\circ$ and 180° (beam in a plane with the RD) are elongated along χ . This is due to the higher out-of-plane misalignment in the TD compared to the RD, as discussed above. (A tilt in χ at $\phi=0^\circ$ or 180° is equivalent to a rotation in ω at $\phi=90^\circ$ or 270° , which gives a TD rocking curve.)

¹None of these reflections (nor the {103}-reflection used in the ϕ -scans, see below) have 2Θ -values close to those of the Y_2O_3 , YSZ and CeO_2 buffer layers. It is, therefore, certain that the data presented in this section relate to the YBCO layer only, not to one of the buffer layers.

²A rocking curve in RD means that the beam is in a plane parallel to the RD. The sample is then rotated about an axis parallel to the TD. The inverse geometry applies in the case of a rocking curve in TD.

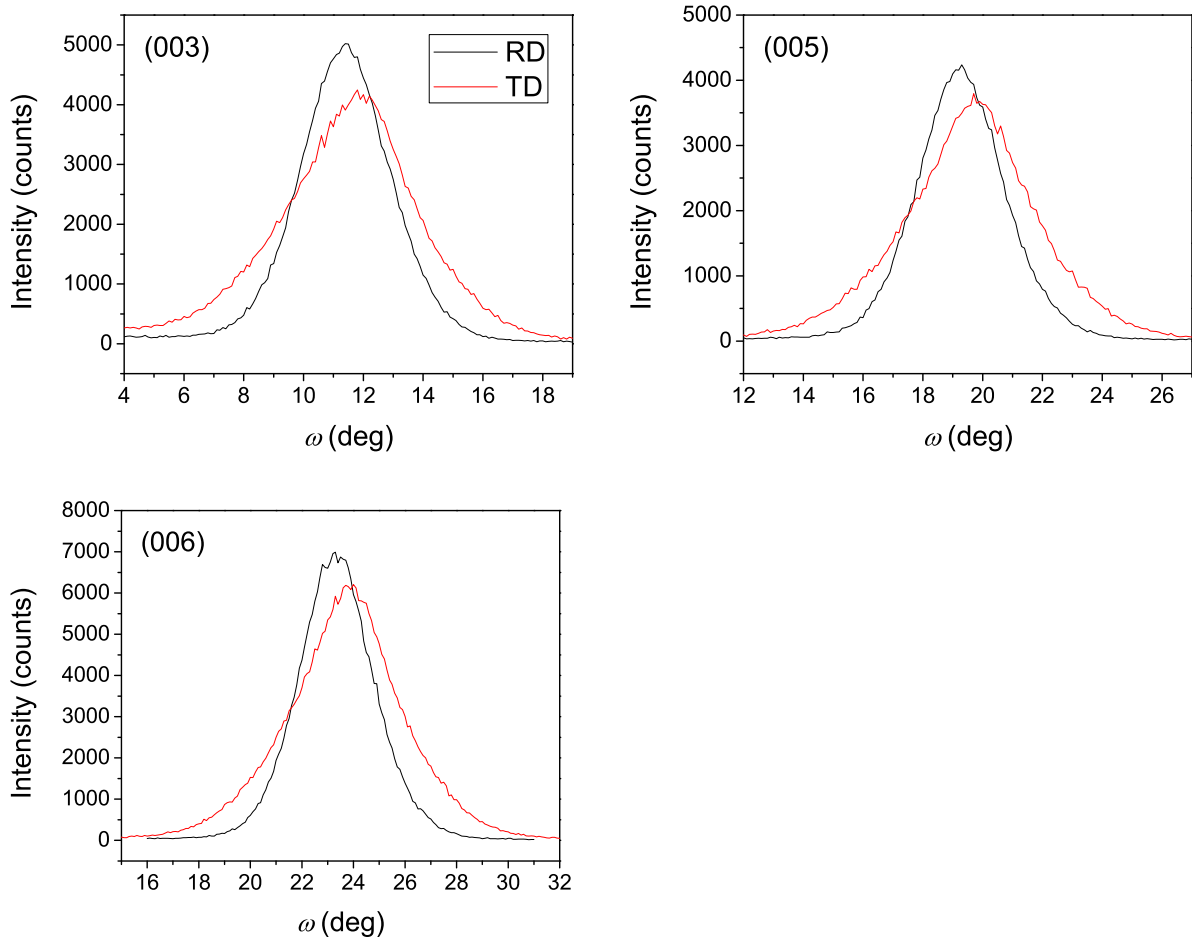


Figure 8.2.: XRD rocking curves for the (003)-, (005)- and (006)-reflections, obtained for the rolling (RD) and transverse (TD) directions.

8.3. Critical Current Densities of a Track of Different Widths

In an initial approach several tracks of different widths, prepared by conventional photolithography and ion milling, were investigated, each of which was located at a different position on the same sample. Due to local inhomogeneities a clear relationship between the behaviour of the critical current density and the track width could not be established.

In order to overcome this problem a sample with only one $250\ \mu\text{m}$ wide and $1\ \text{mm}$ long track was prepared. After being measured the track's width was reduced to $125\ \mu\text{m}$, using the same lithography process, and the same set of measurements were performed

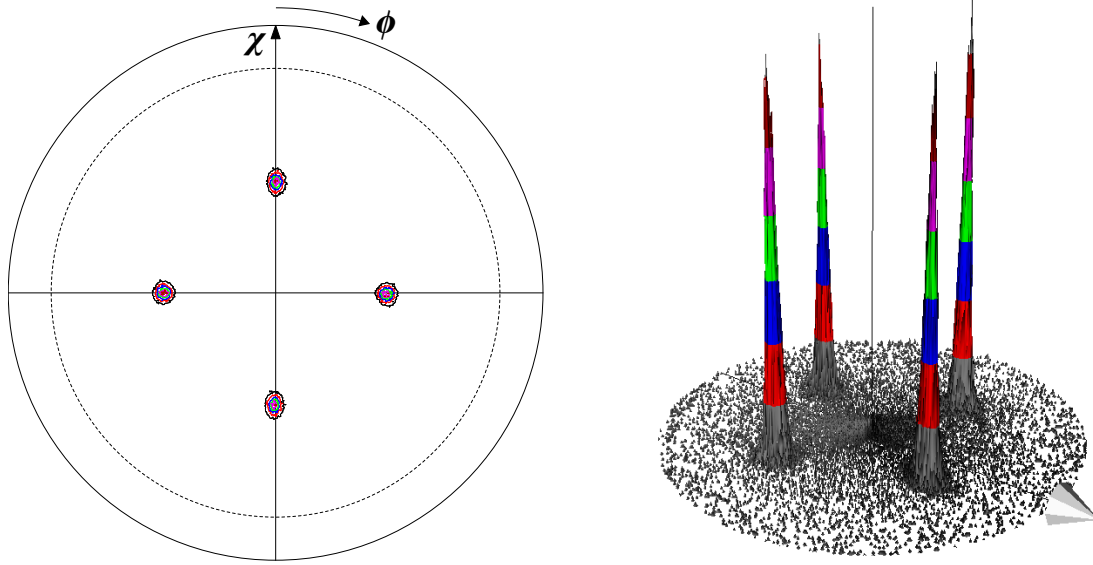


Figure 8.3.: XRD pole figure obtained on the $\{103\}$ -reflection in 2D and 3D representation. The sharp poles indicate a good in-plane grain alignment.

again. This process of narrowing down and measuring the track was repeated for widths of 75, 50 and 25 μm .

The observed transition temperatures were only slightly suppressed due to the repeated patterning (from $T_c = 92.8\text{ K}$ for the 250 μm wide track down to 91.2 K for the 25 μm wide track), hence one can assume that the sample did not suffer any noteworthy damage during preparation.

A 1 μV voltage criterion was used to determine J_c from $V(I)$ -curves. Note that this differs from the 0.5 μV criterion employed in the case of the isolated grain and GBs (see Sec. 7.3).

8.3.1. Fields Perpendicular to the Film Surface

Shown in Fig. 8.4(a) is the critical current density for the different track widths vs. a field applied parallel to the film normal.³ Note that the condition track length \gg grain diameter should be fulfilled as the tracks are 1 mm long. Very similar behaviour

³No low-field data could be obtained for the widest track because of a 5 A limitation of the power supply.

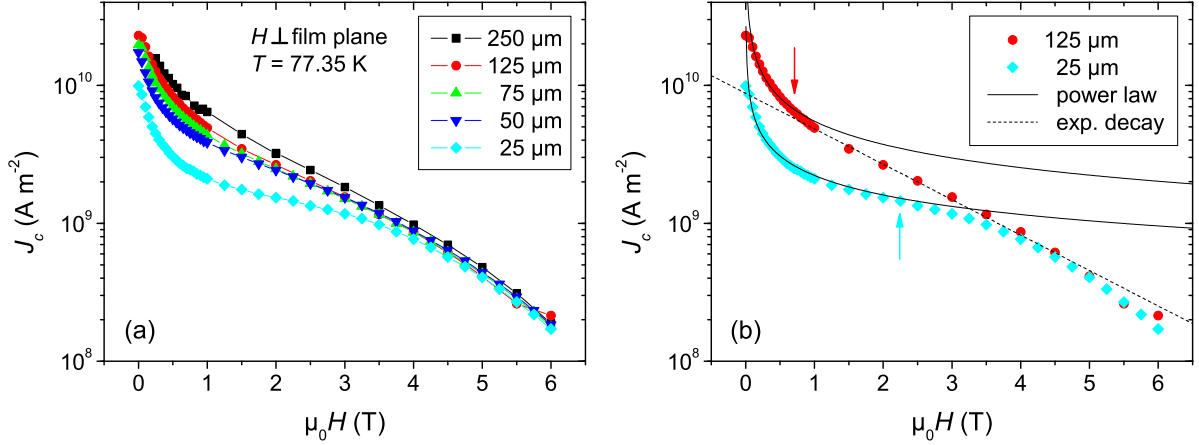


Figure 8.4.: (a) The critical current density vs. field \perp film plane for track widths ranging from 25 to 250 μm . (b) Fits to different field ranges. The arrows indicate where measurements and power law fits diverge.

as that reported by Kim *et al.* [196] (see Sec. 8.1) is found; at low fields J_c decreases monotonically with decreasing width, whereas at high fields the curves merge.

As can be seen in Fig. 8.4(a) the crossover field is highest for the 25 μm wide track. It was found that B_{cr} increases with increasing GB misorientation, hence it is consistent that the narrowest track shows the highest B_{cr} , as it can be expected to be dominated most strongly by GBs.

In Fig. 8.4(b) the same data of the 125 and 25 μm wide tracks were fitted to the power law defined by Eq. (8.1) and an exponential decay. It can be seen clearly that the power law, which describes a GB limited $J_c(H)$, fits the narrower track up to higher fields better than the wider one, implying again that the 25 μm wide track is most strongly governed by boundaries. At higher fields both sets of data are described reasonably well by an exponential decrease.

In a next step J_c was measured for increasing (H^+) and decreasing (H^-) fields, in the same manner as for the isolated grain and grain boundaries (see Sec. 7.3.1), and again hysteretic behaviour was found, for all track widths. As a representative example the curves obtained from the 50 μm wide track are presented in Fig. 8.5(a). The difference between $J_c(H^-)$ and $J_c(H^+)$ increased with decreasing track width, as can be seen in Fig. 8.5(b), where the relative enhancement $[J_c(H^-) - J_c(H^+)]/J_c(H^+)$ is plotted vs. field.

This finding is consistent with the results obtained on the isolated grain and GBs,

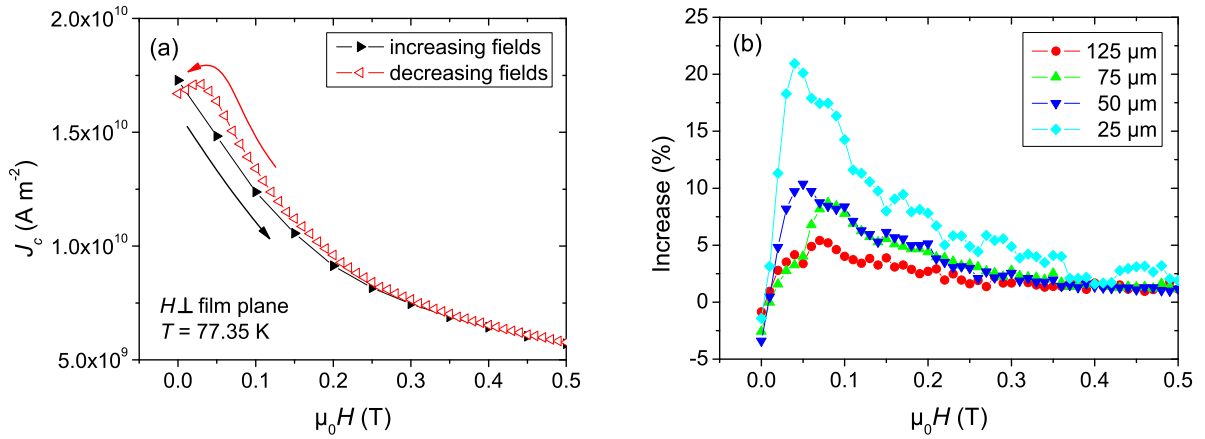


Figure 8.5.: (a) Hysteresis in $J_c(H)$ was found, shown here for the $50\ \mu\text{m}$ wide track. (b) The relative increase of J_c due to the hysteretic $J_c(H)$.

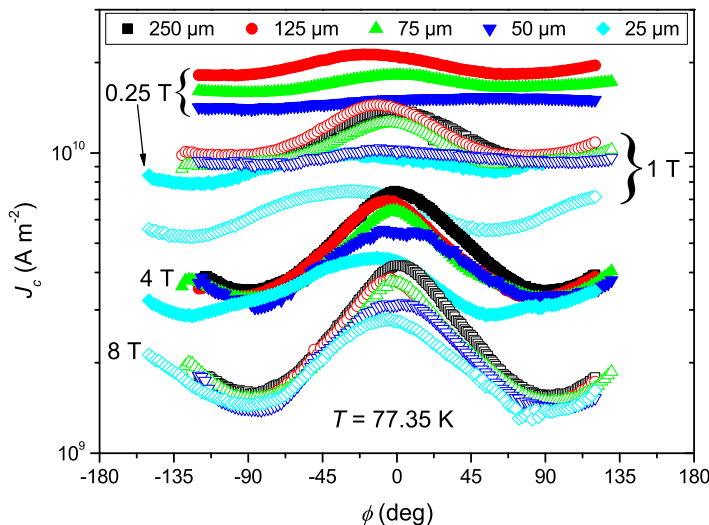
which showed a higher increase for the more misaligned boundaries (see Fig. 7.7). As reducing the width of a polycrystalline track should render its J_c more GB dominated, one would expect a narrower track to exhibit a more pronounced hysteresis, as was indeed observed.

8.3.2. Fields In-Plane

The critical current density for different magnetic fields swept in the plane of a track which has been successively reduced in width and re-measured can be seen in Fig. 8.6. At $0.25\ \text{T}$ J_c decreases for all angles as the track becomes narrower.⁴ This behaviour is consistent with the results obtained by Kim *et al.* [196] for fields applied perpendicular to the plane of the film (see Sec. 8.1).

At $0.75\ \text{T}$ the curves obtained on the $75\ \mu\text{m}$ and the $50\ \mu\text{m}$ track overlap at around $\phi = \pm 90^\circ$. In comparison the $125\ \mu\text{m}$ track still shows a higher, the $25\ \mu\text{m}$ track a lower, J_c at all angles. As the field is increased further, J_c at maximum Lorentz force becomes approximately the same for all track widths (see Fig. 8.6), again a behaviour reported previously for $H \perp$ film plane (see Sec. 8.1 and 8.3.1). At the force free orientation on the other hand the wider tracks still exhibit a superior performance; even at $8\ \text{T}$ the critical current density for angles around $\phi = 0^\circ$ is reduced in the same sequence as is the track width.

⁴Note that low field data for the $250\ \mu\text{m}$ track is missing because of a $5\ \text{A}$ current limitation.

**Figure 8.6:**

In-plane measurements of a track which has been narrowed down from 250 to 25 μm . The measurement geometry is the same as for the isolated grain / GBs (see Fig. 7.8).

In order to quantify the dependence of J_c on track width, the values of the maxima and the averages of the two minima are plotted vs. track width in Fig. 8.7(a). The data were scaled to the corresponding values of the 25 μm track. It can be seen that at $\mu_0 H = 1 \text{ T}$ both minimum and maximum depend on width. The critical current density of the maximum decreases with decreasing track width also at 8 T, whereas J_c of the minimum remains constant at this field.

These findings can be explained using the results on single grain and GBs presented in Sec. 7.3.2. At $\phi \approx \pm 90^\circ$ even at relatively low fields the grains, rather than the boundaries, limit the current carrying capability of the bridges with the isolated GBs. Due to the good out-of-plane alignment of the grains, as shown by XRD, one expects all grains to have a very similar J_c , leading to a high level of homogeneity across the width of the polycrystalline track. As a consequence, narrowing a track down has no noticeable effect on its J_c in this regime. For $\phi \approx 0^\circ$ on the other hand it was demonstrated that GBs can carry only a reduced current compared to grains, even at high applied fields. In a wide track a boundary segment with a high misalignment does not cause a significant reduction of the overall J_c as long as the adjacent boundaries have better properties, allowing current to percolate around the inferior GB segment. Apparently this is still the case for a track 125 μm (3–6 grains) wide, as a very similar behaviour is found for the 250 and the 125 μm tracks. Once the track is narrowed down to three or fewer grains in width, however, the effect of a weak boundary is not negligible any more and a depressed J_c at the force free orientation is measured.

The qualitatively different behaviour for varying track width becomes even more ap-

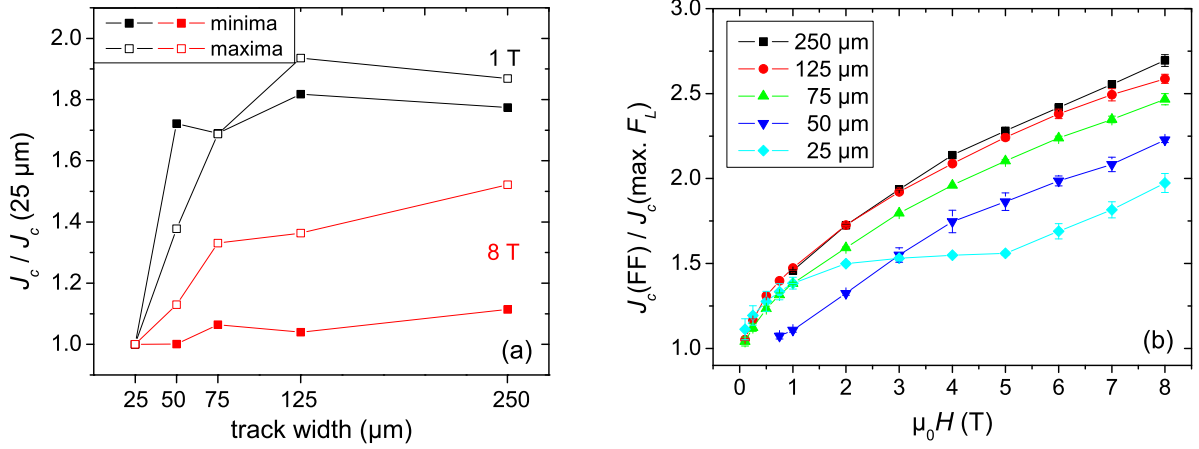


Figure 8.7.: (a) Values of the minima and maxima of in-plane scans vs. track width. (b) The in-plane anisotropy becomes lower with decreasing track width above 1 T. Some ϕ -scans were slightly asymmetric (i.e. the values of the minima at $+90^\circ$ and -90° differed), hence the error bars in this graph.

parent when the in-plane anisotropy $\zeta = J_c(\text{FF})/J_c(\text{max. } F_L)$ is plotted vs. applied field. As can be seen in Fig. 8.7(b) this value is almost exactly the same for the two widest tracks. In the 75, 50 and 25 μm tracks, however, ζ is reduced, which corresponds to the flatter ϕ -scans.

The increase of ζ with field can be understood as follows. At low H the critical current density is predominantly GB dominated and the microscopic currents percolate strongly, which leads to a suppression of the force free effect and thus a low in-plane anisotropy [200]. As the field is increased GBs stop being a barrier for current flow over large angular ranges, as was shown above, and the tape behaves more like a single crystal. Consequently, microscopic currents flow more closely parallel to the macroscopic current direction, causing a strong force free maximum and a high value of ζ .

It is worth pointing out that ζ is virtually independent of track width at $\mu_0 H \leq 1$ T (with the exception of the 50 μm track, see below). Only for higher fields do the curves branch out and a monotonic decrease of the in-plane anisotropy is seen as the width is reduced. This is particularly interesting as J_c , both for $H \perp$ film plane (Ref. [196]) and for H in-plane at maximum Lorentz force (present work), was found to be independent of track width at *high* fields while at low fields narrower tracks showed lower values. The fact that ζ follows the opposite trend is clearly due to J_c depending on width in a very different way for minimum and maximum Lorentz force. Consequently, even at 8 T the

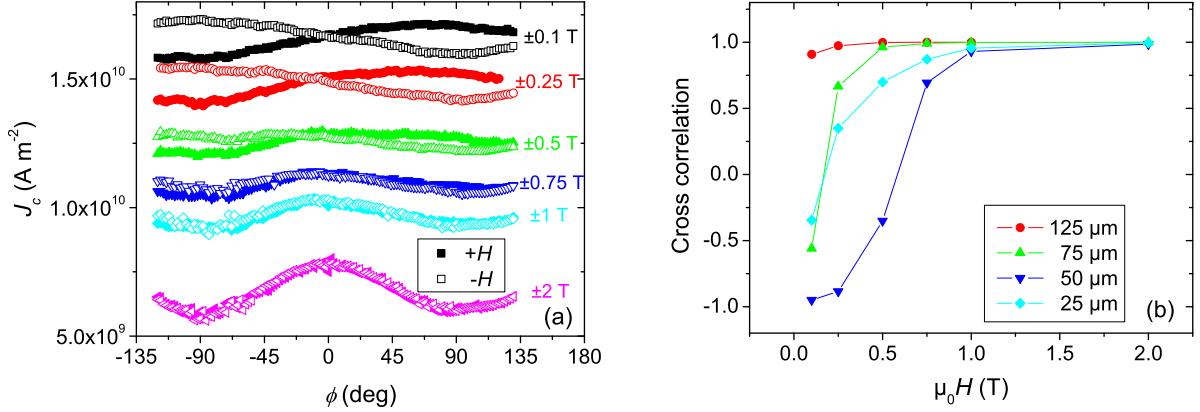


Figure 8.8.: (a) As the track was narrowed down, in-plane scans showed asymmetric behaviour at low fields, as is shown here for a track 50 μm wide. (b) The cross correlation between curves obtained at the same field but with opposite sign.

effect of grain boundaries is still detectable.

The asymmetry of the ϕ -scans at low fields found for single grain boundaries was also present in the curves obtained on the polycrystalline tracks. While not very significant in the 250 and 125 μm wide links, this phenomenon became very pronounced after the track had been narrowed down further, as is depicted in Fig. 8.8(a) for a width of 50 μm . Again changing the sign of the applied field or current polarity reversed this behaviour. The cross correlation r was determined according to Eq. (7.1) for each track width. Figure 8.8(b) shows that the field where r becomes 1 (disappearance of asymmetry) shifts to higher fields as the track gets narrower. For single GBs it was found that asymmetry persists up to higher fields for higher misorientation angles (see Fig. 7.16). It is thus consistent that this is also the case for narrower tracks which are expected to be more dominated by boundaries than wider tracks. The exception is again the 50 μm track: r almost exactly equals -1 at $\mu_0 H = 0.1$ T (maximum but inverse correlation) and a field higher than for all other tracks needs to be applied in order to recover symmetric behaviour.

At low fields the 50 μm track showed only one minimum and one maximum at $\phi \approx \pm 90^\circ$, respectively [see Fig. 8.8(a)], similar to what was observed for GB1 [see Fig. 7.14(a)]. As this track is only one or two grains wide it is reasonable to assume that the same explanation applies, i.e. that minimum and maximum are related to a difference in the surface barrier.

Both minima and the maximum of J_c of the 25 μm wide track shifted by $\sim 30^\circ$ over

the field range investigated (see Fig. 8.6). At $\mu_0 H = 8$ T they are found at the angles where maximum or minimum Lorentz force, respectively, occur for macroscopic current direction. As the field decreases they move to lower values of ϕ . One can reason that this is due to the crossover from grain to GB limited J_c and presume that the limiting GB is not exactly perpendicular to the track. This would lead to an average direction of current flow not parallel to the track, causing the shift of maximum Lorentz force and force free orientations. The behaviour of the $25\ \mu\text{m}$ track was found to be independent of the sign of H and therefore must not be confused with the asymmetry discussed above. Further evidence that the $25\ \mu\text{m}$ track is the one that is most GB dominated can be found in the fact that in this track the 0.1 and 0.25 T ϕ -scans are closer together than in the wider ones.

The surprisingly flat in-plane scans of the $50\ \mu\text{m}$ wide track at lower fields might also be explained by a GB in the $25\ \mu\text{m}$ track which is not perpendicular to the track direction. One could speculate that the rest of the GB segments making up the limiting path of the $50\ \mu\text{m}$ track are at a significantly different angle than those in the $25\ \mu\text{m}$ track, as is sketched in Fig. 8.9(a). It would then follow that the maximum and minima get smeared out because at no particular value of ϕ is the majority of the limiting path perpendicular or parallel to the direction of applied field, respectively. Shown in Fig. 8.9(b) are two (model) in-plane scans with maxima at different values of ϕ , representing the two parts of a track with GB sections at two different angles. If the two ϕ -scans are added up to obtain $J_c(\phi)$ of the whole track, it can be seen that the obtained curve (in blue) becomes flatter. In order to prove such a “macroscopic meandering” effect, however, further investigations would be necessary, e.g. EBSD mapping of the whole track to determine the shape of the limiting path.

8.4. Comparison Between Single Grain/GBs and Polycrystalline Tracks

It is worth comparing the absolute J_c values of the in-plane scans of isolated grain and GBs to those of the wider tracks. As a representative example curves obtained on the $125\ \mu\text{m}$ wide track are plotted in Fig. 8.10. At $\mu_0 H = 0.25$ T the critical current density of the polycrystalline track approximates that of GB3 (note that $J_c(\phi)$ of the $125\ \mu\text{m}$ track has been re-analysed using a $0.5\ \mu\text{V}$ criterion, so it matches that used for GB3).

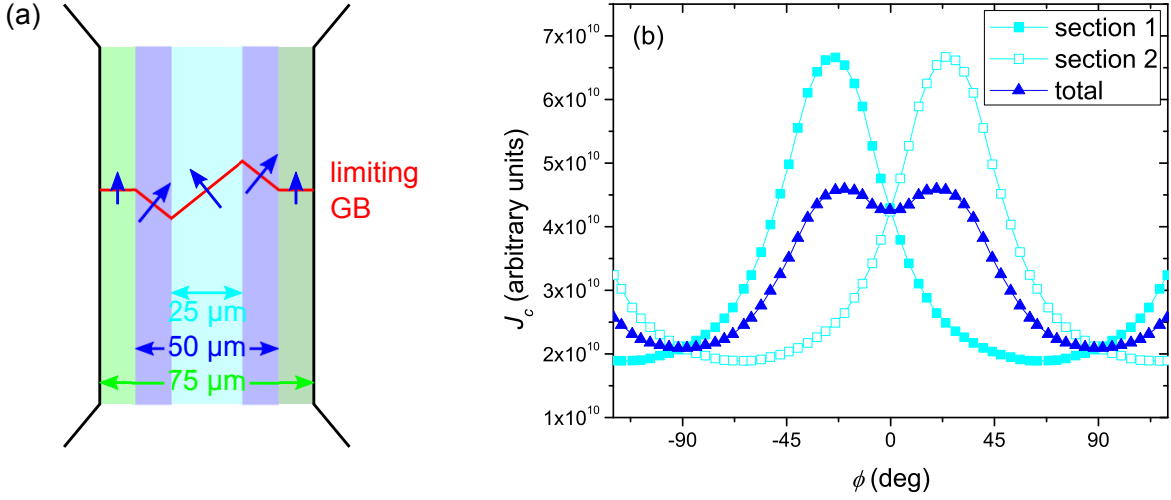
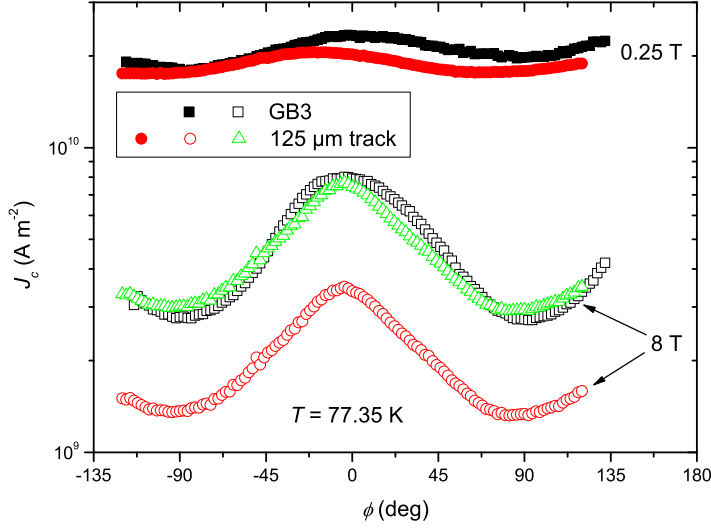


Figure 8.9.: (a) Possible shape of the limiting GB which would explain the flatness of in-plane scans of the $50\ \mu\text{m}$ wide track. (b) Two tracks with in-plane scans with maxima at different ϕ in parallel give a flatter total $J_c(\phi)$.

It is a reasonable assumption that at low fields the limiting path is defined by one set of boundaries crossing the track whose average J_c equals that of GB3.

As the field is increased it is observed that J_c of the $125\ \mu\text{m}$ track is significantly below that of GB3 (see the 8 T curves in Fig. 8.10). The explanation for this can be found in the different length of the FIB bridge ($\sim 15\ \mu\text{m}$) and the polycrystalline track ($1000\ \mu\text{m}$). As J_c is expected to be limited by the properties of the grains over almost the entire angular range at high H , the voltage drop occurs over the whole length of the bridge or track when J_c is exceeded. It is, therefore, not valid to use the same *voltage* criterion for both the FIB bridge and the wide track. Instead, one needs to apply the same *electrical field* criterion, which implies a voltage criterion for the polycrystalline track 1000/15 times as large as that for the FIB bridge. During the measurements current-voltage curves were obtained up to $\sim 7\ \mu\text{V}$ only (in order to minimise the risk of damaging the track). Linear extrapolation of $V(I)$ at different ϕ shows that J_c of the $125\ \mu\text{m}$ track obtained using the correct E -field criterion is ~ 2.2 times as high as that deduced from a $0.5\ \mu\text{V}$ criterion. The data from the 8 T scan of the $125\ \mu\text{m}$ track was, therefore, multiplied by this value, and it can be seen in Fig. 8.10 that it now overlaps almost perfectly with $J_c(\phi)$ of GB3.

At this point a discussion about the employed voltage criterion for the measurements on isolated grain and GBs is warranted. As described in Chap. 5, *bridges* were pat-


Figure 8.10:

Comparison between GB3 and the $125\ \mu\text{m}$ wide (polycrystalline) track. At $\mu_0 H = 8\ \text{T}$ $J_c(\phi)$ is plotted of the polycrystalline track (\circ) and GB3 (\square) using a $0.5\ \mu\text{V}$ criterion as well as $J_c(\phi)$ of the $125\ \mu\text{m}$ track using the correct E -field criterion (\triangle).

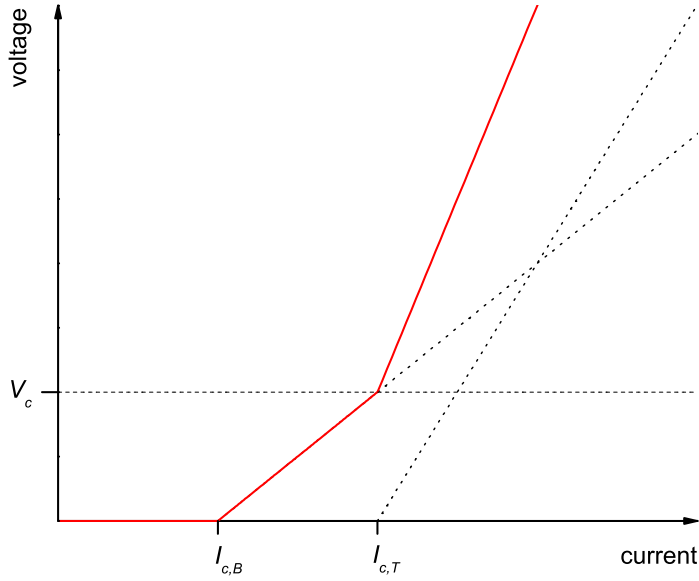
terned using a FIB onto wider *tracks* which had been prepared by conventional photolithography. The FIB bridges are significantly narrower (with a width $w_B \approx 5\ \mu\text{m}$) than the tracks ($w_T = 50\ \mu\text{m}$), hence one would expect that in any case the critical current of the bridge $I_{c,B}$ is exceeded long before that of the track, given by $I_{c,T}$. The length of the tracks $l_T = 600\ \mu\text{m}$, however, is significantly higher than that of the bridges ($l_B \approx 15\ \mu\text{m}$). As a consequence, even a small electric field can lead to a significant voltage across the track as soon as $I_{c,T}$ is exceeded. It needs to be made sure, therefore, that a voltage criterion is chosen at which the track remains fully superconducting and thus only the properties of the bridge are measured.

This is shown schematically in Fig. 8.11. For simplicity, thermally activated flux motion (see Sec. 2.4.5) has been ignored and only linear current-voltage characteristics due to flux flow are considered. At $I_{c,B} < I < I_{c,T}$ the observed voltage across the track (with the bridge) is only due to dissipation in the bridge. Above $I_{c,T}$, however, the track contributes as well, distorting the obtained value of I_c . It is clear from Fig. 8.11 that a voltage criterion smaller than a critical value V_c has to be chosen in order to avoid this. In the following it will be shown that the employed criterion of $0.5\ \mu\text{V}$ satisfies this condition.

The flux flow resistivity ρ_{FF} is related to the flux flow resistance of a track $R_{FF,T}$ and a bridge $R_{FF,B}$ via

$$\rho_{FF} = \frac{w_T d}{l_T} R_{FF,T} = \frac{w_B d}{l_B} R_{FF,B}, \quad (8.2)$$

where d is the film thickness. Here the case of the bridge within a single grain is

**Figure 8.11:**

A schematic $V(I)$ -curve of a track with a (narrower) bridge patterned onto it. The measured voltage is drawn in red. Note that in this idealised picture I_c is given as the current at the onset of the voltage drop, not as the current at a certain criterion voltage > 0 .

considered, which can be expected to have approximately the same flux flow resistivity as the track. In the sample with the isolated grain it is more likely that $I_{c,T}$ is not sufficiently high, rather than in samples with single GBs. With above values for the bridge and track dimensions Eq. (8.2) leads to $R_{FF,T}/R_{FF,B} = 4$, i.e. the flux flow resistance of the track [which gives the slope of the corresponding $V(I)$ -curve] will be notably higher than that of the bridge. This is indicated in Fig. 8.11 by the higher slope of the dotted line originating from $I_{c,T}$, which represents the voltage generated in the track, compared to that originating from $I_{c,B}$.

Using Eq. (8.2) a value for ρ_{FF} can be obtained from the linear part of the $V(I)$ -curves measured on the polycrystalline tracks.⁵ This gives flux flow resistivities between 5×10^{-12} and $2 \times 10^{-11} \Omega \text{m}$ for different field configurations and magnitudes. The values do not depend notably on track width.

As can be seen in Fig. 8.11 the critical voltage, above which dissipation in the track

⁵These are the $1000 \mu\text{m}$ long tracks which were used to obtain the width-dependence of J_c presented in this chapter. These tracks do not contain FIB bridges.

(and not only in the FIB bridge) occurs, follows from⁶

$$\begin{aligned} V_c &= R_{FF,B}(I_{c,T} - I_{c,B}) \\ &= \frac{l_B}{w_B d} \rho_{FF} \left(\frac{w_T}{w_B} - 1 \right) I_{c,B}. \end{aligned} \quad (8.3)$$

Typical values for V_c between 10 and 40 μV are obtained for the samples with the FIB bridges, well above the employed 0.5 μV criterion.

Further evidence that the critical current density measured is in fact that of the bridges, comes from their orientation with respect to the tracks. As can be seen in Fig. 5.2(b), bridges are typically not parallel to the tracks. The samples were mounted such that when the goniometer was rotated to $\phi = 0^\circ$ the track was parallel to the applied field. One would, therefore, expect to see a maximum in in-plane scans at a value of $\phi \neq 0^\circ$, where the bridge, rather than the track, is aligned with the magnetic field. This was in fact observed. The obtained ϕ -scans were then shifted by the angle between track and bridge, as obtained from FIB/SEM micrographs, which led to the curves presented in Sec. 7.3.2, which exhibit maxima at $\phi \approx 0^\circ$.

8.5. Summary and Conclusions

In measurements of $J_c(H)$ with fields applied perpendicular to the film plane it was confirmed that J_c depends on track width at low fields only. Hysteretic behaviour was also found for the polycrystalline tracks, and its extent showed a width dependence consistent with the results obtained on isolated grain boundaries.

In in-plane measurements the same two regimes can be distinguished for polycrystalline tracks as those that have been identified in the case of the isolated grain and GBs (see Sec. 7.4): (1) low H independent of ϕ , as well as high H around the force free orientation and (2) high fields around the maximum Lorentz force configuration.

In regime (1) the critical current density decreases with decreasing track width. In (2), on the other hand, all track widths give the same J_c . This is consistent with data from the isolated GBs, which only in regime (1) have an inferior J_c compared to the grain. A GB limitation of the critical current density is, therefore, responsible for its width

⁶ $I_{c,B}$ was obtained from an extrapolation to zero of the linear part of the $V(I)$ -curves obtained from the single grain, rather than from a voltage criterion.

dependence, which persists up to and beyond fields of 8 T. This behaviour leads to the interesting result that the in-plane anisotropy depends on track width at high but not at low fields. One can conclude that in applications with a strong in-plane component of the field the effect of GBs must be taken into account even at high H .

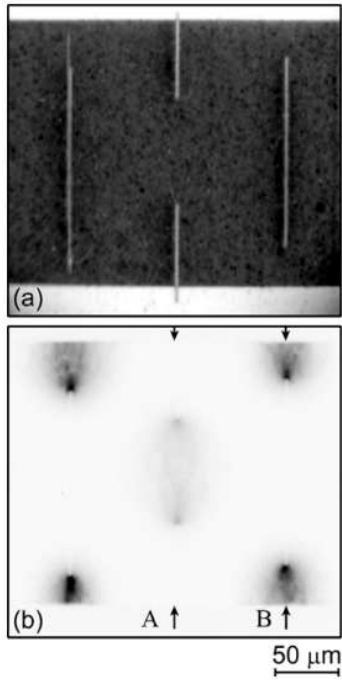
9 Low-Temperature Scanning Laser Microscopy of MOD CCs

Low-temperature scanning laser microscopy (LTSLM) allows one to locate areas on a sample with reduced current carrying capacity. As it can be performed under applied fields, LTSLM is a powerful complementary technique to transport measurements. This fact was exploited for this chapter, which presents LTSLM maps and J_c data obtained from the same RABiTS MOD sample.

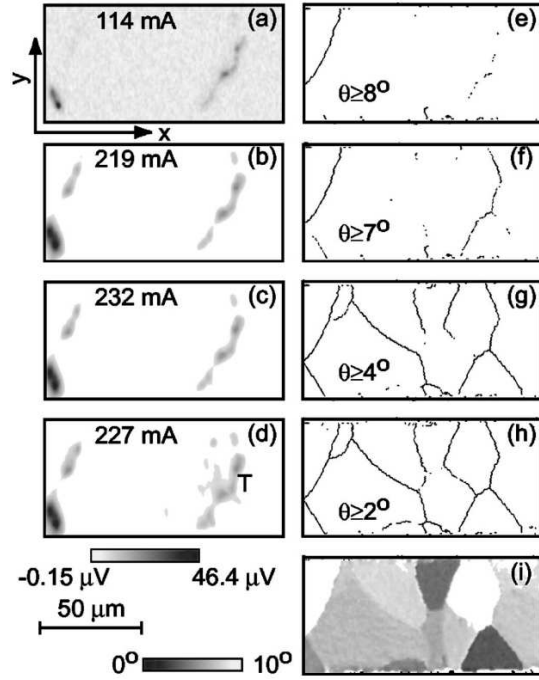
In Sec. 9.1 previous studies using laser scanning are reviewed. This is followed by the results obtained for this thesis by LTSLM (Sec. 9.2) and transport measurements (Sec. 9.3).

9.1. Previous Studies

In order to model defects Abraimov *et al.* [204] made cuts by a FIB in a YBCO film grown on a SrTiO₃ substrate, as shown in Fig. 9.1(a). An LTSLM image gave a strong voltage response δV in areas directly next to the cuts [Fig. 9.1(b)]. At first thought it might appear surprising that pronounced dissipation occurs in intact regions, while no δV is recorded in the damaged areas. One has to consider, however, that the cuts were made through the entire thickness of the YBCO layer, suppressing superconductivity completely; this is why no difference in V was measured when the cuts were hit by the beam. Due to percolative current flow around the cuts, the current density is particularly


Figure 9.1.:

FIB cuts acting as artificial defects. (a) Photo and (b) LTSLM image (the current was applied horizontally; adapted from [204]).


Figure 9.2.:

(a)–(d) LTSLM maps of a coated conductor obtained at different bias currents (in the horizontal direction). (e)–(i) EBSD GB misorientation maps of the same track [205].

high next to them. As a consequence, a high voltage response was recorded in these areas.

LTSLM maps obtained on a RABiTS coated conductor revealed a strong correlation between areas of enhanced voltage response and the grain boundary network as imaged by EBSD [205]. It can be seen in Fig. 9.2 that dissipation occurred in two channels along GBs with significant misorientation, oriented approximately perpendicular to the bias current. It is consistent with the study on artificial defects mentioned above that δV was most pronounced right *next* to the boundary with the highest misorientation angle [bottom left of Fig. 9.2(b)–(d)].

Abramov *et al.* [206] studied the influence of magnetic fields applied in different directions on the voltage response of a RABiTS coated conductor. The results are highly relevant for this thesis. As can be seen in Fig. 9.3(a) dissipation occurred mainly at or near grain boundaries (the position of which had been determined by EBSD) for fields perpendicular to the film plane.

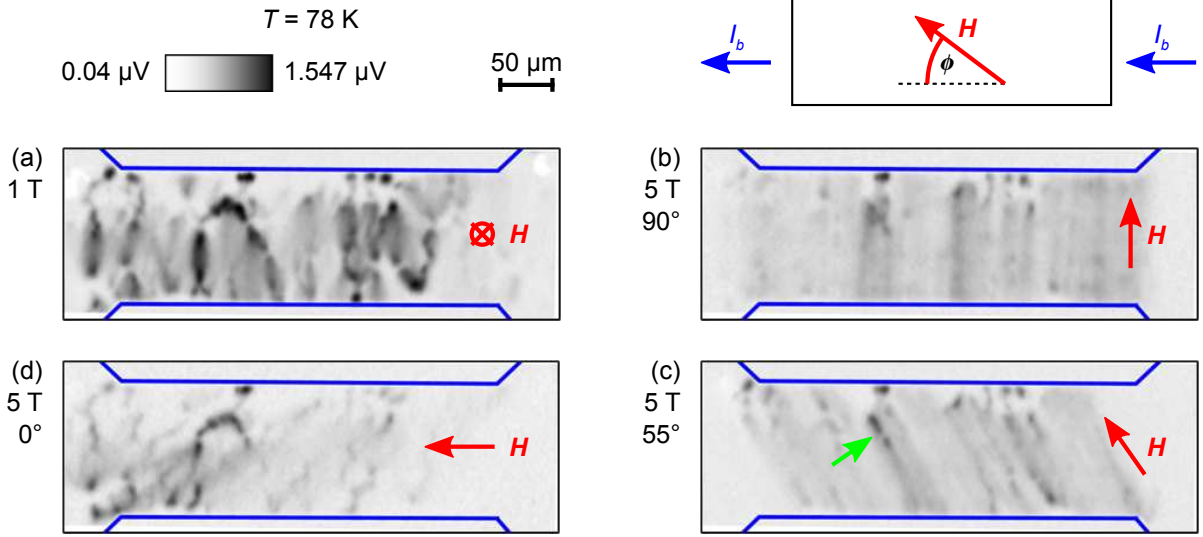


Figure 9.3.: LTSLM images of a RABiTS conductor. (a) Field perpendicular to the film plane, (b)–(d) fields in-plane. (Images courtesy of D. Abraimov.)

A very different picture is found for fields in-plane. At $\phi = 90^\circ$, corresponding to macroscopic maximum Lorentz force, $\delta V(x, y)$ did not replicate the GB network [see Fig. 9.3(b)]. Instead, dissipation occurred in the whole track and lines approximately parallel to the applied field are seen. These flux jets originate from low J_c regions, consistent with previous results [204]. The situation is similar at $\phi = 55^\circ$, where the first GBs show up, however, when the field is aligned parallel to them [indicated by the green arrow in Fig. 9.3(c)]. In the map obtained at macroscopic force free (FF) orientation, shown in Fig. 9.3(d), the situation found for $H \perp$ film plane is recovered, with $\delta V(x, y)$ being determined by the GB network.

These results are in good agreement with the transport measurements presented in Chaps. 7 and 8, which showed a GB limitation around FF while the properties of the grains determined J_c around maximum Lorentz force orientation.

9.2. LTSLM

Two samples (labelled L1 and L2) were cut from the same American Superconductor RABiTS MOD tape used for the experiments in Chaps. 7 and 8. One track $300 \mu\text{m}$ long and $100 \mu\text{m}$ wide was patterned onto each sample for combined LTSLM investigations and transport measurements.

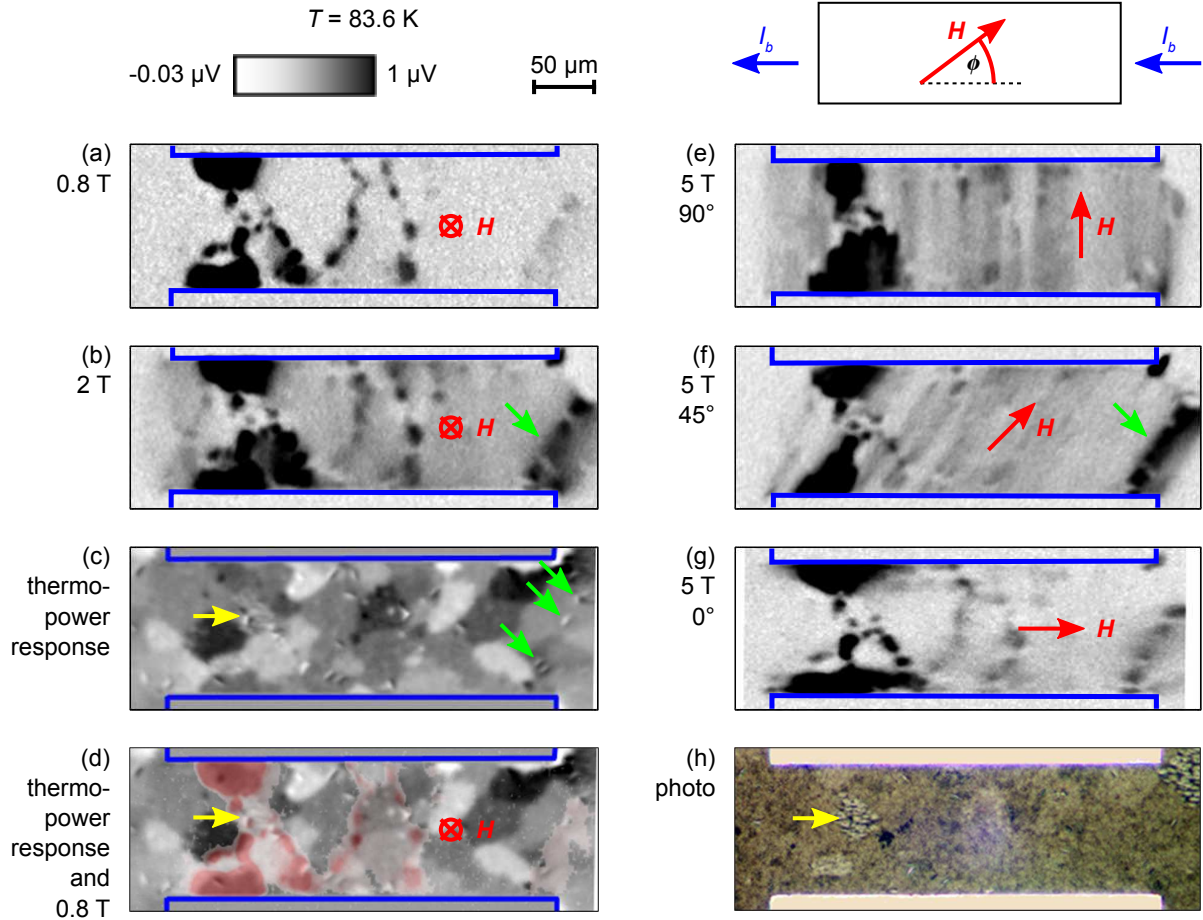


Figure 9.4.: (a), (b) and (e)–(g) LTSLM maps of L1 at different magnitudes and orientations of applied field. (c), (d) Thermoelectric images showing the grains. (h) Photo of the sample surface.

Laser scanning was performed by Dmytro Abraimov with magnetic fields applied both perpendicular to the film surface and in-plane. The resulting maps for sample L1, acquired at a nominal temperature of 83.6 K, which corresponds to a sample temperature of 85 K,¹ are shown in Fig. 9.4.

¹Due to radiation effects present in an optical cryostat, the nominal temperature differs from the actual sample temperature. $T = 85 \text{ K}$ was chosen because at elevated temperatures J_c and the risk of damaging the track in the case of a temperature instability are lower compared to liquid nitrogen temperature.

9.2.1. Fields Perpendicular to the Film Surface

The LTSLM images for $H \perp$ film plane [Fig. 9.4(a), (b)] showed a strong voltage response in the left part of the track. The reason for this is a grain with a high out-of-plane tilt, which is indicated by a yellow arrow in the map obtained in thermoelectric imaging (TEI) mode and in a photo [Fig. 9.4(c), (h)].

A region of suppressed critical current density leads to microscopic currents being focused in the neighbouring areas due to current percolation. As discussed in Sec. 9.1 in such a situation a strong δV is observed not on the low J_c area, but in its vicinity. This is indeed what was found in the maps of L1, as can be seen in Fig. 9.4(d), where the voltage response at $\mu_0 H = 0.8$ T is overlaid on the TEI map.

Dissipation was also detected in three other areas. Two of them are channels in the centre of the maps across the whole track width, most probably related to grain boundaries of a certain misorientation, similar to the results in Fig. 9.2. This is supported by the fact that the voltage response is higher at $\mu_0 H = 0.8$ T than at 2 T, where less GB limitation can be expected.

The fourth dissipative zone is located at the very right of the track [indicated by a green arrow in Fig. 9.4(b)]. It is not caused by GBs, but instead by a number of a -axis grains, placed close together [green arrows in Fig. 9.4(c)]. It has been reported previously [204] that the impact of defects on δV is significantly enhanced if they are located in close proximity.

9.2.2. Fields In-Plane

LTSLM images obtained with fields parallel to the film plane are presented in Fig. 9.4(e)–(g). All three maps again show the strongest voltage response near the highly misaligned grain, which reduces the influence of other sample features or might even conceal them completely. At macroscopic maximum Lorentz force [Fig. 9.4(e)] δV is rather homogeneous over the entire rest of the track with only a weak fine structure consisting of lines approximately parallel to H , similar to Fig. 9.3(b). Note that in this field configuration flux lines span the whole width of the track and the Lorentz force is oriented perpendicular to the film surface. If a vortex segment crosses a region of low J_c the whole flux line is more likely to de-pin and move through the thickness of the film, causing the observed lines of δV parallel to H .

The spatial distribution of the voltage response changes significantly as the field is

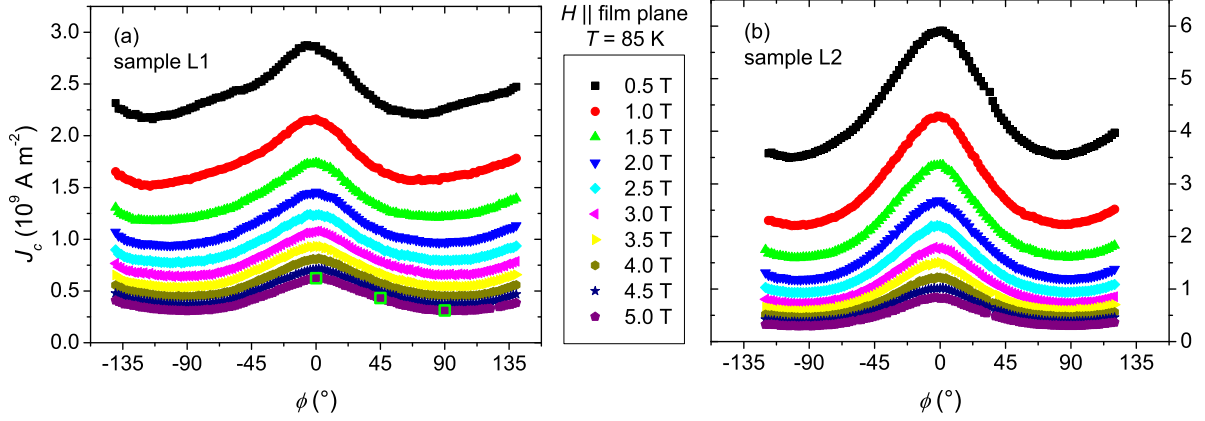


Figure 9.5.: Critical current densities of samples L1 and L2 obtained from transport measurements with magnetic fields swept in-plane. In (a) the field configurations for which LTSLM maps have been obtained (see Sec. 9.2.2) are indicated by green squares.

rotated in the sample plane. At $\phi = 45^\circ$ strong dissipation is detected in the area of the a -axis grains, which are oriented in this direction [indicated by a green arrow in Fig. 9.4(f)]. At the force free configuration [Fig. 9.4(g)] the two grain boundary sections in the centre of the track, which have been completely absent at the other two in-plane orientations, become visible. This result is consistent with Fig. 9.3(b)–(d) and the GB limitation of J_c at FF up to high fields discussed in Chaps. 7 and 8.

9.3. Critical Current Densities

The transition temperatures of L1 and L2 were 92.4 and 92.1 K, respectively. The critical current densities were determined using a $0.5 \mu\text{V}$ criterion.

Shown in Fig. 9.5(a) are in-plane measurements performed on sample L1 at $T = 85 \text{ K}$, i.e. the same temperature at which LTSLM images have been obtained. The usual measurement geometry applies (see Fig. 6.2).

The scans show the expected maximum and minima. While the high field curves are smooth, $J_c(\phi)$ obtained at low H exhibits a certain asymmetry with almost linear sections and extrema shifted to lower values of ϕ . The misaligned grain discussed above is the most likely explanation for this behaviour. As currents percolate around it, they flow in directions different from the macroscopic current direction. Consequently, the orientations where the Lorentz force reaches a minimum or a maximum are shifted. Furthermore, its strong voltage response in LTSLM maps overshadows that of other

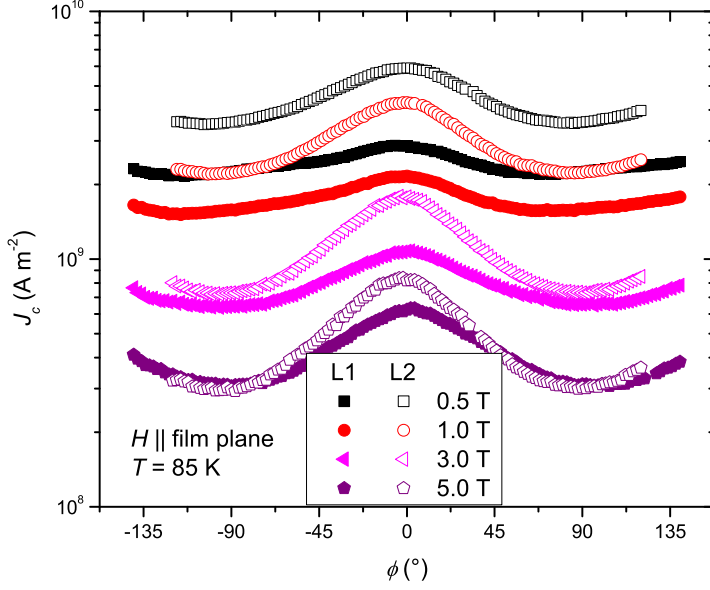


Figure 9.6: Comparison between samples L1 and L2.

features, as discussed in Sec. 9.2.2, which limits the usability of sample L1.

During preparation of L2 care was taken, therefore, to place the track in the area which—from visual inspection—appeared most homogeneous. This approach proved successful, as the critical current density measured on this sample was significantly higher than that of L1, by a factor of ~ 2 at $\mu_0 H = 0.5$ T. As can be seen in Fig. 9.5(b) the obtained ϕ -scans were perfectly symmetric, confirming the good quality of the sample.

Figure 9.6 compares the measurements on the two samples at selected fields. The plot has two striking features. Firstly, at low fields J_c of L1 is suppressed compared to L2 at all angles. This is consistent with the latter track not containing any significantly misoriented grains. Secondly, at $\mu_0 H = 5$ T the curves from the two samples overlap around maximum Lorentz force.

Both observations are consistent with the results presented in Chaps. 7 and 8. A GB with low J_c leads to a reduction in the overall critical current density at low fields regardless of angle and at high fields around FF. Similar behaviour as in Fig. 9.6 was observed at $T = 77.35$ K (not shown), even though complete crossover at $\phi \approx 90^\circ$ did not occur up to $\mu_0 H = 5$ T, the highest field investigated. This agrees with expectations, as the crossover field is higher at lower T .

Not surprisingly, a suppressed J_c of L1 at low fields was also found for fields \perp film plane (not shown). In agreement with its stronger GB limitation L1 showed a more pronounced hysteresis for increasing and decreasing fields compared to L2.

The above observations confirm that L2 would be a suitable candidate for LTSLM investigations. These measurements, however, were not finished by the time this thesis was written.

9.4. Summary and Conclusions

An MOD sample was investigated by both low-temperature scanning laser microscopy and transport measurements. A strong current limitation in the form of a highly misaligned grain was found, which could well be the reason for a slight asymmetry in $J_c(\phi)$ measurements and a reduced overall critical current density. Additionally, dissipation which is (most probably) due to GBs and a -axis grains was detected by laser scanning.

In LTSLM images obtained with fields applied in the film plane the strongest voltage response was observed for defects aligned with H , consistent with previous observations. Of particular interest is the map obtained at the macroscopic force free configuration, where dissipation at grain boundaries was observed, corroborating the fact that at this field orientation GBs limit J_c even at high fields, as was postulated in Chaps. 7 and 8. Laser scanning, therefore, provided a confirmation for the results obtained from transport measurements.

10 MOCVD CCs

One of American Superconductor's main competitors is SuperPower. Their coated conductors differ from American Superconductor's products in several aspects. In order to achieve crystallographic texture SuperPower grows a buffer layer by IBAD (rather than employing RABiTS as a substrate). The superconducting layer is deposited by MOCVD (compared to MOD). Naturally it appeared worthwhile to investigate the properties of a SuperPower coated conductor in detail and to compare them to those of an American Superconductor tape.

In the first part of this chapter results of previous studies are presented. This includes investigations of SuperPower tapes and other, similar, coated conductors. Following this a brief introduction to a phenomenon called vortex channelling is given. In the next sections the results obtained for this thesis are presented. The sample's microstructure was investigated by TEM, FIB and XRD, as discussed in Secs. 10.2 and 10.3. The largest section of this chapter covers angular measurements of the critical current density (Sec. 10.4). This includes investigations of polycrystalline tracks and an isolated grain boundary. In Sec. 10.5, finally, the SuperPower coated conductor is compared to American Superconductor's tape.

10.1. Previous Studies

In this section previous results are discussed which have been obtained on coated conductors produced by SuperPower’s MOCVD process and other, comparable techniques. In particular the samples analysed in Refs. [207, 152] are very similar to the SuperPower tape which has been measured for this thesis. Furthermore, vortex channelling in vicinal films is discussed.

10.1.1. Structural Properties

SuperPower’s MOCVD samples do not comprise of a pure YBCO layer, but are doped with other rare earth elements (e.g. Sm) [62], hence the term “REBCO”. The superconducting layer contains secondary phases (or “nano-precipitates”), usually made up of rare earth oxides, which can act as flux pinning centres [208, 209].

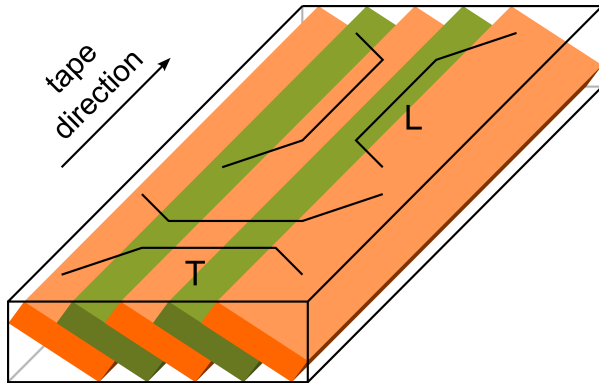
Using TEM the REBCO matrix was found to be tilted by $\sim 2^\circ$ with respect to the buffer layer [207, 152]. This means that the tape is slightly vicinal.

The films show a very rich microstructure. Holesinger *et al.* [152] and Chen *et al.* [207] analysed it in detail using TEM, and they found the following defects:

Planar defects They are made up of layers of nanocrystalline $(\text{Y, Sm})_2\text{O}_3$ precipitates, each of which is 10–15 nm in size. The planes are, in general, tilted by 5° with respect to the REBCO *ab*-planes and by 7° with respect to the buffer layer interface.¹ It is these precipitates which are believed to act as very effective pinning centres in these MOCVD films and thus contribute most to their high critical current density. As a consequence, the defect planes are also responsible for the peak shift in $J_c(\theta)$ -scans (see Secs. 10.1.2 and 10.4.2). The average spacing between the planes is 20–30 nm.

Nanoplates They consist of continuous crystalline phases of YCuO_2 . Their short dimension is perpendicular to the film normal, i.e. they are plates perpendicular to the film surface.

¹In the study presented in Ref. [152] films with one to four REBCO layers, achieved by multiple passes through the MOCVD reactor, were analysed. Whereas the vicinal angle was the same in all deposition layers, it was found by cross-sectional TEM that the nanocrystalline planes in the lowest layer only were *not* tilted. This seems to be the exception to the rule, however, as also the results presented in this thesis indicate an inclination of the planar defects (see Sec. 10.4.2).

**Figure 10.1:**

This schematic shows the direction of an L track (longitudinal) and a T track (transverse) with respect to the tape direction and, thus, the vicinity. The ab -planes are drawn as orange and green layers.

Oriented composite defects a -axis oriented REBCO grains, sandwiched by secondary phases consisting of $(Y, Sm)_2O_3$, $(Y, Sm)CuO_2$ or CuO , make up these defects.

Threading dislocations They are c -axis oriented and continuous across multiple deposition layers, thus they can reach significant lengths.

Stacking faults in the ab -planes Those defects were found in high numbers.

10.1.2. Critical Current Densities

Because the tapes are vicinal two directions of current flow must be distinguished, determined by how a track is patterned onto the sample (see Fig. 10.1). According to the convention in Ref. [97] they are defined as:

L track: in the longitudinal direction, i.e. along the length of the steps. This corresponds to the tape direction and, thus, the direction in which current would flow in most applications.

T track: in the transverse direction, i.e. across the steps.

Both Chen *et al.* [207] and Holesinger *et al.* [152] performed angular J_c measurements on L tracks in which the applied magnetic field was rotated in a plane perpendicular to the track, described by the angle θ . They reported a shift of the peak in the critical current density by several degrees away from the ab -planes, where it would be expected due to intrinsic pinning [210]. This result is reproduced in Fig. 10.2. The offset was explained by the vicinity and the tilted planar defects (see Sec. 10.1.1). It is most pronounced at low fields and temperatures. At 1 T and 10 K a shift of $\sim 12^\circ$ is observed, which is reduced to $\sim 3^\circ$ and $\sim 2^\circ$ as the temperature is increased to 50 K and 77 K,

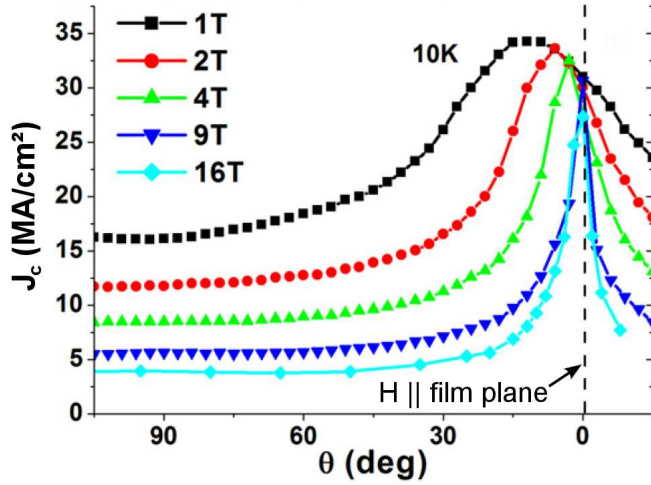


Figure 10.2:

An angular measurement on a SuperPower tape at $T = 10$ K by Chen *et al.* [207]. $\theta = 0^\circ$ corresponds to $H \parallel ab$, $\theta = 90^\circ$ to $H \parallel c$. Note the shift of the maximum as the magnitude of the field is reduced.

respectively [207]. Increasing the field at a fixed temperature also reduces the offset; at 10 K it disappears at 9 T, i.e. the maximum in J_c is found for $H \parallel ab$ at and above this field. A similar behaviour is reported in Ref. [152]. The exception is the bottom layer of a film consisting of several deposition layers analysed in the latter study, where virtually no peak shift is found. The fact that in this sample the precipitate planes were *not* tilted (see footnote on page 143) confirms the connection between peak offset and plane tilt. The bottom layer was still vicinal though, and this on its own should lead to a (very small) peak shift, which in fact has been observed [211].

A simple explanation for the peak shift is that the precipitate planes act as correlated pinning centres at low fields [207], moving the maximum in J_c to $H \parallel$ defect planes. As the field is increased correlation is lost and intrinsic pinning dominates, hence the peak shifts towards $H \parallel ab$. Or—in simpler terms—at elevated fields (and high vortex densities) the number of precipitate planes is not sufficiently high in order to have a significant effect on pinning. The peak thus shifts to where it would be in the absence of defects.

According to this model one would expect the maximum of $J_c(\theta)$ to be shifted with respect to the film plane by 7° at low fields and by 2° at high fields. As mentioned above, however, an offset of up to $\sim 12^\circ$ (at 1 T and 10 K, Ref. [207]) has been found. Also, a similar peak shift has been observed in a previous study on coated conductors by Maiorov *et al.* [212], where the YBCO layer had also been grown on a vicinal IBAD substrate [213]. Their samples showed Y_2O_3 precipitate planes which—unlike the $(Y, Sm)_2O_3$ planes in the SuperPower samples discussed in Refs. [207, 152]—were parallel

to the YBCO ab -planes. This implies that an angular offset between pinning related to planar defects and intrinsic pinning alone cannot be the reason for the peak shift in $J_c(\theta)$.

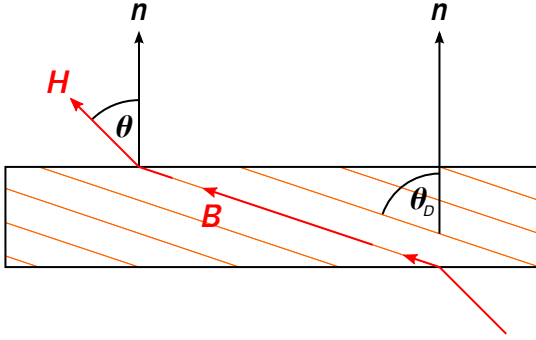
Both Maiorov *et al.* and Chen *et al.*, therefore, concluded that in the field range where the peak shift is observed the internal flux density \mathbf{B} (which corresponds to the direction of vortices) was not parallel to the applied field \mathbf{H} . Consequently, the vortices are aligned with the CuO_2 planes or the defect planes when \mathbf{H} is several degrees off $\parallel ab$.

A misalignment between \mathbf{H} and \mathbf{B} as the reason for a peak shift in $J_c(\theta)$ has first been postulated by Silhanek *et al.* [214], based on magnetic measurements on YBCO and NbSe_2 single crystals. They presented compelling evidence that sample geometry and anisotropy can lead to a shift of the peak in either direction, depending on the sample's aspect ratio and the value of the material's electron mass anisotropy. Their samples contained columnar defects introduced by Au^{26+} ion irradiation, which were not aligned with a main crystallographic direction, thus breaking the symmetry. These defects act as "passive internal field detectors", i.e. rather than changing the internal \mathbf{B} direction (given by the angle θ_B) further, they indicate at what orientation of \mathbf{H} (described by θ) the vortices are parallel to them. If this is the case (i.e. $\theta_B = \theta_D$, where θ_D is the orientation of the defects), a maximum occurs in the irreversible magnetisation $M_i(\theta)$ at $\theta = \theta_{\max}$. $M_i(\theta)$ is (almost exactly) proportional to $J_c(\theta)$. The difference between \mathbf{H} and \mathbf{B} orientations is the same as between θ_{\max} and θ_D . Since θ_D is known and θ_{\max} is obtained from $M_i(\theta)$ curves, the B - H offset can be deduced from $\theta_B - \theta = \theta_D - \theta_{\max}$. It is important to point out that the maximum M_i (and J_c) *always* occur when the vortices (and the direction of \mathbf{B}) are parallel to the defect planes. At low fields, however, in general $B \parallel H$ is not fulfilled, hence the shift of the $M_i(\theta)$ peak.

By minimising the free energy $G(B)$ with respect to B [34], the shift can be calculated by [214]

$$\sin(\theta_B - \theta) = -\frac{f(\nu_y, \nu_z, \epsilon) \sin(2\theta_B) \ln h + 1}{8\kappa^2 h}. \quad (10.1)$$

Here $f(\nu_y, \nu_z, \epsilon) = (1 - \nu_z) - (1 - \nu_y)\epsilon^2$ describes the effects of the sample geometry (given by the components ν_x , ν_y and ν_z of the tensor of the demagnetisation factor $\hat{\nu}$ at the sample principal axes) and of the electron mass anisotropy (given by $\epsilon = \sqrt{m_{ab}/m_c}$). The value of $f(\nu_y, \nu_z, \epsilon)$ reflects whether the B - H offset is (mainly) determined by the sample geometry or by its anisotropy. $\kappa = \lambda_{ab}/\xi_{ab}$ is the Ginzburg-Landau parameter


Figure 10.3:

This schematic explains the tilt of the vortices (and thus the direction of B) with respect to H . The ab -planes (or the precipitate planes) responsible for the intrinsic (or correlated) pinning are indicated in orange. In the anisotropy dominated case depicted here the vortices are tilted towards the ab -planes. In the sketch $\theta = \theta_{\max}$, hence B is aligned with the planes and $\theta_B = \theta_D$.

and $h = H/H_{c2}$ the reduced field. Whereas the magnitude of the term on the right hand side of Eq. (10.1) also depends on θ_B , κ and h , its sign is determined by $f(\nu_y, \nu_z, \epsilon)$ only. Consequently, three different regimes can be distinguished:

Anisotropy dominated case: $f > 0$ and $\theta_B > \theta$. Due to the sample's anisotropy the vortices tilt towards the ab -direction, which allows them to reduce their free energy [212]. In order to align B with the columnar defects and obtain the maximum M_i the applied field H must move closer to the c -axis [215]. This is illustrated in Fig. 10.3. As a consequence B is ahead of H .

Geometry dominated case: $f < 0$ and $\theta_B < \theta$. In thin and not too anisotropic samples the demagnetisation effect dominates. Flux lines, thus, move towards the sample normal n in order to reduce their length [212], the peak in $M_i(\theta)$ shifts towards the ab -planes, and B lags behind H .

Compensated case: $f = 0$. Geometry and anisotropy compensate for each other, hence no offset between H and B is observed.

Using YBCO and NbSe₂ single crystals, which have a (comparably) high and low anisotropy, respectively, Silhanek *et al.* could prove their model [214]. For YBCO samples with $f > 0$ the $M_i(\theta)$ peak shifts towards the c -axis, for NbSe₂ with $f < 0$ towards the ab -planes. YBCO single crystals which are very thin, compared to their lateral dimensions, constitute the compensated case with $f \approx 0$, and indeed no peak shift is observed for them.

As can be seen from Eq. (10.1) the B - H offset also depends on the magnitude of the applied field. It is most pronounced at low H and disappears at high H , where the term $-\mathbf{B} \cdot \mathbf{H}$ dominates the free energy [212]. In the case of transport measurements [212]

at 75.5 K no shift was observed beyond $\mu_0 H \sim 2\text{--}3\text{ T}$ (corresponding to $h \sim 0.02\text{--}0.03$). This value agrees well with $h \sim 0.02$, reported as the reduced field below which the misalignment between \mathbf{B} and \mathbf{H} is relevant by Silhanek *et al.* [214].

It needs to be pointed out that the (vicinal) ab -planes and the precipitate planes in the MOCVD samples have a qualitatively similar effect on the $J_c(\theta)$ peak shift. Even though the specific pinning mechanism is different, both act as directional pinning centres and hence tilt the vortices with respect to the direction of \mathbf{H} . The peak shift is still visible in the absence of one of the two types of pinning. This is confirmed by an earlier study [216] in which the YBCO layer was grown on miscut LaAlO_3 single crystal substrates. Columnar defects were reported, but no planar defects. Nevertheless the peak shift was also seen in these samples, even though to a smaller extent, which is due to the vicinal angle being only $\sim 1.6^\circ$.

It is, however, essential that the ab -planes or defect planes are tilted with respect to the film surface; the effect would not be seen in c -axis oriented films, where the maximum J_c is always found for $\mathbf{H}||ab$ due to the higher symmetry. The columnar defects in Ref. [214], on the other hand, are mere indicators of the vortex direction but they do not tilt the vortices further; the offset between \mathbf{H} and \mathbf{B} would also occur without them.

Maivorov *et al.* [212] also performed angular measurements on a T track. They gave symmetric scans with no peak shift, similar to what is seen in c -axis oriented films.

The out-of-plane anisotropy $J_c^{B||ab}/J_c^{B||c}$ describes the ratio of J_c for fields applied in the plane of the film and perpendicular to it. In the case of SuperPower MOCVD samples it shows a rather peculiar behaviour: $J_c^{B||ab}/J_c^{B||c}$ was found to decrease as the temperature was reduced from 77 K to 50 K and to increase again at even lower T [207].

10.1.3. Vortex Channelling in Films Grown on Vicinal Single Crystal Substrates

Vortex pinning, and thus critical current density, depend on various factors. Intrinsic pinning is a material property due to the layered structure of HTS. Extrinsic pinning, caused by a variety of possible pinning centres, also contributes to the “pinning landscape”. On top of this, the sample’s geometry influences structure and stability of the FLL.

Angular J_c measurements on films grown on single crystal substrates (where the sample is rotated in an applied magnetic field, see Sec. 2.4.10) provide a good way

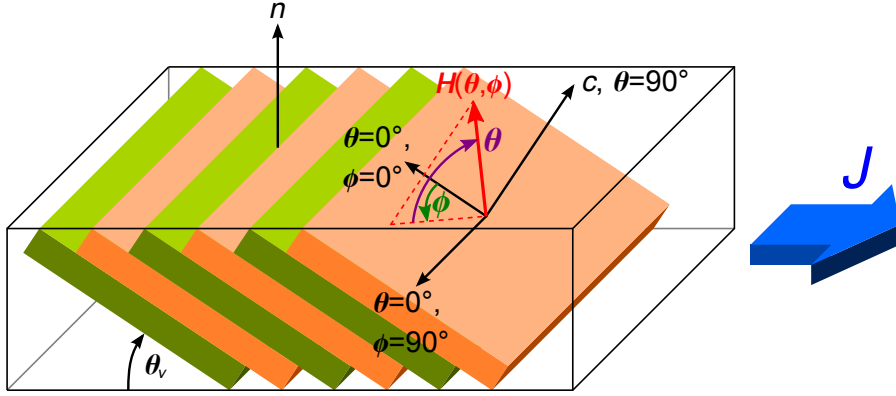


Figure 10.4.: Definition of the angles ϕ and θ for measurements on a T track in a vicinal film, as used in Secs. 10.1.3 and 10.4.4. The orange and green layers represent the ab -planes, n is the sample normal and c the crystallographic c -axis (after [217]).

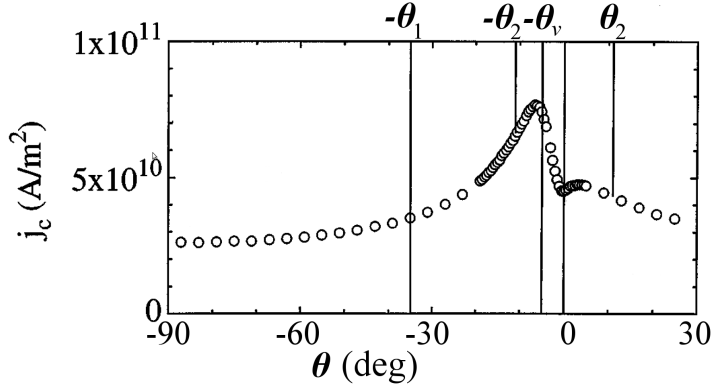
to investigate the pinning mechanisms present. It is difficult, if not impossible, however, to separate the different contributions in measurements on c -axis films (i.e. films where the c -axis is perpendicular to the film surface). This is because the main crystallographic directions coincide with the sample boundaries, and J_c maxima related to different pinning mechanisms occur at the same angle. One way to overcome this problem is to grow the superconducting layer on miscut (or vicinal) substrates, where the c -axis is tilted by a vicinal angle θ_v with respect to the film normal. Consequently, the symmetry is broken and intrinsic pinning and surface pinning are found at different orientations of applied field.

Due to the vicinality it is convenient to define the angles ϕ and θ in a slightly different way with respect to the sample edges than in the rest of this thesis. The convention used in this section and in Sec. 10.4.4 only is depicted in Fig. 10.4. In this way ϕ and θ relate to the ab -planes of a vicinal film in the same way as in the original convention (see Fig. 6.2) when applied to a c -axis film². In fact the new definition reverts to the original one for $\theta_v = 0^\circ$.

In angular scans on tracks patterned in the transverse direction of vicinal films a minimum was found, in addition to minima related to sample anisotropy and maximum Lorentz force. The feature is seen in θ -scans at both $\phi = 0^\circ$ and 90° .

In the first case ($\phi = 0^\circ$) the field is rotated from maximum Lorentz force, where B is perpendicular to the current direction, to minimum F_L , where B lies in the film

²Note that there is a 90° offset in θ between the two definitions.


Figure 10.5:

Vortex channelling at $\phi = 0^\circ$ as observed by Berghuis *et al.* [37] in a T track patterned on a vicinal film. The measurement was performed at $T = 25 \text{ K}$ and $\mu_0 H = 1 \text{ T}$. The minimum is offset from the force free maximum by the vicinal angle $\theta_v = 6^\circ$.

plane (and is, thus, parallel to the current direction). The critical current density vs. θ , obtained from such a measurement, is plotted in Fig. 10.5. A minimum in J_c is found at $\theta = 0^\circ$ in close proximity to the maximum at the force free configuration at $\theta = -\theta_v$. This effect was first reported by Berghuis *et al.* [37].

As discussed in Sec. 2.4.9 at $T < T_{cr}$ flux lines consist of pancake vortices in the c -direction and Josephson string vortices parallel to the ab -planes when θ is below a certain value. The angles θ_1 and θ_2 , where this kinked vortex structure emerges and becomes fully developed, respectively, are indicated in Fig. 10.5. At $\theta = 0^\circ$ the whole vortex is string-like. The configuration for $\theta = 0^\circ$, $\phi = 0^\circ$ is sketched in Fig. 10.6(a). One can write a force balance equation [37]

$$f_{p,\text{str}} = j_c \Phi_0 \sin \theta_v. \quad (10.2)$$

Here $f_{p,\text{str}}$ is the pinning force on a string vortex per unit length, which compensates for the Lorentz force acting on it due to the (microscopic) critical current density j_c and the vortex's flux quantum Φ_0 . If strong pinning is assumed, Eq. (10.2) can be written in a bulk version as

$$F_{p,\text{str}} = J_c B \sin \theta_v. \quad (10.3)$$

Consequently, string vortices in a vicinal sample experience a non-zero Lorentz force when $B \parallel ab$, which is directed parallel to the ab -planes [for $\phi = 0^\circ$, see Fig. 10.6(a)]. While intrinsic pinning would lead to a strong barrier against movement in the c -direction, vortices are pinned only weakly for movement parallel to the CuO_2 -planes. This is particularly true for Josephson string vortices, which are more weakly pinned than pancake vortices [37, 195]. As a consequence, at this field configuration flux lines

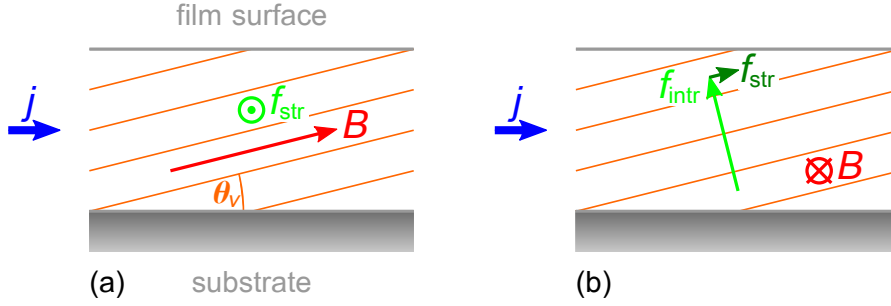


Figure 10.6.: Field configurations with $B \parallel ab$ at (a) $\phi = 0^\circ$ and (b) $\phi = 90^\circ$. In both cases vortex channelling can be observed. The ab -planes are indicated by orange lines. In (a) the Lorentz force on a string vortex f_{str} is directed entirely $\parallel ab$. In (b) it is perpendicular to the film surface with a component f_{intr} , which is compensated for by intrinsic pinning, and a component f_{str} ($\parallel ab$), which is responsible for channelling.

can move easily along a “channel”, suppressing the critical current density. This is why the minimum described above is found in θ -scans. This effect is termed *intrinsic* or *vicinal flux channelling* (compared to vortex channelling due to weak pinning as found in a grain boundary [82]). Note that in a c -axis film it is not possible for a field applied parallel to the CuO_2 planes to cause a Lorentz force which is also parallel to them. Consequently, intrinsic channelling can only be observed in vicinal films.

When the field is swept in θ with $\phi = 90^\circ$ the total Lorentz force on the strings $f_L = j_c \Phi_0$ is constant. The minima and maxima in J_c are related to the material’s anisotropy and layered structure, rather than a change in Lorentz force. As has been shown by Durrell *et al.* [218], the channelling minimum observed in this case overlaps with the intrinsic pinning maximum (see Fig. 10.7).

In this configuration the Lorentz force on the strings is directed parallel to the tape normal, i.e. not in the ab -direction [see Fig. 10.6(b)]. It can, however, be split in two components: f_{intr} parallel c , which is compensated for by strong intrinsic pinning, and f_{str} parallel ab . It is the latter which is responsible for vortex channelling in this case. It follows from geometry that the string pinning force $f_{p,\text{str}}$ is again given by Eq. (10.2).

In angular measurements on vicinal films the critical current density is determined either by pinning of pancake vortices or of Josephson strings, depending on the value of θ . These J_c measurements, thus, allow the separate pinning forces acting on pancakes and strings to be obtained [37, 218].

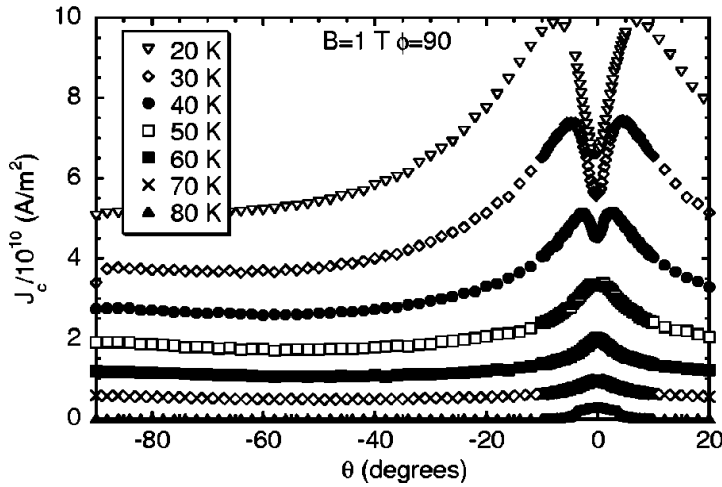


Figure 10.7:

The channelling minimum at $\phi = 90^\circ$, as reported by Durrell *et al.* [218]. In this configuration it occurs at the same value of θ as the maximum due to intrinsic pinning.

10.2. TEM and FIB

In the following sections the results obtained from SuperPower samples for this thesis by TEM, FIB, XRD and transport measurements are presented. Note that their architecture is given in Sec. 4.5.

10.2.1. TEM

A plan-view TEM image, obtained by Suman-Lata Sahonta and presented in Fig. 10.8, shows three separate grains. The grain boundaries, visible as lines of dislocations, are relatively planar. In particular, no meandering was seen, as has been found for films produced by MOD [see Fig. 7.1(b) and 7.4]. The grains in the MOCVD sample as observed by TEM are typically $\sim 3 \mu\text{m}$ in diameter, in good agreement with an EBSD map (see Fig. 10.33).

The high number of parallel lines visible in Fig. 10.8 are twin boundaries. In the centre of the image a large rare earth oxide inclusion is seen at the intersection of the GBs. Such secondary phases, ranging in diameter from ~ 30 to ~ 400 nm were often found at locations where three or more boundaries merge.

10.2.2. FIB Cross Sections

Shown in Fig. 10.9 are images of two cross-sections, prepared and acquired by Focused Ion Beam microscopes. The samples were cut from the same tape which was used for transport measurements (see Sec. 10.4). The Ni-alloy substrate, buffer layers and

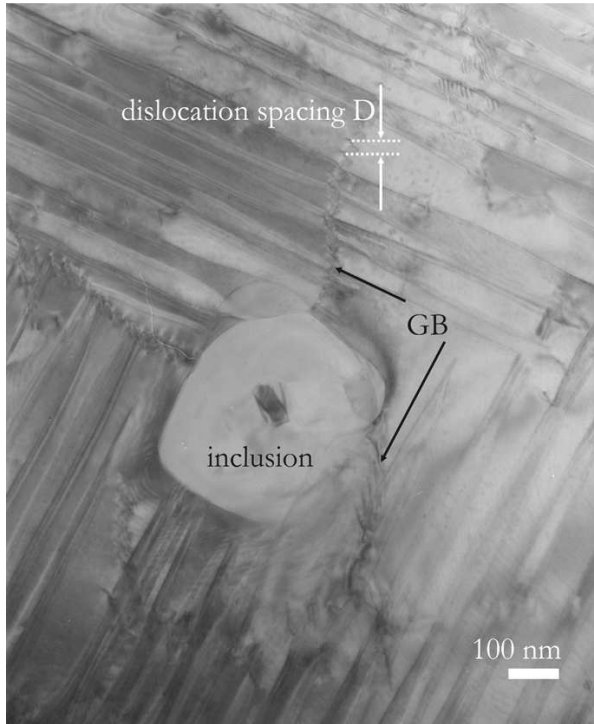


Figure 10.8:
Plan-view TEM image of three grains in an MOCVD sample.

superconducting layer are annotated in Fig. 10.9(a). The Ag layer on this sample had been removed and the surface polished, in order to allow EBSD maps to be obtained (see Sec. 10.4.5). Note the darker area which appears to be an inclusion spanning through almost the whole thickness of the film.

In Fig. 10.9(b) a structure is visible which might be an oriented composite defect (OCD)³. These defects consist of one or more a -axis oriented REBCO grains, sandwiched between secondary phases [(Y, Sm)₂O₃, (Y, Sm)CuO₂ or CuO] [152]. OCDs are significantly bigger than the diameter of a flux line, hence they are unlikely to act as efficient pinning centres (even though a certain amount of surface pinning is conceivable). With their extended structure [they are elongated in a direction perpendicular to the image plane of Fig. 10.9(b)] they can be expected to constitute a certain impediment to current flow. Furthermore, it was shown that if their density becomes too high, they prevent the growth of a connected superconducting layer on top of them in further passes through the MOCVD reactor [152].

³Further analysis by, for example, energy dispersive X-ray (EDX) would be necessary in order to confirm this.

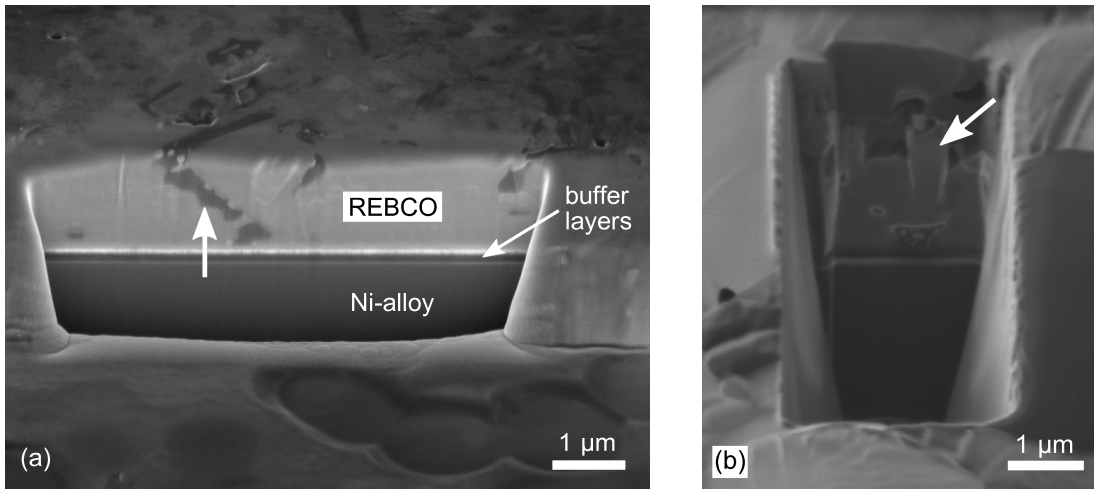


Figure 10.9.: Two FIB cross-sections. (a) The vertical arrow denotes an inclusion (image acquired by Gareth Hughes). (b) This image shows what could well be an oriented composite defect [152], indicated by an arrow. Note that this sample still had a Ag layer on top, visible in dark grey (image acquired by the author).

10.3. XRD – Texture Analysis

In order to quantify the degree of grain alignment x-ray diffraction measurements were performed. It was found that the SuperPower tape has an (even) sharper texture than the American Superconductor tape, which is related to the use of IBAD and RABiTS, respectively.

10.3.1. Out-of-Plane

The out-of-plane alignment was determined from XRD rocking curves, as described in Sec. 6.3. The results for the (003)-, (005)- and (006)-reflections⁴ can be seen in Fig. 10.10. All scans were performed at $\phi = 0^\circ$ and 180° (i.e. beam in a plane parallel to the tape direction) and at $\phi = 90^\circ$ and 270° (i.e. beam in a plane perpendicular to the tape direction).

At $\phi = 90^\circ$ the peaks (found at $\omega = \omega_{\max}$) are shifted to higher values of ω , at $\phi = 270^\circ$ to lower values. This is due to the vicinality of the tape, which has been reported previously (see Sec. 10.1.1). As a consequence a different ω is needed at $\phi = 90^\circ$ and

⁴None of these reflections (nor the {103}-reflection used in the ϕ -scans, see below) have 2Θ -values close to those of the MgO and LaMnO₃ buffer layers. It is, therefore, certain that the data presented in this section relate to the REBCO layer only, not to one of the buffer layers.

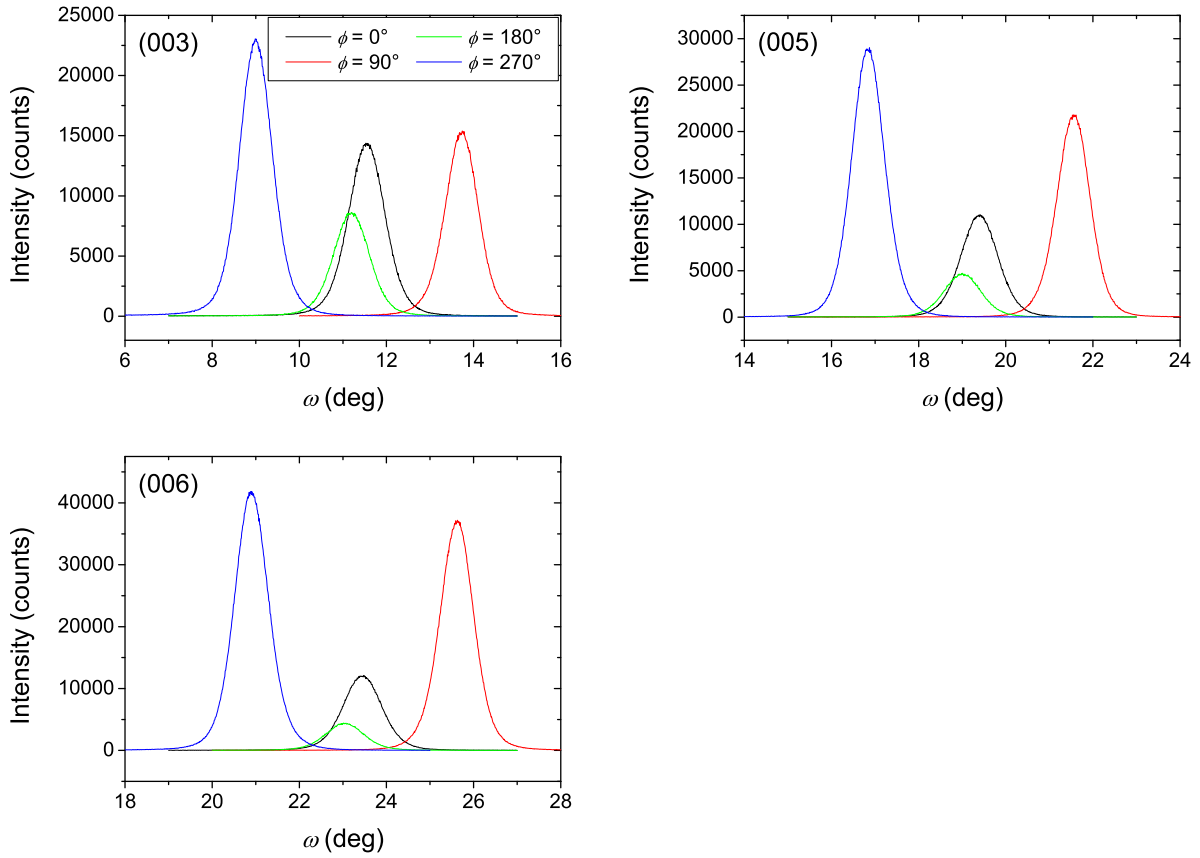


Figure 10.10.: XRD rocking curves for the (003)-, (005)- and (006)-reflections. Note the shift for $\phi = 90^\circ$ and 270° .

270° to bring the ab -planes in the diffraction condition, as is illustrated in Fig. 10.11. The vicinal angle θ_v equals half the offset between the $\phi = 90^\circ$ and the $\phi = 270^\circ$ rocking curves. It was found to be $\theta_v = 2.3^\circ$ – 2.4° . The vicinality is also responsible for the lower count rates when the beam is in a plane parallel to the tape direction ($\phi = 0^\circ$ and 180°): in this configuration the majority of the planes are never in the correct diffraction condition, as they are tilted by $\sim \theta_v$ about an axis parallel to the tape direction. A χ -offset equal to the vicinal angle would have been necessary in order to compensate for the tape's vicinality.

On top of the vicinality a certain grain misalignment is expected, which can be quantified by the FWHM of the rocking curves. For all three diffraction orders analysed, very good values of 1.0 and 0.9° were found in the tape direction and perpendicular to it, respectively. The out-of-plane alignment is, therefore, slightly better in the transverse

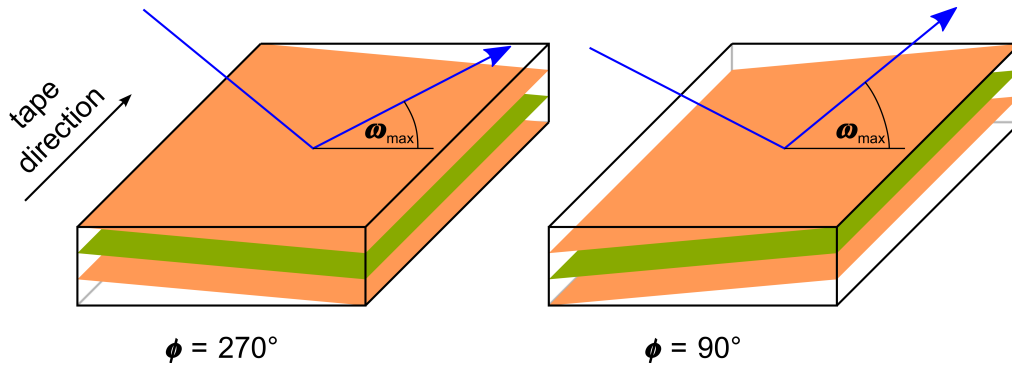


Figure 10.11.: This schematic explains the shift of the XRD rocking curve peaks (found at $\omega = \omega_{\max}$) for different values of ϕ , which is due to the tape's vicinality. The ab -planes are indicated in orange and green, the blue arrows give the direction of the x-ray beam.

than in the longitudinal direction, which is the opposite of what was observed for the American Superconductor tape (see Sec. 8.2.1).

10.3.2. In-Plane

In order to quantify how well the grains are aligned in-plane, ϕ -scans and a pole figure were obtained, both on the $\{103\}$ -reflection. Due to the vicinality the χ -setting had to be optimised for each separate ϕ -scan at $\phi = 0^\circ, 90^\circ, 180^\circ$ and 270° . The peak widths in ϕ (FWHM) were found to be 2.3° – 2.8° .

The pole figure can be seen in Fig. 10.12, which confirms the good in-plane alignment. The poles are slightly shifted upwards (visible in the 2D representation), which is again due to the tape's vicinality. As expected, cuts through the poles in the ϕ -direction resulted in the same FWHM of the peaks as had been derived from the ϕ -scans discussed in the previous paragraph. The fact that the poles are elliptical, rather than circular, is probably related to the x-ray optics. The spot focus is commonly employed for texture work to give approximately the same resolution in both ϕ and χ . The diffractometer used for this work, however, is set on the line focus, which tends to extend peaks in χ but not in ϕ . The advantage of the line focus is better resolution in 2θ and ω .

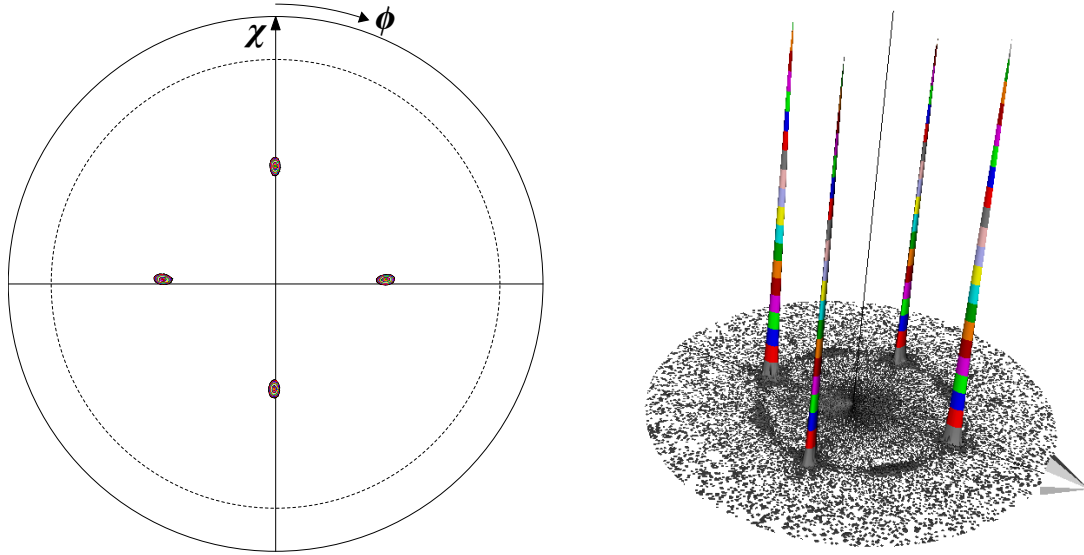


Figure 10.12.: XRD pole figure obtained on the $\{103\}$ -reflection in 2D and 3D representation. The sharp poles indicate a good in-plane grain alignment.

10.4. Critical Current Densities

The T_c values of the samples lay between 89.4 and 89.7 K. These values are slightly lower than those obtained from the American Superconductor samples, which could be due to the Sm doping of the superconducting layer in the SuperPower tape.

All J_c values reported in this chapter were determined using a $0.5 \mu\text{V}$ criterion. A nominal thickness of the superconducting layer of $1 \mu\text{m}$ was used to calculate J_c from I_c , however a certain local variation in thickness has to be expected [208]. Unless stated otherwise the measurements were performed at $T = 77.35 \text{ K}$.

10.4.1. Fields Perpendicular to the Film Surface

The critical current density of two $50 \mu\text{m}$ wide and 1 mm long tracks, patterned in the L (longitudinal) and T (transverse) direction is presented in Fig. 10.13. The field has been applied perpendicular to the film planes. One would expect a suppressed J_c in the T track [97], where currents need to cross from one ab -plane to the next. Consequently, they also need to flow in the c -direction, which shows a reduced J_c [219]. It was a

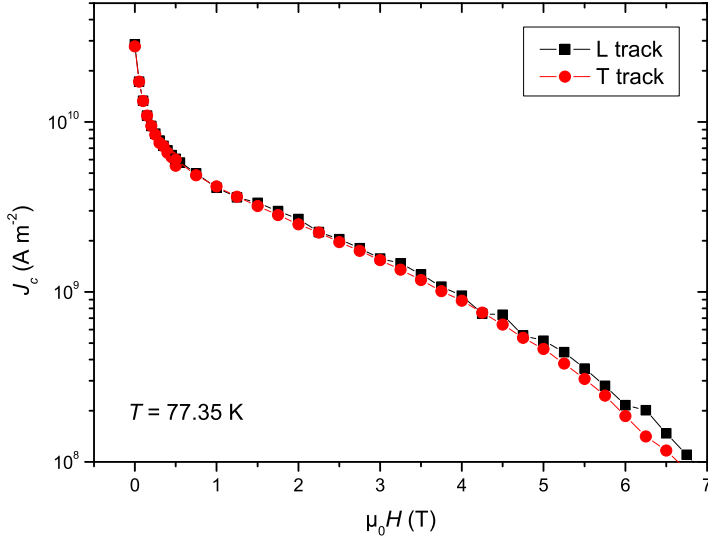


Figure 10.13: Critical current densities for $H \perp$ film plane. The obtained values for an L and a T track are almost identical.

surprise that no significant difference in critical current density between the L and the T track was found. A likely explanation is the low vicinal angle of only $\sim 2^\circ$. In the case of a YBCO film grown on a 2° vicinal single crystal substrate no significant difference in J_c has been reported depending on the track direction [220].

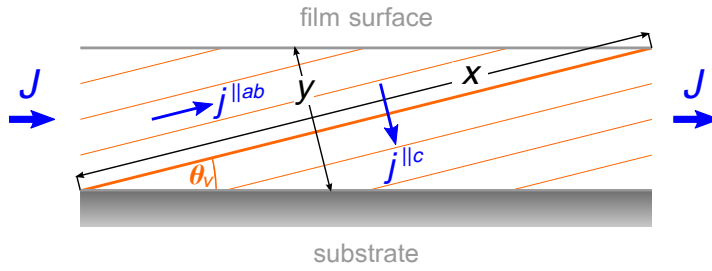
The sketch in Fig. 10.14 exemplifies current flow in a T track. The microscopic currents making up the total injected current will flow mostly in the ab -direction ($j^{\parallel ab}$), i.e. parallel to the CuO_2 planes. At some point, however, they need to cross the ab -plane indicated by a bold orange line, thus flowing in the c -direction ($j^{\parallel c}$). The cross-sectional area for currents in the c -direction is determined by the length x , the cross-section for currents $\parallel ab$ by y . It follows from simple geometrical considerations that a critical current anisotropy⁵

$$\gamma = \frac{J_c^{\parallel ab}}{J_c^{\parallel c}} < \frac{x}{y} = \cot \theta_v \quad (10.4)$$

is required, so that the overall J_c is not limited by currents in the c -direction. $J_c^{\parallel ab}$ and $J_c^{\parallel c}$ are the critical current densities for current flow parallel to the ab -planes and in the c -direction, respectively. If a vicinal angle of $\theta_v = 2^\circ$ is assumed, then $\gamma < 29$ is required.

Whereas $J_c^{\parallel ab}$ can be easily measured in c -axis films, it is more difficult to obtain values for $J_c^{\parallel c}$. One possibility is to investigate a -axis films. In many cases they are, however, strongly twinned: the c -axes of different twin domains are all in the plane of the film, but not necessarily parallel to each other [178]. This problem can be avoided by

⁵Note that this is *not* the J_c anisotropy describing the ratio of J_c for fields applied $\parallel ab$ and $\parallel c$.

**Figure 10.14:**

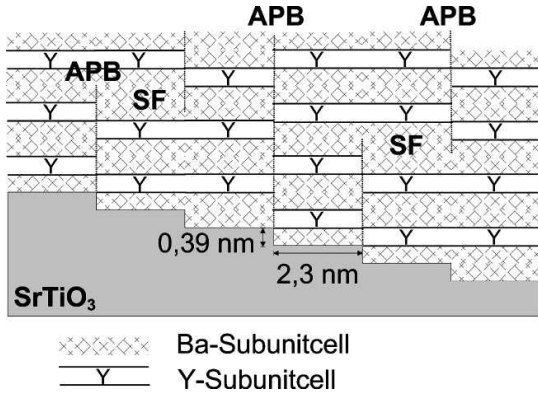
Current flow in a T track in a vicinal film. The ab -planes are indicated in orange. The cross-sectional area for currents parallel to the ab -planes ($j^{\parallel ab}$) is given by y and for those in the c -direction ($j^{\parallel c}$) by x .

growing the superconducting layer on SrTiO₃ substrates polished parallel to the (110) plane. Very different values for γ (obtained by measuring $J_c^{\parallel ab}$ and $J_c^{\parallel c}$ separately) are reported in the literature. Wu *et al.* [221] found $\gamma = 63$ at 4.2 K and $\gamma = 10$ at 77 K and zero applied field. Herzog [178] gives a value of only ~ 10 , even at low temperatures. Both studies were performed on (110) films. In a -axis films which did not show twinning an even lower $\gamma \approx 3$ was found over a broad temperature range [222].

These results show that, using the above very simple model, it is reasonable to assume a γ small enough so that J_c in a T track on a sample with $\theta_v = 2^\circ$ is not suppressed with respect to an L track.

In many cases, however, vicinal films show anti-phase boundaries (APBs). As is sketched in Fig. 10.15 they arise from the steps in the substrate. Neighbouring YBCO unit cells are shifted along the c -axis with respect to each other. APBs can heal by the insertion of a stacking fault (SF). In transport measurements on 4° and 8° vicinal samples anti-phase boundaries were identified as the reason for different J_c values in the L and the T direction [223]. For currents in the longitudinal directions APBs (which are also aligned along the length of the steps) act as pinning centres and can enhance the critical current density compared to a c -axis film. In a T track, on the other hand, currents need to cross the APBs, which potentially reduces J_c . With their width only a fraction of the coherence length, however, they present only a limited barrier to current flow, which becomes negligible at elevated fields and/or temperatures. Consequently, at $T = 77$ K J_c of an 8° film became independent of track direction for fields above ~ 0.3 T [223]. A J_c anisotropy in the basal plane caused by APBs was confirmed by magneto-optical imaging [144, 224]. Again, it was found to decrease with increasing B , T and—particularly interesting for CCs—also with increasing film thickness; a $3 \mu\text{m}$ thick film behaved essentially like a c -axis film.

It is not known to date whether SuperPower's MOCVD samples contain a significant


Figure 10.15:

Anti-phase boundaries (APBs) in a vicinal film [225].

amount of APBs. Above studies imply, however, that their presence should not have a noteworthy impact on most applications of CCs (at $\mu_0 H > 0.1$ T and $T > 60$ K) [223], which is consistent with the results in this thesis.

The critical current density of the MOCVD samples in this thesis was also measured for decreasing fields, similar to the experiment in Sec. 8.3.1. The sample was cooled from $T > T_c$ to 77.35 K in zero applied field, and then J_c was measured while H was increased up to 8 T. Directly afterwards and without warming up another $J_c(H)$ measurement was performed, down to 0 T. The results are presented in Fig. 10.16 for both the L and the T track.

A similar hysteresis as observed in American Superconductor samples was found. As discussed in Sec. 8.3.1, this phenomenon is due to flux trapped in grain boundaries. It is remarkable that it is also visible in samples grown on an IBAD buffer, which show

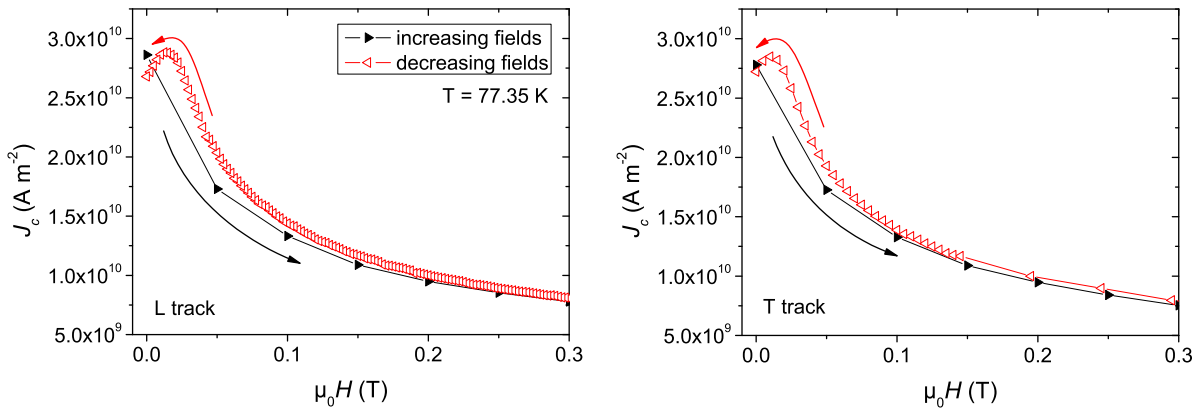
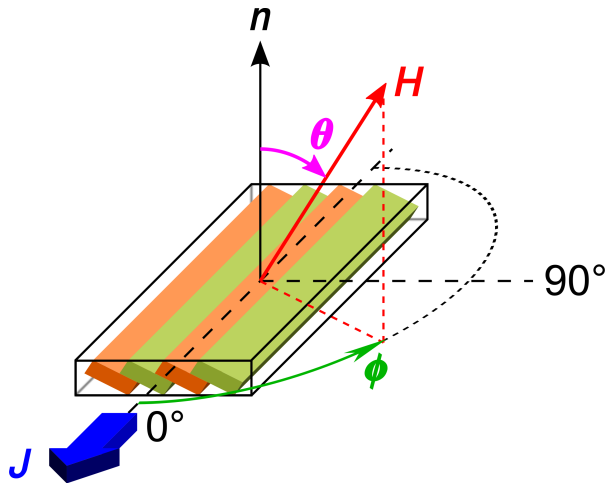


Figure 10.16.: Despite the good grain alignment of the MOCVD tape, hysteretic behaviour was seen in $J_c(H)$ for fields applied perpendicular to the sample plane. This was the case for both an L and a T track.

**Figure 10.17:**

Measurement geometry for in-plane and out-of-plane scans on vicinal films. Here the ab -planes (in orange and green) are drawn as they would lie in an L track.

a significantly better grain alignment than those on RABiTS (see the XRD results in Secs. 8.2 and 10.3). It can be concluded that, at least at low fields, the effects of grain boundaries are noticeable even in almost perfectly aligned coated conductors.

For most applications J_c of T tracks is irrelevant. The important exception are Roebel conductors [226, 227, 228], which are designed to reduce ac losses [169, 170, 171]. In these cables current flow occurs in directions other than the longitudinal one over significant lengths.

10.4.2. Fields Out-of-Plane

Angular out-of-plane scans (“ θ -scans”) have been carried out. The field was swept in θ while ϕ was kept constant at $\phi = 90^\circ$ (see Fig. 10.17 for a definition of the angles). This is the same measurement geometry as in Refs. [207, 152]. Unlike in those studies, however, *both* peaks were measured for this thesis, i.e. an angular range $> 180^\circ$ was investigated. Also, the experiment was performed on an L and a T track (the same $50\ \mu\text{m}$ wide tracks examined in Sec. 10.4.1).

The results are plotted in Fig. 10.18. While the relative angular resolution of the measurement setup employed is very good ($\sim 0.02^\circ$), it is difficult to determine absolute values accurately. The curves, therefore, had to be shifted to ensure that $\theta = \pm 90^\circ$ corresponds to $H \parallel$ sample plane. In the case of the T track this was achieved by moving the right maximum at 8 T to $\theta = 90^\circ$. The curves of the L track were shifted so that the high field peak (which has been shown to correspond to $H \parallel ab$ [207]) is found at $\theta = 88^\circ$. It had been confirmed by XRD on this specific sample that the ab -planes were

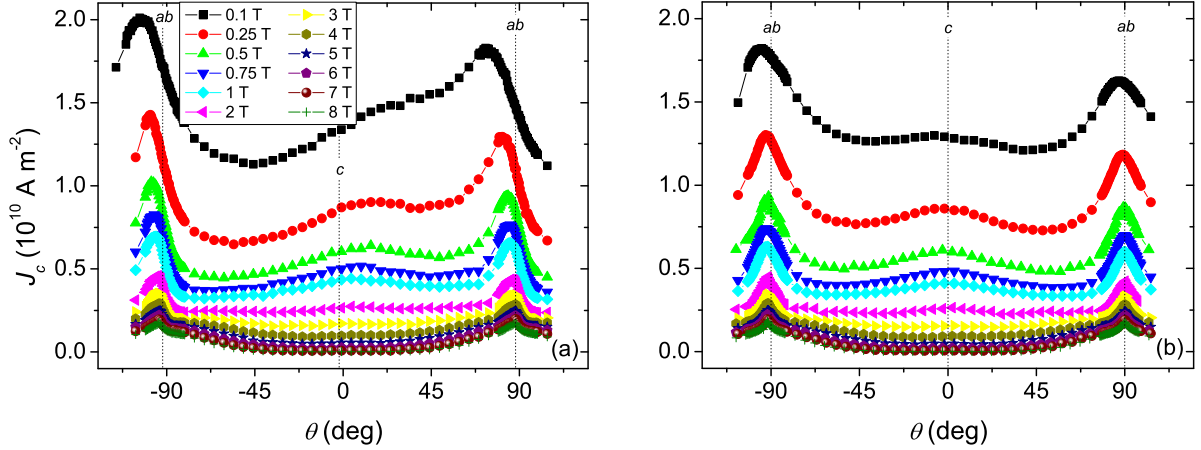


Figure 10.18.: Out-of-plane angular scans on (a) an L track and (b) a T track. The angles corresponding to the ab -planes and the c -axis are indicated by dotted lines.

tilted by $\sim 2^\circ$ in that direction, which justifies this procedure in order to determine the absolute sample orientation. It is consistent with this adjustment that as H is decreased the peak moves to lower values of θ , i.e. towards the precipitate planes and then further towards the c -axis (see below).

Both the L and the T track exhibit the expected maxima at $\theta \approx \pm 90^\circ$ ($H \parallel$ sample plane) and, at low and intermediate fields, a smaller maximum at $\theta \approx 0^\circ$ ($H \perp$ sample plane). The latter can be explained by pinning due to c -axis oriented threading dislocations, as were found in very similar MOCVD films [207, 152]. It is clear at first sight, however, that apart from these general features the two sets of data show a qualitatively different behaviour at $B \lesssim 2$ T.

While the curves obtained on the T track are (almost perfectly) symmetric, in the L track the peak found at $\theta \approx 0^\circ$ at intermediate fields moves to higher values of θ as H is decreased. The shift occurs in the same direction as has been reported for films grown on vicinal LaAlO_3 and SrTiO_3 substrates by Lowndes *et al.* [216], i.e. towards the quadrant opposite the c -axis. They explained this behaviour by the complex interaction between flux lines and columnar defects, found in their samples by TEM. In the present case, however, a more likely explanation for the peak shift can be found in the precipitate planes. In the L track studied in the present work they can be expected at $\theta \approx 83^\circ$ [from the orientation and amount of the vicinality in this sample ($\sim 2^\circ$), determined by XRD, and the fact that the precipitate planes are tilted further towards the sample normal than the ab -planes, by about 5° [207, 152]]. As the applied field is decreased the

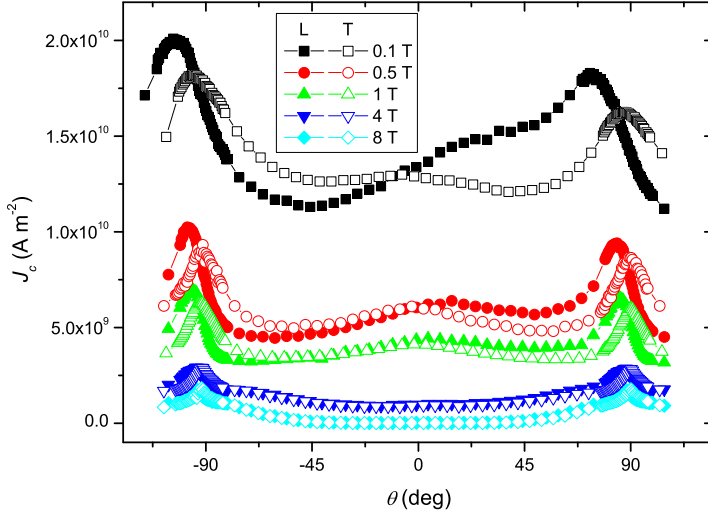


Figure 10.19: Out-of-plane angular scans on both an L and a T track for selected fields. Note the different behaviours at low H .

peak initially normal to the film plane gradually shifts towards the direction of the defect planes. This is consistent with those planes being efficient pinning centres at low H only. At very low fields ($\mu_0 H = 0.1$ T) only a shoulder in $J_c(\theta)$, at $\theta \approx 30^\circ$, is found rather than a distinct maximum, which is similar to what has been reported in Ref. [212]. In other words, the two peaks found at $B \parallel n$ and $B \parallel ab$ at higher fields merge at $B \parallel$ defect planes at very low fields.

In Fig. 10.19 $J_c(\theta)$ of both L and T track at selected fields is plotted in one graph in order to highlight the similarities and differences between the two tracks. It is striking that at high fields the corresponding curves are virtually exactly the same. This is consistent with what has been observed for $B \perp$ film plane for the whole field range investigated (see Sec. 10.4.1). At lower fields the angular scans show a peculiar behaviour, namely that—due to the development of asymmetry in the L track—at certain angles the T track has a slightly *improved* J_c over the L track.

At low fields the two maxima at $\theta \approx \pm 90^\circ$ were found to be of a different height, for both L and T track (see Fig. 10.18). As shown in Fig. 10.20 this behaviour is reversed when the field polarity is changed. The effect is similar to what has been observed in the American Superconductor tape for fields swept in-plane (see Fig. 8.8) and out-of-plane (not shown). In the case of the SuperPower tape the effect occurs in the opposite direction though, i.e. a higher J_c is measured for the sample orientation where the Lorentz force drives vortices from the sample surface towards the buffer layer–REBCO interface. This is consistent with previous reports of a very smooth surface of films grown by MOCVD [229, 230]. It is, thus, very plausible that it is easier for flux lines to enter

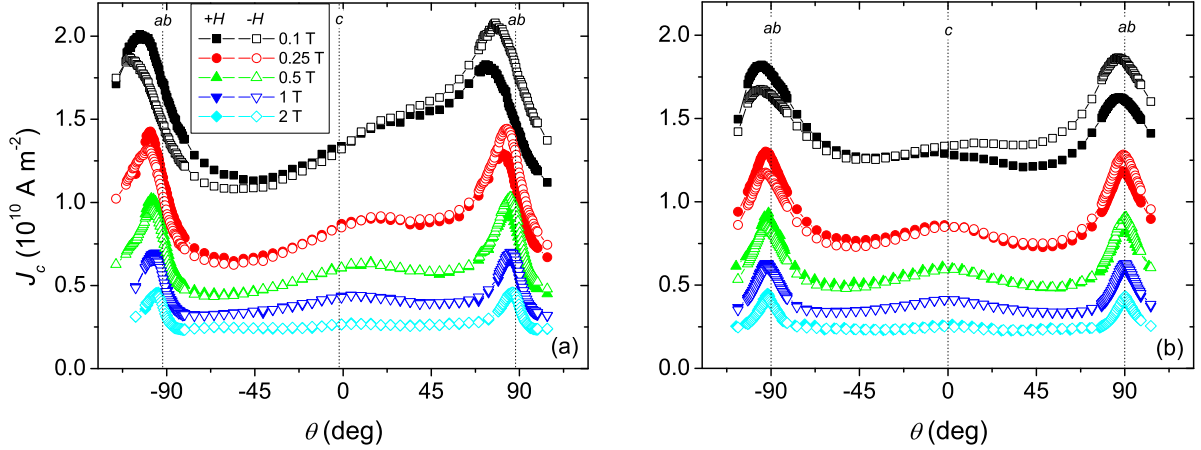


Figure 10.20.: Out-of-plane angular scans on (a) an L track and (b) a T track for positive (+ H) and negative ($-H$) fields.

from the substrate–REBCO interface, similar to what has been reported in Ref. [199]. The effect becomes weaker as the field is increased and disappears at $\mu_0 H \sim 2\text{--}3\text{ T}$.

From a geometrical point of view changing the sign of H is equivalent to a phase shift of 180° in θ . As can be seen in Fig. 10.20 the $+0.1\text{ T}$ curves can be continued smoothly beyond $\theta = 90^\circ$ by shifting the -0.1 T curves to the right by 180° . As a consequence, at low fields θ -scans are not periodic in 180° , but in 360° .

This phenomenon seems to be a general feature, which is found in samples produced by different techniques, both vicinal and c -axis oriented. One would, therefore, expect to see a varying peak height in the data presented in Ref. [212] as well, and in fact the curves shown in Fig. 2 of that publication exhibit the same behaviour.

The difference in critical current density depending on the orientation of Lorentz force implies that measuring one peak only (as in Refs. [207, 152]) is not sufficient for a complete characterisation of the out-of-plane angular dependence. In order to see the whole picture, the scans need to be performed over a range including both maxima.

The amount of the shift of the right maximum (at $\theta \approx 90^\circ$) of the L track is presented in Fig. 10.21(a). At 0.1 T the peak is $\sim 15^\circ$ off the direction of the ab -planes. The misalignment disappears at $\mu_0 H \approx 2\text{--}3\text{ T}$, consistent with Ref. [212]. This corresponds to a reduced field of $h \approx 0.02\text{--}0.03$, which is very similar to the value of $h \approx 0.02$ reported in Ref. [214]. The agreement is remarkable, given that the experiment in the latter study was performed on single crystals, rather than thin films, using magnetic measurements, rather than transport. Also, the misorientation between the defects responsible for

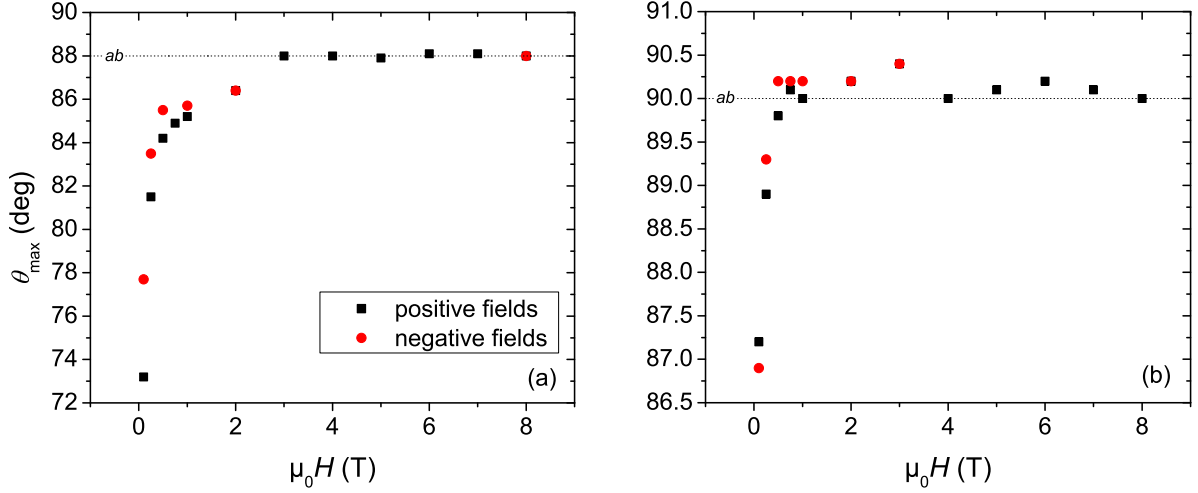


Figure 10.21.: The position of the right peak of the scans on (a) an L track and (b) a T track shifts with applied field. The direction of the ab -planes is indicated by a dotted line.

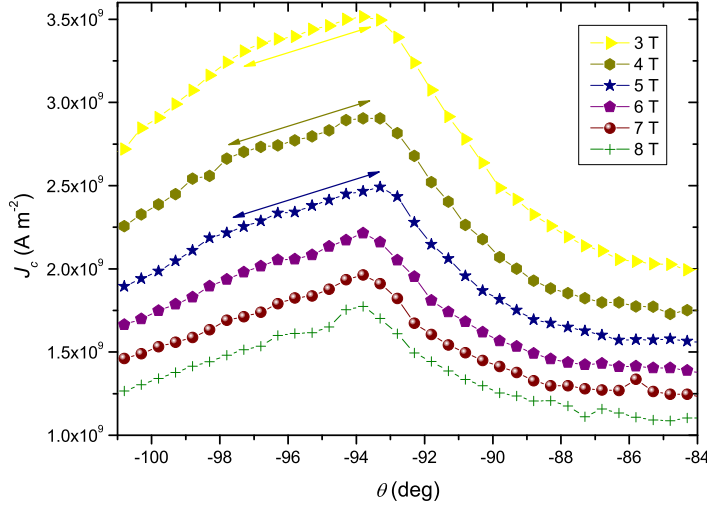
pinning with respect to the sample plane was significantly higher in Ref. [214] than in this thesis.

The shift of the right peak of the L track measured for this thesis at negative fields is lower than at positive H [see Fig. 10.21(a)], which is discussed in Sec. 10.4.3. The left maximum (at $\theta \approx -90^\circ$) exhibited the same behaviour as the right one (not shown).

As the field is decreased the peak shifts from $H||ab$ towards the sample normal, i.e. the “anisotropy dominated case” is observed (see Sec. 10.1.2). As was shown by magnetic measurements on YBCO single crystals, changing the sample’s aspect ratio can lead to the “compensated case”, and (to a certain amount) even to the “geometry dominated case”. In the present thesis the sample dimensions are given by the length and width of the track patterned into the coated conductor, together with its thickness. It would be a worthwhile experiment to investigate if simply changing the track size could push CC samples into the regime where the peak shift is dominated by the track’s geometry, rather than the YBCO electron mass anisotropy.

As can be seen in Fig. 10.21(b) a (smaller) peak shift was also observed for the T track. This is surprising as in this case of course the ab -planes and defect planes are not tilted about an axis parallel to the track direction. Consequently, the measurement geometry is symmetric around $\theta = 90^\circ$ and no peak shift would be expected.

It needs to be mentioned at this point that at high fields the left and right peaks in

**Figure 10.22:**

A certain asymmetry was found in the high field peaks of the L track. A tilted plateau, observed at intermediate fields, is indicated by arrows.

$J_c(\theta)$ were $\sim 182^\circ$ apart from each other for both the L and the T track (see Fig. 10.18). A possible explanation for the deviation from the expected 180° (at least in the case of the L track) would be that one maximum was due to intrinsic pinning while the other was caused by surface pinning. Different pinning mechanisms were shown to lead to different peak positions, depending on the direction of vortex penetration [231], and in fact the Lorentz force is oriented in the opposite direction at $\theta = -90^\circ$ and $+90^\circ$. In the present case this explanation can be ruled out, however, for two reasons. Firstly, surface pinning is only relevant at low fields. Secondly, changing the field polarity at fixed θ should also lead to a shift of the maximum, which (at high fields) was not the case.

The most likely explanation for the peak offset being too high, therefore, is that it is a measurement artefact. The step size in which the current is increased in each $V(I)$ -curve is determined from the previously measured value of I_c . Consequently, the current increment is slightly underestimated to the left of the peak and slightly overestimated to its right (all curves were measured with increasing θ). This difference can lead to a small deviation in J_c which could account for a certain peak shift. Unfortunately scans in the opposite direction (i.e. with decreasing θ) were not carried out for this sample.

At intermediate and high fields the ab -peaks obtained from the L track were asymmetric, as can be seen in Fig. 10.22. This could again be related to the way $V(I)$ -curves are measured, as described in the previous paragraph.

The measurements on the T track did not show this asymmetry. The feature could, thus, be real and related to the inherent asymmetry of an L track. As the sample is rotated in the field first the defect planes are parallel to H , followed by the ab -planes

and finally the film surface. While intrinsic pinning is dominant at high fields, a certain contribution from the defect planes, acting as correlated pinning centres, could cause the peak asymmetry. It would be consistent with this picture that at intermediate fields (3–5 T) a tilted plateau occurs over a range of $\sim 5^\circ$, i.e. the same value as the angular separation between defect planes and ab -planes. Further measurements would be required to confirm this.

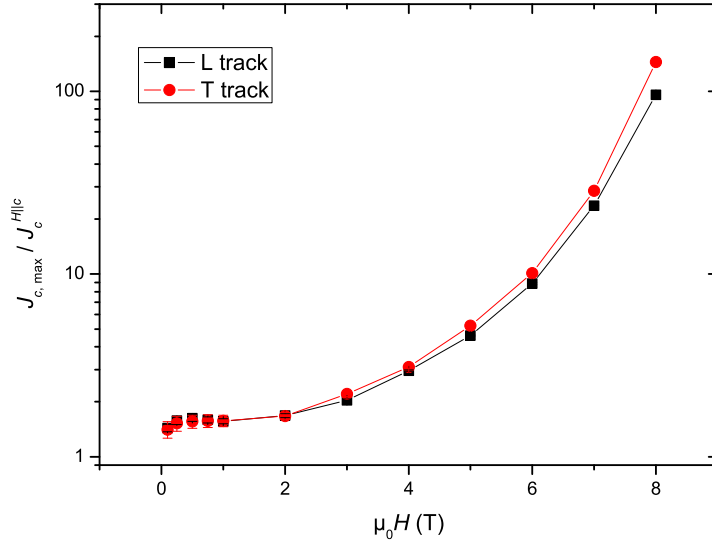
An alternative explanation for a plateau in $J_c(\theta)$ would be the vortex lock-in effect [232]. If the angle between the direction of \mathbf{H} and the CuO_2 planes is smaller than a critical angle θ_c , the flux lines lock in parallel to the ab -planes and J_c is expected to become independent of θ . For $H_{c1} \ll H \ll H_{c2}$ the angular range where lock-in should occur was predicted to be several degrees wide ($\theta_c = 4^\circ$ for YBCO at $\mu_0 H = 3$ T) [232]. In fact a similar value was reported from magnetic measurements at low fields and temperatures on a $\text{La}_{1.9}\text{Sr}_{0.1}\text{CuO}_4$ single crystal [233]. The lock-in angle, however, decreases with increasing H and T . Consequently, in a YBCO single crystal θ_c was found to be only $\sim 0.2^\circ$ at $\mu_0 H \geq 1$ T [234], i.e. considerably smaller than predicted [232]. This implies that the lock-in effect cannot explain the plateau visible in Fig. 10.22, since the width of the latter is significantly larger than the expected value of θ_c at 77.35 K and a field of several Tesla. Furthermore, the measurements of Refs. [233, 234] were carried out on high quality single crystals, which allowed such a small lock-in angle to be observed. In a coated conductor the plateau would be smeared out by the grain-to-grain misalignment.

The difference in J_c between field applied $\parallel ab$ and $\parallel c$ can be described by the anisotropy $J_{c,\text{max}}/J_c^{H\parallel c}$, which is plotted in Fig. 10.23. Not surprisingly there is virtually no difference between the L and the T track.

10.4.3. Fields In-Plane

All measurements discussed in this section were performed on the same $50\ \mu\text{m}$ wide L track investigated in Secs. 10.4.1 and 10.4.2.

As described in Sec. 6.1 the probe used for this thesis allows the sample to be rotated about an axis perpendicular to the film plane, described by the angle ϕ . Because SuperPower samples are vicinal, however, it is not possible to perform a conventional in-plane scan (“ ϕ -scan”) where B is always parallel to the ab -planes. The measurement geometry for a vicinal film is depicted in Fig. 10.17. If a scan is started at $B\parallel ab$ at a

**Figure 10.23:**

The out-of-plane anisotropy, i.e. the ratio between the maximum J_c in out-of-plane scans and the value for $H||c$. The variation due to the different J_c values of the maxima at $\theta = -90^\circ$ and $+90^\circ$ (see above) is smaller than the size of the symbols in the plot.

certain ϕ -angle, a rotation in ϕ will lead to B moving away from the ab -direction if θ remains constant. This is because the ϕ -axis does not coincide with the crystallographic c -axis.

The solution to this problem is to acquire θ -scans at different values of ϕ . The maximum of each θ -scan then gives the corresponding value of $J_c(\phi)$ for $B||ab$ (or $B ||$ precipitate planes, depending on the magnitude of H). This procedure was carried out for ϕ ranging from -120° to $+120^\circ$ in 10° steps (5° steps from $-10^\circ < \phi < +10^\circ$) at different fixed fields. Consequently a set of 27 θ -scans was obtained for each field.

Each set can be plotted in a θ - ϕ -map, two examples of which are shown in Fig. 10.24 for $\mu_0 H = 0.25$ and 8 T. The different colours represent different values of the critical current density. A vertical cut through the maps corresponds to one single $J_c(\theta)$ measurement. Each point of the black lines gives the position of the maximum of a θ -scan, hence the line indicates the “ridge” in $J_c(\theta, \phi)$.

The most striking feature of these maps is their asymmetry; at negative ϕ the maximum is found at higher values of θ than at positive ϕ . This is, of course, the same behaviour as the shift of the peak in θ -scans (see Sec. 10.4.2), associated with the tape’s vicinality and the tilt of the defect planes. At $\phi = -90^\circ$ a different value of θ is necessary in order to align the vortices with the ab -planes or the defect planes, respectively, than at $\phi = +90^\circ$.

A “summit” occurs in the centre of both maps (coloured in red), which is due to the force free orientation at $\phi = 0^\circ$.

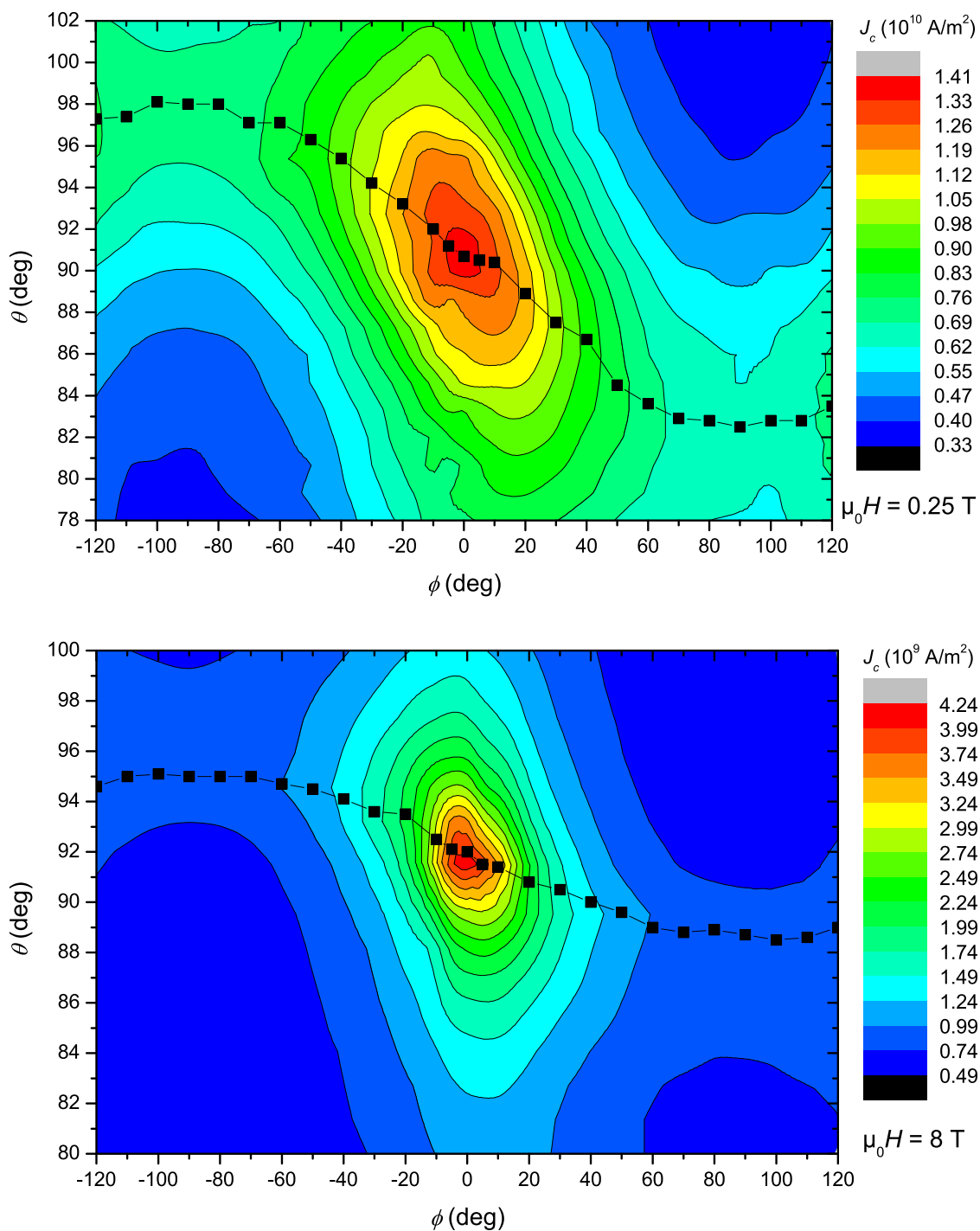
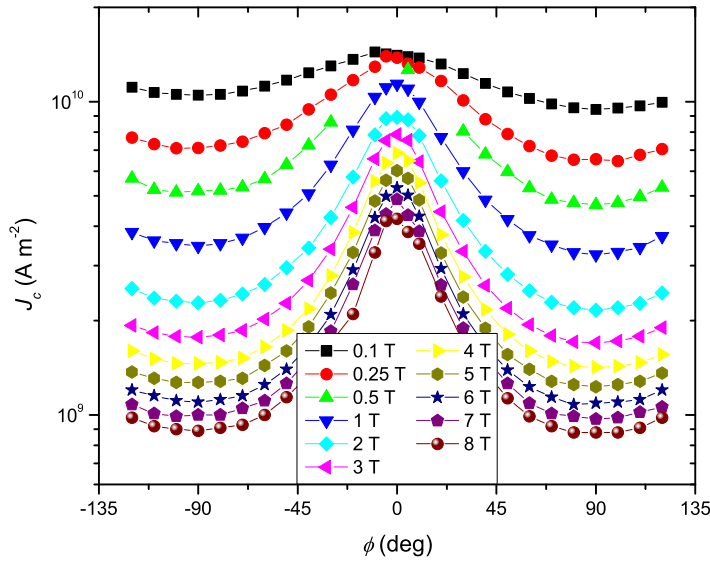


Figure 10.24.: θ - ϕ -maps acquired at $\mu_0 H = 0.25$ and 8 T. The shift of the maxima of $J_c(\theta)$ measurements can be seen clearly. The black line traces these maxima; each square symbol relates to one θ -scan.

**Figure 10.25:**

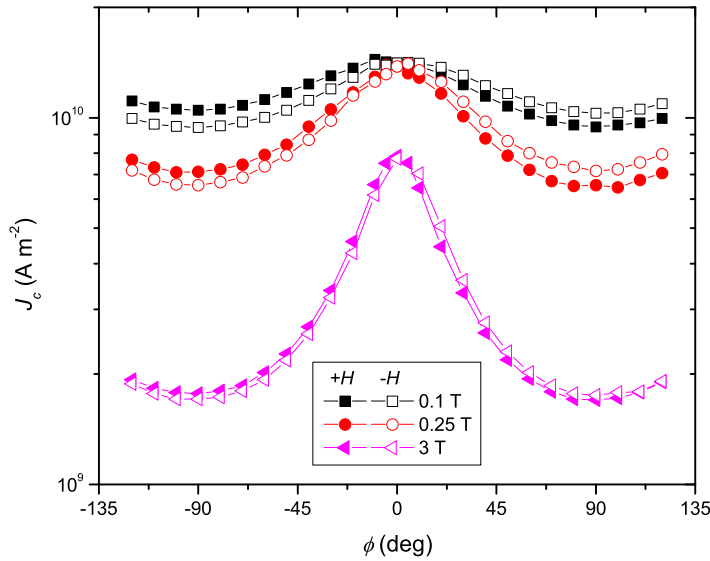
In-plane scans which have been obtained from θ -scans at different ϕ and H .

Upon closer inspection one finds that the asymmetry is stronger in the 0.25 T map than in the 8 T map. This is consistent with the stronger peak shift observed at low fields. At high H , where $B \parallel H$ and the defect planes do not contribute significantly to the total pinning, one would expect a maximum J_c when H is aligned with the ab -planes. Indeed at $\mu_0 H = 8$ T the maximum moves by 6° (from 95° to 89°) between $\phi = -90^\circ$ and $+90^\circ$. This value almost exactly corresponds to twice the vicinal angle (~ 4 – 5°), as would be expected if the shift was due to vicinality and intrinsic pinning only. The fact that a slightly stronger shift is found probably means that the defect planes still contribute a little to the peak shift at 8 T.

The value of the critical current density can now be extracted at each black symbol from the θ - ϕ -maps, which, as mentioned above, is the maximum J_c of the corresponding θ -scan. If these data are plotted vs. ϕ in-plane scans are obtained where $B \parallel ab$ (or $B \parallel$ defect planes) is fulfilled for all angles. The result is presented in Fig. 10.25.

As expected a maximum is found at $\phi \approx 0^\circ$ (force free) and minima at $\phi \approx \pm 90^\circ$ (maximum Lorentz force).

In Fig. 10.26 $J_c(\phi)$ is shown for selected positive and negative fields. The curves are slightly asymmetric, similar to what has been seen in in-plane scans on the American Superconductor tape (see Sec. 8.3.2). Again changing field polarity reverses the asymmetry. As would be expected from the out-of-plane angular measurements performed on the same SuperPower sample (see Sec. 10.4.2), the asymmetry in this material shows the opposite dependence on the sign of H compared to the American Superconductor tape.

**Figure 10.26:**

In-plane measurement for positive (+ H) and negative ($-H$) applied fields. A certain asymmetry is visible at low H .

Consistent with the θ -scans the in-plane measurements revealed a slightly suppressed critical current density when the Lorentz force was directed from the substrate towards the film surface.

As was the case for the American Superconductor sample, the asymmetry is most pronounced at low fields and disappears as H is increased. This confirms that surface pinning, which is only relevant at low fields [231], is involved.

The angle θ_{\max} where $J_c(\theta)$ reaches its maximum is plotted vs. ϕ in Fig. 10.27. Note that these curves are the same as the black lines in Fig. 10.24. Plotting them in one graph for all fields analysed shows more clearly that as expected the shift is enhanced at low fields.

In Fig. 10.28 $\theta_{\max}(\phi)$ is plotted for selected positive and negative fields. Only the curves at ± 3 T overlap. Those obtained at $+0.1$ and $+0.25$ T are shifted to lower θ compared to their counterparts obtained at negative fields. It is unlikely that this is an artefact due to a slippage of the rotator probe, because the $+3$ T measurement was acquired before the low field measurements, and the one at -3 T afterwards. It would be a remarkable coincidence if a second slippage had occurred, exactly cancelling the mechanical offset present at ± 0.1 and ± 0.25 T. What is more, a similar behaviour was found in the θ -scans presented in Sec. 10.4.2, as can be seen in Fig. 10.21(a); also there θ_{\max} was higher for $\mu_0 H = -0.1$ T than for $+0.1$ T.⁶

⁶Note that the $J_c(\theta)$ measurements presented in Sec. 10.4.2 are not the same as the θ -scans used to obtain $J_c(\phi)$ in this section. They were performed on the same sample though. This shows that the

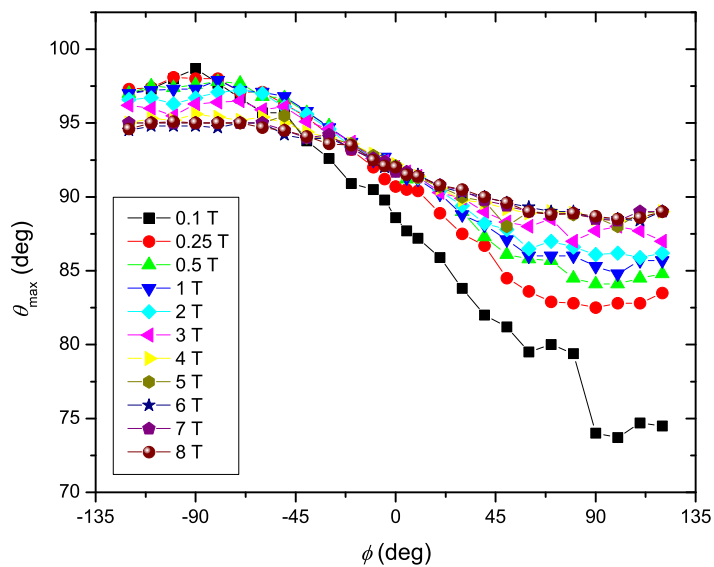


Figure 10.27:

The value of θ where the maximum J_c was found changes with the in-plane angle ϕ . This shift is more pronounced at low fields.

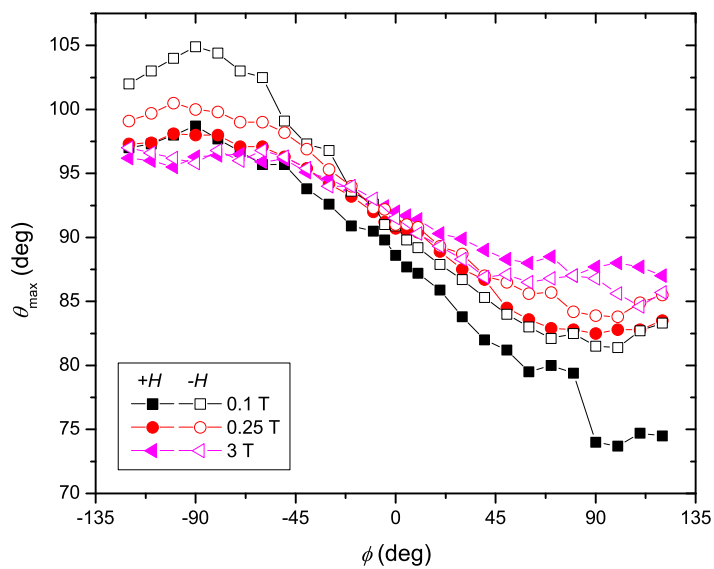


Figure 10.28:

At low fields θ -scans had their maximum at different θ when the field polarity was changed. This offset disappears at higher H .

This suggests that at low fields two different pinning mechanisms are dominant, depending on the direction of Lorentz force F_L :

1. F_L directed from film surface to buffer layer: a higher J_c is measured and θ_{\max} is found at an angle closer to the film plane.
2. F_L directed from buffer to surface: J_c is somewhat lower and θ_{\max} is shifted further towards the film normal.

Consequently, in case (1) surface pinning [231] is stronger than intrinsic pinning due to the ab -planes and extrinsic pinning due to the defect planes. This can be explained by the film surface being smoother than the buffer–REBCO interface. For case (2), on the other hand, the buffer–REBCO interface does not provide a sufficiently high surface barrier. It is, thus, the defect planes which contribute mainly to pinning, which is why θ_{\max} is shifted further away from $H \parallel$ film plane. Note that pinning by defect planes contributes to the overall pinning also in case (1). Consequently, there is a certain offset between \mathbf{H} and \mathbf{B} (as discussed in Sec. 10.1.2), which is why \mathbf{H} is not parallel to the film plane at all ϕ , as would be expected if only surface pinning was present.

Two pairs of θ -scans for positive and negative fields at different ϕ are depicted in Fig. 10.29. It is remarkable that the difference in θ_{\max} for $+H$ and $-H$ is $\sim 7^\circ$, i.e. exactly the tilt angle between film surface and defect planes, which confirms above explanation.

10.4.4. Vortex Channelling

Vortex channelling has been found in vicinal films grown by both dc sputtering [37] and PLD [218]. It can be, thus, considered as an intrinsic property of the material not related to the growth technique. Consequently, it is reasonable to assume that channelling should also occur in IBAD-MOCVD samples, which show both vicinality and very good grain alignment.

In order to be consistent with literature the angular definition depicted in Fig. 10.4 is employed in this section, which differs from the one used in Secs. 10.4.2 and 10.4.3.

Channelling is found at low temperatures only. It became clear soon that I_c of the $50 \mu\text{m}$ wide T track was too high to be measured at the force free orientation at low

dependence of θ_{\max} on the sign of H is a reproducible feature.

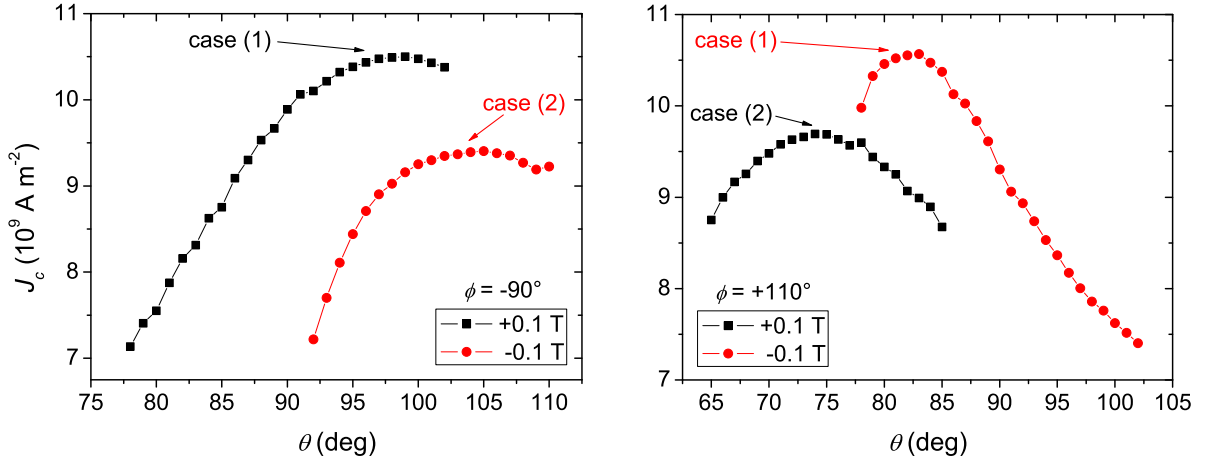


Figure 10.29.: θ -scans at $\phi = -90^\circ$ and $+110^\circ$, measured at $T = 77.35$ K and $\mu_0 H = \pm 0.1$ T. The pinning mechanism changes when the field is reversed: In case (1) surface pinning dominates, in case (2) the defect planes, acting as correlated pinning centres, contribute more strongly.

T , due to limitations of the measurement setup. Consequently, θ -scans were performed at $\phi = 90^\circ$ (where the sample is never in the FF configuration) at $\mu_0 H = 8$ T and temperatures ranging from 40 to 70 K. As discussed in Sec. 10.1.3 vortex channelling can also occur in this geometry.⁷ The results are presented in Fig. 10.30. No channelling minimum is visible, not even at $T = 40$ K.

In order to measure $J_c(\theta)$ at $\phi = 0^\circ$ another sample was patterned with a $6 \mu\text{m}$ wide and $100 \mu\text{m}$ long T track. The result obtained at $T = 40$ K and $\mu_0 H = 8$ T is plotted in Fig. 10.31. A clear channelling effect is visible: the slope of $J_c(\theta)$ is significantly steeper to the right of the FF maximum and a minimum is found at $\theta = 0^\circ$. The offset between the two extrema corresponds exactly to the vicinal angle $\theta_v = 2.5^\circ$ for this specific sample, as determined by XRD. It should also be noted that, unsurprisingly, the J_c minimum was found on that side of the FF peak where it was expected from the XRD measurement.

While clearly visible, the channelling effect found in the SuperPower tape is not as pronounced as in the results presented in Refs. [37, 218]. This can be attributed to the fact that according to Eq. (10.3) the Lorentz force on the strings is proportional to $\sin \theta_v$,

⁷The probe used does not allow a rotation about the axis θ as defined in Fig. 10.4. Consequently, the measurement was carried out by rotating about the *goniometer* axis θ (as defined in Fig. 6.2). Given the small vicinal angle the error caused by this deviation is negligible.

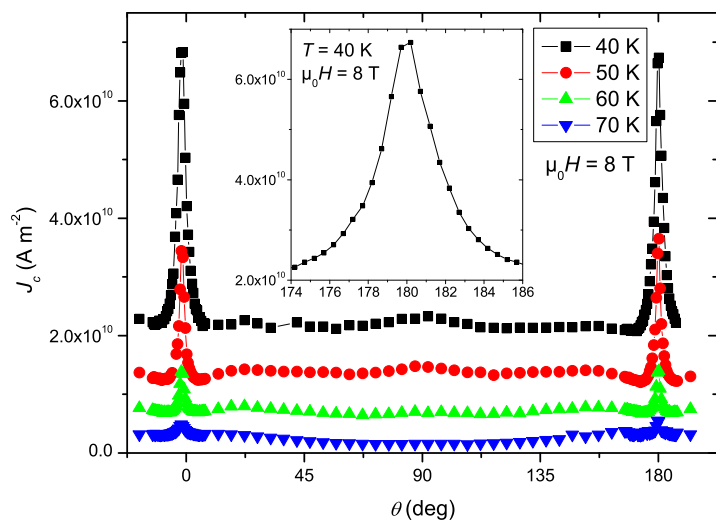


Figure 10.30: No channelling minimum was found at $\phi = 90^\circ$. The inset shows a blowup of the peak at $T = 40 \text{ K}$.

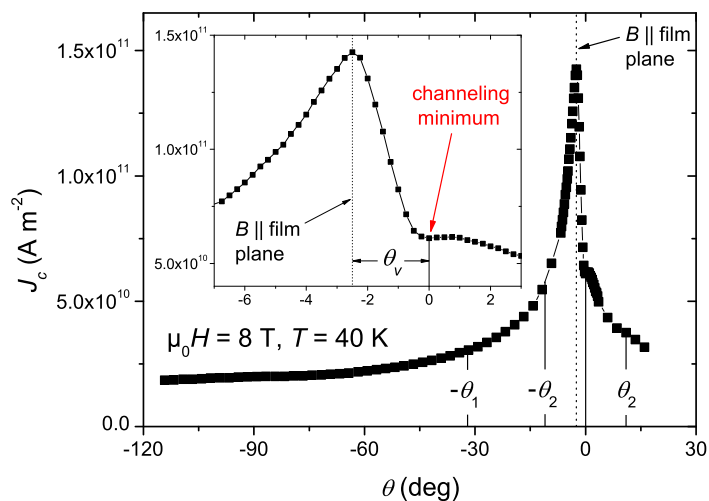


Figure 10.31: Vortex channelling was seen in a θ -scan at $\phi = 0^\circ$. The inset shows a magnified plot of the force free maximum and the channelling minimum to its right.

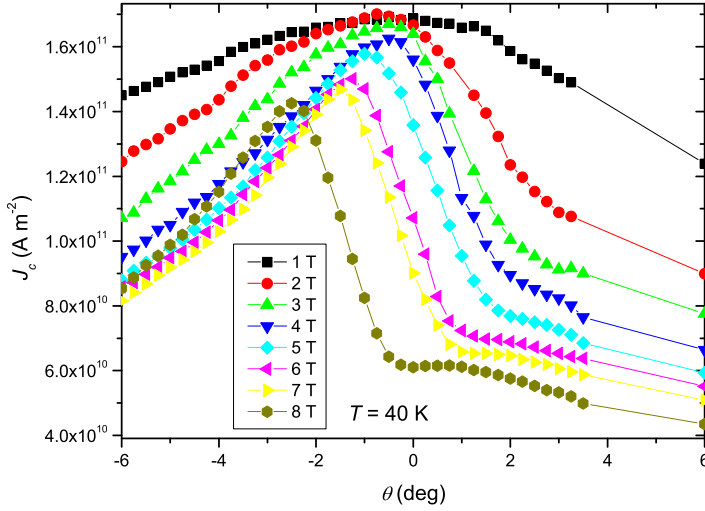


Figure 10.32: Vortex channelling disappears as the field is reduced. In addition a shift of the FF maximum is observed.

hence a stronger channelling minimum would be expected for higher θ_v . The vicinal angle of the MOCVD coated conductor is smaller than that of the samples analysed in above studies. The exception is Fig. 6 of Ref. [218] with $\theta_v = 2^\circ$. Whereas in the latter publication a minimum is reported at $T = 40$ K and $\mu_0 H = 1$ T, the MOCVD sample had to be exposed to a significantly higher field before it exhibited vortex channelling. The most likely explanation is the grain misalignment and the various pinning centres present in the coated conductor, which can be expected to suppress channelling (in all previous studies films grown on single crystal substrates had been used).

A low value of θ_v can also explain why no channelling was found at $\phi = 90^\circ$, where the effect is weaker because the channelling minimum competes with the maximum due to intrinsic pinning. This is consistent with the fact that the $\theta_v = 2^\circ$ sample presented in Ref. [218] showed no channelling at $\phi = 90^\circ$ [217]. It is conceivable, however, that a limited channelling effect leads to a reduction of the intrinsic pinning maximum, even if no channelling minimum is seen because of the small vicinal angle.

Vortex channelling in the MOCVD sample became less pronounced as the field was reduced with T kept at 40 K (see Fig. 10.32). This is again expected from Eq. (10.3). At $\mu_0 H \approx 6$ T the minimum disappears while the peak is still asymmetric, i.e. it is steeper on the right.

A striking feature of Fig. 10.32 is the shift of the maximum towards higher values of θ with decreasing field. This effect was even more pronounced at $\mu_0 H < 1$ T (not shown). A possible explanation would be a mechanical offset, i.e. a shift of the probe's gearwheels. A repeated 1 T scan (after measurements at $\mu_0 H < 1$ T), however, gave a

maximum at the same position as in the first 1 T scan. Also, no offset was found after unloading the probe. It is, therefore, reasonable to assume that the shift is real.

A possible explanation would be an offset between the direction of the applied field \mathbf{H} and the flux lines (given by \mathbf{B}), which can depend on the magnitude of \mathbf{H} (see Secs. 10.1.2 and 10.4.2). As regards the samples' crystallographic structure and vicinality, θ -scans on an L track at $\phi = 90^\circ$ and on a T track at $\phi = 0^\circ$ are equivalent. The FLL structure is, therefore, the same in these two types of scans; only the current direction is different. Consequently, the same explanation for the peak shift found in measurements on the L track (see Sec. 10.4.2) should apply to the curves presented in Fig. 10.32. Further evidence for this explanation can be found in the fact that for both the L track discussed in Sec. 10.4.2 [Fig. 10.18(a)] and the T track in this section (Fig. 10.32) the peak shifts in the same direction as the field is reduced: from $H \parallel ab$ towards $H \parallel$ defect planes and then further towards the c -direction⁸. It is unclear, however, why the peak shift persists up to high fields in the case of the T track. A similar peak shift has not been seen in measurements on films grown on vicinal single crystals. As discussed above the peak shift is (primarily) due to the tilted defect planes, not the vicinality itself. It is very likely that films grown by dc sputtering or PLD do not show these defects, which would explain the absence of the peak shift.

The fact that the position of the maximum depends on H also at high fields could be explained by the small vicinal angle. Because of their close proximity the force free maximum and the channelling minimum might not be independent from each other, i.e. they represent two competing phenomena over a certain angular range. The minimum would then shift the maximum to lower values of θ . As the field is reduced and the channelling effect becomes weaker, the FF maximum moves closer to its actual position.

10.4.5. Isolated Grain Boundary

A grain boundary was isolated on a SuperPower sample. The procedure was the same as in the case of the American Superconductor tape (described in Secs. 5.3, 5.4 and 5.5), except for two additional steps. Firstly, the film surface was polished before the initial patterning by conventional lithography. This was done by hand, using a slurry made of ethanol and Alcoa/Almatis "CT 3000 SG" alumina powder (particle size $0.5 \mu\text{m}$). It was necessary because removal of the Ag layer by ion milling caused a certain damage to the

⁸Note that for both samples the orientation of the vicinality had been determined by XRD.

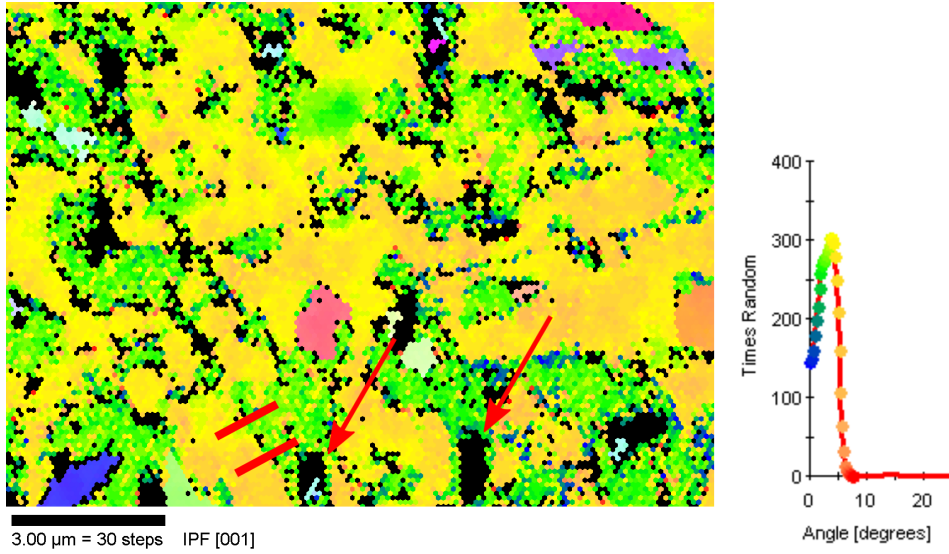


Figure 10.33.: EBSD map of a track on a SuperPower sample. The red lines show the position of a bridge across a single GB. Alignment marks patterned by a FIB are visible as black rectangles (two of them are indicated by arrows). The plot on the right shows the angular distribution and defines the colours in the orientation map. (Image acquired by Susannah Speller.)

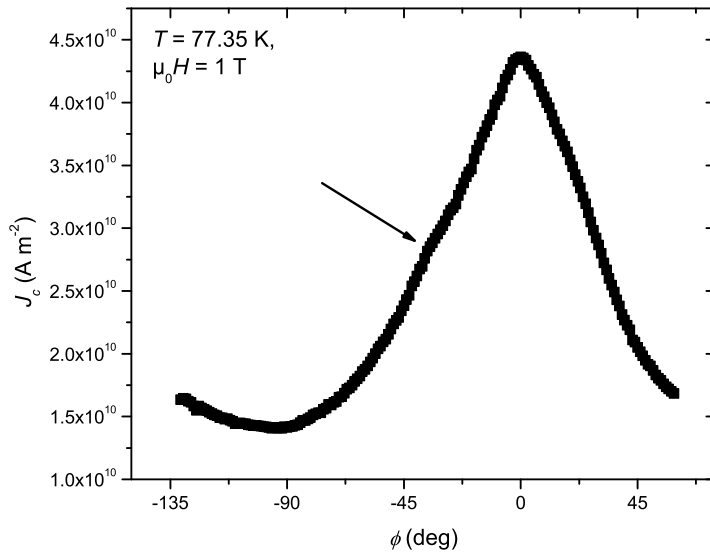
surface of the REBCO layer which prevented the acquisition of EBSD maps. Thanks to the polishing high-quality Kikuchi patterns could be obtained.

The second additional processing step concerns the alignment marks necessary to relate the EBSD map to the FIB image. Due to the small IBAD grain size ($1\text{--}3\ \mu\text{m}$ in diameter) the recesses in the tracks defined by the lithography mask (see Sec. 5.3) were too coarse for a precise alignment. Additional alignment marks were, therefore, made by the author using a FIB. Equally spaced cuts, 0.5 and $1\ \mu\text{m}$ wide, were patterned by the FIB into the track which had been obtained by conventional lithography and ion milling. This was done before the photoresist was removed, in order to prevent surface contamination due to the FIB imaging and cutting.

Shown in Fig. 10.33 is an EBSD map obtained from the sample prepared in this way. The location of the bridge patterned by FIB in the following step is indicated.

An in-plane scan⁹ obtained on the isolated GB is presented in Fig. 10.34. The absolute values of J_c are reasonably high, showing that grain boundaries do not constitute a significant barrier to current flow in SuperPower samples. This is expected from the

⁹Due to time constraints this measurement was kindly performed by John Durrell.

**Figure 10.34:**

The critical current density of an isolated grain boundary for a field of 1 T swept in the film plane. The arrow indicates a kink, which could be related to vortex channelling.

good grain-to-grain alignment achieved by IBAD.

The in-plane anisotropy is comparably high with $\zeta = 3.1$. This is consistent with a grain limitation of J_c , which leads to little current percolation and a pronounced force free maximum[200].

Unfortunately the track broke after the first scan at $\mu_0 H = 1 \text{ T}$, which prevented further measurements at higher fields. These would have been planned in order to answer the question if vortex channelling along GBs occurs in MOCVD coated conductors. This could well be the case, given that MOCVD boundaries are planar, rather than meandering, as was found by TEM (see Sec. 10.2.1). Their morphology is, thus, similar to that of GBs in PLD samples, which exhibited vortex channelling over a certain angular range in experiments on films grown on bicrystal substrates [82] (see Fig. 3.11). The kink in $J_c(\phi)$, indicated in Fig. 10.34 by an arrow, suggests that channelling is present also in the coated conductor GB discussed in this section. The minimum to the left of the kink is slightly more pronounced than what would be expected from the trend of $J_c(\phi)$ to its right. The minimum could, thus, be enhanced by vortex channelling. Further measurements would be necessary to confirm this.

10.5. Comparison between MOCVD and MOD Coated Conductors

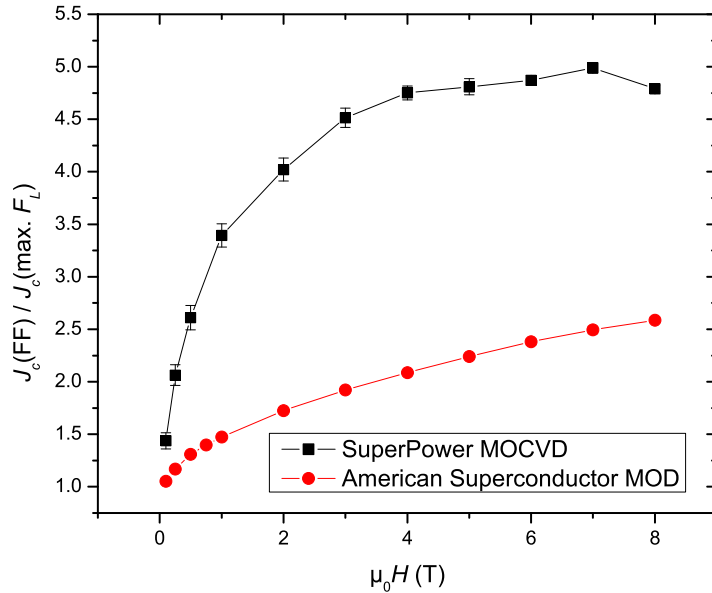
Due to their different architectures and production routes the coated conductors manufactured by SuperPower (IBAD-MOCVD) and American Superconductor (RABiTS-MOD) show a different microstructure and electrical properties.

The MOD grains have a significantly bigger diameter than the MOCVD grains (by a factor of ~ 10), which is determined by the larger RABiTS grain size. Whereas MOD grain boundaries were found to be meandering, both along their length and through the film thickness, MOCVD boundaries are planar. The grain-to-grain alignment, both in- and out-of-plane, of IBAD is significantly better than that of RABiTS.

Despite those differences both manufacturers achieve excellent values of critical current density in their products¹⁰. In the case of SuperPower this is mainly due to the exceptionally good texture and the rare earth doping, which leads to the introduction of various pinning centres. American Superconductor's approach to overcoming the grain boundary problem, namely by promoting GB meandering, is very different but appears equally as successful. In general RABiTS-MOD tapes show more current percolation due to the higher grain misorientation and the GB meandering, while IBAD-MOCVD CCs behave more like single crystals. This is reflected in the higher in-plane anisotropy $\zeta = J_c(\text{FF})/J_c(\text{max. } F_L)$ exhibited by the latter, as is illustrated in Fig. 10.35. The red curve in this plot has been obtained from a $125 \mu\text{m}$ wide American Superconductor track. It was shown in Sec. 8.3.2 that ζ does not depend on track width beyond $125 \mu\text{m}$ in these samples. It is, thus, permissible to compare its in-plane anisotropy to that of a $50 \mu\text{m}$ wide SuperPower track, which, given the small size of IBAD grains, should also be unaffected by its width. While ζ of the MOD tape rises up to $\mu_0 H = 8 \text{ T}$, the anisotropy of the MOCVD CC reaches a saturation value at $\sim 4 \text{ T}$.

Both CC types show a considerable out-of-plane anisotropy. In most applications magnetic fields occur with components in different orientations, i.e. also away from $H||ab$. The manufacturers, therefore, will have to continue their efforts of exploring ways to introduce various pinning centres into their samples in order to achieve flatter angular characteristics.

¹⁰It needs to be borne in mind, however, that the absolute J_c values quoted in this thesis are affected by a certain amount of uncertainty due to inaccuracies in the film thickness used to calculate J_c from I_c .

**Figure 10.35:**

The SuperPower tape showed a significantly higher in-plane anisotropy than the American Superconductor product. The error (indicated by error bars) in the MOCVD curve are due to small deviations in J_c at $\phi = -90^\circ$ and $+90^\circ$.

When it comes to the width dependence of CC tracks and striation to reduce ac losses, the big grain size found in the American Superconductor tape is potentially detrimental. One (or a few) grains or GBs with poor properties can reduce the performance of a track only a few grains wide significantly. The smaller grain size given by IBAD should prove beneficial in this scenario.

10.6. Summary and Conclusions

In this chapter investigations of coated conductors produced by SuperPower's MOCVD process were discussed. TEM micrographs showed that the grain boundaries in these samples are planar, rather than meandering. The high critical current density is due to the good grain-to-grain alignment, which has been confirmed by XRD. XRD measurements also showed that the tape is slightly vicinal.

The critical current density for $H \perp$ film plane does not depend on whether the track is patterned parallel or perpendicular to the tape direction, despite its vicinality. In angular out-of-plane J_c measurements on an L track the shift of the $H||ab$ peak observed previously was confirmed. At low fields those curves are highly asymmetric, which can be explained by the sample's vicinality and by tilted defect planes, acting as correlated pinning centres. As expected a T track did not show this asymmetry. The high J_c values of the T track mean that—in principle—the IBAD system could be rotated by 90° in

order to make the tape direction perpendicular to the vicinal steps and to overcome the J_c asymmetry of L tracks.

A different kind of asymmetry in out-of-plane measurements was seen at very low fields. Changing the polarity of the applied field reverses the asymmetry, which implies that it is related to a different surface barrier depending on the direction of flux penetration.

The in-plane anisotropy was determined for an L track. Significantly higher values than for American Superconductor samples were found, which can be explained by the different microstructure of the two types of CCs, due to the different production routes.

In a T track vicinal channelling was observed, despite the rather small vicinal angle. This is consistent with the sample's good texture, as highly misaligned grains would prevent vortex channelling along the ab -planes. To the author's best knowledge this is the first time vicinal channelling was seen in a coated conductor.

The high J_c values measured in an isolated grain boundary confirm that GBs do not limit current flow significantly in IBAD coated conductors. The onset of an enhanced minimum at maximum Lorentz force was seen, which could be related to vortex channelling along the grain boundary.

11 CCs Based on Different RABiTS Tapes

In this chapter measurements on coated conductors are presented which were fabricated using different RABiTS tapes. As the substrate has a strong influence on the performance of a coated conductor it is crucial to investigate in detail how the critical current density depends on the substrate. The best way to do so is by comparing samples consisting of different substrates which are otherwise the same, i.e. which have the same buffer and YBCO layers. A set of such tapes were supplied to the author by IFW Dresden.

The different types of substrates and the aims behind their development are delineated in Sec. 11.1. This is followed by the presentation of the obtained critical current densities for fields perpendicular to the film plane (Sec. 11.2.1) and swept out-of- and in-plane (Secs. 11.2.2 and 11.2.3).

11.1. Previous Studies and Substrate Fabrication

A significant amount of the work related to coated conductors at IFW is dedicated to the development of RABiT substrates. As discussed in Sec. 4.2 an ideal substrate should combine high yield strength with weak ferromagnetism (i.e. a low Curie temperature). Both can be accomplished by alloying Ni with a certain amount of, for example, W or Cr; in most cases Ni-5at%W tapes are employed. The downside of this approach, however, is a reduced cube texture, which has detrimental consequences on the quality of the buffer

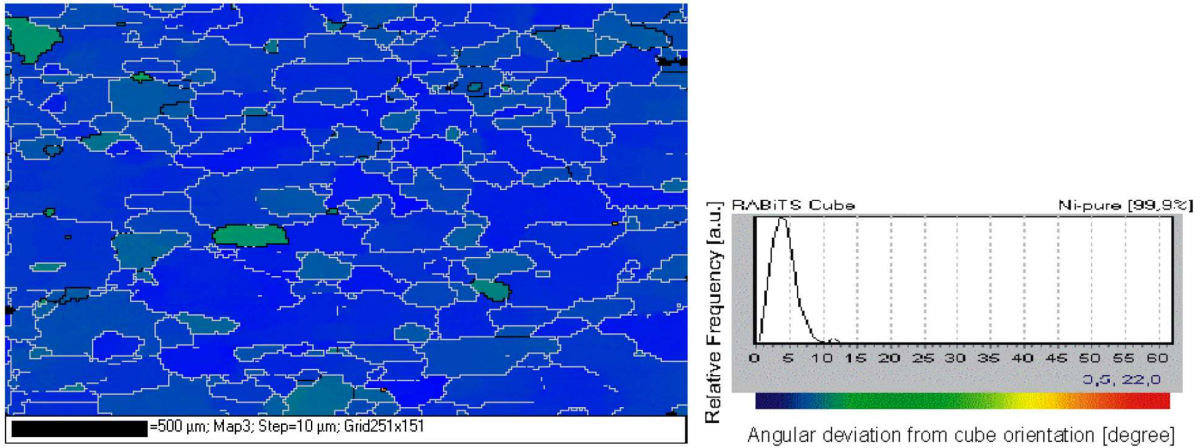


Figure 11.1.: EBSD map showing elongated substrate grains (adapted from [165]).

and superconducting layers. Consequently, efforts were undertaken to find the ideal alloying amount, offering the best compromise between texture and mechanic/magnetic properties [235]. To this end, Eickemeyer *et al.* [164] fabricated Ni-7.5at%W tapes, one of which was measured for this thesis.

A different approach to improve substrate properties are composite tapes, which consist of a highly alloyed core and a weakly alloyed outer shell, thus combining low ferromagnetism and mechanical robustness with a strong cube texture [163].

Another parameter that can be optimised is the grain aspect ratio. It was shown that grains elongated along the rolling direction lead to enhanced critical current densities, as they facilitate currents by-passing GBs with a high misorientation [236, 237]. This is similar to the “brick-wall” model [133] for BSCCO tapes mentioned in Sec. 4.1. Elongated grains can be achieved by a sophisticated combination of tape rolling and heat treatments of a Ni ingot micro-alloyed with, for example, Ag or Ag and Y [165]. An EBSD map of such a sample is shown in Fig. 11.1. A CC with a grain aspect ratio > 2 was measured for this thesis.

11.2. Critical Current Densities

The architecture of the samples supplied by IFW can be found in Sec. 4.5. A summary of their basic properties, in particular the composition of the different substrates, is given in Table 11.1.

Table 11.1.: Summary of the properties of the samples from IFW Dresden. The FWHM (full width at half maximum) of XRD rocking curves for the rolling ($\Delta\omega_{\text{RD}}$) and transverse ($\Delta\omega_{\text{TD}}$) directions and of ϕ -scans, measured on the YBCO layer, are listed (data from IFW). In the case of $\Delta\omega_{\text{RD}}$ the x-ray beam was in a plane parallel to the RD while the sample was rotated about an axis parallel to the TD (and vice versa for $\Delta\omega_{\text{TD}}$). Unlike the in-plane data the rocking curve FWHM values were not obtained on these specific samples, but on comparable tapes. The transition temperatures were measured by the author (onset of zero resistance).

Sample	Substrate	$\Delta\omega_{\text{RD}}$	$\Delta\omega_{\text{TD}}$	$\Delta\phi$	T_c (K)
MU600 [163, 167]	Ni-5at%W	$7.5^\circ \pm 0.2^\circ$	$5.1^\circ \pm 0.2^\circ$	6.8°	90.7
MU644 [164, 167]	Ni-7.5at%W	9.1°	4.9°	8.0°	89.8
MU659 [165, 167]	Ni-Ag-Y (elongated grains)	n/a	n/a	7.5°	89.3

A slight T_c reduction of the Ni-7.5at%W sample compared to Ni-5at%W is consistent with inductive measurements [164]. A similar effect has also been observed for samples with elongated grains¹ [237].

All J_c values reported in this chapter were determined using a $1\ \mu\text{V}$ criterion. The nominal thickness of the superconducting layer of all samples was 300 nm, and the tracks patterned onto them were $250\ \mu\text{m}$ wide and 1 mm long. The measurements were performed at $T = 77.35\ \text{K}$.

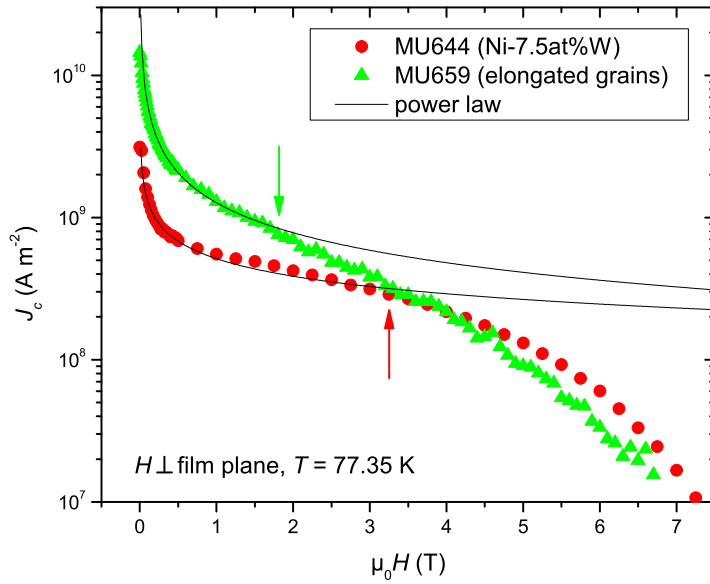
11.2.1. Fields Perpendicular to the Film Surface

The samples MU644 and MU659 were measured for fields applied perpendicular to the film surface. As can be seen in Fig. 11.2 at low fields MU659 exhibits significantly higher values of J_c . This can be attributed to the beneficial effect of elongated grains, attenuating the J_c suppression due to GBs.

Both curves were fitted to the power law given by Eq. (8.1), which has been shown to describe $J_c(H)$ well in a field range where it is limited by GBs [108]. As can be seen in Fig. 11.2, the power law fit and the measured data diverge at a lower field for MU659 than for MU644, implying that the latter is more strongly limited by boundaries and thus supporting above explanation for the enhanced low-field J_c of MU659.

At a field of $\sim 3.5\ \text{T}$ the measured $J_c(H)$ curves of the two samples overlap, suggesting

¹Note, however, that the samples in Ref. [237] were fabricated in a slightly different way compared to MU659.


Figure 11.2:

Power law fits diverge at lower fields for a sample with elongated grains, implying that it is less limited by grain boundaries. The corresponding fields are indicated by arrows.

that no significant GB limitation is present in either sample above this field.

MU659 was also measured for decreasing fields, similar to the experiments performed on American Superconductor and SuperPower samples, discussed in Secs. 8.3.1 and 10.4.1. As can be seen in Fig. 11.3 virtually no hysteresis was observed, corroborating the fact that elongated grains notably reduce the effect of grain boundaries.

11.2.2. Fields Out-of-Plane

Angular measurements with fields out-of-plane were performed on all three samples, i.e. the field was rotated in θ with ϕ held constant at either $\phi = 0^\circ$ or 90° (see Fig. 6.2 for the definition of the angles). The results of these scans are presented in Fig. 11.4. Note that in the first case ($\phi = 0^\circ$) the Lorentz force changes from its maximum value at $\theta = 0^\circ$ to $F_L = 0$ (force free) at $\theta = \pm 90^\circ$. In a θ -scan with $\phi = 90^\circ$, on the other hand, F_L remains at a maximum during the whole measurement.

The maxima in J_c at $\theta = \pm 90^\circ$ are due to $B||ab$ and the resulting intrinsic pinning. The different heights of the peaks for $\phi = 0^\circ$ (filled symbols) and 90° (open symbols) are caused by the difference in Lorentz force. As the latter only depends on the measurement geometry and not on the specific sample this behaviour is seen in all three samples.

In order to compare the tapes, the curves obtained at $\phi = 90^\circ$ and $\mu_0 H = 1$ T are plotted in one graph in Fig. 11.4(d). The most striking feature is that only MU600 exhibits a c -axis peak (at $\theta = 0^\circ$). At 1 T the critical current density can be expected

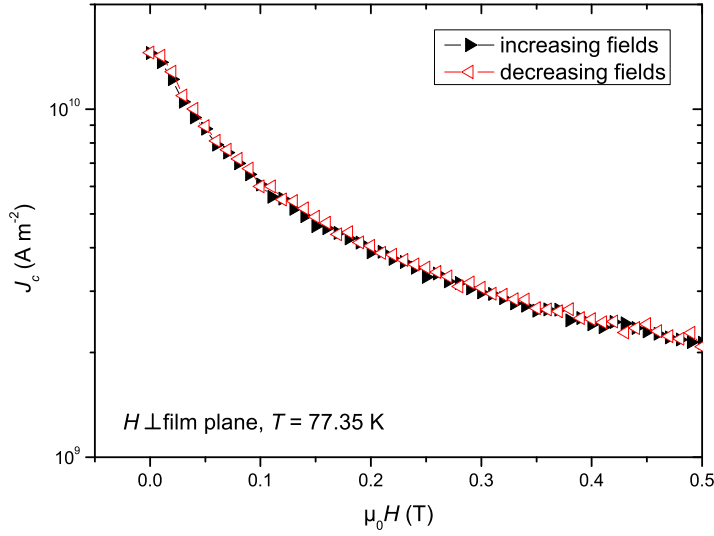


Figure 11.3: No noticeable hysteresis was found for sample MU659.

to be limited by GBs in this sample, hence it is reasonable to conclude that the peak is due to pinning by dislocations in the boundaries [104]. The YBCO layer of the samples supplied by IFW has not been doped by other elements in order to introduce additional pinning centres into the grains [61], which would enhance the overall $J_c(H||c)$ if it was limited by grains. In agreement with this the c -axis peak is not present at $\mu_0 H = 4$ T, as can be seen in Fig. 11.4(a).

The fact that $J_c(\theta)$ of MU659 shows no c -axis peak, despite its comparable behaviour with MU600 at $|\theta| > 45^\circ$ [see Fig. 11.4(d)], could be related to a reduced GB limitation in MU659 due to elongated grains. As a consequence, at $\mu_0 H = 1$ T the critical current density would not be (significantly) governed by the properties of GBs any more, hence the influence of GB dislocations on the overall J_c would be suppressed.

No maximum is observed at $\theta = 0^\circ$ and all fields investigated in the scans on MU600 with $\phi = 0^\circ$, because in this case the enhanced J_c due to dislocations is counteracted by an increasing Lorentz force as θ approaches 0° .

The 1 T θ -scan of MU644 is suppressed at all angles with respect to $J_c(\theta)$ of the other two samples [see Fig. 11.4(d)]. At $\mu_0 H = 4$ T, on the other hand, the curves of MU644 and MU659 overlap over a large angular range (not shown). This is in agreement with what was observed in measurements of $J_c(H)$ for fields perpendicular to the film plane (see Sec. 11.2.1).

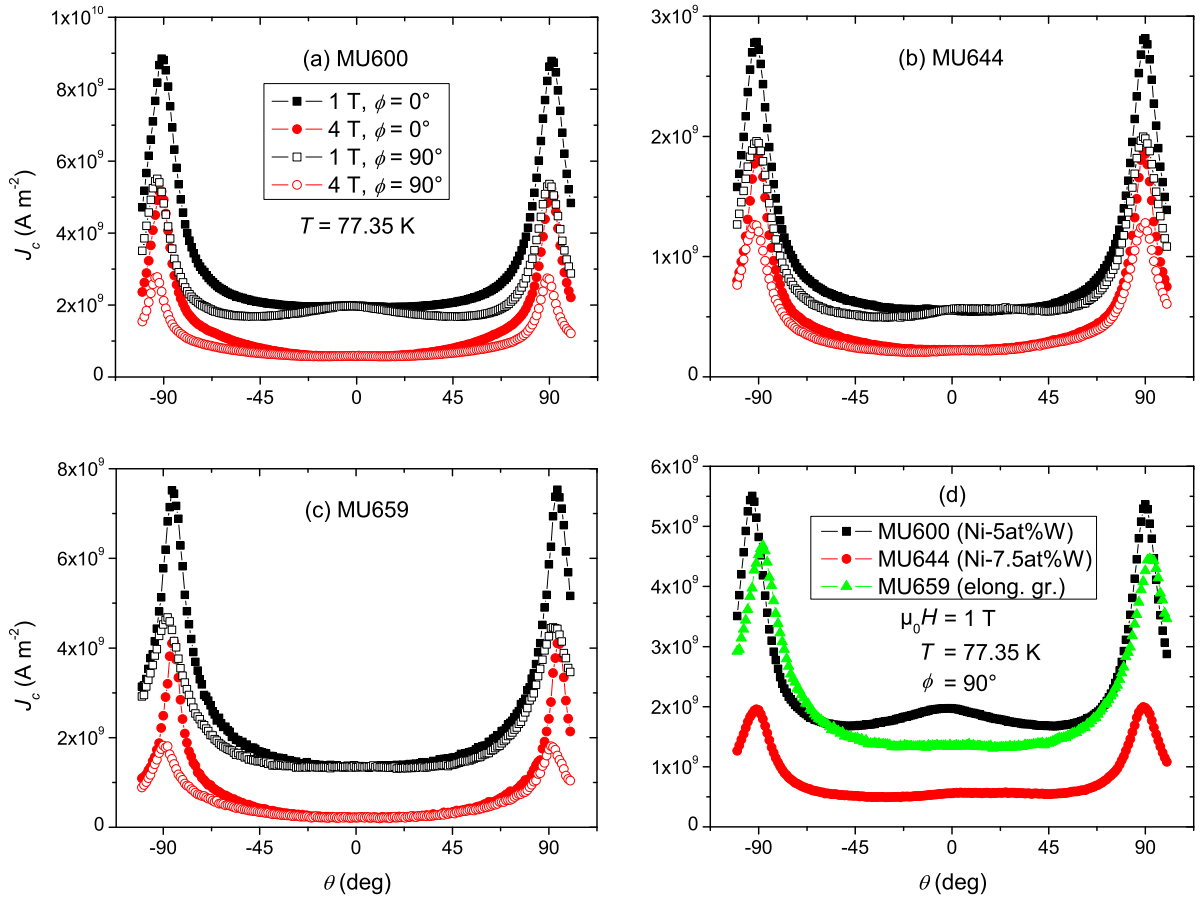
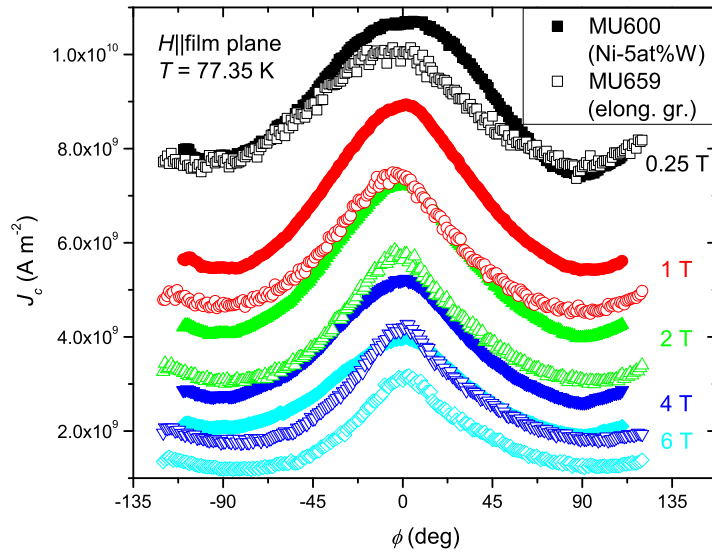


Figure 11.4.: Angular scans on MU600, MU644 and MU659. The legend in (a) applies to (b) and (c) as well. (d) Scans of all three samples at maximum Lorentz force ($\phi = 90^\circ$) and $\mu_0 H = 1 \text{ T}$.

11.2.3. Fields In-Plane

The samples MU600 and MU659 were measured with magnetic fields swept in the plane of the film. The resulting curves at selected fields are plotted in Fig. 11.5. At intermediate and high fields J_c of MU659 is suppressed with respect to MU600. This might appear surprising, as one would expect different samples to behave in a very similar way above their crossover field B_{cr} , no matter what the shape of their GB network is. The obtained result implies that elongated grains (at present) do not supply as good a template for buffer and YBCO growth as conventional Ni-5at%W substrates. One could speculate that the complex treatment necessary to achieve elongated grains leads to a certain degradation of the substrate surface which is then transferred into the supercon-


Figure 11.5:

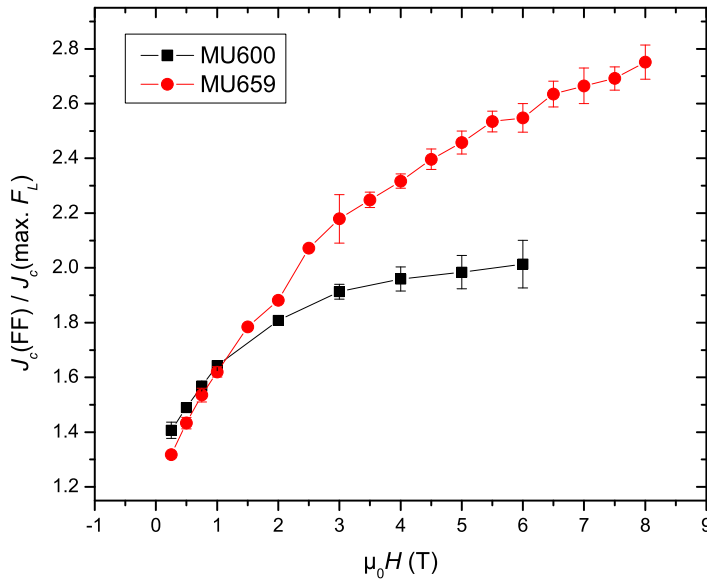
In-plane scans of a sample with a standard Ni-5%W substrate (MU600) and one with elongated grains (MU659).

ducting layer, possibly leading to cracks or other defects. This would only apply to the grains, however; the low-field performance is very good, as discussed below.

As the applied field is reduced, the curves of MU600 and MU659 overlap, at least at $\phi \approx \pm 90^\circ$ (see the 0.25 T scans in Fig. 11.5). This means that the sample with elongated grains behaves comparably better in a field range where J_c is GB dominated, which was of course the motivation for high aspect ratio grains in the first place. Consequently, the in-plane measurements confirm the beneficial properties of elongated grains at low fields.

Upon closer inspection one finds that at $\phi \approx 0^\circ$ (i.e. around the force free orientation) even at $\mu_0 H = 0.25$ T MU659 shows a slightly reduced critical current density. This also manifests itself in the in-plane anisotropy $\zeta = J_c(\text{FF})/J_c(\text{max. } F_L)$, plotted in Fig. 11.6, which is lower for MU659 at $\mu_0 H \leq 1$ T. This finding is consistent with a “brick-wall” model and the resulting flow of currents in directions not parallel to the macroscopic current direction in order to avoid GBs with significant misorientations. It is well documented that pronounced current percolation leads to a flattening of in-plane scans [200].

The high values of ζ of MU659 at elevated fields remain to be discussed now. In general a high in-plane anisotropy is related to microscopic currents parallel to the macroscopic current direction, leading to a strong force-free maximum. The obtained data suggest that grains elongated along the rolling direction encourage this. Intuitively one might expect a grain elongation to force currents to flow more parallel to each other. This,


Figure 11.6:

In-plane anisotropy of MU600 and MU659. The error bars are due to a slight asymmetry of some of the ϕ -scans.

however, disagrees with the fact that at high fields GBs are not expected to limit current flow.

A possible explanation might be found in the out-of-plane tilt of grains. Unfortunately $\Delta\omega$ has not been obtained for MU659, but it is conceivable that “stretching” grains in one direction leads to a reduction of their out-of-plane misorientation in that direction, hence $\Delta\omega_{\text{RD}}$ would be lower, compared to a conventional substrate. A lower out-of-plane tilt in one direction should lead to an enhanced J_c parallel to it, as the currents do not have to cross from one ab -plane into the next that often. Consequently, grain elongation would lead to a J_c enhancement parallel to the long edge of grains, at fields where J_c is grain-limited, and thus reduce percolation; this would cause an increase in the in-plane anisotropy. In a first step to confirm this theory, XRD rocking curves in both directions would have to be acquired.

In summary—according to above models—elongated grains enhance current flow in directions other than the rolling direction at low fields, but they suppress percolation at high H .

11.3. Summary and Conclusions

The critical current densities of films grown on different RABiT substrates were measured for fields in- and out-of-plane.

A CC with a Ni-7.5at%W substrate showed a reduced critical current density, probably due to its weaker cube texture compared to that achievable in Ni-5at%W tapes. A sample with elongated grains, on the other hand, performed particularly well at low fields, where high aspect ratio grains help to overcome the GB limitation to current flow. This was confirmed by analysing the shape of the corresponding $J_c(H)$ curve and by the lack of hysteresis in measurements with decreasing fields. In out-of-plane angular measurements on the Ni-5at%W sample a c -axis peak was observed, which was explained by pinning due to dislocations. In in-plane scans the conductor with elongated grains showed relatively better properties and a *reduced* in-plane anisotropy at low fields, which was explained by the microscopic current flow in such a sample. On the contrary, at high fields grains with a high aspect ratio were found to lead to an *enhanced* in-plane anisotropy.

12 Conclusions and Further Work

12.1. Conclusions

Coated conductors (CCs) produced by different routes were investigated for this thesis using field angle J_c measurements with a special focus on the properties of their grain boundaries.

The most interesting and relevant result of this work is the discovery of an angle dependent crossover from grain boundary (GB) to grain limited critical current density in CCs produced by *Metal-Organic Deposition (MOD)*. When an elevated magnetic field is swept in the film plane J_c is limited by GBs around the force free (FF) configuration and by grains around maximum Lorentz force. This result, found by comparing J_c of isolated GBs to that of a single grain, was confirmed by measurements on wider (i.e. polycrystalline) tracks and by low-temperature scanning laser microscopy. These experiments showed that in-plane scans became flatter as the track was narrowed down, which could be explained by the crossover. In laser scanning clear dissipation at GBs was observed, but only when the field was parallel to the macroscopic current direction (i.e. FF).

These findings can be explained by how microscopic currents flow in MOD tapes, which are known to exhibit meandering GBs. The results are relevant for applications where significant components of magnetic field occur parallel to the plane of the tape. Unlike for $H \perp$ plane, where GBs limit the overall J_c at low fields only, in the force free configuration they need to be taken into account up to and beyond 8 T (at $T = 77.35$ K).

In measurements on a tape produced by *Metal-Organic Chemical Vapour Deposition*

(MOCVD) several published results were confirmed. This includes, in particular, the shift of the intrinsic pinning maximum with magnitude of field, due to a change in the direction of the vortices and the pinning mechanism. Previous studies were extended by in-plane measurements, which showed a significantly higher anisotropy compared to the MOD conductor. This behaviour is consistent with the different grain morphology and a different level of texture in the two products.

In angular scans on a track patterned in the transverse direction of the MOCVD tape vicinal channelling was found. To the best knowledge of the author this is the first report of this phenomenon in a coated conductor. A GB isolated in a sample cut from the same tape exhibited a high critical current density, in agreement with its low misorientation angle, and characteristics which indicate the occurrence of vortex channelling along the boundary.

The critical current densities of coated conductors manufactured from *different Rolling Assisted Bi-axially Textured Substrates (RABiTS)* were compared. A tape with elongated grains gave very promising results at all angles investigated, in particular at low fields, where high aspect ratio grains appear to contribute significantly to overcoming GB limitations. The sample showed a comparably low in-plane anisotropy at low fields and high values at high H , which can be explained by the specific flow of microscopic currents in such a tape.

In summary, it was shown that today's second generation high-temperature superconductors reach impressive critical current densities. This is achieved by very different approaches, whether GB meandering is introduced by the employed deposition technique, a particular sharp cube texture is accomplished by Ion Beam Assisted Deposition (IBAD) or whether the beneficial properties of elongated grains are exploited. After almost 25 years of research in HTS the technology appears to finally have matured enough to allow large-scale applications which can compete with conventional non-superconducting solutions.

12.2. Further Work

Naturally, almost every finding or successful experiment also leads to new questions and ideas. Consequently, several experiments are discussed in the following which might be worthwhile in future studies.

The bridges across single boundaries in *RABiTS MOD* samples (see Chap. 7) were all perpendicular to the macroscopic direction of the GB. Patterning a bridge at an angle other than 90° with respect to the boundary would reduce the symmetry [238]. Maximum Lorentz force and $H \parallel$ GB plane would, thus, occur at different angles in in-plane scans and the effect of the boundary could be separated from that of maximum F_L . One might expect a shift of the the extrema in J_c with field, depending on whether GB or grains are the limiting factor, similar to the behaviour of the $25 \mu\text{m}$ wide track in Fig. 8.6.

An interesting experiment would consist of investigating an isolated GB by both transport measurements and scanning laser microscopy. Ideally the voltage response detected at the boundary should disappear at the same combinations of magnitude of field and in-plane angle ϕ where the crossover from GB to grain limited critical current density occurs.

The MOD tapes investigated exhibited needle-like structures, which are probably a -axis grains [several micrometres long, visible in Fig. 5.2(b)]. It should be possible to isolate one of them to examine if they pose a significant limitation to current flow and whether efforts to avoid them should be undertaken.

In an attempt to confirm the results on the width dependence of J_c presented in Chap. 8 a track was successively measured by the author and cut into filaments by Thomas Thersleff using a FIB. Similar to narrowing down a track, this reduces the number of possible percolation paths, thus rendering the track more GB dominated [197]. The advantage is that the same cross-section is measured in all steps, thus eliminating the risk of distorting the observed width dependence by removing particularly good or bad regions. Due to a lack of time this experiment could not (yet) be finished.

In order to support the explanation for the low field asymmetry of in-plane scans (see Fig. 8.8), namely the rough surface, one could polish a sample. The smoother surface should provide a higher surface barrier, hence reducing the asymmetry.

In the case of the *IBAD MOCVD* tape it would certainly be worthwhile to isolate another GB and confirm if vortex channelling indeed occurs at fields parallel to the boundary plane. Comparing the results to an isolated grain would allow one to determine if GBs cause a noticeable limitation of the current carrying capacity of these conductors.

Several experiments could also be performed on polycrystalline samples. An investigation of the width dependence of J_c would probably involve a FIB to narrow down a track, due to the smaller IBAD grain size.

As discussed in Sec. 10.1.2 the flux lines are tilted in opposite directions depending on whether the effects of material anisotropy or sample geometry prevail. One could investigate if changing the aspect ratio of a track pushes its behaviour from one regime into the other.

The plateau shown in Fig. 10.22 would also warrant further investigations, e.g. by reversing the direction of rotation to confirm its existence or by measuring $J_c(\theta)$ at temperatures where it might be more pronounced.

More data could also be obtained on coated conductors based on *different RABiT substrates*. This includes, in particular, a more detailed measurement of the critical current density for fields swept in-plane, depending on the substrate type and grain shape. No composite tape has been measured for this thesis, and it would certainly be worthwhile to compare their angular behaviour to that of conventional RABiTS tapes.

Another experiment could involve patterning tracks in both rolling and transverse directions on a tape with elongated grains. For fields applied \perp film plane it was shown by Eickemeyer, Hühne *et al.* [236, 237] that a transverse track had a suppressed J_c at low fields. This study could be extended by measurements with fields in the film plane.

Furthermore, the J_c hysteresis for increasing and decreasing fields could be quantified systematically for the different substrates in order to correlate its strength to the amount of GB limitation.

Finally, GBs could be isolated in these tapes in order to investigate how the different substrates influence the properties of boundaries on a local scale.

An experiment conceivable on any type of CC or single crystal sample would be the isolation of a twin boundary to investigate if these boundaries cause at least a very limited J_c suppression. Due to the small size of twinned domains (~ 100 – 150 nm, see Fig. 10.8) this would certainly push the capabilities of EBSD [239] and FIB to the limit. As an alternative to the isolation of single GBs and grains, microbridges could be patterned along and perpendicular to the twin boundaries.

Bibliography

- [1] H. K. Onnes, *Leiden Communications* **120b**, **122b**, **124c** (1911).
- [2] N. A. Rutter, *Microstructural Development and Superconducting Parameters of the $YBa_2Cu_3O_{7-\delta}$ Coated Conductor*, Ph.D. thesis, University of Cambridge (2001).
- [3] W. Meissner and R. Ochsenfeld, *Naturwissenschaften* **21**, 787 (1933).
- [4] F. London and H. London, *Proc. Roy. Soc.* **A149**, 71 (1935).
- [5] L. D. Landau, *Phys. Z. Sowjet.* **11**, 545 (1937).
- [6] V. L. Ginzburg and L. D. Landau, *Zh. Eksp. i Teor. Fiz.* **20**, 1064 (1950).
- [7] J. Bardeen, L. N. Cooper, and J. R. Schrieffer, *Phys. Rev.* **108**, 5, 1175 (1957).
- [8] L. P. Gor'kov, *Zh. Eksperim. i Teor. Fiz.* **36**, 1918 (1959).
- [9] H. W. Weber and O. Hittmair, *Supraleitung*, Verlag Karl Thiemig (1979).
- [10] M. Tinkham, *Introduction to Superconductivity*, McGraw-Hill (1996).
- [11] J. R. Waldram, *Superconductivity of Metals and Cuprates*, IOP Publishing (1996).
- [12] A. A. Abrikosov, *Sov. Phys. JETP* **5**, 1174 (1957).
- [13] H. W. Weber and O. Hittmair, *Supraleitung*, page 207, Verlag Karl Thiemig (1979).
- [14] H. Träuble and U. Essmann, *J. Appl. Phys.* **39**, 4052 (1968).
- [15] J. R. Waldram, *Superconductivity of Metals and Cuprates*, page 80, IOP Publishing (1996).

- [16] B. Dam, J. M. Huijbregtse, F. C. Klaassen, R. C. F. van der Geest, G. Doornbos, J. H. Rector, A. M. Testa, S. Freisem, J. C. Martinez, B. Stauble-Pumpin, and R. Griessen, *Nature* **399**, 6735, 439 (1999).
- [17] J. M. Huijbregtse, B. Dam, R. C. F. van der Geest, F. C. Klaassen, R. Elberse, J. H. Rector, and R. Griessen, *Phys. Rev. B* **62**, 2, 1338 (2000).
- [18] C. P. Bean, *Rev. Mod. Phys.* **36**, 31 (1964).
- [19] H. London, *Phys. Lett.* **6**, 2, 162 (1963).
- [20] A. M. Campbell, *Concise Encyclopedia of Magnetic and Superconducting Materials* (ed. by J. Evetts), chapter AC Losses in Superconducting Materials, page 19, Pergamon Press, Oxford (1992).
- [21] Y. Yang and E. Martinez, *Handbook of Superconducting Materials* (ed. by D. A. Cardwell, D. S. Ginley), chapter AC losses in conductors, page 1385, IOP Publishing, Bristol, Philadelphia (2003).
- [22] A. I. Larkin and Y. N. Ovchinnikov, *J. Low Temp. Phys.* **34**, 3-4, 409 (1979).
- [23] J. Bardeen and M. J. Stephen, *Phys. Rev.* **140**, 4A, A1197 (1965).
- [24] J. R. Waldram, *Superconductivity of Metals and Cuprates*, page 274, IOP Publishing (1996).
- [25] P. W. Anderson, *Phys. Rev. Lett.* **9**, 7, 309 (1962).
- [26] P. W. Anderson and Y. B. Kim, *Rev. Mod. Phys.* **36**, 1, 39 (1964).
- [27] R. Griessen, *Concise Encyclopedia of Magnetic and Superconducting Materials* (ed. by J. Evetts), chapter Flux Creep Phenomena, page 145, Pergamon Press, Oxford (1992).
- [28] J. D. Johnson, D. N. Zheng, and A. M. Campbell, *Research Review*, page 167, IRC, Cambridge University (1994).
- [29] J. R. Clem, *Phys. Rev. B* **43**, 10, 7837 (1991).
- [30] R. Kleiner and P. Müller, *Phys. Rev. B* **49**, 2, 1327 (1994).

- [31] V. G. Kogan and J. R. Clem, *Concise Encyclopedia of Magnetic and Superconducting Materials* (ed. by J. Evetts), chapter Anisotropy in Superconducting Materials, page 43, Pergamon Press, Oxford (1992).
- [32] M. Tinkham, *Introduction to Superconductivity*, page 320, McGraw-Hill (1996).
- [33] W. E. Lawrence and S. Doniach, in E. Kanda, editor, *Proc. 12th Int. Conf. Low Temp. Phys.*, page 361, Kyoto (1970).
- [34] G. Blatter, M. V. Feigelman, V. B. Geshkenbein, A. I. Larkin, and V. M. Vinokur, *Rev. Mod. Phys.* **66**, 4, 1125 (1994).
- [35] J. R. Clem, *Supercond. Sci. Technol.* **11**, 10, 909 (1998).
- [36] J. R. Clem and M. W. Coffey, *Phys. Rev. B* **42**, 10, 6209 (1990).
- [37] P. Berghuis, E. Di Bartolomeo, G. A. Wagner, and J. E. Evetts, *Phys. Rev. Lett.* **79**, 12, 2332 (1997).
- [38] B. Roas, L. Schultz, and G. Saemann-Ischenko, *Phys. Rev. Lett.* **64**, 4, 479 (1990).
- [39] J. R. Gavaler, *Appl. Phys. Lett.* **23**, 8, 480 (1973).
- [40] J. G. Bednorz and K. A. Müller, *Z. Phys. B* **64**, 2, 189 (1986).
- [41] M. K. Wu, J. R. Ashburn, C. J. Torng, P. H. Hor, R. L. M. L. Gao, Z. J. Huang, Y. Q. Wang, and C. W. Chu, *Phys. Rev. Lett.* **58**, 9, 908 (1987).
- [42] S. Hikami, T. Hirai, and S. Kagoshima, *Jpn. J. Appl. Phys.* **26**, 4, L314 (1987).
- [43] Z. X. Zhao, L. Q. Chen, Q. S. Yang, Y. H. Huang, G. H. Chen, R. M. Tang, G. R. Liu, C. G. Cui, L. Chen, L. H. Wang, S. Q. Guo, S. L. Li, and J. Q. Bi, *Kexue Tongbao* **32**, 10, 661 (1987).
- [44] H. Maeda, Y. Tanaka, M. Fukutomi, and T. Asano, *Jpn. J. Appl. Phys.* **27**, 2, L209 (1988).
- [45] Z. Z. Sheng and A. M. Hermann, *Nature* **332**, 6159, 55 (1988).
- [46] Z. Z. Sheng and A. M. Hermann, *Nature* **332**, 6160, 138 (1988).

- [47] J. Clarke and D. C. Larbalestier, *Nature Physics* **2**, 12, 794 (2006).
- [48] J. Nagamatsu, N. Nakagawa, T. Muranaka, Y. Zenitani, and J. Akimitsu, *Nature* **410**, 6824, 63 (2001).
- [49] Y. Kamihara, T. Watanabe, M. Hirano, and H. Hosono, *J. Am. Chem. Soc.* **130**, 11, 3296 (2008).
- [50] R. Zhi-An, L. Wei, Y. Jie, Y. Wei, S. Xiao-Li, Zheng-Cai, C. Guang-Can, D. Xiao-Li, S. Li-Ling, Z. Fang, and Z. Zhong-Xian, *Chinese Phys. Lett.* **25**, 6, 2215 (2008).
- [51] J. R. Waldram, *Superconductivity of Metals and Cuprates*, page 223, IOP Publishing (1996).
- [52] N. M. Alford, S. J. Penn, and T. W. Button, *Supercond. Sci. Technol.* **10**, 4, 169 (1997).
- [53] A. Schilling, M. Cantoni, J. D. Guo, and H. R. Ott, *Nature* **363**, 6424, 56 (1993).
- [54] M. Cyrot and D. Pavuna, *Introduction to Superconductivity and High- T_c Materials*, World Scientific, Singapore, London (1992).
- [55] J. M. Tarascon, *Chemistry of High Temperature Superconductors*, American Chemical Society, Washington (1987).
- [56] J. R. Waldram, *Superconductivity of Metals and Cuprates*, page 273, IOP Publishing (1996).
- [57] G. Deutscher and K. A. Müller, *Phys. Rev. Lett.* **59**, 15, 1745 (1987).
- [58] P. Chaudhari, R. H. Koch, R. B. Laibowitz, T. R. McGuire, and R. J. Gambino, *Phys. Rev. Lett.* **58**, 25, 2684 (1987).
- [59] J. M. Phillips, *J. Appl. Phys.* **79**, 4, 1829 (1996).
- [60] S. R. Foltyn, L. Civale, J. L. MacManus-Driscoll, Q. X. Jia, B. Maiorov, H. Wang, and M. Maley, *Nat. Mater.* **6**, 9, 631 (2007).
- [61] J. Macmanus-Driscoll, S. Foltyn, Q. Jia, H. Wang, A. Serquis, L. Civale, B. Maiorov, M. Hawley, M. Maley, and D. Peterson, *Nature Materials* **3**, 7, 439 (2004).

- [62] V. Selvamanickam, Y. Xie, J. Reeves, and Y. Chen, *MRS Bull.* **29**, 8, 579 (2004).
- [63] J. L. MacManus-Driscoll, S. R. Foltyn, B. Maiorov, Q. X. Jia, H. Wang, A. Serquis, L. Civale, Y. Lin, M. E. Hawley, M. P. Maley, and D. E. Peterson, *Appl. Phys. Lett.* **86**, 3, 032505 (2005).
- [64] M. G. Blamire, R. B. Dinner, S. C. Wimbush, and J. L. MacManus-Driscoll, *Supercond. Sci. Technol.* **22**, 2, 025017 (2009).
- [65] S. Jin, R. C. Sherwood, R. B. van Dover, T. H. Tiefel, and J. D. W. Johnson, *Appl. Phys. Lett.* **51**, 3, 203 (1987).
- [66] J. W. Ekin, A. I. Braginski, A. J. Panson, M. A. Janocko, D. W. C. II, N. J. Zaluzec, B. Flandermeyer, O. F. de Lima, M. Hong, J. Kwo, and S. H. Liou, *J. Appl. Phys.* **62**, 12, 4821 (1987).
- [67] T. R. Dinger, T. K. Worthington, W. J. Gallagher, and R. L. Sandstrom, *Phys. Rev. Lett.* **58**, 25, 2687 (1987).
- [68] P. Chaudhari, J. Mannhart, D. Dimos, C. C. Tsuei, J. Chi, M. M. Oprysko, and M. Scheuermann, *Phys. Rev. Lett.* **60**, 16, 1653 (1988).
- [69] R. A. Camps, J. E. Evetts, B. A. Glowacki, S. B. Newcomb, R. E. Somekh, and W. M. Stobbs, *Nature* **329**, 6136, 229 (1987).
- [70] P. Chaudhari, F. K. LeGoues, and A. Segmüller, *Science* **238**, 4825, 342 (1987).
- [71] D. Larbalestier, A. Gurevich, D. M. Feldmann, and A. Polyanskii, *Nature* **414**, 6861, 368 (2001).
- [72] H. Hilgenkamp and J. Mannhart, *Rev. Mod. Phys.* **74**, 2, 485 (2002).
- [73] J. Ayache, *Phil. Mag.* **86**, 15, 2193 (2006).
- [74] D. M. Feldmann, T. G. Holesinger, R. Feenstra, and D. C. Larbalestier, *J. Am. Ceram. Soc.* **91**, 6, 1869 (2008).
- [75] J. H. Durrell and N. A. Rutter, *Supercond. Sci. Technol.* **22**, 1, 013001 (2009).
- [76] J. Mannhart and P. Chaudhari, *Phys. Today* **54**, 11, 48 (2001).

- [77] D. Dimos, P. Chaudhari, J. Mannhart, and F. K. LeGoues, *Phys. Rev. Lett.* **61**, 2, 219 (1988).
- [78] J. Mannhart, P. Chaudhari, D. Dimos, C. C. Tsuei, and T. R. McGuire, *Phys. Rev. Lett.* **61**, 21, 2476 (1988).
- [79] D. Dimos, P. Chaudhari, and J. Mannhart, *Phys. Rev. B* **41**, 7, 4038 (1990).
- [80] Z. G. Ivanov, P. A. Nilsson, D. Winkler, J. A. Alarco, T. Claeson, E. A. Stepanov, and A. Y. Tzalenchuk, *Appl. Phys. Lett.* **59**, 23, 3030 (1991).
- [81] D. T. Verebelyi, D. K. Christen, R. Feenstra, C. Cantoni, A. Goyal, D. F. Lee, M. Paranthaman, P. N. Arendt, R. F. DePaula, J. R. Groves, and C. Prouteau, *Appl. Phys. Lett.* **76**, 13, 1755 (2000).
- [82] J. H. Durrell, M. J. Hogg, F. Kahlmann, Z. H. Barber, M. G. Blamire, and J. E. Evetts, *Phys. Rev. Lett.* **90**, 24, 247006 (2003).
- [83] D. M. Feldmann, T. G. Holesinger, R. Feenstra, C. Cantoni, W. Zhang, M. Rupich, X. Li, J. H. Durrell, A. Gurevich, and D. C. Larbalestier, *J. Appl. Phys.* **102**, 8, 083912 (2007).
- [84] R. Held, C. W. Schneider, J. Mannhart, L. F. Allard, K. L. More, and A. Goyal, *Phys. Rev. B* **79**, 1, 014515 (2009).
- [85] K. Char, M. S. Colclough, S. M. Garrison, N. Newman, and G. Zaharchuk, *Appl. Phys. Lett.* **59**, 6, 733 (1991).
- [86] K. P. Daly, W. D. Dozier, J. F. Burch, S. B. Coons, R. Hu, C. E. Platt, and R. W. Simon, *Appl. Phys. Lett.* **58**, 5, 543 (1991).
- [87] S. E. Babcock, X. Y. Cai, D. C. Larbalestier, D. H. Shin, N. Zhang, H. Zhang, D. L. Kaiser, and Y. Gao, *Physica C* **227**, 1-2, 183 (1994).
- [88] M. F. Chisholm and D. A. Smith, *Phil. Mag. A* **59**, 2, 181 (1989).
- [89] M. F. Chisholm and S. J. Pennycook, *Nature* **351**, 6321, 47 (1991).
- [90] N. F. Heinig, R. D. Redwing, I. F. Tsu, A. Gurevich, J. E. Nordman, S. E. Babcock, and D. C. Larbalestier, *Appl. Phys. Lett.* **69**, 4, 577 (1996).

- [91] C. Kittel, *Introduction to Solid State Physics*, page 592, John Wiley & Sons, Inc. (1996).
- [92] C. Kittel, *Introduction to Solid State Physics*, page 575, John Wiley & Sons, Inc. (1976).
- [93] A. P. Sutton and R. W. Balluffi, *Interfaces in Crystalline Materials*, Oxford University Press, New York (1995).
- [94] P. Chaudhari and J. W. Matthews, *J. Appl. Phys.* **42**, 8, 3063 (1971).
- [95] D. A. Smith, M. F. Chisholm, and J. Clabes, *Appl. Phys. Lett.* **53**, 23, 2344 (1988).
- [96] D. T. Verebelyi, C. Cantoni, J. D. Budai, D. K. Christen, H. J. Kim, and J. R. Thompson, *Appl. Phys. Lett.* **78**, 14, 2031 (2001).
- [97] T. Haage, J. Zegenhagen, J. Q. Li, H.-U. Habermeier, M. Cardona, C. Jooss, R. Warthmann, A. Forkl, and H. Kronmüller, *Phys. Rev. B* **56**, 13, 8404 (1997).
- [98] S. Bals, G. Rijnders, D. H. A. Blank, and G. V. Tendeloo, *Physica C* **355**, 3-4, 225 (2001).
- [99] Y. Gao, K. L. Merkle, G. Bai, H. L. M. Chang, and D. J. Lam, *Physica C* **174**, 1-3, 1 (1991).
- [100] N. F. Heinig, R. D. Redwing, J. E. Nordman, and D. C. Larbalestier, *Phys. Rev. B* **60**, 2, 1409 (1999).
- [101] K. Char, M. S. Colclough, L. P. Lee, and G. Zaharchuk, *Appl. Phys. Lett.* **59**, 17, 2177 (1991).
- [102] H. Hilgenkamp and J. Mannhart, *Appl. Phys. Lett.* **73**, 2, 265 (1998).
- [103] T. Horide, K. Matsumoto, Y. Yoshida, M. Mukaida, A. Ichinose, and S. Horii, *Phys. Rev. B* **77**, 13, 132502 (2008).
- [104] A. Díaz, L. Mechin, P. Berghuis, and J. E. Evetts, *Phys. Rev. Lett.* **80**, 17, 3855 (1998).
- [105] A. Díaz, L. Mechin, P. Berghuis, and J. E. Evetts, *Phys. Rev. B* **58**, 6, R2960 (1998).

Bibliography

- [106] R. D. Redwing, B. M. Hinaus, M. S. Rzchowski, N. F. Heinig, B. A. Davidson, and J. E. Nordman, *Appl. Phys. Lett.* **75**, 20, 3171 (1999).
- [107] R. G. Humphreys and J. A. Edwards, *Physica C* **210**, 1-2, 42 (1993).
- [108] B. Holzapfel, D. Verebelyi, C. Cantoni, M. Paranthaman, B. Sales, R. Feenstra, D. Christen, and D. P. Norton, *Physica C* **341**, Part 3, 1431 (2000).
- [109] L. Fernández, B. Holzapfel, F. Schindler, B. de Boer, A. Attenberger, J. Hänisch, and L. Schultz, *Phys. Rev. B* **67**, 5, 052503 (2003).
- [110] M. J. Hogg, F. Kahlmann, E. J. Tarte, Z. H. Barber, and J. E. Evetts, *Appl. Phys. Lett.* **78**, 10, 1433 (2001).
- [111] A. Gurevich, M. S. Rzchowski, G. Daniels, S. Patnaik, B. M. Hinaus, F. Carillo, F. Tafuri, and D. C. Larbalestier, *Phys. Rev. Lett.* **88**, 9, 097001 (2002).
- [112] M. J. Hogg, F. Kahlmann, Z. H. Barber, and J. E. Evetts, *Supercond. Sci. Technol.* **14**, 9, 647 (2001).
- [113] J. E. Evetts and B. A. Glowacki, *Cryogenics* **28**, 10, 641 (1988).
- [114] J. R. Thompson, H. J. Kim, C. Cantoni, D. K. Christen, R. Feenstra, and D. T. Verebelyi, *Phys. Rev. B* **69**, 10, 104509 (2004).
- [115] A. A. Polyanskii, A. Gurevich, A. E. Pashitski, N. F. Heinig, R. D. Redwing, J. E. Nordman, and D. C. Larbalestier, volume 53, pages 8687–8697, American Physical Society (1996).
- [116] C. Jooss, K. Guth, V. Born, and J. Albrecht, *Phys. Rev. B* **65**, 1, 014505 (2001).
- [117] V. Born, K. Guth, H. C. Freyhardt, and C. Jooss, *Supercond. Sci. Technol.* **17**, 3, 380 (2004).
- [118] V. K. Vlasko-Vlasov, H. Claus, U. Welp, K. E. Gray, B. Ma, and U. Balachandran, *Appl. Phys. Lett.* **84**, 2, 242 (2004).
- [119] R. B. Dinner, K. A. Moler, D. M. Feldmann, and M. R. Beasley, *Phys. Rev. B* **75**, 14, 144503 (2007).

- [120] R. B. Dinner, K. A. Moler, M. R. Beasley, and D. M. Feldmann, *Appl. Phys. Lett.* **90**, 21, 212501 (2007).
- [121] B. Kalisky, J. R. Kirtley, E. A. Nowadnick, R. B. Dinner, E. Zeldov, Ariando, S. Wenderich, H. Hilgenkamp, D. M. Feldmann, and K. A. Moler, *Appl. Phys. Lett.* **94**, 20, 202504 (2009).
- [122] A. Gurevich and E. A. Pashitskii, *Phys. Rev. B* **57**, 21, 13878 (1998).
- [123] K. Salama, M. Mironova, S. Stolbov, and S. Sathyamurthy, *Physica C* **341-348**, Part 3, 1401 (2000).
- [124] H. Hilgenkamp, C. W. Schneider, B. Goetz, R. R. Schulz, A. Schmehl, H. Bielefeldt, and J. Mannhart, *Supercond. Sci. Technol.* **12**, 12, 1043 (1999).
- [125] T. Amrein, L. Schultz, B. Kabius, and K. Urban, *Phys. Rev. B* **51**, 10, 6792 (1995).
- [126] S. Haindl, M. Kitzun, A. Kauffmann, K. Nenkov, N. Kozlova, J. Freudenberger, T. Thersleff, J. Hänisch, J. Werner, E. Reich, L. Schultz, and B. Holzapfel, *Phys. Rev. Lett.* **104**, 7, 077001 (2010).
- [127] S. Lee, J. Jiang, J. D. Weiss, C. M. Folkman, C. W. Bark, C. Tarantini, A. Xu, D. Abraimov, A. Polyanskii, C. T. Nelson, Y. Zhang, S. H. Baek, H. W. Jang, A. Yamamoto, F. Kametani, X. Q. Pan, E. E. Hellstrom, A. Gurevich, C. B. Eom, and D. C. Larbalestier, *Appl. Phys. Lett.* **95**, 21, 212505 (2009).
- [128] H.-C. Yang, J.-C. Chen, K.-L. Chen, C.-H. Wu, H.-E. Horng, and S. Y. Yang, *J. Appl. Phys.* **104**, 1, 011101 (2008).
- [129] K. Heine, J. Tenbrink, and M. Thöner, *Appl. Phys. Lett.* **55**, 23, 2441 (1989).
- [130] A. P. Malozemoff, D. T. Verebelyi, S. Fleshler, D. Aized, and D. Yu, *Physica C* **386**, 424 (2003).
- [131] A. Godeke, A. den Ouden, A. Nijhuis, and H. H. J. ten Kate, *Cryogenics* **48**, 7-8, 308 (2008).
- [132] B. A. Glowacki, M. Majoros, M. Vickers, J. E. Evetts, Y. Shi, and I. McDougall, *Supercond. Sci. Technol.* **14**, 4, 193 (2001).

- [133] L. N. Bulaevskii, J. R. Clem, L. I. Glazman, and A. P. Malozemoff, *Phys. Rev. B* **45**, 5, 2545 (1992).
- [134] J. L. MacManus-Driscoll, *Handbook of Superconducting Materials* (ed. by D. A. Cardwell, D. S. Ginley), chapter Processing of high T_c conductors: the compound YBCO, page 565, IOP Publishing, Bristol, Philadelphia (2003).
- [135] J. M. S. Skakle, *Mater. Sci. Eng.* **23**, 1, 1 (1998).
- [136] D. P. Norton, A. Goyal, J. D. Budai, D. K. Christen, D. M. Kroeger, E. D. Specht, Q. He, B. Saffian, M. Paranthaman, C. E. Klabunde, D. F. Lee, B. C. Sales, and F. A. List, *Science* **274**, 5288, 755 (1996).
- [137] A. Goyal, D. P. Norton, J. D. Budai, M. Paranthaman, E. D. Specht, D. M. Kroeger, D. K. Christen, Q. He, B. Saffian, F. A. List, D. F. Lee, P. M. Martin, C. E. Klabunde, E. Hartfield, and V. K. Sikka, *Appl. Phys. Lett.* **69**, 12, 1795 (1996).
- [138] A. Goyal, D. P. Norton, D. K. Christen, E. D. Specht, M. Paranthaman, D. M. Kroeger, J. D. Budai, Q. He, F. A. List, R. Feenstra, H. R. Kerchner, D. F. Lee, E. Hatfield, P. M. Martin, J. Mathis, and C. Park, *Appl. Supercond.* **4**, 10-11, 403 (1996).
- [139] L. S. Yu, J. M. E. Harper, J. J. Cuomo, and D. A. Smith, *Appl. Phys. Lett.* **47**, 9, 932 (1985).
- [140] Y. Iijima, N. Tanabe, O. Kohno, and Y. Ikeno, *Appl. Phys. Lett.* **60**, 6, 769 (1992).
- [141] P. N. Arendt and S. R. Foltyn, *MRS Bull.* **29**, 8, 543 (2004).
- [142] R. M. Bradley, J. M. E. Harper, and D. A. Smith, *J. Appl. Phys.* **60**, 12, 4160 (1986).
- [143] D. Dobrev, *Thin Solid Films* **92**, 1-2, 41 (1982).
- [144] A. Polyanskii, R. L. S. Emergo, J. Z. Wu, T. Aytug, D. K. Christen, G. K. Perkins, and D. Larbalestier, *Phys. Rev. B* **72**, 17, 174509 (2005).
- [145] K. Hasegawa, *Advances in superconductivity*, page 745, Springer, Tokyo (1997).

- [146] M. Bauer, R. Semerad, and H. Kinder, *IEEE Trans. Appl. Supercond.* **9**, 2, 1502 (1999).
- [147] H. Kim, J. Yoo, K. Jung, J. Lee, S. Oh, and D. Youm, *Supercond. Sci. Technol.* **13**, 7, 995 (2000).
- [148] Y. Ma, K. Watanabe, S. Awaji, and M. Motokawa, *Appl. Phys. Lett.* **77**, 22, 3633 (2000).
- [149] M. Razeghi, *The MOCVD Challenge*, Institute of Physics Publishing, Bristol (1989).
- [150] V. Selvamanickam, G. Carota, M. Funk, N. Vo, P. Haldar, U. Balachandran, M. Chudzik, P. Arendt, J. R. Groves, R. DePaula, and B. Newnam, *IEEE Trans. Appl. Supercond.* **11**, 1, 3379 (2001).
- [151] V. Selvamanickam, A. Guevara, Y. Zhang, I. Kesgin, Y. Xie, G. Carota, Y. Chen, J. Dackow, Y. Zhang, Y. Zuev, C. Cantoni, A. Goyal, J. Coulter, and L. Civale, *Supercond. Sci. Technol.* **23**, 1, 014014 (2010).
- [152] T. G. Holesinger, B. Maiorov, O. Ugurlu, L. Civale, Y. Chen, X. Xiong, Y. Xie, and V. Selvamanickam, *Supercond. Sci. Technol.* **22**, 4, 045025 (2009).
- [153] M. W. Rupich, D. T. Verebelyi, W. Zhang, T. Kodenkandath, and X. Li, *MRS Bull.* **29**, 8, 572 (2004).
- [154] P. C. McIntyre, M. J. Cima, and M. F. Ng, *J. Appl. Phys.* **68**, 8, 4183 (1990).
- [155] P. C. McIntyre, M. J. Cima, J. A. Smith, R. B. Hallock, M. P. Siegal, and J. M. Phillips, *J. Appl. Phys.* **71**, 4, 1868 (1992).
- [156] T. Araki, H. Kurosaki, Y. Yamada, I. Hirabayashi, J. Shibata, and T. Hirayama, *Supercond. Sci. Technol.* **14**, 9, 783 (2001).
- [157] U. Schoop, M. W. Rupich, C. Thieme, D. T. Verebelyi, W. Zhang, X. Li, T. Kodenkandath, N. Nguyen, E. Siegal, L. Civale, T. Holesinger, B. Maiorov, A. Goyal, and M. Paranthaman, *IEEE Trans. Appl. Supercond.* **15**, 2, Part 3, 2611 (2005).
- [158] M. Ohring, *The Materials Science of Thin Films*, page 101ff, Academic Press, San Diego (1992).

- [159] M. Ohring, *The Materials Science of Thin Films*, page 98ff, Academic Press, San Diego (1992).
- [160] W. Prusseit, G. Sigl, R. Nemetschek, C. Hoffmann, J. Handke, A. Lumkemann, and H. Kinder, *IEEE Trans. Appl. Supercond.* **15**, 2, 2608 (2005).
- [161] M. W. Rupich, U. Schoop, D. T. Verebelyi, C. Thieme, W. Zhang, X. Li, T. Kodendath, N. Nguyen, E. Siegal, D. Buczek, J. Lynch, M. Jowett, E. Thompson, J.-S. Wang, J. Scudiere, A. P. Malozemoff, Q. Li, S. Annavarapu, S. Cui, L. Fritze-meier, B. Aldrich, C. Craven, F. Niu, R. Schwall, A. Goyal, and M. Paranthaman, *IEEE Trans. Appl. Supercond.* **13**, 2, Part 3, 2458 (2003).
- [162] X. Xiong, K. P. Lenseth, J. L. Reeves, A. Rar, Y. Qiao, R. M. Schmidt, Y. Chen, Y. Li, Y.-Y. Xie, and V. Selvamanickam, *IEEE Trans. Appl. Supercond.* **17**, 2, 3375 (2007).
- [163] R. Hühne, V. S. Sarma, D. Okai, T. Thersleff, L. Schultz, and B. Holzapfel, *Supercond. Sci. Technol.* **20**, 7, 709 (2007).
- [164] J. Eickemeyer, R. Huehne, A. Güth, C. Rodig, H. Klauss, and B. Holzapfel, *Supercond. Sci. Technol.* **21**, 10, 105012 (2008).
- [165] J. Eickemeyer, A. Güth, and B. Holzapfel, *Supercond. Sci. Technol.* **21**, 3, 034007 (2008).
- [166] M. W. Rupich, private communication.
- [167] R. Hühne, private communication.
- [168] A. Goyal, M. P. Paranthaman, and U. Schoop, *MRS Bull.* **29**, 8, 552 (2004).
- [169] A. M. Campbell, *IEEE Trans. Appl. Supercond.* **5**, 2, Part 1, 682 (1995).
- [170] S. P. Ashworth, M. Maley, M. Suenaga, S. R. Foltyn, and J. O. Willis, *J. Appl. Phys.* **88**, 5, 2718 (2000).
- [171] J. R. Waldram, *Superconductivity of Metals and Cuprates*, page 369, IOP Publishing (1996).

- [172] N. A. Rutter and A. Goyal, *High Temperature Superconductivity 1* (ed. by A. V. Narlikar), chapter Modelling Current Flow in Granular Superconductors and Implications for Potential Applications, page 377, Springer, Berlin, Heidelberg (2004).
- [173] B. Holzapfel, L. Fernández, F. Schindler, B. de Boer, N. Reger, J. Eickemeyer, P. Berberich, and W. Prusseit, *IEEE Trans. Appl. Supercond.* **11**, 1, Part 3, 3872 (2001).
- [174] N. A. Rutter, B. A. Glowacki, and J. E. Evetts, *Supercond. Sci. Technol.* **13**, 11, L25 (2000).
- [175] S. Reyntjens and R. Puers, *J. Micromech. Microeng.* **11**, 4, 287 (2001).
- [176] D. M. Feldmann, D. C. Larbalestier, D. T. Verebelyi, W. Zhang, Q. Li, G. N. Riley, R. Feenstra, A. Goyal, D. F. Lee, M. Paranthaman, D. M. Kroeger, and D. K. Christen, *Appl. Phys. Lett.* **79**, 24, 3998 (2001).
- [177] R. Herzog and J. E. Evetts, *Rev. Sci. Instrum.* **65**, 11, 3574 (1994).
- [178] R. Herzog, *Critical Currents in YBaCuO Thin Films*, Ph.D. thesis, University of Cambridge (1997).
- [179] J. I. Goldstein, D. E. Newbury, D. C. Joy, C. E. Lyman, P. Echlin, E. Lifshin, L. Sawyer, and J. R. Michael, *Scanning Electron Microscopy and X-Ray Microanalysis*, page 256ff, Springer Science+Business Media, Inc., New York (2003).
- [180] *Electron Backscattered Diffraction Explained*, Oxford Instruments Analytical Ltd. (2004).
- [181] J. I. Goldstein, D. E. Newbury, D. C. Joy, C. E. Lyman, P. Echlin, E. Lifshin, L. Sawyer, and J. R. Michael, *Scanning Electron Microscopy and X-Ray Microanalysis*, page 261, Springer Science+Business Media, Inc., New York (2003).
- [182] C. Kittel, *Introduction to Solid State Physics*, page 28, John Wiley & Sons, Inc. (1996).
- [183] A. P. Zhuravel, A. G. Sivakov, O. G. Turutanov, A. N. Omelyanchouk, S. M. Anlage, A. Lukashenko, A. V. Ustinov, and D. Abraimov, *Low Temp. Phys.* **32**, 6, 592 (2006).

- [184] D. Abraimov, A. G. Sivakov, A. V. Lukashenko, M. V. Fistul, P. Müller, and A. V. Ustinov, *IEEE Trans. Appl. Supercond.* **11**, 1, 3170 (2001).
- [185] D. M. Feldmann, T. G. Holesinger, C. Cantoni, R. Feenstra, N. A. Nelson, D. C. Larbalestier, D. T. Verebelyi, X. Li, and M. Rupich, *J. Mater. Res.* **21**, 4, 923 (2006).
- [186] T. G. Holesinger, P. N. Arendt, R. Feenstra, A. A. Gapud, E. D. Specht, D. M. Feldmann, and D. C. Larbalestier, *J. Mater. Res.* **20**, 5, 1216 (2005).
- [187] D. M. Feldmann, D. C. Larbalestier, T. Holesinger, R. Feenstra, A. A. Gapud, and E. D. Specht, *J. Mater. Res.* **20**, 8, 2012 (2005).
- [188] J. H. Durrell, D. M. Feldmann, and C. Cantoni, *Appl. Phys. Lett.* **91**, 182506 (2007).
- [189] G. Hammerl, A. Schmehl, R. R. Schulz, B. Goetz, H. Bielefeldt, C. W. Schneider, H. Hilgenkamp, and J. Mannhart, *Nature* **407**, 6801, 162 (2000).
- [190] A. A. Gapud, D. K. Christen, R. Feenstra, F. A. List III, and A. Khan, *Supercond. Sci. Technol.* **21**, 7, 075016 (2008).
- [191] A. Palau, T. Puig, X. Obradors, and C. Jooss, *Phys. Rev. B* **75**, 5, 054517 (2007).
- [192] J. A. Xia, N. J. Long, N. M. Strickland, P. Hoefakker, and E. F. Talantsev, *Curr. Appl. Phys.* **8**, 3-4, 262 (2008).
- [193] J. Matsuda, K. Nakaoka, T. Izumi, Y. Yamada, and Y. Shiohara, *Physica C* **468**, 14, 997 (2008).
- [194] S. H. Jang, J. H. Lim, S. Y. Lee, K. T. Kim, C. M. Lee, E. C. Park, S. M. Hwang, S. Park, and J. Joo, *Physica C* **468**, 15-20, 1666 (2008).
- [195] J. H. Durrell, R. Herzog, P. Berghuis, A. P. Bramley, E. J. Tarte, Z. H. Barber, and J. E. Evetts, *Supercond. Sci. Technol.* **12**, 12, 1090 (1999).
- [196] S. I. Kim, D. M. Feldmann, D. T. Verebelyi, C. Thieme, X. Li, A. A. Polyanskii, and D. C. Larbalestier, *Phys. Rev. B* **71**, 10, 104501 (2005).

- [197] J. Hänisch, C. B. Cai, V. S. Sarma, L. Schultz, and B. Holzapfel, *IEEE Trans. Appl. Supercond.* **15**, 2, 2794 (2005).
- [198] C. P. Bean and J. D. Livingston, *Phys. Rev. Lett.* **12**, 1, 14 (1964).
- [199] S. A. Harrington, J. L. MacManus-Driscoll, and J. H. Durrell, *Appl. Phys. Lett.* **95**, 2, 022518 (2009).
- [200] N. A. Rutter, J. H. Durrell, M. G. Blamire, J. L. MacManus-Driscoll, H. Wang, and S. R. Foltyn, *Appl. Phys. Lett.* **87**, 16, 162507 (2005).
- [201] B. A. Glowacki, M. Majoros, N. A. Rutter, and A. M. Campbell, *Physica C* **357-360**, Part 2, 1213 (2001).
- [202] G. A. Levin, P. N. Barnes, J. W. Kell, N. Amemiya, Z. Jiang, K. Yoda, and F. Kimura, *Appl. Phys. Lett.* **89**, 1, 012506 (2006).
- [203] M. Eisterer, R. Fuger, M. Chudy, F. Hengstberger, and H. W. Weber, *Supercond. Sci. Technol.* **23**, 1, 014009 (2010).
- [204] D. V. Abraimov, D. M. Feldmann, A. A. Polyanskii, A. Gurevich, S. Liao, G. Daniels, D. C. Larbalestier, A. P. Zhuravel, and A. V. Ustinov, *IEEE Trans. Appl. Supercond.* **15**, 2, 2954 (2005).
- [205] D. Abraimov, D. M. Feldmann, A. A. Polyanskii, A. Gurevich, G. Daniels, D. C. Larbalestier, A. P. Zhuravel, and A. V. Ustinov, *Appl. Phys. Lett.* **85**, 13, 2568 (2004).
- [206] D. Abraimov, in a talk given at the *MRS Spring Meeting* (2009).
- [207] Z. Chen, F. Kametani, Y. Chen, Y. Xie, V. Selvamanickam, and D. C. Larbalestier, *Supercond. Sci. Technol.* **22**, 5, 055013 (2009).
- [208] X. Y. Song, Z. J. Chen, S. I. Kim, D. M. Feldmann, D. Larbalestier, J. Reeves, Y. Y. Xie, and V. Selvamanickam, *Appl. Phys. Lett.* **88**, 21, 212508 (2006).
- [209] Z. Chen, D. M. Feldmann, X. Song, S. I. Kim, A. Gurevich, J. L. Reeves, Y. Y. Xie, V. Selvamanickam, and D. C. Larbalestier, *Supercond. Sci. Technol.* **20**, 9, S205 (2007).

Bibliography

- [210] M. Tachiki, S. Takahashi, and K. Sunaga, *Phys. Rev. B* **47**, 10, 6095 (1993).
- [211] B. Maiorov, private communication.
- [212] B. Maiorov, B. Gibbons, S. Kreiskott, V. Matias, T. Holesinger, and L. Civale, *Appl. Phys. Lett.* **86**, 13, 132504 (2005).
- [213] B. J. Gibbons, S. Kreiskott, V. Matias, T. G. Holesinger, and J. Y. Coulter, *Mater. Res. Soc. Symp. Proc.* **3**, 9 (2004).
- [214] A. Silhanek, L. Civale, and M. Avila, *Phys. Rev. B* **65**, 17 (2002).
- [215] A. Silhanek, L. Civale, S. Candia, G. Nieva, G. Pasquini, and H. Lanza, *Phys. Rev. B* **59**, 21, 13620 (1999).
- [216] D. H. Lowndes, D. K. Christen, C. E. Klabunde, Z. L. Wang, D. M. Kroeger, J. D. Budai, S. Zhu, and D. P. Norton, *Phys. Rev. Lett.* **74**, 12, 2355 (1995).
- [217] J. H. Durrell, *Critical Current Anisotropy in High Temperature Superconductors*, Ph.D. thesis, University of Cambridge (2001).
- [218] J. H. Durrell, G. Burnell, V. N. Tsaneva, Z. H. Barber, M. G. Blamire, and J. E. Evetts, *Phys. Rev. B* **70**, 21, 214508 (2004).
- [219] A. Polyanskii, L. Dorosinskii, M. Indenbom, V. Nikitenko, Y. Ossipyan, and V. Vlasko-Vlasov, *J. Less-Common Met.* **164-165**, Part 2, 1300 (1990).
- [220] L. Méchin, P. Berghuis, and J. E. Evetts, *Physica C* **302**, 2-3, 102 (1998).
- [221] J. Z. Wu and W. K. Chu, *Phil. Mag. B* **67**, 4, 587 (1993).
- [222] Z. Trajanovic, C. Lobb, M. Rajeswari, I. Takeuchi, C. Kwon, and T. Venkatesan, *Phys. Rev. B* **56**, 2, 925 (1997).
- [223] C. Cantoni, D. T. Verebelyi, E. D. Specht, J. Budai, and D. K. Christen, *Phys. Rev. B* **71**, 5, 054509 (2005).
- [224] M. Djupmyr, G. Cristiani, H.-U. Habermeier, and J. Albrecht, *Phys. Rev. B* **72**, 22, 220507 (2005).
- [225] C. Jooss, R. Warthmann, and H. Kronmüller, *Phys. Rev. B* **61**, 18, 12433 (2000).

- [226] W. Goldacker, R. Nast, G. Kotzyba, S. I. Schlachter, A. Frank, B. Ringsdorf, C. Schmidt, and P. Komarek, *J. Phys.: Conf. Ser.* **43**, 901 (2006).
- [227] W. Goldacker, A. Frank, R. Heller, S. I. Schlachter, B. Ringsdorf, K.-R. Weiss, C. Schmidt, and S. Schuller, *IEEE Trans. Appl. Supercond.* **17**, 2, 3398 (2007).
- [228] N. J. Long, R. Badcock, P. Beck, M. Mulholl, N. Ross, M. Staines, H. Sun, J. Hamilton, and R. G. Buckley, *J. Phys.: Conf. Ser.* **97**, 012280 (2008).
- [229] D. L. Schulz and T. J. Marks, *Adv. Mater.* **6**, 10, 719 (1994).
- [230] M. Matsubara and I. Hirabayashi, *Appl. Surf. Sci.* **82-83**, 494 (1994).
- [231] P. Berghuis, G. A. Wagner, S. C. Fan, and J. E. Evetts, in T. M. Matsushita and K. Yamafuji, editors, *Proc. 8th IWCC in Superconductors*, page 247, World Scientific, Singapore (1996).
- [232] D. Feinberg and C. Villard, *Phys. Rev. Lett.* **65**, 7, 919 (1990).
- [233] Y. V. Bugoslavsky, A. A. Zhukov, G. K. Perkins, A. D. Caplin, H. Kojima, and I. Tanaka, *Phys. Rev. B* **56**, 9, 5610 (1997).
- [234] A. A. Zhukov, H. Kupfer, P. A. J. de Groot, and T. Wolf, *Phys. Rev. Lett.* **83**, 24, 5110 (1999).
- [235] R. Hühne, J. Eickemeyer, V. S. Sarma, A. Güth, T. Thersleff, J. Freudenberger, O. de Haas, M. Weigand, J. H. Durrell, L. Schultz, and B. Holzapfel, *Supercond. Sci. Technol.* **23**, 3, 034015 (2010).
- [236] J. Eickemeyer, D. Selbmann, R. Hühne, H. Wendrock, J. Hänisch, A. Güth, L. Schultz, and B. Holzapfel, *Appl. Phys. Lett.* **90**, 1, 012510 (2007).
- [237] R. Hühne, J. Eickemeyer, D. Selbmann, L. Schultz, and B. Holzapfel, *IEEE Trans. Appl. Supercond.* **17**, 2, 3239 (2007).
- [238] K. R. Schöppl, H. W. Weber, and J. H. Durrell, *Physica C* **460-462**, Part 2, 1188 (2007).
- [239] A. Koblishka-Veneva and M. R. Koblishka, *Mater. Sci. Eng., B* **151**, 1, 60 (2008).